Multi-isotope tracing of complex crustal fluid systems



Rebecca L Tyne
St Anne's College
University of Oxford

A thesis submitted for the degree of
Doctor of Philosophy
Hilary 2021

Abstract

There is significant societal concern regarding environmental issues, including ensuring safe long-term CO_2 storage and safeguarding against groundwater pollution. However, the complex nature of the crustal systems mean there are still many questions surrounding fluid behaviour within the subsurface. This study utilises noble gas, stable and clumped isotopes to investigate, constrain and predict subsurface fluid behaviour within the context of CO_2 storage and hydrocarbon contamination of shallow aquifers. Firstly, a novel method was developed that enabled the first noble gas analysis of multi-phase fluids. This approach was validated by comparing casing gas and produced fluids samples from oil fields in California. We then characterised the noble gas isotopes and abundances in these reservoirs and found a clear relationship between noble gas compositions and injected volumes. This allows for the prediction of both pristine and evolved reservoir compositions, which represents a crucial first step in characterising the various endmember compositions in groundwater contamination studies. Secondly, we use an integrated isotope approach to place constraints on both physical and biogeochemical processes resulting from CO_2 injection into a depleted hydrocarbon reservoir CO_2 storage target. We show that a significant proportion of the injected CO_2 has been consumed by microbial methanogenesis and estimate a rate for this process. These findings are significant as methanogenesis can affect the trapping efficiency of a given system and thus it is a paramount consideration in site selection for future CO_2 storage projects. Finally, the Paradox Basin (Colorado Plateau) is used to investigate the utility of noble gases to understand the role of basin architecture in controlling subsurface fluid composition and connectivity. Here, we use noble gas data to inform conceptual models in order to show that subsurface fluid composition and extent of fluid migration is controlled by the presence of a thick evaporite unit. The data and interpretation presented in this thesis, greatly expands our understanding of both noble gas behaviour in response to anthropogenic perturbations and the resulting processes. Additionally, this study demonstrates the utility of a multi-isotope approach for probing subsurface processes.

Extended Abstract

There is significant societal concern regarding environmental issues which have been exacerbated by climate change, including groundwater security, in particular in regions where water resources are scare. The geological storage of carbon and identification of the source of any groundwater contamination is critical for addressing these concerns and gaining a better understanding of the processes associated with these issues.

During my PhD, we measured noble gas, stable and clumped isotopes in a mixture of multi-phase oil field fluids, pure gas phase hydrocarbons and groundwaters in order to better understand the processes controlling fluid behaviour within the complex subsurface fluid systems. Due to their inert nature, noble gases are powerful tracers of fluid provenance and physical processes and when combined with stable and clumped isotopes can provide useful insights into various chemical and biological processes. Here, we develop a method that enables noble gas analysis of multi-phase fluids, which we use to investigate different aspects of subsurface fluids in the context of groundwater security and carbon capture and storage through multiple case studies.

In order to ensure groundwater security, particularly in regions where water resources are scarce and in high demand, it is important to understand any impact hydrocarbon production could have on the overlying shallow aquifers. In this context, the geochemical characterisation of oil field fluids (gas, water, oil) is critical so that anthropogenic contaminants can be readily identified. In oil field systems, noble gas isotopes and abundances are typically measured in the casing gases, however, it is not always possible to collect casing gases and therefore produced fluids (which are an admixture of water, oil and gas mixtures) must be analysed. We develop a novel extraction system that quantitatively isolates noble gases, while effectively removing all water, oil, and less volatile hydrocarbons. The samples can then be further purified and analysed using standard techniques. Method reproducibility for the key isotopes (^{4}He, ^{20}Ne, ^{36}Ar, ^{84}Kr, ^{132}Xe) is between 2.9 -5.7%. The gas phase in produced fluids is compared to data from casing gases and we find that the two sample types are in agreement and can be used essentially interchangeably. Noble gas isotope ratios and abundances were determined for four oil fields across California which have been subjected to variable degrees of fluid injection for enhanced oil recovery (EOR). This approach allows for the characterisation of both the pristine geochemical fluid signatures (i.e., those unmodified by hydrocarbon resource development) and provides insight into how these signals may have been modified by production (i.e., EOR). We show that EOR signatures can be easily identified by their distinct air-derived noble gas elemental ratios (i.e., $^{20}Ne/^{36}Ar$) which are elevated relative to the pristine reservoir and trend towards an air value. We observe a clear correlation (r^2= 0.88-0.98) between the $^{20}Ne/^{36}Ar$ in the reservoir fluids and the volume of injected fluids within 500m of a well, however the rate of the increase in $^{20}Ne/^{36}Ar$ is field dependent. We develop a mixing model in order to examine and quantify the reservoir evolution with enhanced oil recovery and ascertain that the volume of fluid interacting with the injectate (i.e., the effective water-to-oil ratio), and the composition of the injectate, are key in controlling the reservoir composition. This is important, as it allows us to predict predevelopment and evolved noble gas compositions of a given reservoir, which is critical for distinguishing the sources of hydrocarbons observed in proximal groundwaters.

Secondly, the processes that control the behaviour of carbon within the depleted hydrocarbon reservoir CO_2 storage targets, are investigated through a case study of the Olla Oil Field (Louisiana).

We present noble gas, stable isotope and clumped isotope data from two comparable oil fields with contrasting production histories. The Olla Field (n=7) was CO_2-flooded during the 1980s. Data from this site are compared to the nearby Nebo-Hemphill Field (n = 7), which has never been subjected to CO_2 injection. This integrated approach allows us to place constraints on both physical and biogeochemical processes resulting from CO_2 injection. From noble gas data, we estimate that there is a minimum CO_2 loss of ~90% within the Olla Field and that solubility trapping is the dominant CO_2 sink. However, stable and clumped isotopes and constraints on the presence of microbial methane show that even with the most conservative estimates, CO_2 consumption via methanogenesis is significant (consumption of 13-19% of emplaced CO_2) within the Olla Field. Although this is quantitatively less than the amount of CO_2 that has been dissolved into water, it represents a substantial CO_2 loss mechanism. We calculate the first *in-situ* microbial methanogenesis rate from within a natural system, yielding 73-109 mmol CH_4/m^3(STP)/yr for the Olla Field, which is significant on engineering timescales. Similar geochemical trends in other injected and natural CO_2 fields suggest that microbial methanogenesis may be a globally significant process. For CO_2 storage sites within the environmental window for microbial methanogenesis, this presents a significant consideration, as CH_4 is less soluble and more mobile than CO_2, thus there is an enhanced potential of gas loss associated with CH_4 production.

Finally, we use noble gases to investigate the role of basin architecture in controlling the evolution and migration of fluids in the Paradox Basin (Colorado Plateau, USA). The Paradox Basin is a flexural basin that is defined by the extent of a thick evaporate unit (Paradox Formation). It contains multiple paleofluid features including extensive sandstone bleaching and abundant hydrocarbon, He and CO_2 accumulations. Noble gas concentrations and isotope characteristics were determined for 16 groundwater and 20 hydrocarbon samples across the interior of the Paradox Basin, including from within the Paradox Formation (n=7). Air corrected helium isotopes are consistent with noble gases being groundwater derived, with radiogenic overprinting. There is also a significant difference in both the radiogenic noble gas ratios ($^{40}Ar/^{36}Ar$ and $^{21}Ne/^{22}Ne$) above and below the Paradox Formation. We develop phase fractionation models using the atmospheric noble gas elemental ratios to investigate fluid circulation and find evidence of fluid migration both above and below the Paradox Formation. More partial redissolution is observed in the formations above the Paradox Formation, consistent with two distinct hydrogeological regimes. We use a 1D vertical ^4He diffusion model to assess formation connectivity. We demonstrate the Paradox Formation is an impermeable barrier to fluid migration within the system, allowing for the evolution of the distinct noble gas compositions observed on either side of the Formation. Our findings show that noble gases can be used to quantify the effectiveness of the Paradox Formation (and evaporites more generally) as a seal, which is important for ensuring groundwater security in the area, as well as identifying potential CO_2 storage targets.

Overall, the data and interpretations presented within this thesis explores some of the uncertainties surrounding subsurface fluid behaviour, particularly within the context of groundwater contamination and CO_2 storage. Additionally, this work demonstrates the utility of a multi-isotope approach in understanding these and other subsurface processes.

Declaration

I declare that this thesis has been composed by myself and that the work has not been submitted for any other degree or professional qualification. I confirm that the work submitted is my own, except where work which has formed part of jointly authored publications has been included. My contributions to these publications have been explicitly indicated below and in the signed authorship statements at the end of the relevant Chapters. I confirm that appropriate credit has been given within this thesis where reference has been made to the work of others.

The work presented in Chapter 2, was previously published in Geochemistry, Geophysics, Geosystems (Technical Reports: Methods), Vol 20, Issue 11 as "A Novel Method for the Extraction, Purification, and Characterization of Noble Gases in Produced Fluids" by **Tyne, R.L.,** Barry, P. H., Hillegonds, D.J., Hunt, A.G., Kulongoski, J.T., Stephens, M.J., Byrne, D. J., and Ballentine, C. J. I led the development of laboratory protocols and phase reconstructions, carried out noble gas analyses and wrote the manuscript.

The work presented in Chapter 3 is published in Chemical Geology as "Investigating the effect of enhanced oil recovery on the noble gas signature of casing gases and produced waters from selected California oil fields" by **Tyne, R.L.,** Barry, P. H., Karolytė R., Byrne, D. J., Kulongoski, J.T., Hillegonds, D.J., and Ballentine, C. J. I carried out noble gas analyses, led interpretation and model development, and wrote the manuscript.

The work presented in Chapter 4 has been accepted in. Nature as "Rapid microbial methanogenesis during CO_2 storage in hydrocarbon reservoirs" by **Tyne, R.L.,** Barry, P. H., Lawson, M., Byrne, D. J., Warr, O., Xie, H., Hillegonds, D., Formolo, M., Summers, Z.M., Skinner, B., Eiler, J.M., and Ballentine, C. J. I carried out noble gas analyses, managed the project, led interpretation and model development, and wrote the manuscript.

The work presented in Chapter 5 is currently under review in EPSL as "Basin architecture controls on the chemical evolution and ^{4}He distribution of groundwater in the Paradox Basin" by **Tyne, R.L.,** Barry, P. H., Cheng, A., Kim, J-H., McIntosh, J.M., Hillegonds, D.J., and Ballentine, C. J. I carried out noble gas analyses, led interpretation and model development, and wrote the manuscript.

Rebecca L. Tyne

Acknowledgments

There have been so many people whom have helped me throughout and contributed towards this thesis and although I would love to list them all here, it would probably be nearly as long as my thesis itself, so thank you all! I would, however, I like to give a special mention to those whom I would not have been able to make it through without!

First of all, I would like to thank my supervisors Chris Ballentine and Peter Barry for their unfailing support, guidance and encouragement throughout the course of this project. Their exhaustive knowledge of noble gases has been both terrifying and invaluable and I will be forever indebted to them for their help and encouragement to develop my own research. They have both provided me with more opportunities than I could have wished for, as well as some incredible experiences! I would like to thank Pete in particular for time he took training me on the mass spec, his patience with my daily questions and teaching me to say no (which I have now mastered ~1% of the time). I'd also like to thank him for the great times we had on field trips, letting me crash his post field trip holidays/family visits and letting me stay with him when he moved to WHOI.

I have also been lucky enough to have extra supervision from Justin Kulongoski and Michael Lawson, both of whom I cannot thank enough for sharing their knowledge, their advice and enthusiasm throughout. I would like to give Mike a special thank you for his help and perseverance with the difficulties of information releases.

I would like to thank both the past and present members of the Noble Lab that I have been privileged enough to endure the highs and lows of lab work with and who were always willing to eat my latest baking creations, especially Olly, Dave, Darren, Annie, James, Rosie, Rūta and Steph. Dave Byrne deserves a special mention for knowing all the mass spec settings by heart (and being on call from the pub), for his continuing mentorship and being probably the only other person to read my thesis from front to back! I'd also like to thank Jen McIntosh for involving me in her projects, sharing her knowledge and insights into hydrogeochemistry, the fieldwork opportunities she gave me and letting me stay with her. I am also grateful to Jess Marcusa at the USGS for her amazing ability to organise fieldwork, for letting me use her spare room, and the many fun activities she always had planned for us.

Thank you to all the great friends I have made during my time in Oxford, who have made my time much more enjoyable and given me a welcome respite from my thesis! I'd particularly like to thank Annie and Rellie, whose friendships has been so important over past few years, and whom have provided me with much needed sanity breaks and distractions! I am also very grateful for Hayley for her friendship and letting me escape to her house and garden when I needed it most and for Mel Murphy for taking me under her wing when I arrived and being my mentor and friend throughout.

A massive thank you goes to Caleb, without whom I would never have started (or finished!) this thesis! Even during the lows, your love, support and belief in me got me through and for that, I will be eternally grateful. I also could not think of a better 'office' mate for the past year and a half! Finally, I would like to thank my parents for providing me with all the love and opportunities that I could have wished for and my sister for always making me smile.

Table of Contents

List of Figures xi
List of Tables xiii
List of Abbreviations xv

1 Introduction 1
1.1 Motivation 2
1.2 Thesis overview 3
1.3 Literature review 5
1.3.1 Introduction 5
1.3.2 Origin of terrestrial noble gases 6
1.3.3 Terrestrial noble gas inventories 10
1.3.4 Noble gas solubility 15
1.3.5 Dating radiogenic growth 17
1.3.6 Noble gas transport through sedimentary basins 19
1.3.7 Noble gases in petroleum systems 20
1.3.8 Noble gases in carbon capture and storage analogues 23
1.3.9 Introduction to methane clumped isotopologues 27
1.3.10 Summary 32
References 33

2 A novel method for the extraction, purification and characterisation of noble gases in produced fluids 47
Abstract 48
2.1 Introduction 48
2.2 Analytical methods 50
2.3 Air-saturated water data 54
2.3.1 Air-saturated water generation 54
2.3.2 Calculating air-saturated water concentrations 55
2.3.3 Reproducibility of air-saturated water 56
2.4 Produced fluid results 60
2.4.1 Geological context 60
2.4.2 Sample collection 60
2.4.3 Calculating concentrations in multi-phase fluids 61
2.4.4 Produced fluid compositions 63
2.5 Conclusions 64
S2.1 Supplementary figures 65
S2.2 Supplementary tables 67

S2.3 Supplementary information 69
Acknowledgments, samples, and data 74
Authorship statement 75
References 76

3 Investigating the effect of enhanced oil recovery on the noble gas signature of casing gases and produced waters from selected California oil fields 79
Abstract 80
3.1 Introduction 81
3.2 Geological context 83
3.3 Methods 84
3.3.1 Sample collection 84
3.3.2 Analytical techniques 88
3.3.3 Calculating noble gas concentrations within produced fluids 88
3.4 Results 90
3.4.1 Casing gas results 90
3.4.2 Produced fluid results 98
3.5 Discussions 99
3.5.1 Comparison of casing gas and produced fluids at the wellhead 99
3.5.2 Reconstructing noble gas concentrations in the reservoir oil 100
3.5.3 Determining pre-development reservoir characteristics 102
3.5.4 Assessing the effects of injection 106
3.6 Conclusions 112
S3.1 Supplementary figures 114
S3.2 Supplementary tables 119
S3.3 Supplementary information 120
Acknowledgments, samples, and data 125
Authorship statement 126
References 127

4 Rapid microbial methanogenesis during CO_2 storage in hydrocarbon reservoirs 133
Abstract 134
4.1 Main text 134
4.2 Methods 144
4.2.1 Modelling 144
4.2.2 Sample collection and analysis 145
S4.1 Supplementary figures 147
S4.2 Supplementary tables 153

S3.3 Supplementary information 157
Acknowledgments 169
Authorship statement 170
References 171

5 Noble gases reveal the role of basin architecture in controlling the chemical evolution of groundwater in the Paradox Basin 177
Abstract 178
5.1 Introduction 179
5.2 Geological context 181
5.3 Methods 183
5.4 Results 184
5.4.1 Helium 184
5.4.2 Neon 192
5.4.3 Argon 192
5.4.4 Krypton and xenon 192
5.5 Discussions 192
5.5.1 Assessing fluid provenance using noble gas isotope ratios 192
5.5.2 Radiogenic noble gases concentrations 195
5.5.3 Fractionation of atmospheric noble gases (ANG) ratios due to fluid interactions 205
5.5.4 Investigating ^{4}He distribution 211
5.6 Implications and conclusions 216
S5.1 Supplementary figures 219
S5.2 Supplementary tables 222
S5.3 Supplementary information 227
Acknowledgments 234
Authorship statement 235
References 236

6 Conclusions 243
6.1 Summary and impact 244
6.2 Outlook and future work 247
References 251

List of Figures

1.1	Overview of noble gas provenance in crustal systems	11
1.2	Isotope dating methods in groundwater	18
1.3	Schematic of noble gas evolution in hydrocarbon fields	22
1.4	Pathways for hydrocarbon contamination in groundwater	23
1.5	CO_2 -helium vs. carbon systematics from previous studies	25
1.6	CO_2 -helium vs. helium systematics from previous studies	26
1.7	Methane clumped isotopes model framework	30
2.1	Noble gas extraction line	52
2.2	Air saturated water reproducibility	57
S2.1	Oil well schematic	65
S2.2	Map of the Fruitvale Oil Field	66
3.1	Sample map of California oil fields	84
3.2	California oil fields helium systematics	91
3.3	Casing gas- produced fluid neon abundance comparison	101
3.4	Atmospheric noble gas injection mixing models (Fruitvale)	107
3.5	Relationship between atmospheric noble gas and injection volume	109
S3.1	Stratigraphic columns for the sampled fields	114
S3.2.	Casing gas- produced fluid argon abundance comparison	115
S3.3	Heavy atmosphere derived noble gas compilation	116
S3.4.	Relationship between atmospheric noble gas and injection volume (Lost Hills and Orcutt)	117
S3.5	Atmospheric noble gas injection mixing models (Lost Hills and Belridge)	118
4.1	Olla sample map	136
4.2	Methanogenesis-dissolution models	138
4.3	Olla clumped methane isotopologues	140
S4.1	Olla helium and neon isotopes	147
S4.2.	Olla CO_2 -helium vs. helium and neon systematics	148
S4.3	Olla methane stable isotopes	149
S4.4.	Olla alkane stable isotopes	149
S4.5	Olla microbial community analysis	150
S4.6	Methanogenesis-dissolution models	151
S4.7	Methanogenesis-dissolution model Pannonian Basin	152
5.1	Paradox Basin map	180
5.2	Paradox Basin cross section and stratigraphic column	182
5.3	Paradox Basin helium isotope distribution with depth	191
5.4	Paradox Basin neon and argon isotopes	193
5.5	Comparison of calculated ^4He concentrations in groundwater	200
5.6	Paradox Basin radiogenic isotopes	202
5.7	Paradox Basin helium concentrations with depth	203
5.8	Phase fractionation models	207
5.9	Vertical 1D ^4He diffusion models	213
S5.1	Paradox Basin helium-neon distribution with depth	219
S5.2	Paradox Basin radiogenic isotope distribution with depth	220
S5.3	Helium sources and sinks to sedimentary formations	221

List of Tables

1.1	Terrestrial noble gas isotopes and their major sources.	7
1.2	Noble gas composition of air	12
2.1	Fruitvale meta data	54
2.2	Air saturated water reproducibility	58
S2.1	Equation parameters	67
S2.2.	Fruitvale well information and USGS ID's	67
S2.3.	Fruitvale noble gas abundances	68
3.1	California oil fields well information and USGS ID's	85
3.2	California oil fields meta data	86
3.3	California oil fields noble gas abundances	92
3.4	California oil fields noble gas isotope ratios	96
3.5	California oil fields noble gas reservoir abundances	104
3.6	California oil fields injection model results	108
S3.1	California oil fields recharge and reservoir conditions	119
S4.1	Olla bulk composition, stable isotopes and helium isotopes	153
S4.2	Olla clumped isotopologues	154
S4.3	Olla noble gas abundances and isotope ratios	155
S4.4	Olla alkane isotope composition	156
5.1	Paradox Basin noble gas abundances	185
5.2	Paradox Basin noble gas isotope ratios	188
5.3	Paradox Basin radiogenic isotope	198
5.4	Paradox Basin atmospheric noble gas ratios	208
S5.1	Paradox Basin sample location, formation and type	222
S5.2	Paradox Basin reservoir conditions	224
S5.3	Paradox Basin calculated helium concentrations in groundwater	225
S5.4	Helium diffusion models inputs	226

List of Abbreviations

ANG	Atmosphere-derived noble gas
API	American petroleum institute gravity units
ASW	Air-saturated water
CCS	Carbon capture and storage
EOR	Enhanced oil recovery
MORB	Mid-ocean ridge basalts
OIB	Ocean island basalts
R_A	Atmospheric helium isotope ratio
ID	Inside diameter
STP	Standard temperature and pressure
RTP	Reservoir temperature and pressure
WOR	Water-to-oil ratio
GOR	Gas-to-oil ratio
GWR	Gas-to-water ratio
SWRCB	State Water Resource Control Board
RMP	Regional monitoring program
SJB	San Joaquin Basin
AOM	Anaerobic oxidation of methane
ANME	Anaerobic methanotrophs
WOGC	Whole oil gas chromatography
OCLC	Open column liquid chromatography
GC/MS	Gas chromatography mass spectroscopy
DIC	Dissolved inorganic carbon

Chapter 1

Introduction

Contents

1.1	Motivation		2
1.2	Thesis overview		3
1.3	Literature review		5
	1.3.1	Introduction	5
	1.3.2	Origin of terrestrial noble gases	6
	1.3.3	Terrestrial noble gas inventories	10
	1.3.4	Noble gas solubility	15
	1.3.5	Dating radiogenic growth	17
	1.3.6	Noble gas transport through sedimentary basins	19
	1.3.7	Noble gases in petroleum systems	20
	1.3.8	Noble gases in carbon capture and storage analogues	23
	1.3.9	Intorduction to methane clumped isotopolgues	27
	1.3.10	Summary	32
References			33

1.1. Motivation

Climate change is one of the biggest challenges facing humanity and as a result there is significant societal concern regarding environmental issues such as groundwater security and the reduction of greenhouse gas emissions. My PhD project was conceived to address some of the uncertainties surrounding these issues, by developing a better understanding of the multi-phases processes within crustal systems associated with groundwater contamination and the behaviour of CO_2 within the subsurface.

As part of the Paris Agreement many of the world's largest economies have pledged to have net-zero emissions by 2050. Rapid CO_2 emission reductions are not likely to be sufficient to meet climate targets and negative emission technologies will be required (IPCC, 2018). Geological storage of carbon is an essential component of the negative emission technologies and is considered effective when CO_2 is introduced into a reservoir that is conducive for long-term storage. Trapping mechanisms, listed in order of increasing geological storage stability include structural and stratigraphic trapping, residual CO_2 trapping, solubility trapping and mineral trapping (carbonate mineralisation and adsorption)(IPCC, 2005). An understanding of the processes controlling CO_2 behaviour and thus the potential trapping and storage mechanisms in the subsurface is critical.

In many water-stressed region, hydrocarbon production is also prevalent and elevated hydrocarbon gas concentrations have been identified in many shallow aquifers (e.g., Osborn et al., 2011; Vengosh et al., 2014; Darrah et al., 2014; Kulongoski et al., 2018; Anders et al., 2019). The extent to which production may (or may not) have caused local hydrocarbon contamination of shallow aquifers and whether this contamination is a result of natural or anthropogenic processes, is not well constrained. Therefore, an understanding of the pristine composition of the various different system endmembers (e.g., hydrocarbon reservoir, surface disposal ponds, and injection fluids), the processes occurring and the migration pathways, is required.

Geochemical tracers have a huge potential for understanding the different processes occurring within the subsurface (e.g., Ballentine et al., 2002; Holland and Gilfillan, 2013; Vengosh et al.,

2014; Stolper et al., 2018; McIntosh et al., 2019; Young, 2019). Given the growing societal concern regarding the environment, it is timely to revisit and further developed the use of multi-isotope tracers (noble gases, stable isotopes, clumped isotopes) to better understand, constrain and predict subsurface fluid behaviour.

Furthermore, the permanency of CO_2 storage and insurance of groundwater security, both rely on having a good subsurface reservoir seal. It is therefore not only important to understand the processes which are controlling CO_2 and hydrocarbon behaviour within the subsurface, but also to understand how the fluid composition and migration is effected by the basin architecture. The application of these multi-isotope tracers has huge potential in developing this understanding (Barry et al., 2016, 2017; Danabalan, 2017; Cheng, 2020; Byrne et al., 2020).

The findings from the noble gas, stable and clumped isotope analysis will also have implications for related fields. An understanding of the fluid behaviour could lead to a better understanding of other subsurface engineering projects, such as for sustainable hydrocarbon development (Pinti and Marty, 1995; Ballentine et al., 1996; Zhou and Ballentine, 2006; Hunt et al., 2012; Barry et al., 2018a, 2018b; Byrne et al., 2018, 2020) or nuclear water disposal (Hendry et al., 2015). In addition, understanding fluid behaviour in sedimentary basins could aid in resource prospecting, in particular for less abundant gases such as H_2 and He.

1.2. Thesis overview

The primary aim of my thesis is to gain a better understanding of the different processes that can occur in complex multiphase crustal systems, in particular in those associated with geological CO_2 storage and groundwater contamination, through the application of noble gas, stable and clumped isotope tracers.

Chapter 1 of this thesis contains a comprehensive literature review of noble gas and clumped isotope gas tracers. The original contributions contained within this thesis comprise of 4 papers, the first of which details the development of analytical methods and the remaining three papers each focusing on individual case studies.

Chapter 2 focusses on the development of a new experimental technique that allow for the analysis of noble gases in multi-phase fluids and a summary of the analytical protocols used for the noble gases measurements within this thesis. This work has been previously published in Geochemistry, Geophysics, Geosystems (Tyne et al., 2019).

Chapter 3, provides a comparison of multi-phase and gas phase sample types, to verify previous assumption used in reconstructing noble gas concentrations within the subsurface and to determine whether these disparate sample types can be compared. We then focus on characterising the evolution of the noble gas composition of a hydrocarbon reservoir with enhanced oil recovery. The geochemical characterisation of a hydrocarbon reservoir is the critical first step in being able to trace hydrocarbon contributions to protected shallow groundwaters. We utilise samples from four different oil fields across California to investigate the effects of injection. This work is part of the California State Water Resource Control Board's Oil, Gas and Groundwater regional monitoring program. This program aims to determine if any fluid exchange has occurred between oil and gas activities and the surrounding groundwater and provide information to resource managers about the relative risks to groundwater security (Taylor et al., 2014). This work has been submitted and is in review in Chemical Geology.

Chapter 4 aims to investigate the behaviour of carbon within geological CO_2 storage targets by using noble gas, stable and clumped isotopes. Understanding the behaviour of carbon within potential storage reservoirs is important for determining the trapping efficiency and overall storage potential of a system. We exploit samples from a depleted oil reservoir, in La Salle County Louisiana, that was CO_2 injected in the 1980s, in order to investigate and model the processes controlling the carbon's behaviour at depth and the rates at which these processes can occur. We also identify other potential locations globally where these processes could have occurred. This work has been submitted and is in review at Nature.

In Chapter 5, we investigate the use noble gases in investigating how basin architecture can control the geochemical composition of fluids within a sedimentary basin. This is crucial in identifying potential CO_2 and nuclear waste storage sites, tracing hydrocarbon contributions detected in shallow

aquifers and in sustainable resource development (e.g., He, H_2 and hydrocarbons). We utilise a sample suite from across seven different stratigraphic units in the Paradox Basin, Colorado Plateau, USA, to examine fluid composition and interactions within each formation. Through the noble gas compositions and the utilisation of diffusion models (e.g., Cheng, 2020), we investigate how a thick evaporite unit has impacted the chemical evolution of groundwater and fluid migration within the basin.

A summary of findings, study impacts and a future research outlook can be found in Chapter 6.

1.3. Literature review

1.3.1. Introduction

The interaction of multiphase fluids within sedimentary basins has been the subject of thousands of studies. These studies try to better understand, constrain and characterise the composition of the fluids and the processes that control the fluid's behaviour within a basin. Geochemical tracers have been at the forefront of many of these studies and allow us to understand and place constraints on fluid behaviour within the subsurface. For example, they can provide insights into the time and temperature constraints of a system (e.g., Sweeney and Burnham, 1990; Zhou and Ballentine, 2006; Stolper et al., 2014a; Barry et al., 2017; Warr et al., 2018; Young, 2019). In addition, they can provide insights into storage, accumulation and migration of hydrocarbon fluids, as well as the accumulation of less abundant gases such as helium and hydrogen (e.g., Schoell, 1983; Chung et al., 1988; Ballentine et al., 1991; Hughes et al., 1995; Ballentine and Sherwood Lollar, 2002; Stolper et al., 2014a, 2018; Barry et al., 2016; Young, 2019; Byrne et al., 2020), and can aid in the understanding of connectivity within a basin (e.g., Sherwood Lollar et al., 1997; Gilfillan et al., 2008; Barry et al., 2017; Cheng, 2020; Byrne et al., 2020). An understanding of these behaviours will be critical for resource prospecting, developing sustainable hydrocarbon extraction, CCS and nuclear waste disposal protocols, as well as for protecting shallow freshwater aquifers.

There are six noble gases: helium, neon, argon, krypton, xenon and radon. There are no stable isotopes of radon and therefore its use as tracers within crustal systems is restricted; radon will not

be discussed further within this thesis. Noble gases are inert, have a high volatility and low abundance and thus are susceptible to physical changes within a system. Therefore, noble gases are useful in tracing many crustal fluid processes over a wide range of geologically important systems that are not always amenable to other analytical techniques. Comprehensive reviews on tracing fluid origin, transport and interactions in crustal systems using noble gases can be found in Ballentine et al. (2002) and Holland and Gilfillan (2013).

More recently, advances in instrumentation have allowed for the measurement of the clumped isotopologues of methane (e.g., Wang et al., 2004; Cao and Liu, 2012; Stolper et al., 2014a, 2014b, 2015; Young et al., 2017; Shuai et al., 2018; Gruen et al., 2018). Although this is still a nascent field, clumped isotopologues of methane are becoming more widely used as they can inform on origin of methane, reservoir temperature and potential processes occurring within the reservoir. These can have economic, biogeochemical and environmental implications. The theory and applications of methane clumped isotopologues are summarised in Douglas et al. (2017), Stolper et al. (2018) and Young (2019).

1.3.2. Origin of terrestrial noble gases

Terrestrial noble gas isotopes are primarily produced primordial in origin or form from nuclear decay processes. A list of stable noble gas isotopes and their formation processes has been compiled in Table 1.1 (Porcelli et al., 2002).

1.3.2.1. Primordial noble gases

Primordial noble gases are those incorporated into Earth during planetary accretion. Proposed capture mechanisms include but are not limited to: gravitational capturing of volatiles from the proto-star nebula (e.g., Pepin, 2006); adsorption to accumulating dust (Marrocchi et al., 2005, 2011); implantation by solar wind (Podosek et al., 2000) and; contribution of volatile-rich cometary material during the Late Heavy Bombardment (Owen et al., 1992; Dauphas, 2003; Holland et al., 2009). As a result of their high volatility, the bulk Earth is depleted in noble gases by several orders of magnitude compared to the proto-solar nebula from which the Earth formed. Noble gas isotopes which are not produced in significant quantities on Earth (e.g., ^{20}Ne, ^{36}Ar, ^{84}Kr, ^{130}Xe) are assumed

Isotope	Primary terrestrial source	Present day production rate* cm^3(STP)/kg/yr	Parents	Half Life (years)
^{3}He	Primordial, Radiogenic, Cosmogenic	$2.49x10^{-18}$	^{3}H	12.26
^{4}He	Radiogenic	$3.31x10^{-10}$	^{232}Th, ^{235}U, ^{238}U	$1.401x10^{10}$, $7.038x10^{8}$, $4.468x10^{9}$
^{20}Ne	Primordial, Nucleogenic	$1.47x10^{-18}$	$^{17}O(\alpha,n)$, $^{23}Na(n,\alpha)$	
^{21}Ne	Primordial, Nucleogenic	$1.51x10^{-17}$	$^{18}O(\alpha,n)$, $^{24}Mg(n,\alpha)$	
^{22}Ne	Primordial, Nucleogenic	$3.03x10^{-17}$	$^{25}Mg(n,\alpha)$, $^{19}F(\alpha,n)$ $^{22}Na(\beta+)$,$^{19}F(\alpha,p)$	
^{36}Ar	Primordial, Radiogenic	$2.38x10^{-18}$	^{36}Cl	$3.01x10^{8}$
^{38}Ar	Primordial	$1.09x10^{-18}$		
^{40}Ar	Radiogenic	$6.05x10^{-11}$	^{40}K	$1.251x10^{9}$
^{78}Kr	Primordial			
^{80}Kr	Primordial			
^{82}Kr	Primordial			
^{83}Kr	Fissiogenic	$5.86x10^{-21}$	^{235}U, ^{238}U	$7.038x10^{8}$, $4.468x10^{9}$
^{84}Kr	Fissiogenic	$2.12x10^{-20}$	^{235}U, ^{238}U, ^{244}Pu	$7.038x10^{8}$, $4.468x10^{9}$, $8x10^{7}$
^{86}Kr	Fissiogenic	$1.39x10^{-19}$	^{235}U, ^{238}U, ^{244}Pu	$7.038x10^{8}$, $4.468x10^{9}$, $8x10^{7}$
^{124}Xe	Primordial			
^{126}Xe	Primordial			
^{128}Xe	Primordial			
^{129}Xe	Radiogenic, Fissiogenic		^{129}I	$1.57x10^{7}$
^{130}Xe	Primordial			
^{131}Xe	Fissiogenic	$7.89x10^{-20}$	^{235}U, ^{238}U, ^{244}Pu	$7.038x10^{8}$, $4.468x10^{9}$, $8x10^{7}$
^{132}Xe	Fissiogenic	$5.24x10^{-19}$	^{235}U, ^{238}U, ^{244}Pu	$7.038x10^{8}$, $4.468x10^{9}$, $8x10^{7}$
^{134}Xe	Fissiogenic	$7.50x10^{-19}$	^{235}U, ^{238}U, ^{244}Pu	$7.038x10^{8}$, $4.468x10^{9}$, $8x10^{7}$
^{136}Xe	Fissiogenic	$9.09x10^{-19}$	^{235}U, ^{238}U, ^{244}Pu	$7.038x10^{8}$, $4.468x10^{9}$, $8x10^{7}$

Table 1.1. Terrestrial noble gas isotopes and their major sources. Including their half lives and their present day production rates within a typical crustal environment. *in typical continental crust.

to be 100% primordial (Burnard et al., 1997; Moreira et al., 1998). With the exception of Xe, their abundance can be explained by a combination of capture during planetary accretion (from the protosolar nebula) and carbonaceous chondrites during the Late Heavy Bombardment (e.g., Ballentine et al., 2005; Ballentine and Holland, 2008; Marty, 2012; Halliday, 2013). Xe is an order of magnitude more depleted compared to chondritic abundances, with a relative enrichment in the heavy isotopes, this is known as the 'Xenon paradox' (Pepin, 2000; Sanloup et al., 2005; Lee and Steinle-Neumann, 2006; Pepin and Porcelli, 2006; Marty, 2012). Recent research has suggested that atmospheric Xe was progressively fractionated during the Achaean supporting gradual Xe depletion from the atmosphere until approximately 2.1Ga (Pujol et al., 2011; Bekaert et al., 2018; Avice et al., 2018, 2020). This fractionation most likely occurred during hydrodynamic hydrogen escape (Zahnle et al., 2019).

1.3.2.2.Nuclear decay

Some noble gas isotopes are produced by either direct or indirect radioactive processes within the Earth. The crust contains 35-55% of Earth's radioelement budget (Rudnick and Fountain, 1995) and thus is associated with high levels of noble gas production. This production is either radiogenic, nucleogenic, fissiogenic or cosmogenic. The concentration of these noble gases into the crustal fluid system results from their release from the host rock into the surrounding fluids by diffusion, recoil and chemical transformation (Ballentine et al., 2002; Ballentine and Burnard, 2002; Barry et al., 2015; Warr et al., 2018). This release is controlled by temperature, grain size and mineral alteration (Honda et al., 1982; Brooker et al., 1998; Baxter et al., 2002). An understanding of these radioactive decay processes has allowed for the successful establishment of dating tools such as Ar-Ar dating, ^{4}He and ^{81}Kr dating (e.g., Merrihue and Turner, 1966; Farley, 2002; Kelley, 2002; Purtschert et al., 2013; Torgersen and Stute, 2013).

1.3.2.2.1. Radiogenic production

Radiogenically produced noble gas isotopes are the daughter products of radioactive decay. On Earth the major radioactive decay series is U and Th. The α-decay of U and Th releases a ^{4}He nucleus which collects electrons from nearby ionised material to form ^{4}He. High ^{4}He concentrations

are therefore associated with elevated U and Th, and as both U and Th are incompatible within the mantle, they are concentrated within the Earth's crust, this results in ^{4}He production being predominantly within the crust. Potassium constitutes approximately 2% of the continental crust (Heier, 1965), and decays by electron capture producing ^{40}Ar. The production of radiogenic ^{40}Ar within the crust and subsequent release and accumulation in the atmosphere has resulted in the ^{40}Ar/^{36}Ar ratio in the atmosphere increasing from a primordial value of ~ 10^{-4}-10^{-3} to the current atmospheric value of 298.56±0.31 (Allègre et al., 1996; Lee et al., 2006; Pepin and Porcelli, 2006).

Expected in-situ production rates for ^{4}He and ^{40}Ar, as a function of U, Th and K concentrations in a rock can be calculated using the following equations (Craig and Lupton, 1976, Ballentine and Burnard, 2002):

$$J(^{4}He) = 0.2355 \times 10^{-12}[U](1 + 0.123\left(\frac{[TH]}{[U]} - 4\right)) \quad \text{(Eq. 1.1)}$$

$$J(^{40}Ar) = 102.2[K] \times V_m/N_a \quad \text{(Eq. 1.2.)}$$

where *J(i)* is the production of species in cm^{3}(STP)/g/yr and U, Th and K concentrations are in ppm. V_m and N_a are the molar gas volume and Avogadros number respectively. Typical in-situ production rates for the continental crust can be found in Table 1.1.

1.3.2.2.2. Nucleogenic production

Nucleogenic production occurs when α-particles and neutrons are released during radioactive decay and interact with the nuclei of nearby atoms. Noble gases formed in measurable quantities from nucleogenic decay are listed in Table 1.1 along with their decay pathways. Neutrons and α-particles are primarily sourced from the radioactive decay of U and Th, and have a typical ejection ranges between 15-45μm and 10-100cm respectively (Ziegler, 1977; Martel et al., 1990). This results in mineral scale heterogeneities being observable within crustal systems. Observed radiogenic ^{21}Ne/^{22}Ne ratios in crustal fluids are below that expected from an average crustal O/F ratios, this difference has been inferred to be a result of the crustal fluids reflecting lower O/F ratios in the mineral environments around U and Th (Kennedy et al., 1990; Hiyagon and Kennedy, 1992). The in-situ production rate of ^{21}Ne* is calculated using the concentrations of U and Th in ppm and O

and Mg in wt % (Eq. 3, Ballentine and Burnard, 2002) and the typical crustal rate is given in Table 1.1.

$$J\left(^{21}Ne\right) = \left((1.48[U] + 0.186[Th])[O] + (0.105[U] + 0.0179[Th])[Mg]\right) x\ 10^{-22} \qquad \text{(Eq. 1.3)}$$

1.3.2.2.3. Fissiogenic production

The fission of unstable, heavy nuclei can result in the formation of some Kr and Xe isotopes (Table 1.1). The production rates of these noble gases are relatively well constrained and lower than those formed by radiogenic and nucleogenic decay (Wieler and Eikenberg, 1999). Low production rates of fissiogenic Xe result in it only being observable in samples which have been isolated for significant periods of time (Holland et al., 2013).

1.3.2.2.4. Cosmogenic production

Cosmogenic rays can interact with the upper portions (~3.5m) of the crust to generate noble gases, in particular ^{3}He and ^{38}Ar (Ballentine and Burnard, 2002; Niedermann, 2002). However, when compared to total crustal production, cosmogenic production is considered negligible for most geological systems (Ballentine and Burnard, 2002).

1.3.3. Terrestrial noble gas inventories

1.3.3.1. Atmospheric noble gases

Atmospheric noble gases are predominantly primordial in origin (Porcelli et al., 2002). The composition of the atmospheric noble gases is distinct from the solar composition, likely due to atmospheric losses during early Earths history, potential from either a catastrophic loss or gradual escape (Pepin and Porcelli, 2006; Pepin, 2006; Tucker and Mukhopadhyay, 2014). However, when considering crustal fluids, it is reasonable to assume that the atmospheric noble gas composition (Table 1.2) has been constant over the timescale since their introduction to the subsurface.

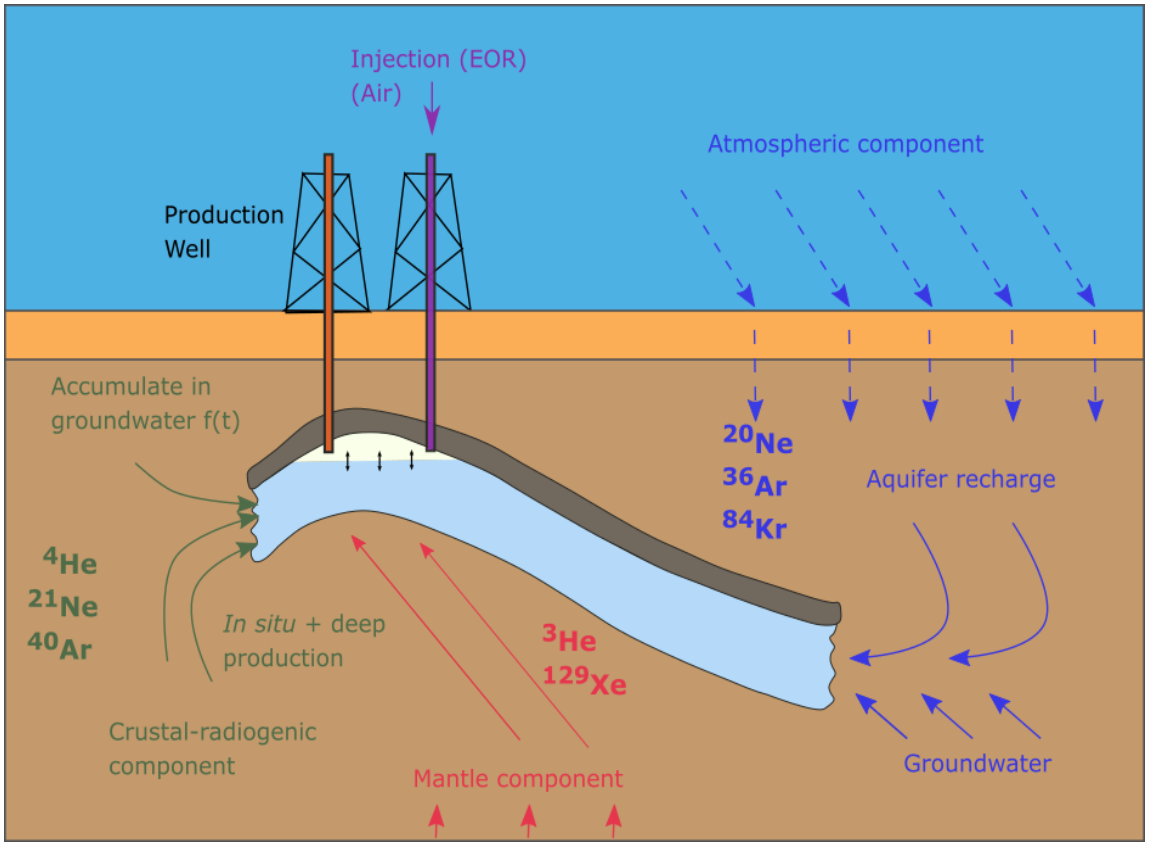


Figure 1.1: Schematic diagrams of a reservoir, illustrating the different noble gas components which could occur within crustal fluids. Atmosphere-derived noble gases (e.g., ^{20}Ne and ^{36}Ar) are input through equilibration with groundwater at recharge or through the injection of surface fluids. Radiogenic noble gases (e.g., ^{4}He, ^{40}Ar) are produced by natural decay of radioelements in the crust and incorporated into fluids. Mantle derived noble gases (e.g., ^{3}He) can also be present in crustal fluids in certain systems. Adapted from Ballentine and O'nions, 1994.

1.3.3.2.Hydrosphere

When water is direct contact with the atmosphere, the noble gases will quickly equilibrate following Henry's Law (described in Section 1.3.4.1, Figure 1.1). The solubility of each noble gas varies and as a result the composition of noble gases within water is not 'air-like', however changes to isotopic ratios of an individual noble gas during equilibrium partitioning are small and are can be considered negligible in comparison to other processes in many scenarios and thus we assume they retain 'air-like' ratios (Kipfer et al., 2002). The equilibrium partitioning of the noble gases, which is dependent on the temperature, pressure and salinity of the system, is well known and therefore, it is possible to calculate the composition of air saturated water (ASW) under ambient conditions in a given environment. The dependency of the ASW composition on temperature, pressure and salinity can

Element/Isotope	Relative abundance	Concentration in air
Helium		$5.24 \pm 0.05 \times 10^{-6}$
^{4}He	≡ 1	
^{3}He	$1.399 \pm 0.013 \times 10^{-6}$	
Neon		$1.818 \pm 0.004 \times 10^{-5}$
^{20}Ne	9.80 ± 0.08	
^{21}Ne	0.0290 ± 0.0003	
^{22}Ne	≡ 1	
Argon		$9.34 \pm 0.01 \times 10^{-3}$
^{40}Ar	298.56 ± 0.31	
^{38}Ar	0.1885 ± 0.0003	
^{36}Ar	≡ 1	
Krypton		$1.14 \pm 0.01 \times 10^{-6}$
^{78}Kr	0.06087 ± 0.0020	
^{80}Kr	3.9599 ± 0.002	
^{82}Kr	20.217 ± 0.004	
^{83}Kr	20.136 ± 0.021	
^{84}Kr	≡ 100	
^{86}KR	30.524 ± 0.025	
Xenon		$8.7 \pm 0.1 \times 10^{-8}$
^{124}Xe	2.337 ± 0.008	
^{126}Xe	2.180 ± 0.011	
^{128}Xe	47.15 ± 0.07	
^{130}Xe	≡ 100	
^{131}Xe	521.3 ± 0.8	
^{132}Xe	660.7 ± 0.5	
^{134}Xe	256.3 ± 0.4	
^{136}Xe	217.6 ± 0.3	

Table 1.2. Noble gas concentrations in dry air and their isotopic ratios. Data from Porcelli et al., 2002; Lee et al., 2006.

also be used to define paleo-environmental conditions (Ballentine and Hall, 1999; Aeschbach-Hertig et al., 1999; Seltzer et al., 2019). A complication of this approach is the addition of 'excess air', an additional atmospheric noble gas component, above that predicted by Henrys Law, empirically measured in meteoric groundwater. It is thought that this excess air is introduced to system by the entrapment of air bubbles in the unsaturated/quasi-saturated zones during water table fluctuations (Heaton and Vogel, 1981). Once beneath the water table the increase in hydrostatic pressure results in these gases dissolving, creating the observed excess. Theoretical models have been made to account for this phenomenon including the closed system equilibration (CE model;

Aeschbach-Hertig et al., 2000, 2008), unfractionated excess air (UA model; Heaton and Vogel, 1981), partial re-equilibration (PR model; Stute et al., 1995) and multi-step partial equilibration (MR Model; Kipfer et al., 2002).

1.3.3.3.Mantle derived noble gases

The noble gas composition of the Earth's mantle is poorly constrained compared to the atmospheric reservoir. It contains a high proportion of primordial noble gases which accumulated during the early accretionary period (Lupton and Craig, 1975; Allègre et al., 1987; Caffee et al., 1999; Broadley et al., 2020) as well as radiogenically derived noble gases (Ballentine and Holland, 2008). It is introduced to crustal systems in CO_2-rich gases which either permeate through the crust or are released at mid-ocean ridges and volcanoes. ^{3}He is the key noble gas isotope used for tracing mantle contributions as it depleted in both the crust and atmosphere (e.g., Allègre et al., 1987; Pepin and Porcelli, 2002; Ballentine and Holland, 2008). As a result, mantle fluids have elevated (but variable) $^{3}He/^{4}He$ ratios relative to the atmosphere (R_A). Mid-ocean ridge basalts (MORB) mantle $^{3}He/^{4}He$ are $8\pm1R_A$ (Graham, 2002), and sub-continental lithospheric mantle is $6.1\pm2.1R_A$ (Day et al., 2015), suggesting the upper mantle is well mixed. In contrast, mantle plumes display much more variable $^{3}He/^{4}He$ values which extend as high as $\sim50R_A$ (Stuart et al., 2003; Harðardóttir et al., 2018). The mantle is likewise defined by elevated $^{20}Ne/^{22}Ne$, $^{40}Ar/^{36}Ar$ and Xe isotopic ratios (most commonly in $^{129}Xe/^{130}Xe$) (Sarda et al., 1988; Marty, 1989; Staudacher et al., 1989; Burnard et al., 1997; Caffee et al., 1999; Graham, 2002; Holland and Ballentine, 2006; Ballentine and Holland, 2008; Mukhopadhyay, 2012, Williams and Mukhopadhyay, 2019). The addition of mantle derived noble gases to crustal systems can be useful for constraining the origin and accumulation of different fluids within a system, in particular CO_2 and N_2.

1.3.3.4.Crustal production

The Earth's crust acts as both a source (Section 1.3.2.2.) and reservoir for a significant proportion of the terrestrial noble gas isotopes. Despite the heterogeneous and complex nature of the Earth's crust, crustal fluids are defined by high concentrations of radiogenic isotopes. In most cases, higher concentrations of radiogenically produced noble gas isotopes reflect older systems which have been

isolated for long periods of time. Fracture fluids from mines in the Precambrian shields have been found to have concentrations which would have taken billions of years to accumulate (Holland et al., 2013; Warr et al., 2018, 2020).

1.3.3.5.Resolving components

The distinct noble gas compositions of the atmospheric, crustal and mantle reservoirs allow for the relative contribution of these three reservoirs to a particular crustal system to be determined. This is an important step in understanding the subsurface environment and how this has evolved with time. For example, in the absence of anthropogenic fluid additions to a particular system, the detection of mantle derived fluids can provide insights about the geological history and connectivity of a system (e.g., Gilfillan et al., 2009; Karolytė et al., 2019; Byrne et al., 2020).

For helium isotopes (^{3}He/^{4}He), the average radiogenic production ratio is well-known, although local heterogeneities can cause significant deviations (Ballentine and Burnard, 2002). MORB and OIB ^{3}He/^{4}He ratios are reasonably well constrained and orders of magnitude greater than radiogenic production. Any atmospheric helium contributions can be deconvolved using the ^{4}He/^{20}Ne, given their similar solubility's and assuming an atmospheric ^{20}Ne origin, using Eq. 1.4 (Hilton, et al., 1996).

$$R_c = \frac{R_s X - (R)_{air}}{X - 1} \qquad \text{(Eq. 1.4)}$$

where x= $(\frac{^4He}{^{20}Ne})_m/(\frac{^4He}{^{20}Ne})_{air}$. R is the ^{3}He/^{4}He ratio. The subscripts *c*, *s* and *air* represent the air corrected, measured and air values respectively. A ^{4}He/^{20}Ne close to air (0.319) suggest a higher degree of atmospheric helium, and crustal samples typically have values orders of magnitude higher (Ballentine et al., 1996). Atmospheric helium derived from air-saturated can be corrected for analogously using the calculated R_{asw} values for the recharge conditions (Hilton, 1996). Using the air-corrected helium isotope ratio the mantle contribution to a particular system can be determined using an endmember mixing model (Eq. 1.5):

$$R_c = f_m R_m + f_{rad} R_{rad} \quad \text{(Eq. 1.5)}$$

where *f* is the fractional contribution to the measured sample. Subscripts *m* and *rad* represent the mantle and crustal endmembers.

1.3.4. Noble gas solubility

1.3.4.1.Henry's Law

Noble gases are highly volatile and thus have a strong affinity to the gaseous phase. Where liquids are also present, some of the noble gases will dissolve in order to maintain chemical equilibria. This dissolution follows Henry's Law and has been reviewed in Ballentine et al. (2002). Assuming ideal gas behaviour in both the gas and fluid phases, Henry's Law states that the concentration of gas (*X*) in solution is directly proportional to the partial pressure (*p*) of that gas (*i*) in the gas phase (Eq. 1.6).

$$p_i = K_i X_i \quad \text{(Eq. 1.6)}$$

K is Henry's constant which are specific to the solute at a given temperature and salinity. The Henry's Constants for noble gases in water have been defined in Crovetto et al. (1982), Smith (1985) and Fernández-Prini et al. (2003). Establishing of Henry's Constants in oil is much more complex given the variable nature of the oil composition, trace element concentrations and the concentration of polar compounds. To date, there has only been one study of two oils (API gravities of 25° and 31°) and a relationship between the two is assumed for calculation at different API gravities (Kharaka and Specht, 1988). Further work into the determination of Henry's constants in oil from a molecular simulations perspective is ongoing (Galliero et al., 2019, 2020).

Non-ideal behaviour in the gas and fluid phases can be accounted for using both a gas phase fugacity coefficient (φ_i) and liquid phase activity coefficient (γ_i) as in Eq. 1.7:

$$\varphi_i p_i = \gamma_i K_i x_i \quad \text{(Eq. 1.7)}$$

Fugacity is temperature and pressure dependent and is calculated form empirically measurements (Dymond and Smith, 1980). The liquid phase activity coefficient is dependent on temperature and salinity of a system and can be described using the Setschenow equation (Eq.1 8).

$$\gamma_i = e^{CK_i(T)} \quad \text{(Eq. 1.8)}$$

where C is the concentration of salt in solution and K_i is the temperature dependent Setschenow Coefficient. Noble gas Setschenow Coefficients in a range of NaCl brines (0-5.2M) between 0-65ºC have been empirically derived (Smith and Kennedy, 1983). k_{Ar} has been found to be independent of electrolyte species, and this relationship is also assumed for the other noble gases (Ben-Naim and Egel-Thal, 1965). Additionally, it is assumed that interactions between gaseous non-electrolytes must be small with negligible effects on activity coefficients of noble gases. However, recent work in CO_2-water systems highlighted measurable deviations from predicted noble gas partitioning in high-pressure environments (Warr et al., 2015). The interactions of gaseous non-electrolytes represents a potential sources of error in the solubility coefficients. In addition, there is likely an error resulting from the extrapolating of the empirically derived solubility coefficients to much higher temperatures and pressures than they were derived for. Although these errors are unlikely to affect the general outcomes of any models, further work is required to address them.

1.3.4.2. Partitioning

There have been many studies into noble gas partitioning and solubility fractionation within equilibrated crustal fluids (e.g., Goryunov and Kozlov, 1940; Zartman et al., 1961; Bosch and Mazor, 1988; Zaikowski and Spangler, 1990; Ballentine et al., 1991, 1996; Hiyagon and Kennedy, 1992; Pinti and Marty, 1995; Torgersen and Kennedy, 1999; Battani et al., 2000) and has been reviewed in Ballentine and O'Nions (1994;) and Ballentine et al. (2002). Assuming ideal behaviour, Henry's Law can also be defined as in Eq. 1.9 (Goryunov and Kozlov, 1940; Zartman et al., 1960).

$$C_g^i = K_d^i C_l^i \quad \text{(Eq. 1.9)}$$

where C_g^i is the concentration of i in the gas phase, C_l^i is the concentration in the liquid phase and K_d^i is the dimensionless Henry's Constant. This equation then allows the partitioning of noble gases between a gas a liquid for a given total number of moles of i ($[i]_T$) and liquid-to-gas ratio (V_l/V_g) to be calculated (Eq. 1.10).

$$[i]_g = [i]_T(\frac{V_l}{V_g K_d^i} + 1)^{-1} \quad \text{(Eq. 1.10)}$$

where $[i]_g$ is the number of moles of i in the gas phase. If Henry's Constant has units (e.g., GPa, atm kg/mol), Eq.1.10 can be modified to take them into account (Ballentine, et al., 2002). For systems where there are two liquids interacting, the ratio of Henry's constants in the two liquids (e.g., 1 and 2) can be used and partition described as in Eq. 1.11.

$$[i]_{l1} = [i]_T(\frac{\rho_{l2} V_{l2} K_{m1}^i}{\rho_{l1} V_{l1} K_{m2}^i} + 1)^{-1} \quad \text{(Eq. 1.11)}$$

If concentrations within a system are not well determined, but reasonable estimates of the relative concentrations exist, it is possible to investigate the fractionation in the noble gas ratios from an initial predicted ratio (Bosch and Mazor, 1988; Ballentine et al., 1996). By convention the fractionation is usually given relative to ^{36}Ar (Ballentine et al., 2002).

It is important to note here, that models based on this partitioning are limited by the input parameters of the reservoir conditions and $[i]_T$ and errors associated with the extrapolation of the empirically derived Henry's constants.

1.3.5. Dating radiogenic growth

Determination of groundwater residence times using the decay and production of noble gas isotopes is a well-established technique (Torgersen and Clarke, 1985; Marty et al., 1993; Zhou and Ballentine, 2006; Mahara et al., 2009; International Atomic Energy Agency, 2013). Several isotope systems can be used (e.g., ^{3}He, ^{4}He, ^{39}Ar, ^{40}Ar, ^{81}Kr), albeit with multiple assumptions, to determine groundwater residence times on a range of different timescales (Figure 1.2). Within crustal fluids the accumulation of stable ^{4}He and ^{40}Ar are the most established of these techniques (Torgersen and Clarke, 1985; Marty et al., 1993; Zhou and Ballentine, 2006; Mahara et al., 2009; International Atomic Energy Agency, 2013).

The amount of a noble gas within groundwater is a function of the amount of that noble gas initially in the groundwater, the amount from in-situ production and contributions from an external flux

(e.g., Eq. 1.12). The in-situ production rates can then be compared with the theoretical production rates (based on the decay of the parent isotopes) to give a residence time.

$$[\,^4He]_{total} = [\,^4He]_{ASW} + [\,^4He]_{in-situ} + [\,^4He]_{external\ flux} \qquad \text{(Eq. 1.12)}$$

where *total* is the amount of ^{4}He measured in the groundwater, *ASW* is the ^{4}He contribution from ASW, *in-situ* is the amount of ^{4}He produced by in-situ production over the subsurface lifetime of the groundwater and *external flux* is the amount of ^{4}He in the system which has been derived from external sources. Both $[^4He]_{in\text{-}situ}$ and $[^4He]_{external\ flux}$ are functions of time. $[^4He]_{in\text{-}situ}$ for groundwater is defined as (Torgersen, 1980):

$$[\,^4He]_{in-situ} = \frac{\rho J(\,^4He)\Lambda}{\varphi} t \qquad \text{(Eq. 1.13)}$$

where ρ is the rock density (g/cm^3), φ is the porosity and t is the groundwater residence time. Λ is a parameter defining the efficiency of transfer from mineral to groundwater. This can be between 0 and 1, but is thought to be ~1 over geological time (Ballentine and Burnard, 2002). $J(^4He)$ is the in-situ production of helium (in cm^3(STP)/g) (defined in Eq. 1.1)

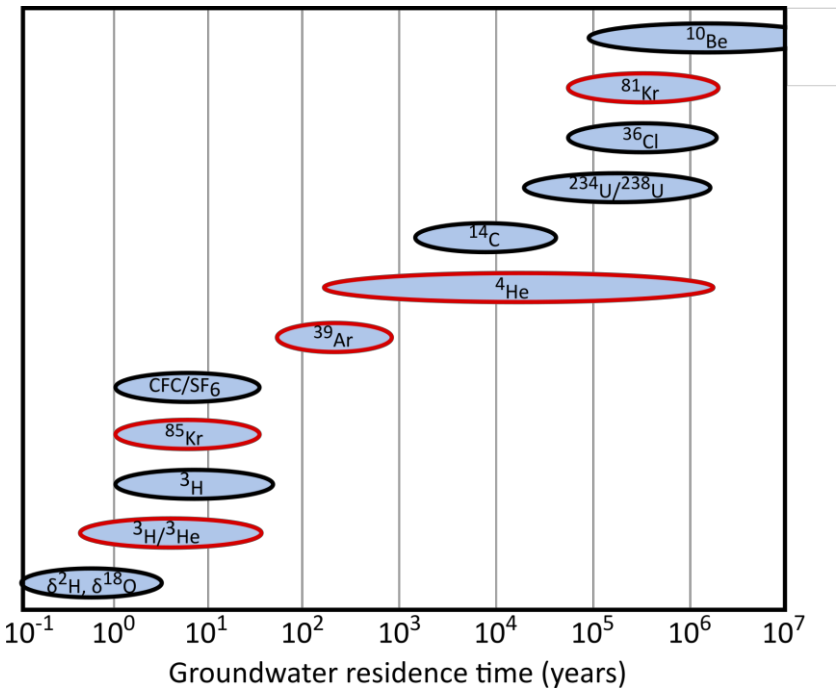


Figure 1.2: Isotope and chemical tracers used for estimating groundwater residence time, and their respectively dating limits. Noble gas residence time dating tools are circles in red.

Calculated helium water residence times commonly exceed radiocarbon and hydrological ages, with ^{4}He concentrations being orders of magnitude greater than can be explained by local production (e.g., Torgersen and Clarke, 1985; Solomon et al., 1996; Ballentine et al., 2002; Kipfer et al., 2002; Zhou and Ballentine, 2006; Cheng, 2020) and thus requiring an external flux (Torgersen, 1980; Torgersen and Clarke, 1985; Tolstikhin et al., 1996; Solomon et al., 1996; Pinti and Marty, 1998; Ballentine et al., 2002; Zhou and Ballentine, 2006; Lowenstern et al., 2014; Cheng, 2020). It is also possible for ^{4}He to have originated from the mantle, however this contribution is easily resolved using the $^{3}He/^{4}He$ ratios (Ballentine et al., 2002). An understanding of basin-scale hydrological features is critical to determine the impact of each input. Significant uncertainties exist with this method as can be difficult to obtain porosity and grain size data, U and Th concentrations including their heterogeneities and the ^{4}He release mechanisms. In addition, this model assumes a steady state of crustal degassing that can be applied to all systems, however the case studies cited above show a variation in this flux.

Groundwater residence times associated with different fluid reservoirs can be used to make inferences regarding the behaviour of groundwater within the system. Zhou and Ballentine (2006) related the ^{4}He age to the microbial degradation of coal and as a result enabled a microbial gas production rate to be calculated. Schlegel et al. (2011) found that the ^{4}He age of the groundwater was associated with different pathways of methane formation. In addition, McMahon et al (2013) used ^{4}He and ^{14}C ages associated with natural gases in the Piceance Basin, Colorado, to determine that compartmentalisation within the basin has resulted in the difference in gas compositions.

1.3.6. Noble gas transport through sedimentary basins

The distribution of noble gases within a sedimentary basin largely depends on groundwater transport and its interactions with other crustal fluids and it is primarily controlled by the hydrogeology of the basin. Subsurface fluids can be transported by either advection or diffusion. Advection is driven by a hydraulic pressure gradient or gravity and occurs through fractures, faults or permeable aquifers whilst diffusion is caused by concentrations gradients and is therefore a much slower process.

Understanding the controls on the migration of noble gases is therefore an important tool to aid in the understanding of transport, accumulation and storage of subsurface fluids within the basin. The noble gas signatures within the different formations of a sedimentary basin can be compared to assess the vertical connectivity, in a similar manner to other geochemical tracers (e.g., Connolly et al., 1990; Bachu and Underschultz, 1993; Marty et al., 1993, 2003; Bachu and Hitchon, 1996; Castro et al., 1998a, 1998b; Worden et al., 1999, Gardner et al., 2012; Clark et al., 2013; Hendry et al., 2015). Recent work has seen the development of 1D steady state diffusional models of helium to investigate vertical cross formational transport in a static water column, as well as characterising the ^{4}He flux from the basement (Cheng, 2020).

1.3.7. Noble gases in petroleum systems

1.3.7.1. *Utility of noble gases in petroleum systems*

Helium was first observed in natural gases over 100 years ago (Cady and McFarland, 1906), and the first isotopic measurements of noble gases in hydrocarbons were made 50 years later (Zartman et al., 1961). Noble gases have been successfully applied to many hydrocarbon systems and provide insights into the development of such systems. For example, by characterising or modelling the inheritance and evolution of noble gases during the migration and accumulation within conventional reservoirs (e.g., Zaikowski and Spangler, 1990; Ballentine et al., 1991, 1996; Pinti and Marty, 1995; Torgersen and Kennedy, 1999; Zhou et al., 2005; Hunt et al., 2012; Darrah et al., 2015; Barry et al., 2016, 2017, 2018a, 2018b; Byrne et al., 2018a, 2020). Recently, there have been several studies of unconventional systems where the lack of secondary migration alongside the better constrained pressure-temperature histories of the system and smaller influence of basin-scale fluid flow allow for the initial composition of hydrocarbons to be measured directly (Zhou et al., 2006; Hunt et al., 2012; Moore et al, 2018, Byrne et al., 2018a, 2020). Although, noble gas studies in unconventional hydrocarbon systems are relatively sparse, they have found: excess atmospheric Kr and Xe, which is also observed within conventional hydrocarbon systems (e.g., Torgersen and Kennedy, 1999; Zhou et al., 2005); a relationship between noble gas concentrations and thermal maturity (Byrne et al., 2018a) and; differences in radiogenic noble gas concentrations for differing thermal maturities. (Hunt et al., 2012). In addition, studies have shown the importance of

understanding the provenance of the different fluids within the system and how these have interacted within a reservoir (Wen et al., 2017; Byrne et al., 2020). Recent reviews of the utility of noble gases in both conventional and unconventional hydrocarbon systems include Ballentine et al. (2002), Prinzhofer (2013) and Byrne et al. (2018b).

1.3.7.2.Noble gas solubility models for hydrocarbon reservoirs

Within hydrocarbon systems, it is assumed that the hydrocarbon phase is initially devoid of noble gases and acquires atmospheric noble gas isotopes (^{20}Ne, ^{36}Ar, ^{84}Kr, ^{130}Xe) by interaction with ASW. In a closed system the noble gas composition in hydrocarbon reservoirs can be modelled based on partitioning under reservoir conditions (Section 1.3.4.2.). In such equilibrium models, the first bubble of gas or droplet of oil to come into contact with the groundwater (infinitesimally large water-to oil or water-to gas ratio) represents the initial charging of the hydrocarbon reservoir. As the water-hydrocarbon ratio decreases the concentration of the noble gas will decrease in the hydrocarbon phase as a result of dilution and the elemental ratio will trend toward that initially in the ASW (Figure 1.3).

In reality, many crustal systems are often more complex and exhibit open system behaviours. In these more complex scenarios, the loss of hydrocarbons/water can be accounted for on a system-by-system basis using a variety or combination of models for hydrocarbon loss and/or partitioning and Rayleigh fractionation (Zhou et al., 2005; Barry et al., 2016). In open systems, the elemental ratio remains fractionated compared to ASW (Figure 1.3).

Deviations from the expected hydrocarbon behaviour based on solubility, is indicative of added complexities and processes occurring within the system and thus, has been used to identify dynamic aquifer system and/or migration pathways, anthropogenic additions and sample contamination (Barry et al., 2016; Barry et al., 2018a; Cheng, 2020). Furthermore, the extent of groundwater interaction can have implications for quality of the hydrocarbons (Palmer, 1984; Lafargue and Barker, 1988; Leahy and Colwell, 1990; Horstad et al., 1992).

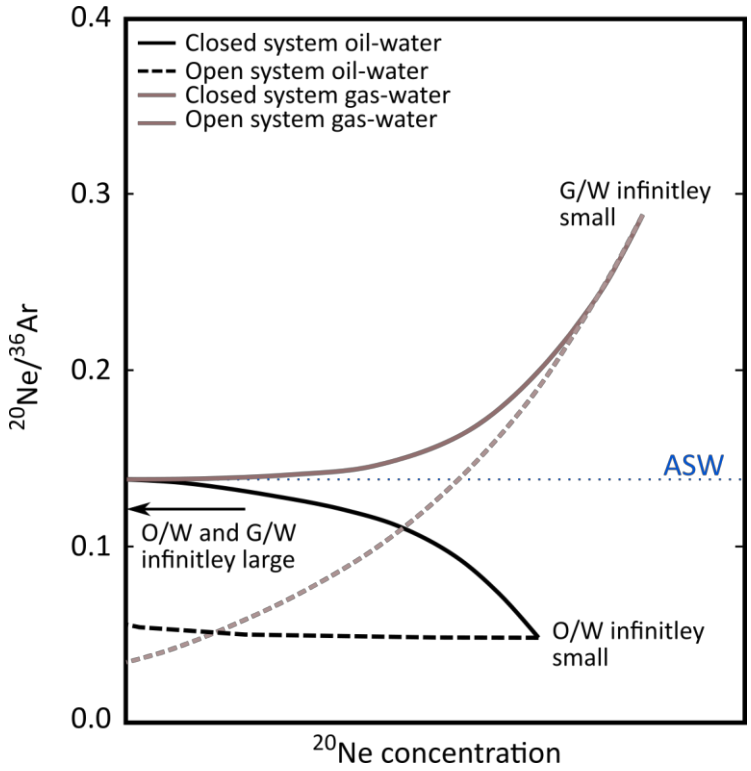


Figure 1.3: Schematic diagram showing the evolution of a pristine oil (black) and gas (brown) field with increasing oil-water or gas-water contact for both a closed (solid lines) and an open (dashed line) system in terms of its $^{20}Ne/^{36}Ar$ ratio and ^{20}Ne concentration. As a hydrocarbon migrates to the reservoir, any contact will result in the partitioning of the noble gases based on their relative solubilities under the reservoir conditions. In an oil-water system the initial oil-water contact is likely to have a low $^{20}Ne/^{36}Ar$ and evolve towards that of ASW as it comes into contact with more water. In an open system the $^{20}Ne/^{36}Ar$ ratio is likely to remain low. For gas-water systems, initial water contact will result in a very elevated $^{20}Ne/^{36}Ar$, which will decrease towards ASW in a closed system and decrease beyond this in an open system. In both oil-water and gas-water systems as more water interaction occurs the concentration of the noble gases within the hydrocarbon phase will decrease.

1.3.7.3.Hydrocarbon systems and groundwater contamination

Noble gases provide an ideal tool for investigating hydrocarbon contamination within groundwater, as they can provide unique insight into subsurface fluid (gas, liquid hydrocarbons, and water) sources and transport mechanisms. Hydrocarbon additions in groundwaters can come from a variety of both natural and anthropogenic sources, such as shallow microbial methane production, natural seepage or anthropogenic additions due to well integrity issues, surface spills or leaking storage tanks (Figure 1.4). Noble gases may therefore be particularly important in differentiating between natural and anthropogenic input of deep fluids into shallow aquifers.

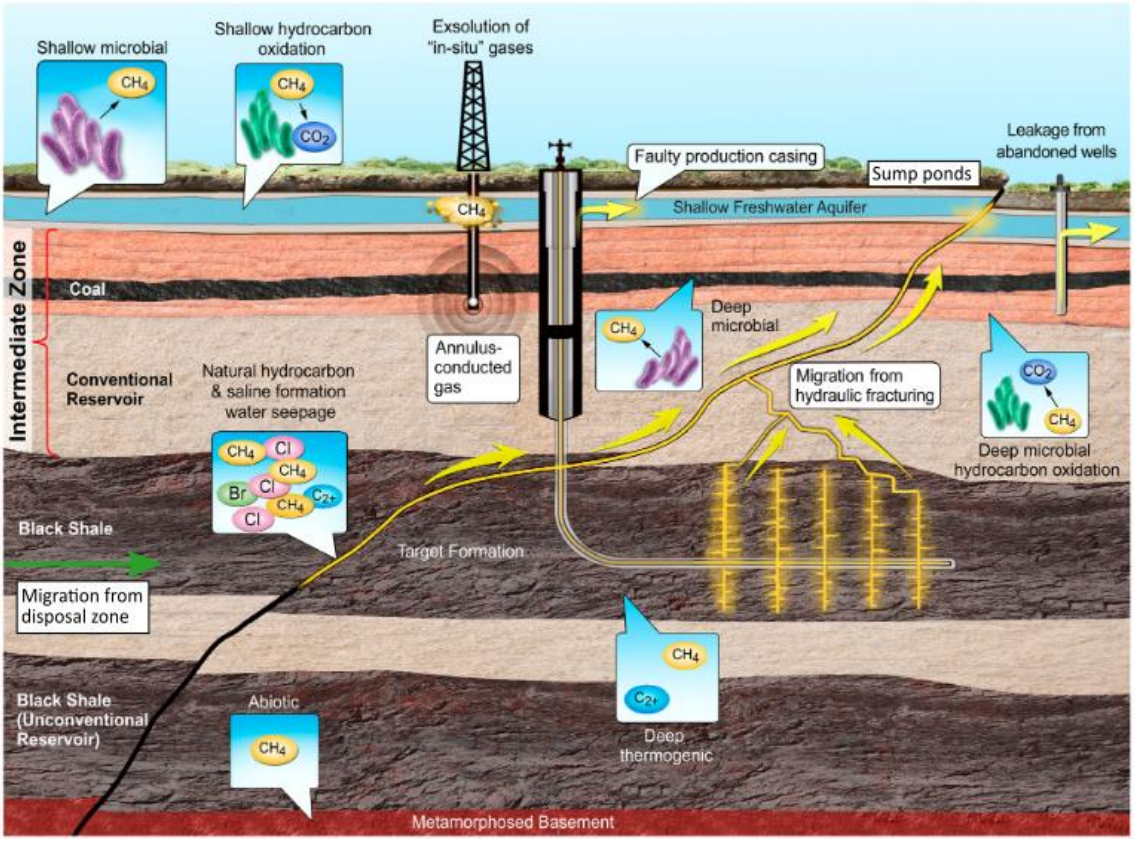


Figure 1.4: Conceptual model of the sources and pathways of hydrocarbon contributions to shallow aquifers. Adapted from McIntosh et al. (2019).

Deeper hydrocarbon fluids will have higher radiogenic and lower atmospheric noble gas abundances than ASW, this has been shown to be useful in identifying localised deep fluid contributions associated with hydraulic fracking to shallow water systems (Darrah et al., 2014, 2015; Wen et al., 2016, 2017; Harkness et al., 2017). The investigation and characterisation of both noble gases within hydrocarbon systems and overlying aquifers is critical to better understand the sources of fluids and migration pathways where hydrocarbon contributions to groundwaters are found.

1.3.8. Noble gases in carbon capture and storage analogues

Noble gases are becoming an increasing important tool to help understand the multi-phase interactions and processes operating within the CO_2 injected reservoir (Gilfillan et al., 2008, 2009; Györe et al., 2015, 2017; Flude et al., 2016; Roberts et al., 2017; Karolytė et al., 2019). Commercial scale CO_2 storage projects will be required to monitor the CO_2 at depth for seepage and leakage as well as for understanding the processes controlling the behaviour and trapping mechanisms of

carbon to ensure storage security. An early review of the application of noble gases to CO_2 storage can be found in Holland and Gilfillan (2013).

Due to their inert nature noble gases have been found to have significant potential for detecting, tracing and quantifying the migration leakage and seepage of CO_2. Their utility has been illustrated by multiple studies such as in the Mabee EOR field (Nimz and Hudson, 2005), Cranfield oil field (Györe et al., 2015, 2017) and at Green River Springs, Utah (Wilkinson et al., 2010), as well as playing a role in the legal dispute over CO_2 leakage at Weyburn, Canada (Gilfillan and Haszeldine, 2011). The addition of artificial He, Kr and Xe isotopes are also being explored as system tracers (Flude et al., 2016, Roberts et al., 2017, Flohr, et al., 2021).

In addition to characterising fluid origin, a combined noble gas and CO_2 isotope approach can provide insight into processes associated with any CO_2 loss following injection. ^3He is inert and insoluble with no significant sources within the crust. As such, variations in $CO_2/^3He$ post-injection are directly attributable to the addition or removal of CO_2 within the system (Figure 1.5; Sherwood Lollar et al., 1997; Gilfillan et al., 2009). Within the subsurface, ^4He accumulates in groundwater, which also contains ^{20}Ne, with time. These can subsequently partition into different fluids. All CO_2 reservoirs where ^4He and ^{20}Ne data are available show a decrease in $CO_2/^3He$ correlated with ^4He, and almost all see this correlation also with ^{20}Ne (Figure 1.6). This relationship is thought to be a result of CO_2 loss being proportional to the amount of formation water which has degassed, suggestive of either solubility or mineral trapping occurring within the field (Gilfillan et al., 2009).

Combining the $CO_2/^3He$ with $\delta^{13}C$ of CO_2, allows for the identification and quantification of the principal mechanism controlling CO_2 loss (solubility and mineral trapping). The fractionation in $\delta^{13}C$ of CO_2 associated with CO_2 loss can be expressed as a Rayleigh fractionation (Eq. 1.14; Clark and Fritz, 1997).

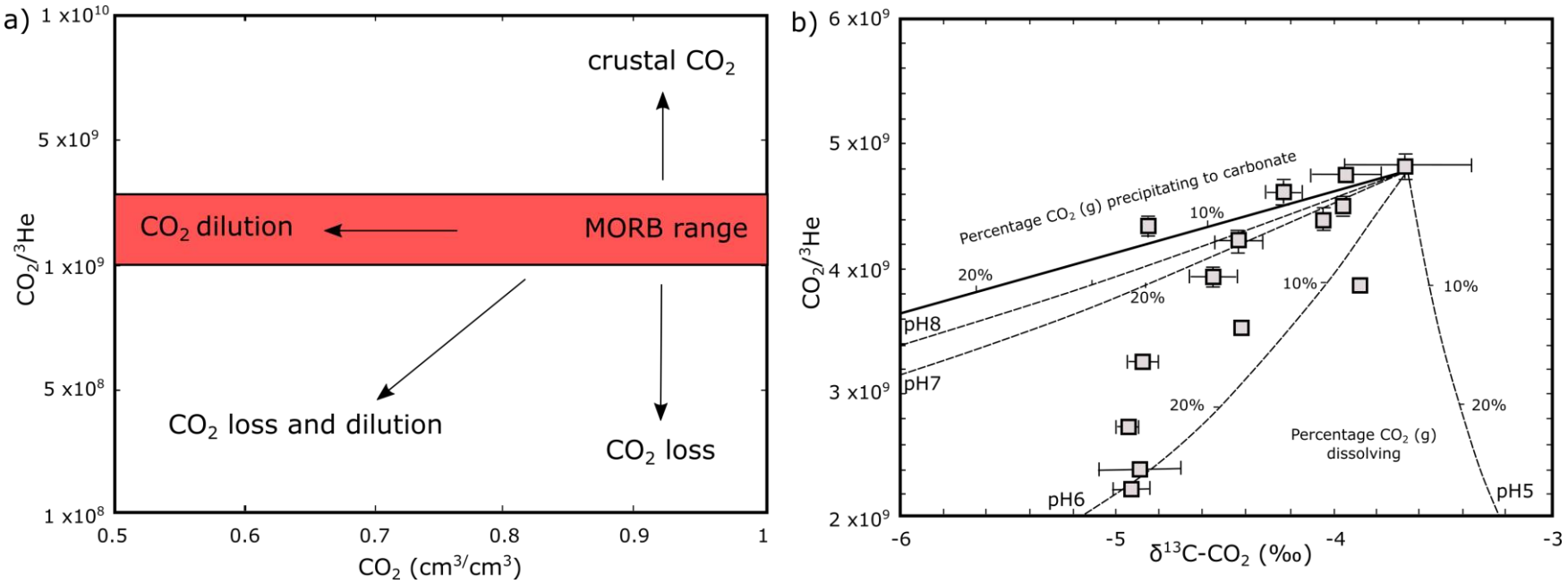


Figure 1.5: Plot for $CO_2/^3He$ ratio against a) CO_2 concentration and b) $\delta^{13}C_{CO2}$ a) MORB range (2 ± 1 x10^9) is highlighted by the red shaded area. Ratios above this range must contain crustal CO_2 (Sherwood Lollar et al., 1997; Ballentine et al., 2002). b) Plot of $\delta^{13}C_{CO2}$ against $CO_2/^3He$ for the Bravo Dome field as CO_2 gas (Gilfillan et al., 2009). Modelled lines for both dissolution under different pH (dashed lines) and precipitation in an open system by Rayleigh fractionation (solid line) are shown.

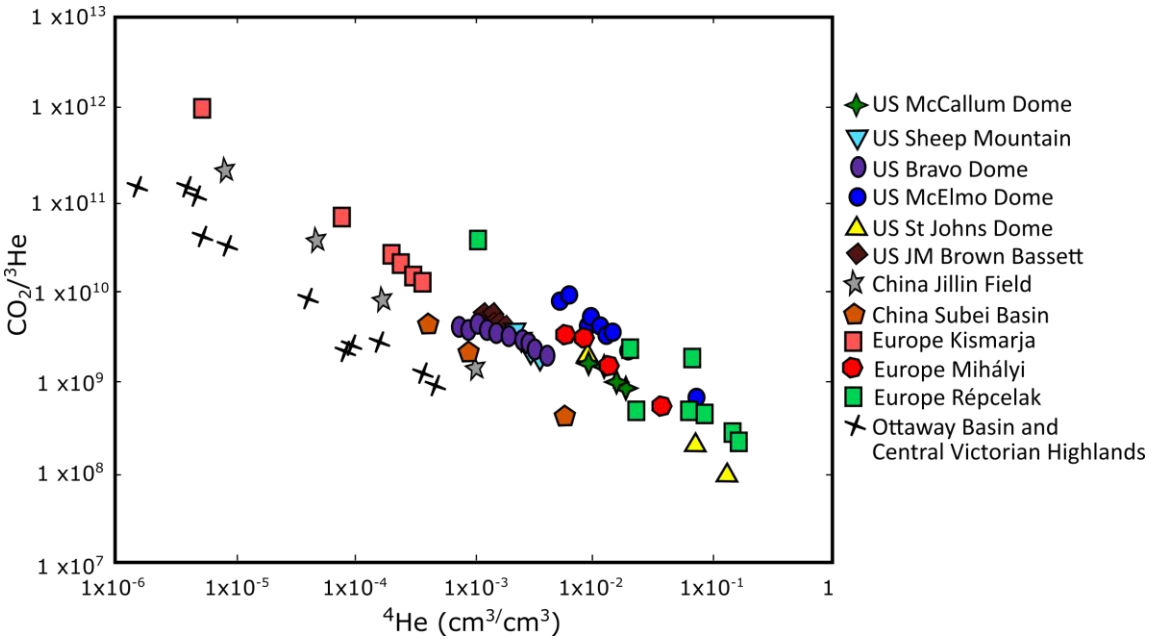


Figure 1.6: $CO_2/^3He$ vs ^4He concentrations in natural CO_2 gas field fields. Fields show a strong correlation between increasing ^4He concentration and decreasing $CO_2/^3He$, as a reuslt of interaction with formation waters. Figure is adapted from Gilfillan et al. (2009) and data sourced from: Sheng et al. (1997); Ballentine et al. (2001); Gilfillan et al. (2009); Palcsu et al. (2014); Karolytė et al. (2019).

$$\delta^{13}C_{CO2} = \delta^{13}C_{CO2i} \times \varepsilon \ln f \qquad \text{(Eq. 1.14)}$$

where f is the fraction of the original CO_2 lost and $\delta^{13}C_{CO2}$ and $\delta^{13}C_{CO2i}$ are the carbon isotopic composition of the CO_2 for post dissolution and in the initial CO_2 respectively. ε is the carbon isotope fractionation factor for either mineral or solubility trapping and can be approximated using $\varepsilon=1000ln\alpha$ where α is the fractionation factor. These fractionation factors are a function of temperature (mineral trapping) or pH (solubility trapping). This principle has been applied to multiple natural CO_2 fields to allow for the investigation of the behaviour of CO_2 over timescales that are not amenable for test CO_2 injection sites and found that solubility trapping is the dominant CO_2 trapping mechanism and over millennial timescale precipitation represents only a small mechanism for CO_2 trapping, particularly within siliclastic reservoirs (Figure 1.5; Gilfillan et al., 2009).

Subsequent studies have further shown the utility of a combined stable and noble gas isotope approach to investigate both the CO_2 behaviour within the reservoir (e.g., Gilfillan and Haszeldine, 2011; Gilfillan et al., 2014; Györe et al., 2015, 2017) and for identifying the migration of injected

CO_2 to the shallow subsurface (e.g., Wilkinson et al., 2010; Gilfillan et al., 2011, 2014, 2017; Karolytė et al., 2019).

1.3.9. Introduction to methane clumped isotopologues

Subsurface methane generally has one of three sources: thermogenic, microbial or abiotic. Thermogenic methane forms as a result of the thermal cracking of longer chain hydrocarbon molecules from either solid, liquid or gaseous hydrocarbons (e.g., Hunt, 1996; Seewald, 2003; Tissot and Welte, 2013). Microbial methane is that produced by microorganisms known as methanogens, this can occur either via hydrogenotrophic methanogenesis (conversion of CO_2 to CH_4) or via the reduction of a methyl group from larger organic molecules such as acetate (e.g., Rice and Claypool, 1981). Methane can also form 'abiotically' through the hydrogenation of CO_2, however it is not known to contribute in great quantities to the types of systems that will be explored throughout this thesis and thus will not be discussed further (Etiope and Lollar, 2013).

Establishing the origin of methane in a particular system can be important for economic, biogeochemical and environmental reasons. Typically, this has been done using molecular and stable isotopic measurements, for example using $\delta^{13}C$ and δD (Whiticar et al., 1986; Whiticar, 1999; Etiope and Lollar, 2013) or $\delta^{13}C$ and $C_1/(C_2+C_3)$ (Bernard et al., 1976), and their integration with basin models. However, these methods trace the isotopic composition of the source material which can cause complications in interpretation. Recent advancements in the measurements of the methane clumped isotopologues have allowed us to investigate the origin of methane without the added complication of provenance (e.g., Stolper et al., 2014a, 2018; Douglas et al., 2016, 2017; Young et al., 2017; Giunta et al., 2019; Ash et al., 2019; Young, 2019; Thiagarajan et al., 2020a). A simplified overview of the theory and application of methane clumped isotopologues is given below, more comprehensive reviews can be found in Douglas et al. (2017), Stolper et al. (2018) and Young (2019).

1.3.9.1. Theory and nomenclature

An 'isotopologue' is a specific isotopic version of a molecule, for example $^{12}CH_3D$ could also be $^{12}CH_2DH$, $^{12}CHDH_2$ or $^{12}CDH_3$. 'Clumping' in this context refers to having multiple heavy isotopic

substitutions to a molecule. Therefore, a clumped isotopologue refers to a specific isotope version of a molecule with multiple heavy isotopes. The clumped isotopologues of methane that are currently measured and used are $^{13}CH_2D$ and $^{12}CH_2D_2$. Clumped isotopologues are of interest because the abundance of an isotopologue is dependent on the 'bulk' composition of a system and the systems temperature (e.g., Wang et al., 2004). In a purely random 'stochastic' distribution, predicted isotopologue concentrations are constrained by the average isotopic composition of methane (i.e., $\delta^{13}C$ and δD) and are products of the fractional isotope abundances. The isotope exchange can be described by the following isotopic equilibriums for $^{13}CH_3D$ and $^{12}CH_2D_2$:

$$^{13}CH_4 + {}^{12}CH_3D \rightleftarrows {}^{13}CH_3D + {}^{12}CH_4 \quad \text{(Eq. 1.15)}$$

$$2\,{}^{12}CH_3D \rightleftarrows {}^{12}CH_2D_2 + {}^{12}CH_4 \quad \text{(Eq. 1.16)}$$

These yield rate constants of:

$$K_{eqm.^{13}CH_3D} = \frac{[^{13}CH_3D][^{12}CH_4]}{[^{13}CH_4][^{12}CH_3D]} \quad \text{(Eq. 1.17)}$$

$$K_{eqm.^{12}CH_2D_2} = \frac{[^{12}CH_2D_2][^{12}CH_4]}{[^{12}CH_3D]^2} \quad \text{(Eq. 1.18)}$$

Below 1000K, the isotopologue abundances are not random and equilibrium is a monotonic function of temperature (e.g., Wang et al., 2004; Ma et al., 2008; Cao and Liu, 2012; Stolper et al., 2014b; Liu and Liu, 2016), where equilibrated methane formed at lower temperatures will have larger proportions of $\Delta^{13}CH_3D$ and $\Delta^{12}CH_2D_2$ compared to the stochastic distribution (Stolper et al., 2014a, 2014b; Young et al., 2017; Eldridge et al., 2019). In such cases, the equilibrium constant can be related to the abundance of a clumped isotopologue if reported relative to its calculated stochastic distribution using (Wang et al., 2004; Stolper et al., 2014b):

$$K_{eqm.\ i} \cong e^{\frac{\Delta_i}{-1000}} \quad \text{(Eq. 1.19)}$$

where *i* is the clumped isotopologue of interest (either $^{13}CH_3D$ or $^{12}CH_2D_2$) and the abundance of a clumped isotopologue is reported relative to its calculated stochastic distribution using a Δ notation:

$$\Delta_i = \left(\frac{i_R}{i_{R^*}} - 1\right) 10^3 \quad \text{(Eq. 1.20)}$$

where $R = [i]/[^{12}CH_4]$ and * indicate the expected stochastic distribution. This allows for the calculation of 'apparent' methane formation temperature in K (Eq. 1.21 and 1.22; Young et al., 2017).

$$\Delta_{^{13}CH_3D} \approx 1000\left(\frac{0.0355502}{T} - \frac{433.038}{T^2} + \frac{1270210.0}{T^3} - \frac{5.94804x10^8}{T^4} + \frac{1.196630x10^{11}}{T^5} - \frac{9.07230\,x10^{12}}{T^6}\right) \quad \text{(Eq. 1.21)}$$

$$\Delta_{^{12}CH_2D_2} \approx 1000\left(\frac{0.183798}{T} - \frac{785.483}{T^2} + \frac{1056280.0}{T^3} + \frac{93730700}{T^4} - \frac{89194800000}{T^5} + \frac{9.90723\,x10^{12}}{T^6}\right) \quad \text{(Eq. 1.22)}$$

Assuming that methane has formed an internal isotopic equilibrium, the relationship between $\Delta^{13}CH_3D$ and $\Delta^{12}CH_2D_2$ under thermodynamic equilibrium can be calculated. This relationship can be visualized in Figure 1.7 and is used as a reference for sample comparisons.

1.3.9.2.Thermogenic methane

Generation of thermogenic methane is kinetically controlled by time, temperature and organic matter composition. It has been found to form at temperatures between ~60 – 300°C (Figure 1.7, e.g., Behar et al., 1992; Hunt, 1996; Tsuzuki et al., 1999; Vandenbroucke et al., 1999; Tang et al., 2000; Stolper et al., 2014a). There have been several studies of methane clumped isotopologues thermogenic gases from a variety of different hydrocarbon systems (e.g., Stolper et al., 2014a, 2015; Douglas et al., 2016, 2017; Young et al., 2017; Giunta et al., 2019; Thiagarajan et al., 2020a). The observed range in apparent clumped isotopologue temperatures recorded in thermogenic methane (72-298°C) are geologically reasonable and within range of biomarker maturity estimates. In addition, the clumped isotopologues appear to be in internal isotopic equilibrium.

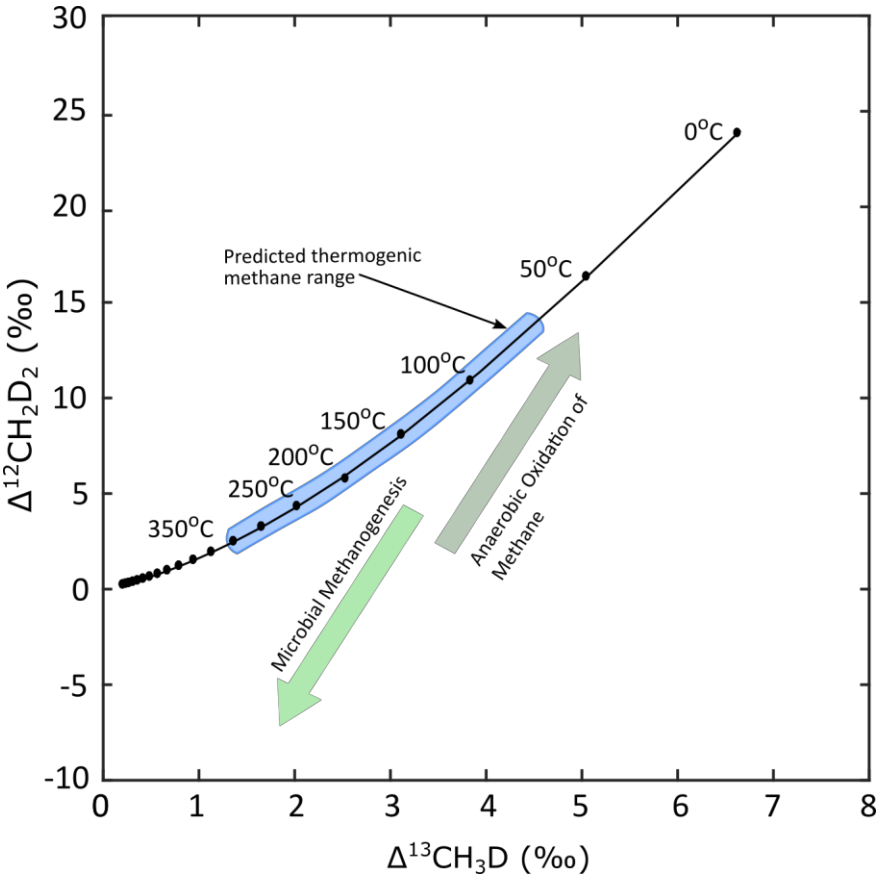


Figure 1.7: Plot of $\Delta^{13}CH_3D$ vs $\Delta^{12}CH_2D_2$, illustrating internal thermodynamic equilibrium (black line) (calculated following the methods in Young et al. (2017)). The blue shaded region represents the range in methane clumped isotopologue signature and temperatures in which thermogenic methane is expected to form. The light green arrow represent the theoretical trend for microbial methane formed via methanogenesis and the dark green arrow is the theoretical trend for anaerobic oxidation of methane (AOM)(Young, 2019; Ono et al., 2021).

The bulk isotopic composition of methane is generally thought to be a kinetically controlled process (e.g., Chung et al., 1988; Tang et al., 2000), thus, the formation of thermogenic methane in apparent isotopic equilibrium requires an originally unanticipated isotope-exchange process. Although the mechanism for equilibrium is not fully understood (Stolper et al., 2018), it is thought that C and H isotope can equilibrate with the methyl precursors whilst still expressing kinetic bulk isotope effects (Thiagarajan et al., 2020b). Recent lab experiments and theoretical models have shown thermogenic methane can form out of internal isotopic equilibrium (Shuai et al., 2018; Xia and Gao, 2019), this dis-equilibria is thought to be a result of kinetically driven processes such as the abiotic Sabatier Reaction, pyrolysis of organic material under certain conditions, quantum tunnelling or as a result of additional processes imposed on the system which could affect the overall isotopic compositions

e.g., mixing of methane with different origins (Young et al., 2017; Giunta et al., 2019; Xia and Gao, 2019; Young, 2019).

1.3.9.3.Microbial methane

The thermal limit for microbial life is thought to be 122°C (Takai et al., 2008; D'Hondt et al., 2019), however microbial methane formation tends to be limited in natural environments to below 80°C (Wilhelms et al., 2001; Röling et al., 2003; Head et al., 2014). Measurement of $\Delta^{13}CH_3D$ and $\Delta^{12}CH_2D_2$ in microbial methane are variable, with both equilibrium (e.g., Douglas et al., 2017; Thiagarajan et al., 2020b) and non-equilibrium compositions (e.g., Wang et al., 2015; Giunta et al., 2019; Young, 2019). This variation is likely a result of the kinetic effects associated with different microbial pathways and processes (Stolper et al., 2014a, 2015; Wang et al., 2015; Young et al., 2017; Gruen et al., 2018; Giunta et al., 2019; Ash et al., 2019; Young, 2019; Ono et al., 2021). As a result, apparent clumped isotope temperatures from microbial methane can obtain unrealistically high temperatures and caution must be used when using them as a geothermometer in such environments. Studies have suggested that the anaerobic oxidation of methane (AOM, conversion of CH_4 to CO_2) can drive the clumped isotopic composition back towards equilibrium (Gruen et al., 2018; Giunta et al., 2019; Ash et al., 2019). The reactions during AOM are low energy and close to the limit for sustaining life (Holler et al., 2011; Timmers et al., 2017) and thus have the potential for back reactions and reformation of methane. In addition, AOM also requires the presence of substrate in the form of an external electron acceptor such as SO_4^{2-}. Where substrate concentrations are low, the enzymatic back flux can increase to up to 78% of net AOM (Yoshinaga et al., 2014; Timmers et al., 2017). Preliminary experiments of this proposed reprocessing mechanism have shown that AOM can push the residual methane in a system towards reservoir temperature clumped isotopic equilibrium, with $\Delta^{13}CH_3D$ being more affected at lower temperatures (<60 °C) and lower sulphate concentrations than $\Delta^{12}CH_2D_2$ (Young, 2019; Ono et al., 2021).

1.3.10. Summary

The effects of anthropogenic climate change and increasing resource demand (i.e., on fresh water, energy, elemental resources) are growing societal concerns. To reduce atmospheric CO_2 levels, we

need to safely store CO_2 within the subsurface. To ensure groundwater security, we need to constrain contamination pathways to subsurface aquifers. To find accumulations of less abundant gases such as helium and hydrogen we need to understand both flow and accumulation within the crust. As a result, the understanding on multi-phase fluid interactions within the crust that govern the processes and behaviour of the fluids is critical.

Despite the routine use of bulk composition and stable isotopes to investigate subsurface fluid interaction, the preceding sections demonstrate that noble gas and clumped isotopes provide additional constraints on system processes and properties, which may not otherwise be quantified using these more traditional methods. The integration of multi-isotope gas tracers (e.g., stable, clumped and noble gas) in crustal fluid studies is therefore vital. A key step in the development of this toolkit is the continued acquisition and compilation of case studies especially with the use of the less widely used tracers. Comparison of these studies will allow for more universal patterns to be identified and thus easier future use of the multi-isotope gas tracers, making their use less descriptive and more predictive.

References

Aeschbach-Hertig W., El-Gamal H., Wieser M. and Palcsu L. (2008) Modeling excess air and degassing in groundwater by equilibrium partitioning with a gas phase: Modelling gas partitioning. *Water Resources Research* **44**.

Aeschbach-Hertig W., Peeters F., Beyerle U. and Kipfer R. (1999) Interpretation of dissolved atmospheric noble gases in natural waters. *Water Resources Research* **35**, 2779–2792.

Aeschbach-Hertig W., Peeters F., Beyerle U. and Kipfer R. (2000) Palaeotemperature reconstruction from noble gases in ground water taking into account equilibration with entrapped air. *Nature* **405**, 1040-1044

Allègre C. J., Hofmann A. and O'Nions K. (1996) The argon constraints on mantle structure. *Geophysical Research Letters* **23**, 3555–3557.

Allègre C. J., Staudacher T. and Sarda P. (1987) Rare gas systematics: formation of the atmosphere, evolution and structure of the Earth's mantle. *Earth and Planetary Science Letters* **81**, 127–150.

Anders R., Landon M. K. and McMahon P. B. (2019) Groundwater quality results from the Regional Monitoring Program study of the Orcutt Oil Field. In *California State Water Resources Control Board Stakeholder Meeting* California State Water Resources Control Board Stakeholder Meeting. Sacramento.

Ash J. L., Egger M., Treude T., Kohl I., Cragg B., Parkes R. J., Slomp C. P., Sherwood Lollar B. and Young E. D. (2019) Exchange catalysis during anaerobic methanotrophy revealed by $\Delta^{12}CH_2D_2$ and $\Delta^{13}CH_3D$ in methane. *Geochemical Perspective Letters* **10**, 26–30.

Avice G., Marty B., Burgess R., Hofmann A., Philippot P., Zahnle K. and Zakharov D. (2018) Evolution of atmospheric xenon and other noble gases inferred from Archean to Paleoproterozoic rocks. *Geochimica et Cosmochimica Acta* **232**, 82–100.

Avice G., Moreira M. and Gilmour J. D. (2020) Xenon Isotopes Identify Large-scale Nucleosynthetic Heterogeneities across the Solar System. *The Astrophysical Journal* **889**, 68.

Bach W., Naumann D. and Erzinger J. (1999) A helium, argon, and nitrogen record of the upper continental crust (KTB drill holes, Oberpfalz, Germany): implications for crustal degassing. *Chemical Geology* **160**, 81–101.

Bachu S. and Hitchon B. (1996) Regional-Scale Flow of Formation Waters in the Williston Basin. *AAPG Bulletin* **80**, 248–264.

Bachu S. and Underschultz J. R. (1993) Hydrogeology of Formation Waters, Northeastern Alberta Basin. *AAPG Bulletin* **77**, 1745–1768.

Ballentine C. J., Burgess R. and Marty B. (2002) Tracing fluid origin, transport and interaction in the crust. In: *Noble Gases in Geochemistry and Cosmochemistry.(*Eds: D. Porcelli, C.J. Ballentine,, R. Wieler) Reviews in Mineralogy and Geochemistry **47**. Geochemical Society, Mineralogical Society of America, Chapter 12, 539–614.

Ballentine C. J. and Burnard P. G. (2002) Production, Release and Transport of Noble Gases in the Continental Crust. In: *Noble Gases in Geochemistry and Cosmochemistry.(*Eds: D. Porcelli, C.J. Ballentine,, R. Wieler) Reviews in Mineralogy and Geochemistry **47**. Geochemical Society, Mineralogical Society of America, Chapter 13, **47**, 481–538.

Ballentine C. J. and Hall C. M. (1999) Determining paleotemperature and other variables by using an error-weighted, nonlinear inversion of noble gas concentrations in water. *Geochimica et Cosmochimica Acta* **63**, 2315–2336.

Ballentine C. J. and Holland G. (2008) What CO_2 well gases tell us about the origin of noble gases in the mantle and their relationship to the atmosphere. *Philosophical Transactions of the Royal Society A: Mathematical, Physical and Engineering Sciences* **366**, 4183–4203.

Ballentine C. J., Marty B., Lollar B. S. and Cassidy M. (2005) Neon isotopes constrain convection and volatile origin in the Earth's mantle. *Nature* **433**, 33–38.

Ballentine C. J. and O'Nions R. K. (1994) The use of natural He, Ne and Ar isotopes to study hydrocarbon-related fluid provenance, migration and mass balance in sedimentary basins. *Geological Society, London, Special Publications* **78**, 347–361.

Ballentine C. J., O'Nions R. K. and Coleman M. L. (1996) A Magnus opus: Helium, neon, and argon isotopes in a North Sea oilfield. *Geochimica et Cosmochimica Acta* **60**, 831–849.

Ballentine C. J., O'Nions R. K., Oxburgh E. R., Horvath F. and Deak J. (1991) Rare gas constraints on hydrocarbon accumulation, crustal degassing and groundwater flow in the Pannonian Basin. *Earth and Planetary Science Letters* **105**, 229–246.

Ballentine C. J., Schoell M., Coleman D. and Cain B. A. (2001) 300-Myr-old magmatic CO_2 in natural gas reservoirs of the west Texas Permian basin. *Nature* **409**, 327–331.

Ballentine C. J. and Sherwood Lollar B. (2002) Regional groundwater focusing of nitrogen and noble gases into the Hugoton-Panhandle giant gas field, USA. *Geochimica et Cosmochimica Acta* **66**, 2483–2497.

Barry P.H., Kulongoski J. T., Tyne R. L., Landon M. K., Gillespie J. M., Stephens M. J., Hillegonds D. J., Byrne D. J. and Ballentine C. J. (2018a) Tracing enhanced oil recovery signatures in casing gases from the Lost Hills oil field using noble gases. *Earth and Planetary Science Letters* **496**, 57–67.

Barry P. H., Lawson M., Meurer W. P., Cheng A. and Ballentine C. J. (2018b) Noble Gases in Deepwater Oils of the U.S. Gulf of Mexico. *Geochemistry, Geophysics, Geosystems* **19**, 4218–4235.

Barry P. H., Lawson M., Meurer W. P., Danabalan D., Byrne D. J., Mabry J. C. and Ballentine C. J. (2017) Determining fluid migration and isolation times in multiphase crustal domains using noble gases. *Geology* **45**, 775–778.

Barry P. H., Lawson M., Meurer W. P., Warr O., Mabry J. C., Byrne D. J. and Ballentine C. J. (2016) Noble gases solubility models of hydrocarbon charge mechanism in the Sleipner Vest gas field. *Geochimica et Cosmochimica Acta* **194**, 291–309.

Battani A., Sarda P. and Prinzhofer A. (2000) Basin scale natural gas source, migration and trapping traced by noble gases and major elements: the Pakistan Indus basin. *Earth and Planetary Science Letters* **181**, 229–249.

Baxter E. F., DePaolo D. J. and Renne P. R. (2002) Spatially correlated anomalous $^{40}Ar/^{39}Ar$ "age" variations in biotites about a lithologic contact near Simplon Pass, Switzerland: a mechanistic explanation for excess Ar. *Geochimica et Cosmochimica Acta* **66**, 1067–1083.

Behar F., Kressmann S., Rudkiewicz J. L. and Vandenbroucke M. (1992) Experimental simulation in a confined system and kinetic modelling of kerogen and oil cracking. *Organic Geochemistry* **19**, 173–189.

Bekaert D. V., Broadley M. W., Delarue F., Avice G., Robert F. and Marty B. (2018) Archean kerogen as a new tracer of atmospheric evolution: Implications for dating the widespread nature of early life. *Science Advances* **4**(2), eaar2091.

Ben-Naim A. and Egel-Thal M. (1965) Thermodynamics of Aqueous Solutions of Noble Gases. III. Effect of Electrolytes. *Journal of Physical Chemistry* **69**, 3250–3253.

Bernard B. B., Brooks J. M. and Sackett W. M. (1976) Natural gas seepage in the Gulf of Mexico. *Earth and Planetary Science Letters* **31**, 48–54.

Bosch A. and Mazor E. (1988) Natural gas association with water and oil as depicted by atmospheric noble gases: case studies from the southeastern Mediterranean Coastal Plain. *Earth and Planetary Science Letters* **87**, 338–346.

Broadley M. W., Barry P. H., Bekaert D. V., Byrne D. J., Caracausi A., Ballentine C. J. and Marty B. (2020) Identification of chondritic krypton and xenon in Yellowstone gases and the timing of terrestrial volatile accretion. *Proceedings of the National Academy of Sciences* **117**, 13997–14004.

Brooker R. A., Wartho J.-A., Carroll M. R., Kelley S. P. and Draper D. S. (1998) Preliminary UVLAMP determinations of argon partition coefficients for olivine and clinopyroxene grown from silicate melts. *Chemical Geology* **147**, 185–200.

Burnard P., Graham D. and Turner G. (1997) Vesicle-Specific Noble Gas Analyses of "Popping Rock": Implications for Primordial Noble Gases in Earth. *Science* **276**, 568–571.

Byrne D.J., Barry P. H., Lawson M. and Ballentine C. J. (2018a) Determining gas expulsion vs retention during hydrocarbon generation in the Eagle Ford Shale using noble gases. *Geochimica et Cosmochimica Acta* **241**, 240–254.

Byrne D J., Barry P. H., Lawson M. and Ballentine C. J. (2018b) Noble gases in conventional and unconventional petroleum systems. *Geological Society, London, Special Publications* **468**, 127–149.

Byrne D. J., Barry P. H., Lawson M. and Ballentine C. J. (2020) The use of noble gas isotopes to constrain subsurface fluid flow and hydrocarbon migration in the East Texas Basin. *Geochimica et Cosmochimica Acta* **268**, 186–208.

Cady H. P. and McFarland D. F. (1906) Helium in Natural Gases. *Science* **24**, 344.

Caffee M. W., Hudson G. B., Velsko C., Huss G. R., Alexander E. C. and Chivas A. R. (1999) Primordial Noble Gases from Earth's Mantle: Identification of a Primitive Volatile Component. *Science* **285**, 2115–2118.

Cao X. and Liu Y. (2012) Theoretical estimation of the equilibrium distribution of clumped isotopes in nature. *Geochimica et Cosmochimica Acta* **77**, 292–303.

Castro M. C., Goblet P., Ledoux E., Violette S. and de Marsily G. (1998a) Noble gases as natural tracers of water circulation in the Paris Basin: 2. Calibration of a groundwater flow model using noble gas isotope data. *Water Resources Research* **34**, 2467–2483.

Castro M. C., Jambon A., de Marsily G. and Schlosser P. (1998b) Noble gases as natural tracers of water circulation in the Paris Basin: 1. Measurements and discussion of their origin and mechanisms of vertical transport in the basin. *Water Resources Research* **34**, 2443–2466.

Cheng A. (2020) Noble Gas Sources, Transport and Groundwater Interaction in Sedimentary Basins. DPhil Thesis, University of Oxford.

Chung H. M., Gormly J. R. and Squires R. M. (1988) Origin of gaseous hydrocarbons in subsurface environments: Theoretical considerations of carbon isotope distribution. *Chemical Geology* **71**, 97–104.

Clark I. D., Al T., Jensen M., Kennell L., Mazurek M., Mohapatra R. and Raven K. G. (2013) Paleozoic-aged brine and authigenic helium preserved in an Ordovician shale aquiclude. *Geology* **41**, 951–954.

Clark I. D. and Fritz P. (1997) *Environmental isotopes in hydrogeology*. CRC Press/Lewis Publishers, Boca Raton, FL.

Connolly Cathy A, Walter L. M. and Baadsgaard H. (1990) Origin and evolution of formation waters, Alberta Basin, Western Canada Sedimentary Basin. II. Isotope systematics and water mixing. *Applied Geochemistry* **5**, 397–413.

Connolly C. A., Walter L. M., Baadsgaard H. and Longstaffe F. J. (1990) Origin and evolution of formation waters, Alberta Basin, Western Canada sedimentary Basin. I. Chemistry. *Applied Geochemistry* **5**, 375–395.

Craig H. and Lupton J. E. (1976) Primordial neon, helium, and hydrogen in oceanic basalts. *Earth and Planetary Science Letters* **31**, 369–385.

Crovetto R., Fernández-Prini R. and Japas M. L. (1982) Solubilities of inert gases and methane in H_2O and in D_2O in the temperature range of 300 to 600 K. *Journal Chemical Physics* **76**, 1077–1086.

Danabalan D. (2017) Helium: Exploration Methodology for a strategic resource. PhD Thesis, Durham University.

Darrah T. H., Jackson R. B., Vengosh A., Warner N. R., Whyte C. J., Walsh T. B., Kondash A. J. and Poreda R. J. (2015) The evolution of Devonian hydrocarbon gases in shallow aquifers of the northern Appalachian Basin: Insights from integrating noble gas and hydrocarbon geochemistry. *Geochimica et Cosmochimica Acta* **170**, 321–355.

Darrah T. H., Vengosh A., Jackson R. B., Warner N. R. and Poreda R. J. (2014) Noble gases identify the mechanisms of fugitive gas contamination in drinking-water wells overlying the Marcellus and Barnett Shales. *Proceedings of the National Academy of Sciences* **111**, 14076–14081.

Dauphas N. (2003) The dual origin of the terrestrial atmosphere. *Icarus* **165**, 326–339.

Day J. M. D., Barry P. H., Hilton D. R., Burgess R., Pearson D. G. and Taylor L. A. (2015) The helium flux from the continents and ubiquity of low-$^3He/^4He$ recycled crust and lithosphere. *Geochimica et Cosmochimica Acta* **153**, 116–133.

D'Hondt S., Pockalny R., Fulfer V. M. and Spivack A. J. (2019) Subseafloor life and its biogeochemical impacts. *Nature Communications* **10**, 3519.

Douglas P. M. J., Stolper D. A., Eiler J. M., Sessions A. L., Lawson M., Shuai Y., Bishop A., Podlaha O. G., Ferreira A. A., Santos Neto E. V., Niemann M., Steen A. S., Huang L., Chimiak L., Valentine D. L., Fiebig J., Luhmann A. J., Seyfried W. E., Etiope G., Schoell M., Inskeep W. P., Moran J. J. and Kitchen N. (2017) Methane clumped isotopes: Progress and potential for a new isotopic tracer. *Organic Geochemistry* **113**, 262–282.

Douglas P. M. J., Stolper D. A., Smith D. A., Walter Anthony K. M., Paull C. K., Dallimore S., Wik M., Crill P. M., Winterdahl M., Eiler J. M. and Sessions A. L. (2016) Diverse origins of Arctic and Subarctic methane point source emissions identified with multiply-substituted isotopologues. *Geochimica et Cosmochimica Acta* **188**, 163–188.

Dymond J. D. and Smith E. P. (1980) *The virial coefficients of pure gases and mixtures*. In: Physical Chemsitry. (Eds: Fenkel, M., Marsh, K.N.) Springer-Verlag Berlin-Heidelberg

Eldridge D. L., Korol R., Lloyd M. K., Turner A. C., Webb M. A., Miller T. F. and Stolper D. A. (2019) Comparison of Experimental vs Theoretical Abundances of $\Delta^{13}CH_3D$ and $\Delta^{12}CH_2D_2$ for Isotopically Equilibrated Systems from 1 to 500 °C. *ACS Earth Space Chemistry* **3**, 2747–2764.

Etiope G. and Lollar B. S. (2013) Abiotic Methane on Earth. *Reviews of Geophysics* **51**, 276–299.

Farley K. A. (2002) (U-Th)/He Dating: Techniques, Calibrations, and Applications In: *Noble Gases in Geochemistry and Cosmochemistry*.(Eds: D. Porcelli, C.J. Ballentine,, R. Wieler) Reviews in Mineralogy and Geochemistry **47**. Geochemical Society, Mineralogical Society of America, Chapter 18, pp. 819–844.

Fernández-Prini R., Alvarez J. L. and Harvey A. H. (2003) Henry's Constants and Vapor–Liquid Distribution Constants for Gaseous Solutes in H_2O and D_2O at High Temperatures. *Journal of Physical and Chemical Reference Data* **32**, 903–916.

Flohr, A., Matter, J.M., James, R.H., Saw, K., Brown, R., Ballentine, C.J., Day, C., Connelly, D., Flude, S., Gros, J., Hillegonds, D.J., Lichtschlag A., Pearce, C.R., Peel, K., Strong, J., Tyne, R.L. (2021). Utility of natural and artificial geochemical tracers for leakage monitoring and quantification during an offshore controlled CO_2 release experiment. *International Journal of Greenhouse Gas Control.* **In review**.

Flude S., Johnson G., Gilfillan S. M. V. and Haszeldine R. S. (2016) Inherent Tracers for Carbon Capture and Storage in Sedimentary Formations: Composition and Applications. *Environmental Science and Technology* **50**, 7939–7955.

Galliero G., Hoang H. and Pujol M. (2020) Noble Gas Fractionation: Some Insights from Molecular Simulations. In *Goldschmidt Abstracts* Goldschmidt2020. Online.

Galliero G., Hoang H., Vermorel R. and Pujol M. (2019) Noble Gas fractionation: Some insights from Molecular Simulations. In *Goldschmidt Abstracts* Goldschmidt. Barcelona.

Gardner W. P., Harrington G. A. and Smerdon B. D. (2012) Using excess ^4He to quantify variability in aquitard leakage. *Journal of Hydrology* **468–469**, 63–75.

Gilfillan S., Haszedline S., Stuart F., Gyore D., Kilgallon R. and Wilkinson M. (2014) The application of noble gases and carbon stable isotopes in tracing the fate, migration and storage of CO_2. *Energy Procedia* **63**, 4123–4133.

Gilfillan S. M. V., Ballentine C. J., Holland G., Blagburn D., Lollar B. S., Stevens S., Schoell M. and Cassidy M. (2008) The noble gas geochemistry of natural CO_2 gas reservoirs from the Colorado Plateau and Rocky Mountain provinces, USA. *Geochimica et Cosmochimica Acta* **72**, 1174–1198.

Gilfillan S. M. V. and Haszeldine R. S. (2011) *Report of noble gad, carbon stable isotopes and HCO_3^- measurements from the Kerr quarter and surrounding area, Goodwater, Saskatchewan.*, IPAC-CO_2, research incorporated. Regina.

Gilfillan S. M. V., Lollar B. S., Holland G., Blagburn D., Stevens S., Schoell M., Cassidy M., Ding Z., Zhou Z., Lacrampe-Couloume G. and Ballentine C. J. (2009) Solubility trapping in formation water as dominant CO_2 sink in natural gas fields. *Nature* **458**, 614–618.

Gilfillan S. M. V., Sherk G. W., Poreda R. J. and Haszeldine R. S. (2017) Using noble gas fingerprints at the Kerr Farm to assess CO_2 leakage allegations linked to the Weyburn-Midale CO_2 monitoring and storage project. *International Journal of Greenhouse Gas Control* **63**, 215–225.

Gilfillan S. M. V., Wilkinson M., Haszeldine R. S., Shipton Z. K., Nelson S. T. and Poreda R. J. (2011) He and Ne as tracers of natural CO_2 migration up a fault from a deep reservoir. *International Journal of Greenhouse Gas Control* **5**, 1507–1516.

Giunta T., Young E. D., Warr O., Kohl I., Ash J. L., Martini A., Mundle S. O. C., Rumble D., Pérez-Rodríguez I., Wasley M., LaRowe D. E., Gilbert A. and Sherwood Lollar B. (2019) Methane sources and sinks in continental sedimentary systems: New insights from paired clumped isotopologues $\Delta^{13}CH_3D$ and $\Delta^{12}CH_2D_2$. *Geochimica et Cosmochimica Acta* **245**, 327–351.

Goryunov M. S. and Kozlov A. L. (1940) *A Study of the geochemistry of helium-bearing gases and the conditions for accumulation of helium in the Earth's crust.* Leningrad-Moscow.

Graham D. W. (2002) Noble Gas Isotope Geochemistry of Mid-Ocean Ridge and Ocean Island Basalts: Characterization of Mantle Source Reservoirs In: *Noble Gases in Geochemistry and Cosmochemistry.(*Eds: D. Porcelli, C.J. Ballentine,, R. Wieler) Reviews in Mineralogy and Geochemistry **47**. Geochemical Society, Mineralogical Society of America, Chapter 8, 247–317.

Gruen D. S., Wang D. T., Könneke M., Topçuoğlu B. D., Stewart L. C., Goldhammer T., Holden J. F., Hinrichs K-U. and Ono S. (2018) Experimental investigation on the controls of clumped

isotopologue and hydrogen isotope ratios in microbial methane. *Geochimica et Cosmochimica Acta* **237**, 339–356.

Györe D., Gilfillan S. M. V. and Stuart F. M. (2017) Tracking the interaction between injected CO_2 and reservoir fluids using noble gas isotopes in an analogue of large-scale carbon capture and storage. *Applied Geochemistry* **78**, 116–128.

Györe D., Stuart F. M., Gilfillan S. M. V. and Waldron S. (2015) Tracing injected CO_2 in the Cranfield enhanced oil recovery field (MS, USA) using He, Ne and Ar isotopes. *International Journal of Greenhouse Gas Control* **42**, 554–561.

Halliday A. N. (2013) The origins of volatiles in the terrestrial planets. *Geochimica et Cosmochimica Acta* **105**, 146–171.

Harðardóttir S., Halldórsson S. A. and Hilton D. R. (2018) Spatial distribution of helium isotopes in Icelandic geothermal fluids and volcanic materials with implications for location, upwelling and evolution of the Icelandic mantle plume. *Chemical Geology* **480**, 12–27.

Harkness J. S., Darrah T. H., Warner N. R., Whyte C. J., Moore M. T., Millot R., Kloppmann W., Jackson R. B. and Vengosh A. (2017) The geochemistry of naturally occurring methane and saline groundwater in an area of unconventional shale gas development. *Geochimica et Cosmochimica Acta* **208**, 302–334.

Head I. M., Gray N. D. and Larter S. R. (2014) Life in the slow lane; biogeochemistry of biodegraded petroleum containing reservoirs and implications for energy recovery and carbon management. *Frontiers in Microbiology* **5**.

Heaton T. H. E. and Vogel J. C. (1981) "Excess air" in groundwater. *Journal of Hydrology* **50**, 201–216.

Heier K. S. (1965) Radioactive Elements in the Continental Crust. *Nature* **208**, 479–480.

Hendry M. J., Solomon D. K., Person M., Wassenaar L. I., Gardner W. P., Clark I. D., Mayer K. U., Kunimaru T., Nakata K. and Hasegawa T. (2015) Can argillaceous formations isolate nuclear waste? Insights from isotopic, noble gas, and geochemical profiles. *Geofluids* **15**, 381–386.

Herzberg O. and Mazor E. (1979) Hydrological applications of noble gases and temperature measurements in underground water systems: Examples from Israel. *Journal of Hydrology* **41**, 217–231.

Hilton D.R. (1996) The helium and carbon isotope systematics of a continental geothermal system: results from monitoring studies at Long Valley caldera (California, USA). *Chemical Geology* **127**(4), 269-295.

Hiyagon H. and Kennedy B. M. (1992) Noble gases in CH_4-rich gas fields, Alberta, Canada. *Geochimica et Cosmochimica Acta* **56**, 1569–1589.

Holland G. and Ballentine C. J. (2006) Seawater subduction controls the heavy noble gas composition of the mantle. *Nature* **441**, 186–191.

Holland G., Cassidy M. and Ballentine C. J. (2009) Meteorite Kr in Earth's Mantle Suggests a Late Accretionary Source for the Atmosphere. *Science* **326**, 1522–1525.

Holland, G., Gilfillan, S.M.V. (2013). Application of noble gases to the viability of CO_2 storage. In: *The Noble Gases as Geochemical Tracers*. (Ed. P. Burnard). Advances in Isotope Geochemistry. Springer, Berlin, Heidelberg. pp 177-223.

Holland G., Lollar B. S., Li L., Lacrampe-Couloume G., Slater G. F. and Ballentine C. J. (2013) Deep fracture fluids isolated in the crust since the Precambrian era. *Nature* **497**, 357–360.

Holler T., Wegener G., Niemann H., Deusner C., Ferdelman T. G., Boetius A., Brunner B. and Widdel F. (2011) Carbon and sulfur back flux during anaerobic microbial oxidation of methane and coupled sulfate reduction. *Proceedings of the National Academy of Sciences* **108**, E1484–E1490.

Honda M., Kurita K., Hamano Y. and Ozima M. (1982) Experimental studies of He and Ar degassing during rock fracturing. *Earth and Planetary Science Letters* **59**, 429–436.

Horstad I., Larter S. R. and Mills N. (1992) A quantitative model of biological petroleum degradation within the Brent Group reservoir in the Gullfaks Field, Norwegian North Sea. *Organic Geochemistry* **19**, 107–117.

Hughes W. B., Holba A. G. and Dzou L. I. P. (1995) The ratios of dibenzothiophene to phenanthrene and pristane to phytane as indicators of depositional environment and lithology of petroleum source rocks. *Geochimica et Cosmochimica Acta* **59**, 3581–3598.

Hunt A. G., Darrah T. H. and Poreda R. J. (2012) Determining the source and genetic fingerprint of natural gases using noble gas geochemistry: A northern Appalachian Basin case study. *AAPG Bulletin* **96**, 1785–1811.

Hunt J. M. (1996) *Petroleum Geochemistry and Geology*. 1st Edition. W.H. Freeman.

International Atomic Energy Agency (2013) *Isotope methods for dating old groundwater*. International Atomic Energy Agency, Vienna.

IPCC (2005) *Carbon dioxide capture and storage*. Technical Report. (Eds: Metz, B., Davidson, O., de Coninck, H., Loos, M., and Meyer, L.) Cambridge University Press, Cambridge, UK.

IPCC (2018) *Global Warming of 1.5ºC.* Special Report on the impacts of global warming of 1.5°C above pre-industrial levels and related global greenhouse gas emission pathways, in the context of strengthening the global response to the threat of climate change, sustainable development, and efforts to eradicate poverty. (Eds: Masson-Delmotte, V., Zhai, P., Pörtner, H-O., Roberts, D., Skea, J., Shukla, P.R.) Cambridge University Press, Cambridge, UK.

Karolytė R., Johnson G., Györe D., Serno S., Flude S., Stuart F. M., Chivas A. R., Boyce A. and Gilfillan S. M. V. (2019) Tracing the migration of mantle CO_2 in gas fields and mineral water springs in south-east Australia using noble gas and stable isotopes. *Geochimica et Cosmochimica Acta* **259**, 109–128.

Kelley S. (2002) K-Ar and Ar-Ar Dating. In: *Noble Gases in Geochemistry and Cosmochemistry.(*Eds: D. Porcelli, C.J. Ballentine,, R. Wieler) Reviews in Mineralogy and Geochemistry **47**. Geochemical Society, Mineralogical Society of America, Chapter 17, 785–818.

Kennedy B. M., Hiyagon H. and Reynolds J. H. (1990) Crustal neon: a striking uniformity. *Earth and Planetary Science Letters* **98**, 277–286.

Kipfer R., Aeschbach-Hertig W., Peeters F. and Stute M. (2002) Noble gases in Lakes and Groundwaters. In: *Noble Gases in Geochemistry and Cosmochemistry.(*Eds: D. Porcelli, C.J. Ballentine,, R. Wieler) Reviews in Mineralogy and Geochemistry **47**. Geochemical Society, Mineralogical Society of America, Chapter 14, 615–700.

Kulongoski J. T., McMahon P. B., Land M., Wright M. T., Johnson T. A. and Landon M. K. (2018) Origin of Methane and Sources of High Concentrations in Los Angeles Groundwater. *Journal of Geophysical Research: Biogeosciences* **123**.

Lafargue E. and Barker C. (1988) Effect of Water Washing on Crude Oil Compositions. *AAPG Bulletin* **72**, 263–276.

Leahy J. G. and Colwell R. R. (1990) Microbial Degradation of Hydrocarbons in the Environment. M*icrobiology. Reviews.* **54**, 11.

Lee J.-Y., Marti K., Severinghaus J. P., Kawamura K., Yoo H.-S., Lee J. B. and Kim J. S. (2006) A redetermination of the isotopic abundances of atmospheric Ar. *Geochimica et Cosmochimica Acta* **70**, 4507–4512.

Lee K. K. M. and Steinle-Neumann G. (2006) High-pressure alloying of iron and xenon: "Missing" Xe in the Earth's core? *Journal of Geophysical Research: Solid Earth* **111**.

Liu Q. and Liu Y. (2016) Clumped-isotope signatures at equilibrium of CH_4, NH_3, H_2O, H_2S and SO_2. *Geochimica et Cosmochimica Acta* **175**, 252–270.

Lowenstern J. B., Evans W. C., Bergfeld D. and Hunt A. G. (2014) Prodigious degassing of a billion years of accumulated radiogenic helium at Yellowstone. *Nature* **506**, 355–358.

Lupton J. E. and Craig H. (1975) Excess ^{3}He in oceanic basalts: Evidence for terrestrial primordial helium. *Earth and Planetary Science Letters* **26**, 133–139.

Ma Q., Wu S. and Tang Y. (2008) Formation and abundance of doubly-substituted methane isotopologues ($\Delta^{13}CH_3D$) in natural gas systems. *Geochimica et Cosmochimica Acta* **72**, 5446–5456.

Mahara Y., Habermehl M. A., Hasegawa T., Nakata K., Ransley T. R., Hatano T., Mizuochi Y., Kobayashi H., Ninomiya A., Senior B. R., Yasuda H. and Ohta T. (2009) Groundwater dating by estimation of groundwater flow velocity and dissolved 4He accumulation rate calibrated by ^{36}Cl in the Great Artesian Basin, Australia. *Earth and Planetary Science Letters* **287**, 43–56.

Marrocchi Y., Marty B., Reinhardt P. and Robert F. (2011) Adsorption of xenon ions onto defects in organic surfaces: Implications for the origin and the nature of organics in primitive meteorites. *Geochimica et Cosmochimica Acta* **75**, 6255–6266.

Marrocchi Y., Razafitianamaharavo A., Michot L. J. and Marty B. (2005) Low-pressure adsorption of Ar, Kr, and Xe on carbonaceous materials (kerogen and carbon blacks), ferrihydrite, and montmorillonite: Implications for the trapping of noble gases onto meteoritic matter. *Geochimica et Cosmochimica Acta* **69**, 2419–2430.

Martel D. J., O'Nions R. K., Hilton D. R. and Oxburgh E. R. (1990) The role of element distribution in production and relaease of radiogenic helium: the Carnmenellis Garnie, southwest England. *Chemical Geology* **88**, 207–221.

Marty B. (1989) Neon and xenon isotopes in MORB: implications for the earth-atmosphere evolution. *Earth and Planetary Science Letters* **94**, 45–56.

Marty B. (2012) The origins and concentrations of water, carbon, nitrogen and noble gases on Earth. *Earth and Planetary Science Letters* **313–314**, 56–66.

Marty B., Dewonck S. and France-Lanord C. (2003) Geochemical evidence for efficient aquifer isolation over geological timeframes. *Nature* **425**, 55–58.

Marty B., Torgersen T., Meynier V., O'Nions R. K. and Marsily G. de (1993) Helium isotope fluxes and groundwater ages in the Dogger Aquifer, Paris Basin. *Water Resources Research* **29**, 1025–1035.

McIntosh J. C., Hendry M. J., Ballentine C. J., Haszeldine R. S., Mayer B., Etiope G., Elsner M., Darrah T. H., Prinzhofer A., Osborn S. G., Stalker L., Kuloyo O., Lu Z.-T., Martini A. M. and Sherwood Lollar B. (2019) A Critical Review of State-of-the-Art and Emerging Approaches to Identify Fracking-Derived Gases and Associated Contaminant in Aquifers. *Environmental Science & Technology* **53**, 1063–1077.

Merrihue C. and Turner G. (1966) Potassium-argon dating by activation with fast neutrons. *Journal of Geophysical Research (1896-1977)* **71**, 2852–2857.

Moore, M.T., Vinson, D.S., Whyte, C.J., Eymold, W.K., Walsh, T.B., Darrah, T.H. (2018). Differentiating between biogenic and thermogenic sources of natural gas in coalbed methane reservoirs from the Illinois Basin using noble gas and hydrocarbon geochemistry. *Geological Society, London, Special Publications* **468**, 151–188.

Moreira M., Kunz J. and Allègre C. (1998) Rare Gas Systematics in Popping Rock: Isotopic and Elemental Compositions in the Upper Mantle. *Science* **279**, 1178–1181.

Mukhopadhyay S. (2012) Early differentiation and volatile accretion recorded in deep-mantle neon and xenon. *Nature* **486**, 101–104.

Niedermann S. (2002) Cosmic-Ray-Produced Noble Gases in Terrestrial Rocks: Dating Tools for Surface Processes. In: *Noble Gases in Geochemistry and Cosmochemistry.(*Eds: D. Porcelli, C.J. Ballentine,, R. Wieler) Reviews in Mineralogy and Geochemistry **47**. Geochemical Society, Mineralogical Society of America, Chapter 16, 731–784.

Nimz G. and Hudson G. B. (2005) The Use of Noble Gas Isotopes for Monitoring Leakage of Geologically Stored CO_2. In: *Carbon Dioxide Capture for Storage in deep geologic formations* (Eds: Benson, S. and Thomas D.C) Elsevier, Amsterdam. Chapter 24 pp. 1113–1128.

Ono S., Rhim J. H., Gruen D. S., Taubner H., Kölling M. and Wegener G. (2021) Clumped isotopologue fractionation by microbial cultures performing the anaerobic oxidation of methane. *Geochimica et Cosmochimica Acta* **293**, 70–85.

Osborn S. G., Vengosh A., Warner N. R. and Jackson, Robert B. (2011) Methane contamination of drinking water accompanying gas-well drilling and hydraulic fracturing. *Proceedings of the National Academy of Sciences* **108**, 8172–8176.

Owen T., Bar-Nun A. and Kleinfeld I. (1992) Possible cometary origin of heavy noble gases in the atmospheres of Venus, Earth and Mars. *Nature* **358**, 43–46.

Palcsu L., Vető I., Futó I., Vodila G., Papp L. and Major Z. (2014) In-reservoir mixing of mantle-derived CO_2 and metasedimentary CH_4–N_2 fluids – Noble gas and stable isotope study of two multistacked fields (Pannonian Basin System, W-Hungary). *Marine and Petroleum Geology* **54**, 216–227.

Palmer S. E. (1984) Effect of Water Washing on C_{15}^+ Hydrocarbon Fraction of Crude Oils from Northwest Palawan, Philippines. *AAPG Bulletin* **68**, 137–149.

Pepin R. O. (2006) Atmospheres on the terrestrial planets: Clues to origin and evolution. *Earth and Planetary Science Letters* **252**, 1–14.

Pepin R. O. (2000) On the Isotopic Composition of Primordial Xenon in Terrestrial Planet Atmospheres. In *From Dust to Terrestrial Planets* (Eds. W. Benz, R. Kallenbach, and G. W. Lugmair). Space Sciences Series of ISSI. Springer Netherlands. pp. 371–395.

Pepin R. O. and Porcelli D. (2002) Origin of Noble Gases in the Terrestrial Planets. In: *Noble Gases in Geochemistry and Cosmochemistry.(*Eds: D. Porcelli, C.J. Ballentine,, R. Wieler) Reviews in Mineralogy and Geochemistry **47**. Geochemical Society, Mineralogical Society of America, Chapter 7, 191–245.

Pepin R. O. and Porcelli D. (2006) Xenon isotope systematics, giant impacts, and mantle degassing on the early Earth. *Earth and Planetary Science Letters* **250**, 470–485.

Pinti D. L. and Marty B. (1995) Noble gases in crude oils from the Paris Basin, France: Implications for the origin of fluids and constraints on oil-water-gas interactions. *Geochimica et Cosmochimica Acta* **59**, 3389–3404.

Pinti D. L. and Marty B. (1998) The origin of helium in deep sedimentary aquifers and the problem of dating very old groundwaters. *Geological Society, London, Special Publications* **144**, 53–68.

Podosek F. A., Woolum D. S., Cassen P. and Nichols R. H. (2000) Solar Gases in the Earth by Solar Wind Irradiation? Goldschmidt Abstract. September 3rd-8th. Oxford, UK. Journal of Conference Abstracts **5**(2), 804.

Porcelli D., Ballentine C. J. and Wieler R. (2002) An Overview of Noble Gas Geochemistry and Cosmochemistry In: *Noble Gases in Geochemistry and Cosmochemistry.(*Eds: D. Porcelli, C.J. Ballentine,, R. Wieler) Reviews in Mineralogy and Geochemistry **47**. Geochemical Society, Mineralogical Society of America, Chapter 1, 1- 19.

Prinzhofer A. (2013) Noble Gases in Oil and Gas Accumulations. In: *The Noble Gases as Geochemical Tracers*. (Ed. P. Burnard). Advances in Isotope Geochemistry. Springer, Berlin, Heidelberg. 225–247.

Pujol M., Marty B. and Burgess R. (2011) Chondritic-like xenon trapped in Archean rocks: A possible signature of the ancient atmosphere. *Earth and Planetary Science Letters* **308**, 298–306.

Purtschert R., Yokochi R. and Sturchio N. C. (2013) Krypton-81 dating of old groundwater. In *Isotope methods for dating old groundwater*. International Atomic Energy Agency, Vienna. Chapter 5 pp. 91–124.

Rice D. D. and Claypool G. E. (1981) Generation, Accumulation, and Resource Potential of Biogenic Gas. *AAPG Bulletin* **65**, 5–25.

Roberts J. J., Gilfillan S. M. V., Stalker L. and Naylor M. (2017) Geochemical tracers for monitoring offshore CO_2 stores. *International Journal of Greenhouse Gas Control* **65**, 218–234.

Röling W. F. M., Head I. M. and Larter S. R. (2003) The microbiology of hydrocarbon degradation in subsurface petroleum reservoirs: perspectives and prospects. *Research in Microbiology* **154**, 321–328.

Rudnick R. L. and Fountain D. M. (1995) Nature and composition of the continental crust: A lower crustal perspective. *Reviews of Geophysics* **33**, 267–309.

Sanloup C., Schmidt B. C., Perez E. M. C., Jambon A., Gregoryanz E. and Mezouar M. (2005) Retention of Xenon in Quartz and Earth's Missing Xenon. *Science* **310**, 1174–1177.

Sarda P., Staudacher T. and Allègre C. J. (1988) Neon isotopes in submarine basalts. *Earth and Planetary Science Letters* **91**, 73–88.

Schlegel M. E., Zhou Z., McIntosh J. C., Ballentine C. J. and Person M. A. (2011) Constraining the timing of microbial methane generation in an organic-rich shale using noble gases, Illinois Basin, USA. *Chemical Geology* **287**, 27–40.

Schoell M. (1983) Genetic Characterization of Natural Gases. *AAPG Bulletin* **67**, 2225–2238.

Seewald J. S. (2003) Organic–inorganic interactions in petroleum-producing sedimentary basins. *Nature* **426**, 327–333.

Seltzer A. M., Ng J., Danskin W. R., Kulongoski J. T., Gannon R. S., Stute M. and Severinghaus J. P. (2019) Deglacial water-table decline in Southern California recorded by noble gas isotopes. *Nature Communications* **10**, 5739.

Sheng X., Nakai S., Wakita H., Yongchang X. and Wang X. (1997) Carbon isotopes of hydrocarbons and carbon dioxide in natural gases in China. *Journal of Asian Earth Sciences* **15**, 89–101.

Sherwood Lollar B., Ballentine C. J. and Onions R. K. (1997) The fate of mantle-derived carbon in a continental sedimentary basin: Integration of C-He relationships and stable isotope signatures. *Geochimica et Cosmochimica Acta* **61**, 2295–2307.

Sherwood Lollar B., O'Nions R. K. and Ballentine C. J. (1994) Helium and neon isotope systematics in carbon dioxide-rich and hydrocarbon-rich gas reservoirs. *Geochimica et Cosmochimica Acta* **58**, 5279–5290.

Shuai Y., Douglas P. M. J., Zhang S., Stolper D. A., Ellis G. S., Lawson M., Lewan M. D., Formolo M., Mi J., He K., Hu G. and Eiler J. M. (2018) Equilibrium and non-equilibrium controls on the abundances of clumped isotopologues of methane during thermogenic formation in laboratory experiments: Implications for the chemistry of pyrolysis and the origins of natural gases. *Geochimica et Cosmochimica Acta* **223**, 159–174.

Smith S. (1985) Noble Gas solubility in water at high temperatures. *Eos* **66**, 397.

Smith S. P. and Kennedy B. M. (1983) The solubility of noble gases in water and in NaCl brine. *Geochimica et Cosmochimica Acta* **47**, 503–515.

Solomon D. K., Hunt A. and Poreda R. J. (1996) Source of radiogenic helium 4 in shallow aquifers: Implications for dating young groundwater. *Water Resources Research* **32**, 1805–1813.

Staudacher Th., Sarda Ph., Richardson S. H., Allègre C. J., Sagna I. and Dmitriev L. V. (1989) Noble gases in basalt glasses from a Mid-Atlantic Ridge topographic high at 14°N: geodynamic consequences. *Earth and Planetary Science Letters* **96**, 119–133.

Stolper D. A., Lawson M., Davis C. L., Ferreira A. A., Neto E. V. S., Ellis G. S., Lewan M. D., Martini A. M., Tang Y., Schoell M., Sessions A. L. and Eiler J. M. (2014a) Formation temperatures of thermogenic and biogenic methane. *Science* **344**, 1500–1503.

Stolper D. A., Lawson M., Formolo M. J., Davis C. L., Douglas P. M. J. and Eiler J. M. (2018) The utility of methane clumped isotopes to constrain the origins of methane in natural gas accumulations. *Geological Society, London, Special Publications* **468**, 23–52.

Stolper D. A., Martini A. M., Clog M., Douglas P. M., Shusta S. S., Valentine D. L., Sessions A. L. and Eiler J. M. (2015) Distinguishing and understanding thermogenic and biogenic sources of methane using multiply substituted isotopologues. *Geochimica et Cosmochimica Acta* **161**, 219–247.

Stolper D. A., Sessions A. L., Ferreira A. A., Santos Neto E. V., Schimmelmann A., Shusta S. S., Valentine D. L. and Eiler J. M. (2014b) Combined ^{13}C–D and D–D clumping in methane: Methods and preliminary results. *Geochimica et Cosmochimica Acta* **126**, 169–191.

Stuart F. M., Lass-Evans S., Fitton J. G. and Ellam R. M. (2003) High $^{3}He/^{4}He$ ratios in picritic basalts from Baffin Island and the role of a mixed reservoir in mantle plumes. *Nature* **424**, 57–59.

Stute M., Forster M., Frischkorn H., Serejo A., Clark J. F., Schlosser P., Broecker W. S. and Bonani G. (1995) Cooling of Tropical Brazil (5°C) During the Last Glacial Maximum. *Science* **269**, 379–383.

Sweeney J. J. and Burnham A. K. (1990) Evaluation of a Simple Model of Vitrinite Reflectance Based on Chemical Kinetics. *AAPG Bulletin* **74**.

Takai K., Nakamura K., Toki T., Tsunogai U., Miyazaki M., Miyazaki J., Hirayama H., Nakagawa S., Nunoura T. and Horikoshi K. (2008) Cell proliferation at 122°C and isotopically heavy CH_4 production by a hyperthermophilic methanogen under high-pressure cultivation. *Proceedings of the National Academy of Science*, 10949–10954.

Tang Y., Perry J. K., Jenden P. D. and Schoell M. (2000) Mathematical modeling of stable carbon isotope ratios in natural gases. *Geochimica et Cosmochimica Acta* **64**, 2673–2687.

Taylor K. A., Fram M. S., Landon M. K., Kulongoski J. T. and Faunt C. C. (2014) *Oil, Gas, and Groundwater Quality in California—a discussion of issues relevant to monitoring the effects of well stimulation at regional scales*. Prepared in Cooperation with the California State Water Resources Control Board ftp://ftp.consrv.ca.gov/pub/oil/SB4EIR/docs/Taylor_et_al_2014.pdf [Accessed November 2018]

Thiagarajan N., Kitchen N., Xie H., Ponton C., Lawson M., Formolo M. and Eiler J. (2020a) Identifying thermogenic and microbial methane in deep water Gulf of Mexico Reservoirs. *Geochimica et Cosmochimica Acta* **275**, 188–208.

Thiagarajan N., Xie H., Ponton C., Kitchen N., Peterson B., Lawson M., Formolo M., Xiao Y. and Eiler J. (2020b) Isotopic evidence for quasi-equilibrium chemistry in thermally mature natural gases. *Proceedings of the National Academy of Science* **117**, 3989–3995.

Timmers P. H. A., Welte C. U., Koehorst J. J., Plugge C. M., Jetten M. S. M. and Stams A. J. M. (2017) Reverse Methanogenesis and Respiration in Methanotrophic Archaea. *Archaea* **2017**, 1–22.

Tissot B. P. and Welte D. H. (2013) *Petroleum Formation and Occurrence*. (Eds: Tissot B.P., Welte D.H.) Springer Science & Business Media. Berlin Heidelberg New York.

Tolstikhin I., Lehmann B. E., Loosli H. H. and Gautschi A. (1996) Helium and argon isotopes in rocks, minerals, and related ground waters: A case study in northern Switzerland. *Geochimica et Cosmochimica Acta* **60**, 1497–1514.

Torgersen T. (2010) Continental degassing flux of ^{4}He and its variability. *Geochemistry, Geophysics, Geosystems* **11**(6).

Torgersen T. (1980) Controls on pore-fluid concentration of ^{4}He and ^{222}Rn and the calculation of ^{4}He/^{222}Rn ages. *Journal of Geochemical Exploration* **13**, 57–75.

Torgersen T. (1989) Terrestrial helium degassing fluxes and the atmospheric helium budget: Implications with respect to the degassing processes of continental crust. *Chemical Geology: Isotope Geoscience section* **79**, 1–14.

Torgersen T. and Clarke W. B. (1985) Helium accumulation in groundwater, I: An evaluation of sources and the continental flux of crustal ^{4}He in the Great Artesian Basin, Australia. *Geochimica et Cosmochimica Acta* **49**, 1211–1218.

Torgersen T. and Kennedy B. M. (1999) Air-Xe enrichments in Elk Hills oil field gases: role of water in migration and storage. *Earth and Planetary Science Letters* **167**, 239–253.

Torgersen T. and Stute M. (2013) Helium (and other noble gases) as a tool for understanding long timescale groundwater transport. In: *Isotope methods for dating old groundwater*. International Atomic Energy Agency, Vienna. Chapter 8, 179–216.

Tsuzuki N., Takeda N., Suzuki M. and Yokoi K. (1999) The kinetic modelling of oil cracking by hydrothermal pyrolysis experiments. *International Journal of Coal Geology* **39**, 227–250.

Tucker J. M. and Mukhopadhyay S. (2014) Evidence for multiple magma ocean outgassing and atmospheric loss episodes from mantle noble gases. Elsevier Enhanced Reader. *Earth and Planetary Science Letters* **393**, 254–265.

Vandenbroucke M., Behar F. and Rudkiewicz J. L. (1999) Kinetic modelling of petroleum formation and cracking: implications from the high pressure/high temperature Elgin Field (UK, North Sea). *Organic Geochemistry* **30**, 1105–1125.

Vengosh A., Jackson R. B., Warner N., Darrah T. H. and Kondash A. (2014) A Critical Review of the Risks to Water Resources from Unconventional Shale Gas Development and Hydraulic Fracturing in the United States. *Environmental Science & Technology* **48**, 8334–8348.

Wang D. T., Gruen D. S., Lollar B. S., Hinrichs K.-U., Stewart L. C., Holden J. F., Hristov A. N., Pohlman J. W., Morrill P. L., Könneke M., Delwiche K. B., Reeves E. P., Sutcliffe C. N., Ritter D. J., Seewald J. S., McIntosh J. C., Hemond H. F., Kubo M. D., Cardace D., Hoehler T. M. and Ono S. (2015) Non-equilibrium clumped isotope signals in microbial methane. *Science* **348**, 428–431.

Wang Z., Schauble E. A. and Eiler J. M. (2004) Equilibrium thermodynamics of multiply substituted isotopologues of molecular gases. *Geochimica et Cosmochimica Acta* **68**, 4779–4797.

Warr O., Ballentine C. J., Onstott T. C., Nisson D., Kieft T. L. and Sherwood Lollar B. (2020) Novel Radiogenic Noble Gas Signatures in the Crust: The Krypton Factor. AGU abstracts. AGU Online.

Warr O., Rochelle C. A., Masters A. and Ballentine C. J. (2015) Determining noble gas partitioning within a CO_2–H_2O system at elevated temperatures and pressures. *Geochimica et Cosmochimica Acta* **159**, 112–125.

Warr O., Sherwood Lollar B., Fellowes J., Sutcliffe C. N., McDermott J. M., Holland G., Mabry J. C. and Ballentine C. J. (2018) Tracing ancient hydrogeological fracture network age and compartmentalisation using noble gases. *Geochimica et Cosmochimica Acta* **222**, 340–362.

Wen T., Castro M. C., Nicot J.-P., Hall C. M., Larson T., Mickler P. and Darvari R. (2016) Methane Sources and Migration Mechanisms in Shallow Groundwaters in Parker and Hood Counties, Texas—A Heavy Noble Gas Analysis. *Environmental Science & Technology* **50**, 12012–12021.

Wen T., Castro M. C., Nicot J.-P., Hall C. M., Pinti D. L., Mickler P., Darvari R. and Larson T. (2017) Characterizing the Noble Gas Isotopic Composition of the Barnett Shale and Strawn Group and Constraining the Source of Stray Gas in the Trinity Aquifer, North-Central Texas. *Environmental Science & Technology* **51**, 6533–6541.

Whiticar M. J. (1999) Carbon and hydrogen isotope systematics of bacterial formation and oxidation of methane. *Chemical Geology* **161**, 291–314.

Whiticar M. J., Faber E. and Schoell M. (1986) Biogenic methane formation in marine and freshwater environments: CO_2 reduction vs. acetate fermentation—Isotope evidence. *Geochimica et Cosmochimica Acta* **50**, 693–709.

Wieler R. and Eikenberg J. (1999) An upper limit on the spontaneous fission decay constant of ^{232}Th derived from xenon in monazites with extremely high Th/U ratios. *Geophysical Research Letters* **26**, 107–110.

Wilhelms A., Larter S. R., Head I., Farrimond P., di-Primio R. and Zwach C. (2001) Biodegradation of oil in uplifted basins prevented by deep-burial sterilization. *Nature* **411**, 1034–1037.

Wilkinson M., Gilfillan S. M. V., Haszeldine R. S. and Ballentine C. J. (2010) Plumbing the depths: testing natural tracers of subsurface CO_2 origin and migration, Utah. In *Carbon Dioxide sequestration in geological media- State of the Science* AAPG Studies.

Williams C. D. and Mukhopadhyay S. (2019) Capture of nebular gases during Earth's accretion is preserved in deep-mantle neon. *Nature* **565**, 78–81.

Worden R. H., Coleman M. L. and Matray J.-M. (1999) Basin scale evolution of formation waters: a diagenetic and formation water study of the Triassic Chaunoy Formation, Paris Basin. *Geochimica et Cosmochimica Acta* **63**, 2513–2528.

Xia X. and Gao Y. (2019) Kinetic clumped isotope fractionation during the thermal generation and hydrogen exchange of methane. *Geochimica et Cosmochimica Acta* **248**, 252–273.

Yoshinaga M. Y., Holler T., Goldhammer T., Wegener G., Pohlman J. W., Brunner B., Kuypers M. M. M., Hinrichs K.-U. and Elvert M. (2014) Carbon isotope equilibration during sulphate-limited anaerobic oxidation of methane. *Nature Geoscience* **7**, 190–194.

Young E. D. (2019) A Two-Dimensional Perspective on CH_4 Isotope Clumping: Distinguishing Process from Source. In *Deep Carbon* (Eds. Orcutt, B. N., Daniel, I., Dasgupta R.). Cambridge University Press. Chapter 13 pp. 388–414.

Young E. D., Kohl I. E., Lollar B. S., Etiope G., Rumble D., Li S., Haghnegahdar M. A., Schauble E. A., McCain K. A., Foustoukos D. I., Sutclife C., Warr O., Ballentine C. J., Onstott T. C., Hosgormez H., Neubeck A., Marques J. M., Pérez-Rodríguez I., Rowe A. R., LaRowe D. E., Magnabosco C., Yeung L. Y., Ash J. L. and Bryndzia L. T. (2017) The relative abundances of resolved $\Delta^{l2}CH_2D_2$ and $\Delta^{13}CH_3D$ and mechanisms controlling isotopic bond ordering in abiotic and biotic methane gases. *Geochimica et Cosmochimica Acta* **203**, 235–264.

Zahnle K., Gacesa M. and Catling D. C. (2019) Strange messenger: A new history of hydrogen on Earth, as told by Xenon. *Geochimica et Cosmochimica Acta* **244**, 56–85.

Zaikowski A. and Spangler R. R. (1990) Noble gas and methane partitioning from ground water: An aid to natural gas exploration and reservoir evaluation. *Geology* **18**, 72.

Zartman R. E., Wasserburg G. J. and Reynolds J. H. (1961) Helium, argon, and carbon in some natural gases. *Journal of Geophysical Research (1896-1977)* **66**, 277–306.

Zhou Z. and Ballentine C. J. (2006) ^{4}He dating of groundwater associated with hydrocarbon reservoirs. *Chemical Geology* **226**, 309–327.

Zhou Z., Ballentine C. J., Kipfer R., Schoell M. and Thibodeaux S. (2005) Noble gas tracing of groundwater/coalbed methane interaction in the San Juan Basin, USA. *Geochimica et Cosmochimica Acta* **69**, 5413–5428.

Ziegler J. F. (1977) *Helium: Stopping Powers and Ranges in All Elemental Matter*. Pergamon Press, Michigan.

Chapter 2

A novel method for the extraction, purification and characterisation of noble gases in produced fluids

R.L. Tyne[1], P.H. Barry[2], D.J. Hillegonds[1], A.G. Hunt[3], J.T. Kulongoski[4], M.J. Stephens[5], D.J. Byrne[6], C.J. Ballentine[1]

[1] Department of Earth Sciences, University of Oxford, Oxford, UK. [2] Department of Marine Chemistry and Geochemistry, Woods Hole Oceanographic Institution, Woods Hole, MA, USA. [3] USGS, Denver Federal Center, Denver, CO, USA. [4] USGS, California Water Science Center, San Diego, CA, USA. [5] USGS, California Water Science Center, Sacramento, CA, USA. [6] CRPG-CNRS, Université de Lorraine, Nancy, France

Contents

Abstract 48
2.1 Introduction 48
2.2 Analytical methods 50
2.3 Air-saturated water data 54
2.3.1 Air-saturated water generation 54
2.3.2 Calculating air-saturated water concentrations 55
2.3.3 Reproducbility of air-saturated water 56
2.4 Produced fluid results 60
2.4.1 Geological context 60
2.4.2 Sample collection 60
2.4.3 Calculating concentrations in multi-phase fluids 61
2.4.4 Produced fluid compositions 63
2.5 Conclusions 64
S2.1 Supplementary figures 65
S2.2 Supplementary tables 67
S2.3 Supplementary information 69
Acknowledgments, samples, and data 74
Authorship statement 75
References 76

Abstract

Hydrocarbon systems with declining or viscous oil production are often stimulated using enhanced oil recovery (EOR) techniques, such as the injection of water, steam and CO_2, in order to increase oil and gas production. As EOR and other methods of enhancing production such as hydraulic fracturing have become more prevalent, environmental concerns about the impact of both new and historical hydrocarbon production on overlying shallow aquifers have increased. Noble gas isotopes are powerful tracers of subsurface fluid provenance and can be used to understand the impact of EOR on hydrocarbon systems and potentially overlying aquifers. In oil systems, produced fluids can consist of a mixture of oil, water and gas. Noble gases are typically measured in the gas phase; however, it is not always possible to collect gases and therefore produced fluids (which are water, oil and gas mixtures) must be analysed. We outline a new technique to separate and analyse noble gases in multi-phase hydrocarbon-associated fluid samples. An offline double capillary method has been developed to quantitatively isolate noble gases into a transfer vessel, while effectively removing all water, oil, and less volatile hydrocarbons. The gases are then cleaned and analysed using standard techniques. Air-saturated water reference materials (n=24) were analysed and results show a method reproducibility of 2.9% for ^{4}He, 3.8% for ^{20}Ne, 4.5% for ^{36}Ar, 5.3% for ^{84}Kr and 5.7% for ^{132}Xe. This new technique was used to measure the noble gas isotopic compositions in six produced fluid samples from the Fruitvale Oil Field, Bakersfield, California.

2.1. Introduction

The increasing use of enhanced oil recovery (EOR) and other techniques to increase hydrocarbon recovery such as hydraulic fracturing has led to concerns that shallow aquifers could be contaminated due to these more intensive hydrocarbon production practices (Vengosh, et al. 2014; Darrah et al. 2014, 2015; Gilfillan et al., 2017, Harkness et al., 2017). It is imperative to understand subsurface fluid provenance and dynamics when investigating such systems. In systems with long hydrocarbon production histories, it is valuable to determine the pristine signature (before EOR) and how the system has evolved geochemically with production; injected

fluids play a significant role on this evolution. Noble gases represent powerful geochemical tracers, as they are chemically inert and therefore act conservatively in geologically dynamic systems (Bosch and Mazor, 1988; Pinti and Marty, 1995; Ballentine et al., 1996, 2002; Gilfillan et al., 2009; Darrah et al., 2015). Noble gases are most readily determined in systems dominated by a single phase (e.g., gas, groundwater); however, they can reside in multiple phases (i.e., oil, water and gas) within a hydrocarbon system, and thus may be present in each component.

Terrestrial reservoirs of noble gases (atmospheric, crustal and mantle) have well-characterised and diagnostic isotopic and abundance compositions, meaning fluid contributions from each reservoir can be easily differentiated. Previous studies have successfully used noble gas isotopes and abundances to quantify water-oil-gas interactions in both conventional and unconventional hydrocarbon systems and those effected by EOR techniques (Ballentine et al., 1991, 1996, 2002; Prinzhofer, 2013; Darrah, et al., 2014, 2015; Györe et al., 2015, 2017, Barry et al., 2016, 2017, 2018a, 2018b; Byrne et al., 2018a, 2018b). These studies have primarily focused on natural gas systems, although some have specifically investigated oil systems (e.g., Ballentine et al., 1996; Györe et al., 2017), unconventional systems (e.g., Zhou et al., 2005; Byrne et al., 2018b) and multi-component systems (Barry et al., 2018b). The use of noble gases as tracers in oil-dominated systems is not yet well established due to the multi-phase nature of these samples meaning they are not amenable to the normal high-vacuum noble gas purification procedures for natural gases. As a result, the focus of previous studies has been primarily on gas phase hydrocarbon samples, which are exsolved from oil as they decompress during production (Supplementary Figure S2.1; Ballentine et al., 2002; Prinzhofer, 2013). Recent studies reconstructed the noble gas composition of the oil phase from casing gas measurements using broad assumptions about gas solubility in oil (e.g. Barry et al., 2018a, 2018b). However, production practices are often not amenable to collecting casing gas samples, and therefore produced fluids must be used to geochemically characterise the hydrocarbon reservoir. Additionally, if casing gas flow is controlled or diverted during production, produced waters samples may provide a better representation of reservoir conditions.

We present a new method for isolating noble gases from produced fluids, containing water-gas-oil mixtures. The technique required construction of an offline extraction system, which interfaced with existing purification systems and two noble gas mass spectrometers (Thermo Argus VI and Thermo Helix SFT). New composition and isotope data for air-saturated water (ASW) is reported. The precision, accuracy and reproducibility of both ASW and produced fluid samples measured is assessed using the new method. Produced fluid data indicates that this technique is robust at isolating and measuring noble gas isotope compositions in oil-water-gas mixtures and can be used to investigate processes within hydrocarbon reservoirs.

2.2. Analytical methods

Noble gas analyses were conducted in the Noble Laboratory at the University of Oxford, UK, where the analysis of gas phase samples is well-established using a custom-built high vacuum gas purification system to purify and separate noble gas species before measurement (e.g., Barry et al., 2016, 2017, 2018a, 2018b; Byrne et al., 2018a, 2018b). Samples containing significant liquid volumes cannot be analysed in this way, as the liquids are not adequately removed using conventional cryogenic or gettering techniques, are adsorbed easily to the inside of the stainless-steel system and are difficult to remove even using ultra-high vacuum turbomolecular and diaphragm pump combinations. Single-phase water samples are routinely characterised in other laboratories (e.g., Beyerle et al., 2000; Hunt, 2015). However, the introduction of hydrocarbons into these types of systems will contaminate the mass-spectrometers, the increased backgrounds and isobaric interferences will significantly reduce measurement precision and reliability. A new, inlet line and vacuum system were developed for the extraction of the noble gases from multi-phase fluid samples using a double capillary method to quantitatively transfer all the noble gases. Water vapour in the system is cryogenically drawn across the capillary towards a stainless-steel cold trap cooled to -196^{o}C. The strong flow of water vapour entrains the noble gases and quantitatively draws them across towards the cold trap, preventing any backflow of noble gases and resulting in their isolation in the transfer vessel (Beyerle et al., 2000). The capillaries were effective at isolating the noble gases in the transfer vessel and minimizing water transfer; the

liquid volume transferred was typically less than 0.5ml compared to the initial sample size of approximately 13ml. The transfer vessel is later attached to a gas purification system (Figure 2.1). The extraction line system consists of high-vacuum circular knife-edge (ConFlat fittings) fittings with copper flanges, VCR fittings with silver-coated stainless-steel gaskets and bellow-sealed valves. It is split into two volumes (A, B), and the Cu tube which interfaces the sample to the extraction system. Volume A represents the dedicated inlet section and is comprised of a degassing volume and a 1 mm (inside diameter, ID) by 30 mm capillary on the horizontal between the degassing vessel and the transfer vessel. The 1mm capillary is included to minimize the transfer of water and low-volatility hydrocarbons out of the transfer vessel. In volume B, the noble gases are stored and transferred to the gas purification system; it includes a 0.5 mm ID by 30 mm capillary screwed into a solid Cu disk below valve E2.

Initially volumes A and B are pumped to low-vacuum (to $<2 \times 10^{-2}$ mbar) using a rotary pump and then to high-vacuum using a turbo molecular pump (to $<3 \times 10^{-6}$ mbar). Valves E2 and E3 are then closed and the bottom of volume B (up to where the vessel separates to the two valves) is cooled to -196ºC using a liquid nitrogen bath. Volume A is heated to 600ºC using a thermostatically controlled heater, whilst being actively pumped. After 3 minutes, E4 is closed and the sample is released into the extraction volume by opening clamp E1, with valves E2-E4 closed. The Cu tube sample and volume A are then heated (using a thermostatically controlled heater at 600^{o}C) for an additional 3 minutes. Valve E2 is then opened to allow for the cryogenic transfer of noble gases and water vapour across the capillary into volume B. To further facilitate the degassing of the sample and noble gas transfer, the degassing vessel is agitated in an ultra-sonic bath and the sample tube and capillaries are heated (as above) for two minutes every 15 minutes, to ensure the system stays at temperature. After one hour, valve E2 is closed and the transfer vessel is moved to the dedicated gas purification system. The extraction of noble gases from water typically takes between 18-30 minutes (e.g., Hunt 2015). In implementing a double capillary method for the produced fluids, the transfer time was increased to one hour to establish a safety margin ensuring quantitative gas transfer into the transfer vessel and sufficient water

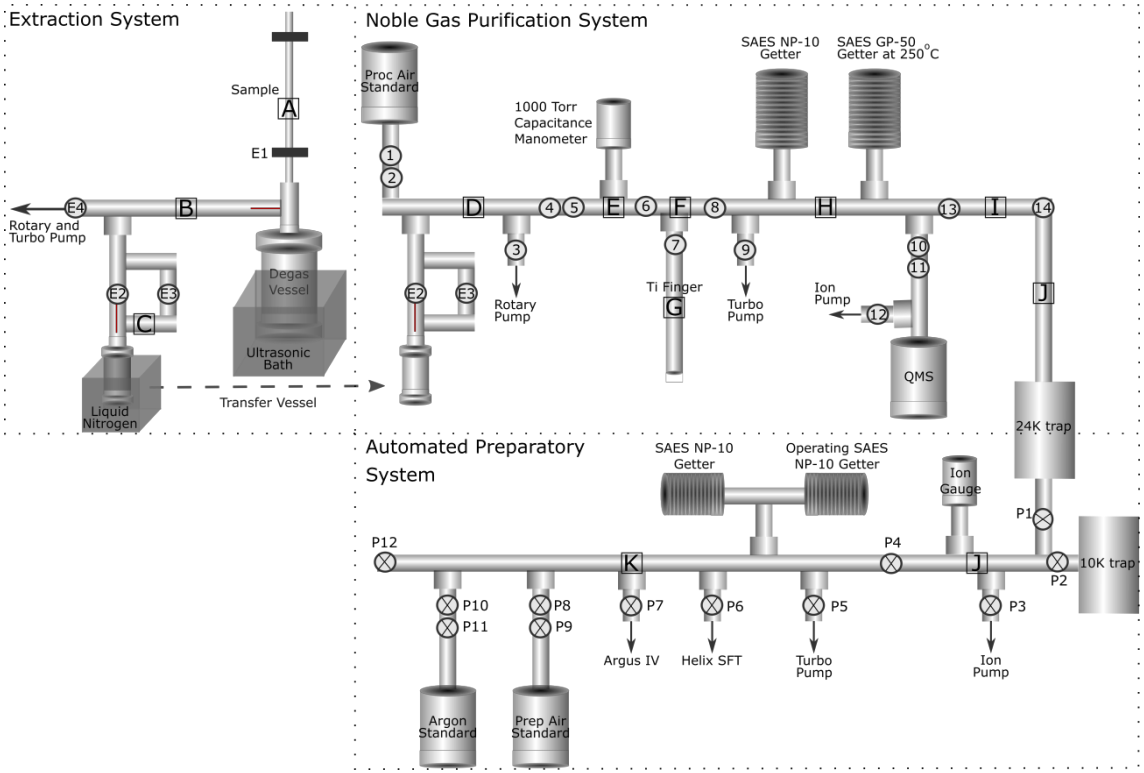


Figure 2.1: Schematic diagram of the noble gas extraction system, noble gas purification system and automated preparatory system. The systems are constructed of stainless steel with high-vacuum circular knife-edge (ConFlat (CF) fittings) fittings with copper flanges and bellow-sealed valves, with the exception of the fittings to both the vessels on the extraction systems, which are ¼" VCR fittings with silver-coated stainless steel gaskets. The procedure is split across three different systems (extraction, noble gas purification and automated preparatory) with 11 distinct volumes held at vacuum by turbomolecular pumps. The Hidden Analytical HAL-200 quadrupole mass spectrometer on the gas purification system is held separately at vacuum by a dedication ion pump. The procedural air standard was collected in a cylinder from University Parks, Oxford, UK on November 24th 2014 (Pressure: 1027mBar, Temperature: 5 ºC and Humidity: 89%). The prep air standard was collected in a cylinder from University Parks on May 13th 2016 (Pressure: 1010mBar, Temperature: 14 ºC and Humidity: 71%).

vapour accumulation to enable quantitative gas transfer back out of the transfer vessel onto the noble gas purification system.

Once extracted, the transfer vessel is moved to a gas purification line. The noble gases are transferred back through the capillary by establishing a flow of water vapour from the transfer vessel onto a titanium sponge held at 950°C. Details about the subsequent purification and analysis steps can be found in the supplementary information (S2.3.1). In addition, the supplementary information contains information on the types of standards, blanks and corrections used (S2.3.2).

After gases are extracted, the relative amounts of gas (V_g(cm^3)), water (V_w(cm^3) and oil (V_o(cm^3)) in each Cu tube are measured using the full Cu tube volume (V_t=*length*pi*(ID/2)^2*), the weight of sample processed, and the ratio of oil-water collected within the degas vessel, after the extraction of each sample (Table 2.1).

Sample ID	Production conditions		API	Volumes sampled			GORs	WORs
	Temperature °C	Salinity M	°	Oil cm^3	Gas cm^3	Water cm^3		
F1	29	0.095	18.5	0	0.5	12.9	76	41
F2	36	0.095	18.5	0	0.8	12.4	75	17
F3	35	0.095	18.5	0.3	0.6	12.4	75	147
F4	36	0.095	18.5	0	0.4	12.9	75	25
F5	36	0.095	18.5	0	0.4	12.9	76	28
F6	43	0.095	16.7	0	0.7	12.7	48	39

Table 2.1: Oil Metadata for the produced waters from the Fruitvale Oil Field. Volumes sampled are those in the Cu tube measured in the laboratory. All other information is from the California Division of Oil, Gas, and Geothermal Resources (2018). GORs and WORs are the gas-oil ratio and water-oil ratio respectively for the production well during the month of sampling. For additional meta data see Table S2.2.

As it is highly probable that an oily residue remains within the extraction system, the system (past E4) is dismantled and cleaned after each extraction. Parts are washed and sonicated in an acetone bath to remove any oily residue and then placed in an oven at 100 °C for a minimum of 1 hour to remove the acetone. The parts are then scrubbed with a plastic brush and neutracon detergent (Decon) and rinsed in DI water, to ensure the removal of any leftover salt before being returned

to the oven for 1 hour. Parts are also washed with Petroleum Ether and left to dry for 1 hour under a fume hood. The system is then reassembled and He leak checked.

2.3. Air-saturated water data

ASWs were used as a reference material for checking the method reproducibility and calibrating sample measurements. These were chosen over an air standard, as they are more comparable to the samples. Due to the length of time that is required to run an ASW, only 24 have been analysed.

2.3.1. Air-saturated water generation

ASWs were made in the Oxford Noble Laboratory, by equilibrating 20L of water in a plastic carboy with the atmosphere. Equilibration is ensured using an aquarium bubbler (bubbling at a rate of 2 L/min) suspended in the water (Hillegonds et al., 2013). Water is bubbled for a minimum of seven days with the laboratory air temperature next to the carboy recorded every 15 minutes. Temperature variations are typically ±0.2 ºC. The bubbler is stopped at least three hours prior to sampling of the ASWs. The noble gas concentrations in the ASW generated are as expected under those conditions.

ASW samples were taken in copper tubes held in clamp holders to ensure consistent liquid volume. The final equilibration temperature was taken as the average air temperature of the 48 hours prior to sampling. ASW were extracted using the method described in this paper and were analysed between every three unknown samples through the system.

2.3.2. Calculating air-saturated water concentrations

The concentration of each noble gas in ASW can be calculated using Henry's Law solubility equilibrium. The expected concentration (cm^3/cm^3) in the ASW under laboratory conditions can be calculated using:

$$C_i^{ex\ asw} = \frac{\left(P_{dry} - e^{\left(-5375.83/T+21.20\right)}\right) \times P_i}{Mr_{H20} \times P_{dry} \times {K_i}^{gw}} \times e^{\left(h/8350\right)} \qquad \text{(Eq. 2.1)}$$

where $C_i^{ex\ asw}$ is the expected concentration of *i* in the ASW, *h* is the elevation (m) and *T* is the mean laboratory temperature (17°C). P_{dry} represents the partial pressure of water vapour in dry air (760 Torr). P_i is the partial pressure of *i* in the atmosphere (GPa). Mr_{H20} is the molar mass of H2O (18.02 g/mol). K_i^{gw} is Henrys Constant for ASW generation (17°C, 0M and 65m)(Crovetto et al., 1982, Fernández-Prini et al., 2003, Smith and Kennedy 1983, Wagner and Pruss, 1992). All Parameters are defined in Supplementary Table S2.1.

The noble gas concentrations for each ASW analysed were calculated using the expected concentrations for the corresponding equilibration temperature (Eq. 2.2). Temperature differences between different ASWs generated could cause He, Ne, Ar, Kr, Xe concentration variations of 0.34%, 1.2%, 3.2%, 3.9% and 4.9% respectively. In order to compare all the ASW, they were all subsequently corrected to 17°C. In addition, the signals had to be corrected for any internal machine changes (i.e. machine drift) over the 10-month period they were analysed and normalized to the internal air standards.

$$C_i^{\ asw} = \frac{S_i\ /V_w}{S_i^{\ asw\ av}/V_{asw\ av}} \times C_i^{ex\ asw} \qquad \text{(Eq. 2.2)}$$

C_i^{asw} = ASW concentration (cm^3/cm^3), S_i= corrected signal for *i* (fA), V_w= weight of water processed (cm^3), $V_{asw\ av}$= average ASW weight (cm^3) and $S_i^{asw\ av}$ is the average ASW signal for *i* (fA).

2.3.3. Reproducibility of air-saturated waters

Concentrations of air-derived noble gases (^{4}He, ^{20}Ne, ^{36}Ar, ^{84}Kr, ^{132}Xe) in the water phase were calculated to be 4.5±0.1 x 10^{-8} cm^3/cm^3 , 1.7±0.1 x 10^{-7} cm^3/cm^3, 1.1±0.1 x 10^{-6} cm^3/cm^3, 4.4±0.2 x 10^{-8} cm^3/cm^3, and 3.0±0.2 x 10^{-9} cm^3/cm^3 respectively (Figure 2.2, Table 2.2).

Instrument error (associated with the internal air standards, supplementary information S2.3.1.) is <1.2 % for all isotopes, the method reproducibility between ASWs is the most significant source of error. The elemental ratios are ^{20}Ne/^{36}Ar 0.15±0.01, ^{84}Kr/^{36}Ar 0.039±0.003 and ^{132}Xe/^{36}Ar 0.0027±0.0002. This is significantly less than the difference in the important natural

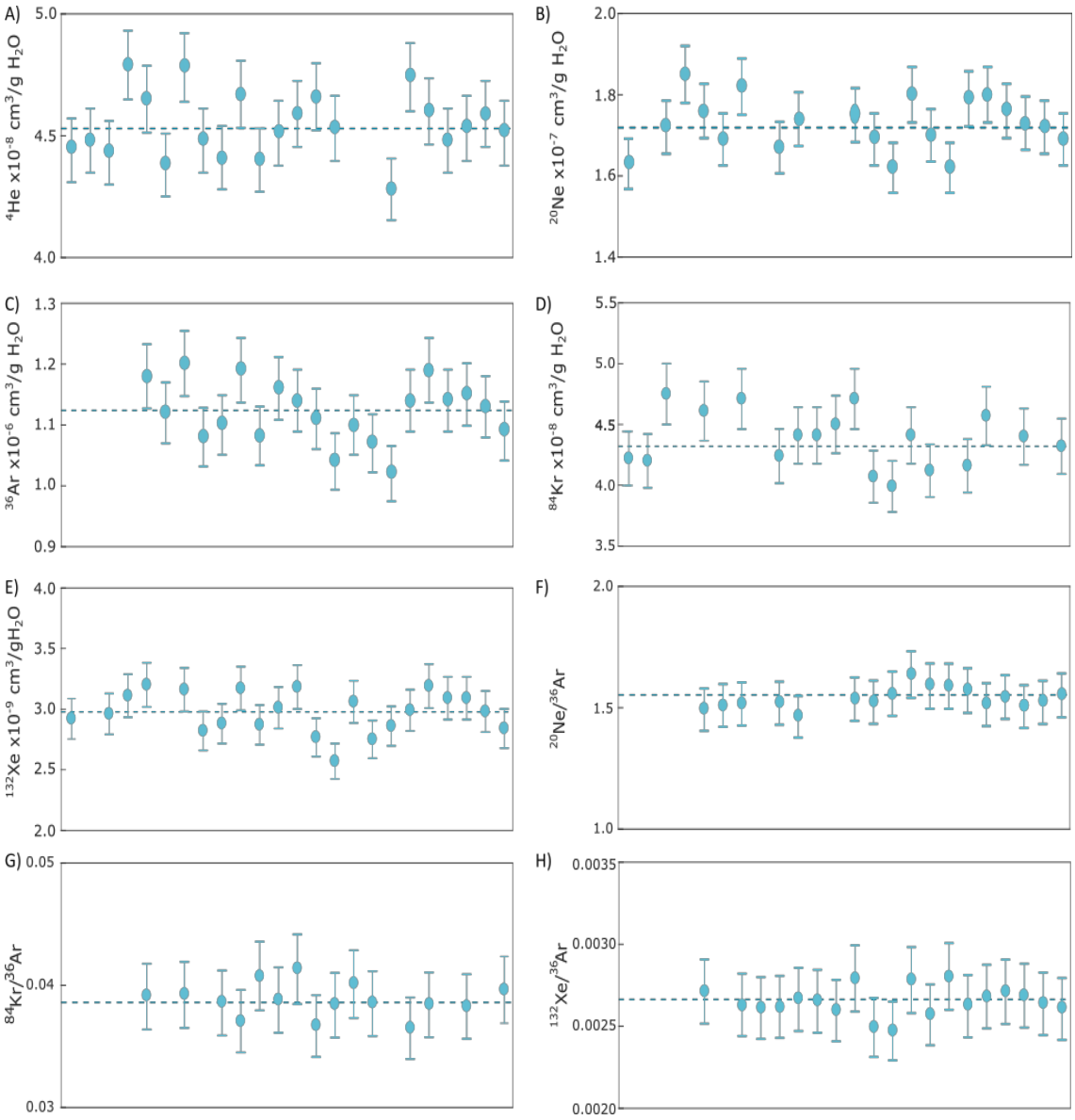


Figure 2.2.: Overall reproducibility of the ASW reference materials. Mean values are given by dashed line and errors are for 1 standard deviation. A) Reproducibility of the ^{4}He concentrations across all the ASWs. Mean concentration was 4.54±0.13 x10^{-8} cm^3/cm^3. B) Reproducibility of the ^{20}Ne concentrations in the ASWs. Mean concentration was 1.73±0.07 x10^{-7} cm^3/cm^3. C) Reproducibility of the ^{36}Ar concentrations across all the ASWs. Mean concentration was 1.12±0.05 x10^{-6} cm^3/cm^3. D) Reproducibility of the ^{84}Kr concentrations in the ASWs. Mean concentration was 4.38±0.23 x10^{-8} cm^3/cm^3. E) Reproducibility of the ^{132}Xe concentrations in the ASWs run. Mean concentration was 2.98±0.17 x10^{-9} cm^3/cm^3. F) Reproducibility of the elemental ratio ^{20}Ne/^{36}Ar. Mean ^{20}Ne/^{36}Ar was 0.15±0.009. G) Reproducibility of the elemental ratio ^{84}Kr/^{36}Ar. Mean ^{84}Kr/^{36}Ar was 0.039±0.003. H) Reproducibility of the elemental ratio ^{132}Xe/^{36}Ar. Mean ^{132}Xe/^{36}Ar was 0.0027±0.0002

	^{4}He x10^{-8}	^{20}Ne x10^{-7}	^{36}Ar x10^{-6}	^{84}Kr x10^{-8}	^{132}Xe x10^{-9}	$^{3}He/^{4}He$ (R/R_A)	$^{20}Ne/^{22}Ne$	$^{40}Ar/^{36}Ar$	$^{84}Kr/^{82}Kr$	$^{132}Xe/^{130}Xe$	$^{20}Ne/^{36}Ar$
Air	**520**	**170**	**31**	**65**	**24**	**1**	**9.8**	**296**	**4.9**	**6.6**	**0.52**
ASW at 17°C	**4.5**	**1.7**	**1.1**	**4.3**	**2.9**	**1**	**9.8**	**296**	**4.9**	**6.6**	**0.15**
ASW 1	4.4	1.6	n.d	4.2	2.9	0.96	9.2	n.d.	4.8	6.5	n.d.
ASW 2	4.5	n.d.	n.d.	4.2	n.d.	0.96	9.2	n.d.	n.d.	6.5	n.d.
ASW 3	4.4	1.7	n.d.	4.8	3.0	1.00	9.5	n.d.	4.8	6.6	n.d.
ASW 4	4.8	1.9	n.d.	n.d.	3.1	0.95	9.5	n.d.	4.8	6.6	n.d.
ASW 5	4.7	1.8	1.2	4.6	3.2	1.00	9.6	301	4.5	6.6	0.15
ASW 6	4.4	1.7	1.1	n.d.	n.d.	1.00	9.8	301	n.d.	n.d.	0.15
ASW 7	4.8	1.8	1.2	4.7	3.2	1.00	9.8	302	4.5	6.6	0.15
ASW 8	4.5	n.d.	1.1	n.d.	2.8	0.99	9.5	294	4.4	6.8	n.d.
ASW 9	4.4	1.7	1.1	4.2	2.9	n.d.	9.6	300	4.5	6.5	0.15
ASW 10	4.7	1.7	1.2	4.4	3.2	1.01	9.9	298	4.5	6.5	0.15
ASW 11	4.4	n.d.	1.1	4.4	2.9	1.00	9.9	301	4.8	6.5	n.d.
ASW 12	4.5	n.d.	1.2	4.5	3.0	n.d.	9.8	298	4.9	6.6	n.d.
ASW 13	4.6	1.8	1.1	4.7	3.2	1.05	9.7	293	4.8	6.5	0.15
ASW 14	4.7	1.7	1.1	4.1	2.8	0.97	9.7	292	4.7	6.4	0.15
ASW 15	4.5	1.6	1.0	4.0	2.6	0.99	9.8	299	4.8	6.6	0.16
ASW 16	n.d.	1.8	1.1	4.4	3.1	n.d.	9.7	291	4.9	6.4	0.16
ASW 17	n.d.	1.7	1.1	4.1	2.8	1.05	9.3	292	4.9	6.4	0.16
ASW 18	4.3	1.6	1.0	n.d.	2.9	1.03	9.3	292	n.d.	6.6	0.16

Table 2.2: Measured concentrations in ASW (cm^3/cm^3) and associated ratios. Errors are given for 1 standard deviatio

	^{4}He	^{20}Ne	^{36}Ar	^{84}Kr	^{132}Xe	^{3}He/^{4}He (R/R$_A$)	^{20}Ne/^{22}Ne	^{40}Ar/^{36}Ar	^{84}Kr/^{82}Kr	^{132}Xe/^{130}Xe	^{20}Ne/^{36}Ar
	x10^{-8}	x10^{-7}	x10^{-6}	x10^{-8}	x10^{-9}						
ASW 19	4.7	1.8	1.1	4.2	3.0	1.01	9.5	295	4.5	6.6	0.16
ASW 20	4.6	1.8	1.2	4.6	3.2	1.01	9.7	304	4.8	6.5	0.15
ASW 21	4.5	1.8	1.1	n.d.	3.1	1.01	9.7	303	n.d.	6.5	0.15
ASW 22	4.5	1.7	1.2	4.4	3.1	1.00	9.6	304	4.5	6.5	0.15
ASW 23	4.6	1.7	1.1	n.d.	3.0	0.98	9.7	304	n.d.	6.5	0.15
ASW 24	4.5	1.7	1.1	4.3	2.8	1.00	9.7	305	4.8	6.5	0.15
Average ASW	4.5	1.7	1.1	4.4	3.0	1.00	9.6	299	4.7	6.5	0.15
Standard error (%)	2.9%	3.8%	4.5%	5.3%	5.7%	2.7%	2.0%	1.6%	3.6%	1.2%	5.9%

Table 2.2: continued.

ratios (i.e., for $^{20}Ne/^{36}Ar$ Air = 0.52, ASW = 0.15, and an infinitely small volume of oil equilibrated with ASW = 0.04) (Figure 2.2, Table 2.2). The concentration percentage standard error was 1.2%, 2.1%, 2.3%, 2.7% and 2.8% for ^{4}He, ^{20}Ne, ^{40}Ar, ^{84}Kr and ^{132}Xe respectively, in a consecutive set of five ASW noble gas determinations.

Due to the variable nature of the phases in produced water samples at the wellheads, it was not possible to collect repeatable samples to use for sample standardization. However, due to the rigorous clean-up procedure between samples, the ASWs are sufficient to determine the method reproducibility. The water salinity could be altered to match that of the samples being run if necessary

2.4. Produced fluid results

2.4.1. Geological context

The Fruitvale Oil Field is located in the south of the San Joaquin basin (SJB), within the city limits of Bakersfield, California, USA (Supplementary Figure S2.2). Fruitvale, like most oil fields in the SJB is characterised by spatially variable geology and hydrocarbon production depths as well as by widely varying amounts of water injection (Long et al., 2015; DOGGR, 2018). Most of the water injected is produced water from oil wells, although some waste water from refineries is injected in places (Wright et al., 2019). Analyses of casing gas samples from injectate storage tanks in Fruitvale indicated substantial mixing with air (Barry et al., 2018a). Geological and depositional history for the field can be found in the supplementary information (S2.3.3).

The injection and long production history have resulted in temporal variations in the total amount of hydrocarbons and produced waters being produced in the Fruitvale Oil Field (McMahon et al., 2018). The average reservoir temperature is 51ºC and salinity is 0.095M (DOGGR, 2018). The relatively low salinity of the field compared to many oil-field waters is a result of the significant recharge over geologic timescales from the Kern River and other smaller streams draining the high altitude Sierra Nevada (McMahon et al. 2018). There has been no significant change in reservoir

salinity since injection began (Stephens et al., 2018). Production data shows no evidence for gas cap formation at Fruitvale (DOGGR, 1998, 2018).

2.4.2. Sample collection

Six produced water samples were collected from the Fruitvale Oil Field, as part of the California State Water Resources Control Board's oil and gas regional groundwater monitoring program (RMP) (Supplementary Table S2.2). The RMP aims to determine the relations of regional water quality in aquifers located near to oil and gas sources (U.S, Geological Survey, 2019). Produced fluids in the oil wells sampled were pumped to the surface as part of normal production activities and appear as surges of oil, water, and gas at a sampling port on the well discharge pipe. Measured gas-oil (GOR) and water-oil (WOR) ratios during sample collection were >2 and >41 respectively, compared to GOR= 48-76 and WOR=17-147 reported for the wells during the month of sampling (July 2016) by the Division of Oil, Gas and Geothermal Resources (Table 2.1; DOGGR, 2018). With the exception of F5, where no injection has been recorded within 500m since 1977 and is considered pristine, the samples represent wells which have been effected by the injection of produced water for EOR and waste disposal purposes.

Fluid samples were collected in 3/8" refrigeration grade copper tubes connected to sample ports at the wellhead using standard noble gas sampling techniques (Weiss, 1968; Burnard, 2013). The copper tubing was flushed with produced oil well fluids prior to sampling. During water sampling, precautions are typically taken to ensure there are no bubbles present within the tubes (as noble gases preferentially partition to the gas phase); however, as produced fluids are variable mixtures of water, oil, and gas in variable quantities, gas was inherently present within these oil well samples. Copper tubes were connected to the wellhead sampling port using reinforced polytetrafluoroethylene tubing and hose clamps were used to seal each sample from atmospheric exposure during storage. A 'T' was fitted at the wellhead to ensure the tubing did not become over-pressurized once the copper tubes were sealed with stainless steel clamps. Complementary casing gases were not available for collection from oil wells sampled at Fruitvale; this made it an ideal location to test what could be learnt solely from produced water samples.

2.4.3. Calculating concentrations in multi-phase samples

Total concentration of noble gases within the sampled Cu tube can be calculated using Eq. 2.2, where C_i^{asw} is replaced with the total concentration in the sample C_i^S (cm^3/cm^3) and V_w is replaced with the total volume of the Cu tube sampled (V_t,(cm^3)). The total number of mols of noble gases (n_i^t (mol)) within the sample can be calculated using equation 2.3. The total amount of the noble gases within in the Cu tube will not change between production and analysis.

$$n_i^t = \frac{C_i^s \times V_t}{22413} \quad \text{(Eq. 2.3)}$$

Produced fluid samples contain variable mixtures of water, gas, and oil; therefore, it is important to consider the concentration of noble gas in each phase. To calculate the concentration of noble gas in each phase at the time of sampling, the relative solubilities (Henry's Constants) of the noble gases within each phase in the Cu tube must be calculated under production temperature, sample salinity and oil density. For the gas water equilibrium, the solubility coefficient (K_i^{gw}, atm kg/mol) can be calculated in the same way as for ASW (Crovetto et al., 1982; Fernández-Prini et al., 2003; Smith and Kennedy 1983; Wagner and Pruss, 1992). The solubility coefficients between a gas and oil phase (K_i^{go}, atm kg/mol) are calculated using Kharaka and Specht (1988) and Smith and Kennedy (1983). The expected distribution of noble gases between the phases within the Cu tube can then be calculated. The amount in the oil, gas and water phase are calculated relative to each other using equations 2.4 and 2.5.

$$n_i^o = \frac{n_i^g \times V_o}{K_i^{go} \times V_g} \quad \text{(Eq. 2.4)}$$

$$n_i^w = \frac{n_i^g \times V_w}{K_i^{gw} \times V_g} \quad \text{(Eq. 2.5)}$$

where n_i^g is the amount in the gas phase. As just the relative proportions of water, oil and gas are required, any value can be used for n_i^g. The concentration of the noble gases between the phases can then be calculated using equations 2.6-2.8.

$$C_i^g = \frac{n_i^t \times n_i^g}{(n_i^g + n_i^o + n_i^w) \times V_g} \quad \text{(Eq. 2.6)}$$

$$C_i^o = \frac{n_i^t \times n_i^o}{(n_i^g + n_i^o + n_i^w) \times V_o} \quad \text{(Eq. 2.7)}$$

$$C_i^w = \frac{n_i^t \times n_i^w}{(n_i^g + n_i^o + n_i^w) \times V_w} \quad \text{(Eq. 2.8)}$$

where C_i^g, C_i^o and C_i^w are the concentration in the gas, oil and water phase respectively in mol/cm^3. All parameters are defined in Supplementary Table S2.1.

The variable nature of the produced water compositions at the wellhead means that the water oil ratio (WOR) and gas-oil ratio (GOR) are not consistent during sampling and are not representative of the average GOR and WOR for production (Table 2.1). As a result, a collected sample may not contain all three phases. By assuming that the phases are in equilibrium at the wellhead, the concentration in the missing phase can be calculated using equations 2.9-2.10.

$$K_i^{go} = \frac{C_i^g}{C_i^o} \quad \text{(Eq. 2.9)}$$

$$K_i^{gw} = \frac{C_i^g}{C_i^w} \quad \text{(Eq.2.10)}$$

The concentration of noble gases between the three phases at the point of production can be found in Supplementary Table S2.3. The concentrations in the Cu tube were originally reported in Gannon et al. (2018) in cm^3/g (total fluid) at standard temperature and pressure; these values can be converted to the total amount of noble gases in the Cu tube (n_i^t) by multiplying by V_w+V_o. It is important to note that it is assumed that solubility equilibrium has been reached at the wellhead between all phases. If equilibrium has not been reached, the results will be skewed.

2.4.4. Produced fluid compositions

Concentrations of noble gases in both the oil and water phases are significantly depleted in comparison to the gas phase and ASW for recharge conditions at the Fruitvale Oil Field (15ºC, 0M, 123m) (Supplementary Table S2.3). The gas phase is likely to resemble the composition expected

within casing gas samples. The oil and water phase have similar concentrations for the lighter noble gases; however, there is a noticeable enrichment of Kr and Xe within the oil phases due to their higher solubility in oil. Within each phase, concentrations range by up to two orders of magnitude. ^{20}Ne concentrations range from 0.42±0.02 to 57±3 x10^{-12} mol/cm^3 in the gas phase, 0.22±0.01 to 35±2 x10^{-15} mol/cm^3 in the oil phase and 0.19±0.01 to 25±1 x10^{-15} mol/cm^3 in the water phase (Supplementary Table S2.3). Single-element isotope ratios are consistent throughout all the samples; however, the elemental ratios show significant difference between the samples and phases. For example the ^{20}Ne/^{36}Ar in the gas phase ranges from 0.080±0.005 to 0.40±0.03, from 0.0065±0.0005 to 0.033±0.002 in the oil phase, and 0.029±0.002 to 0.15±0.01 in the water phase.

Blank contributions to the samples analysed were <0.40% He, <1.5% Ne, <1.5% Ar, <0.15% Kr and <0.020% Xe, suggesting that the main source of analytical uncertainty on the concentrations is from the variability in the ASW reproducibility.

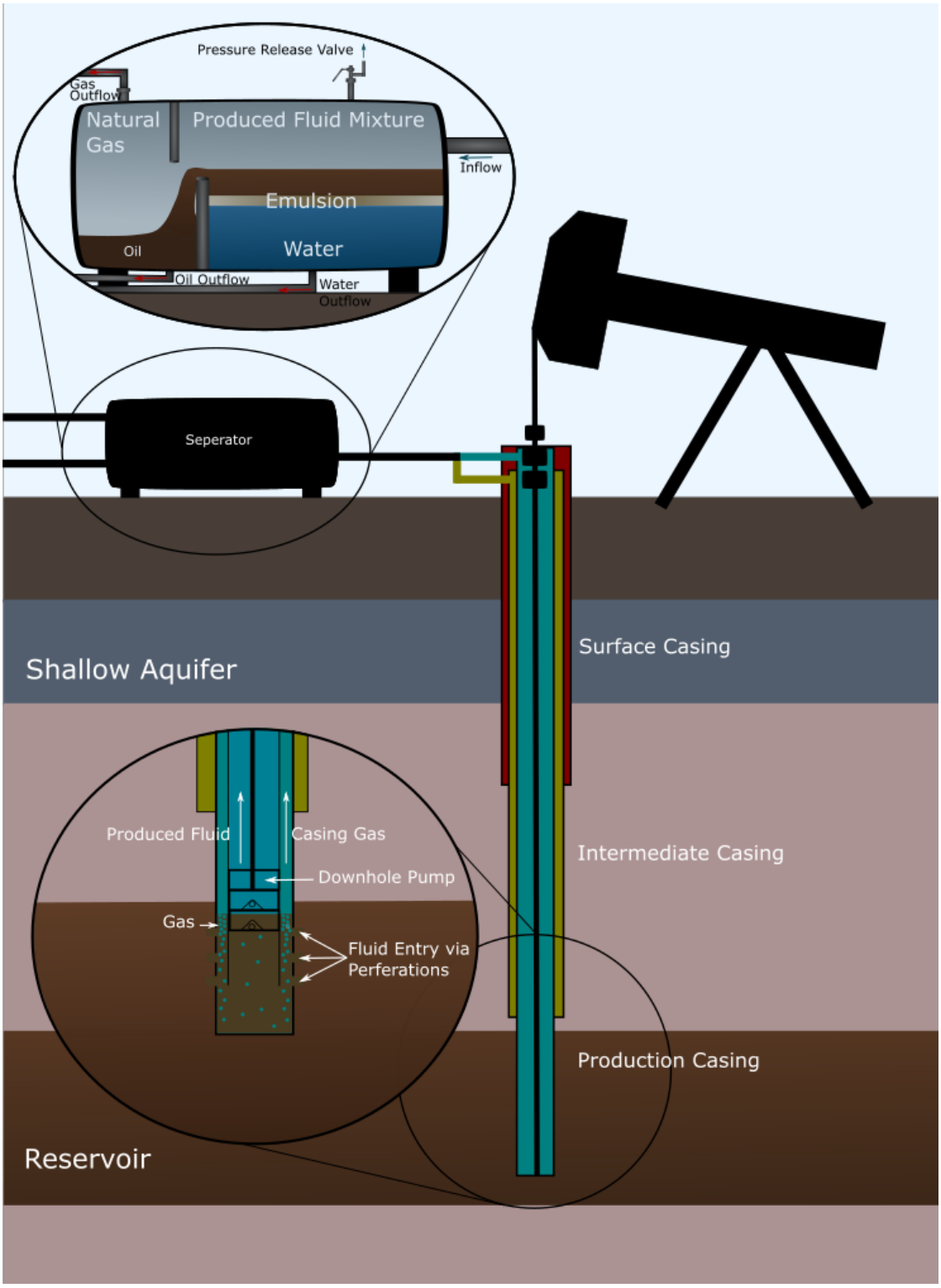
2.5. Conclusions

A newly designed noble gas extraction system, interfaced with a gas purification system, automated preparatory system and Argus IV and Helix SFT mass spectrometers, has been constructed to allow multi-phase oil-water-gas samples from oil wells to be separated and the fluids analysed for their noble gas abundance and isotopic composition. We are able to reproducibly purify and measure noble gases from air-saturated waters and produced fluids using this system. The reproducibility of the ASW reference material was within 2.9% for ^{4}He, 3.8% for ^{20}Ne, 4.5% for ^{36}Ar, 5.3% for ^{84}Kr and 5.7% for ^{132}Xe. We demonstrate the need for and advantages of this new system, which allows us to fully characterise oil field fluids without damaging the ultra-high vacuum systems required for noble gas analysis.

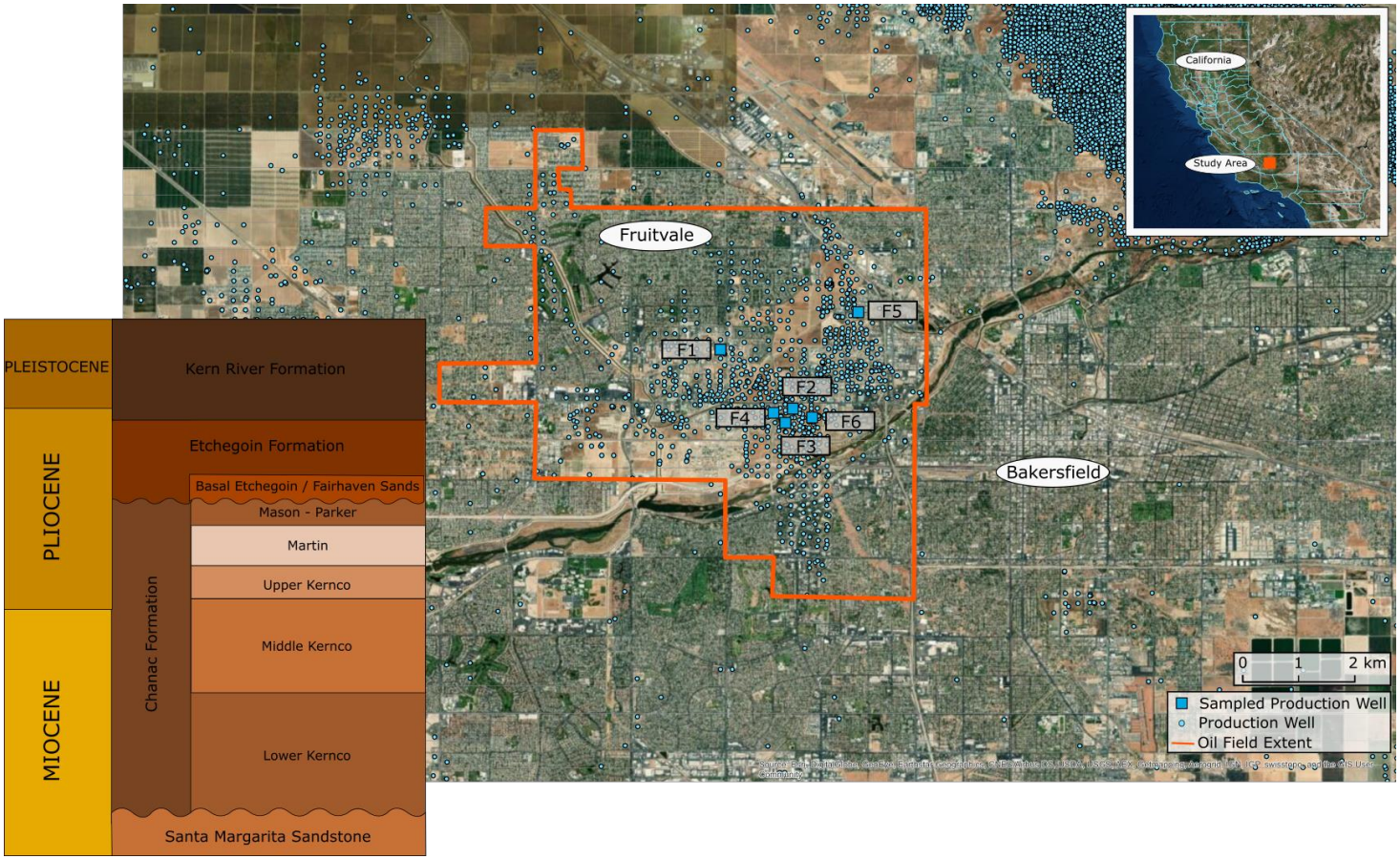
The system was tested for concentrations and isotope ratios with six produced fluid samples from oil wells in the Fruitvale Oil Field, California. The oil and water phases are significantly depleted in noble gases compared to the gas phase and ASW. The ability to calculate noble gas concentrations in each of the phases means produced fluids alone can be effective samples for

geochemically characterising hydrocarbon systems and could be used in similar ways to casing gases to reconstruct hydrocarbon reservoir compositions. Once the reservoir has been fully characterised, reservoir evolution can be modelled, which will be critical when identifying if there is a presence of fugitive gases in overlying aquifers and, if present, determining their source.

S2.1. Supplementary figures



Supplementary Figure S2.1: Schematic conceptual diagram of an oil well set-up based on the wells sampled at the Fruitvale Oil Field, California, U.S.A. The system is purely an oil-water system. Oil enters the well and decompresses due to the pumping allowing for gas formation. This gas travels up in the casing and the produced fluids are pulled up the centre of the well. As the produced fluids rise, decreasing pressure results in more exsolution of gas. The gas, oil and water are then piped to a separator and separated.



Supplementary Figure S2.2: Map showing the location of where the produced water samples (large blue squares) were collected in the Fruitvale Oil Field (outlined in orange). The small blue circles represent all the production wells in Fruitvale and the surrounding oil fields. Well location and oil field boundary data are from the California Division of Oil, Gas, and Geothermal Resources (DOGGR, 2017). Inset shows a stratigraphic column for the field modified from DOGGR (1992) and Scheirer and Magoon (2007).

S2.2. Supplementary tables

Parameter Description	Symbol	Units
Volume water	V_w	cm^3
Volume oil	V_o	cm^3
Volume gas	V_g	cm^3
Volume total	V_t	cm^3
Volume average ASW	$V_{asw\ av}$	cm^3
Henry's Coefficient for gas and water systems	K_i^{gw}	atm kg/mol
Henry's Coefficient for gas and oil systems	K_i^{go}	atm kg/mol
Partial pressure of i in the atmosphere	P_i	Gpa
Temperature of equilibration	T	K
Elevation of equilibration	h	m
Salinity	s	M
Concentration expected of i in ASW	$C_i^{ex\ asw}$	cm^3/cm^3
Concentration of i in ASW	C_i^{asw}	cm^3/cm^3
Signal sample	S_i	fA
Signal average ASW	$S_i^{asw\ av}$	fA
Amount of i in water	n_i^w	mol
Amount of i in oil	n_i^o	mol
Amount of i in gas	n_i^g	mol
Total amount of i	n_i^t	mol
Concentration of i in water	C_i^w	mol/cm^3
Concentration of i in oil	C_i^o	mol/cm^3
Concentration of i in gas	C_i^g	mol/cm^3

Supplementary Table S2.1: Parameters used for concentration calculations and models.

Sample ID	Site ID	COGG ID	API	Site type	Sample Date
F1	352336119043201	4_FRUT_PW01	02906886	Oil Well	7/26/2016
F2	352256119034201	4_FRUT_PW02	02958737	Oil Well	7/26/2016
F3	352246119034801	4_FRUT_PW03	02908164	Oil Well	7/26/2016
F4	352253119035701	4_FRUT_PW04	02908174	Oil Well	7/26/2016
F5	352401119025901	4_FRUT_PW05	02906854	Oil Well	7/26/2016
F6	352250119033001	4_FRUT_PW06	02908153	Oil Well	7/26/2016

Supplementary Table S2.2: Information on sample sites. Additional data from these wells can be found in Gannon et al. (2018).

Sample	^{4}He (x10^{-14})	±	^{20}Ne (x10^{-15})	±	^{36}Ar (x10^{-13})	±	^{84}Kr (x10^{-14})	±	^{132}Xe (x10^{-14})	±	^{20}Ne/^{36}Ar	±
Concentration in water phase (mol/cm^3)												
ASW	20		7800		510		200		14		0.15	
F1	22	1	4.9	0.2	0.46	0.02	1.7	0.1	0.85	0.1	0.11	0.01
F2	4.0	0.2	0.19	0.01	0.36	0.02	0.20	0.01	0.25	0.01	0.053	0.004
F3	14	1	5.6	0.3	0.38	0.02	0.65	0.03	0.27	0.02	0.15	0.01
F4	70	3	7.7	0.4	0.81	0.04	1.9	0.1	1.1	0.1	0.095	0.01
F5	1.4	0.1	0.22	0.01	0.077	0.004	0.42	0.02	0.32	0.02	0.029	0.002
F6	41	2	25	1	3.8	0.2	2.8	0.1	0.55	0.03	0.065	0.005
Concentration in gas phase (mol/cm^3)												
F1	55000	2000	11000	1000	380	20	790	40	250	20	0.30	0.02
F2	10000	0	420	20	27	1	82	4	61	4	0.16	0.01
F3	36000	1000	13000	1000	320	20	310	20	780	10	0.40	0.03
F4	180000	10000	17000	1000	660	30	890	40	310	20	0.27	0.02
F5	3500	100	510	30	63	3	200	10	90	5	0.08	0.006
F6	100000	0	57000	3000	3400	200	1500	100	180	10	0.17	0.01
Concentration in oil phase (mol/cm^3)												
F1	38	2	6.4	0.3	2.7	0.1	14	1	12	1	0.024	0.002
F2	6.3	0.3	0.22	0.01	0.19	0.01	1.6	0.1	3.0	0.2	0.012	0.001
F3	25	1	7.4	0.4	2.3	0.1	5.6	0.3	3.7	0.2	0.033	0.002
F4	120	4.9	10	0	4.7	0.2	16	1	15	1	0.021	0.002
F5	2.5	0.1	0.30	0.01	0.45	0	3.6	0.2	4.3	0.3	0.0065	0.0005
F6	75	3	35	2	25	1	26	1	7.8	0.5	0.014	0.001

Supplementary Table S2.3: Calculated concentration of noble gas isotopes (mol/cm^3) and ^{20}Ne/^{36}Ar values in each phase at the wellhead. Samples are from the Fruitvale Oil Field (under production conditions). If a given phase was not present within the sample taken, the concentrations in that phase were calculated assuming that equilibrium had been reached. Errors are given as one standard deviation. Recharge conditions were 15°C, 0M, 123m elevation. The original measured concentrations in cm^3/g (fluid) at standard temperature and pressure were reported in Gannon et al. (2018).

S2.3. Supplementary information

S2.3.1. Analytical methods for produced fluid analysis

S.2.3.1.1. Gas purification system

After noble gases are extracted from the fluid/multiphase sample and transferred into the sample transfer vessel (section 2.2), it is attached to the existing gas purification system, which consists of volumes C-I (Figure 2.1). Volume C represents the sample inlet volume; gas inlet is either from the transfer vessel or from an air-standard tank. Volume D is a known volume (69.7±0.6 cm^3), fitted with a 1000 Torr capacitance manometer, at laboratory temperature (set at 17^{o}C and recorded every 15 minutes) enabling the gas pressure to be determined and allowing for the clean-up to be monitored. Volume E is an expansion volume. Volume F is the initial clean up volume, consisting of a finger of titanium (Ti) sponge held at 950°C. The second clean-up volume is volume G, where the system is interfaced with both a SAES GP-50 getter at 250°C and SAES NP-10 getter at room temperature. It is also interfaced, via a pipette, to a Hidden Analytical HAL-200 quadrupole mass spectrometer (QMS); the QMS is held at vacuum by a dedicated ion pump. Volume H is another expansion volume and Volume J represents the inlet volume onto the automated prep-system.

Initially, the gas purification system is pumped to a vacuum (with E2, E3, 1, 2 and 11 closed) of at least 4 x 10^{-6} mbar on the high vacuum side of the turbomolecular pump. Once vacuum is reached, all remaining valves are closed and the background pressure on the capacitance manometer is recorded. The sample is expanded into volume C and D by opening valves E2, 3, 5 and 6, and the initial pressure recorded. Valves 7 and 8 are opened to establish water vapour flow and sample gas transfer back through the capillary and into the hot titanium. After 30 minutes the 'transferred' gas pressure is recorded and E2 is closed. The sample is exposed to titanium sponge held at 950 °C for 10 minutes to chemically remove any hydrocarbons, water vapour and reactive gases (Stout and Gibbons, 1955). The titanium sponge is then cooled to room temperature for 10 minutes, allowing the removal of hydrogen (Stout and Gibbons, 1955). Valves 9, 11, 12 and 13 are then opened, exposing the sample to the SAES getters for further gas clean-up for 10 minutes. The hot getter is designed to remove H_2, H_2O, CO, CO_2 and CH_4, and the cold to remove H_2, H_2O, CO, CO_2, N_2 and

O_2 (SAES Getters, 1986). The gas pressure is monitored to ensure the sample has successfully been purified and the pressure returns to background. A small aliquot of gas is transferred into the QMS by closing valve 13 and opening valve 14. The aliquot is analysed in the QMS to estimate purified noble gas concentrations prior to inlet to the automated preparatory line and the data is used to make volumetric splits appropriate for inlet into the noble gas mass spectrometers.

S.2.3.1.2. Automated preparatory system

The automated preparatory system is controlled by the Thermo Qtegra software version 1.6.1221.34. It consists of two volumes, J and K (Figure 2.1). Volume J interfaces the stainless-steel cryogenic trap and the charcoal cryogenic trap, as well as containing an ion gauge to measure pressure. Volume K consists of two SAES NP-10 getters, one of which is set to operate (heated), the volume is also interfaced with both the mass spectrometers, a turbo pump, standards tanks (for both Ar and internal air standard) and a separate extraction system beyond P12. At the start of a sample analysis, the system is held at vacuum with all valves closed.

The gas is expanded into Volume J and the Ar, Kr, Xe are frozen down onto a nude stainless-steel cryogenic trap held at 15K for 10 minutes; the He and Ne are then expanded into volume K and frozen onto the 10K charcoal trap (by opening P1 and P2). After 10 minutes, valve 17 on the gas purification system is closed and the 10K charcoal trap is heated to 34K to release the He. The He is expanded into volume L (opening P4) then inlet into the Helix SFT (opening P6 for 30s for equilibration). Any remaining He is removed and the temperature of the 10K trap was then raised further to 90K to release the Ne. This is inlet to the ARGUS VI. Once the Ne analysis is complete, the volumes are pumped and the 24K stainless steel trap is heated to 200K and an aliquot of Ar is inlet to the ARGUS VI. The trap temperature is dropped to 50K and valves P1-P4 closed, to isolate residual Kr and Xe fractions before the remaining Ar is removed out of volume K. The Kr and Xe fractions are then separated from any Ar remaining on the steel cryogenic trap, by three sequential heating and cooling cycles, where volume K is pumped by the turbo pump and the stainless-steel trap heated to 70K, (i.e., pump, warm to 70K, cool to 52K, pump). After the third cycle, Kr and Xe fractions are simultaneously let into the Argus VI for analysis.

S.2.3.1.3. Analytical protocol

The samples are analysed for noble gas concentrations and isotopes using the Helix SFT and Argus IV mass spectrometers, which are interfaced by an automated preparatory system. The Helix SFT is used for helium (^{3}He, ^{4}He) analysis, while the Argus VI is used to measure neon (^{20}Ne, ^{21}Ne, ^{22}Ne), argon (^{36}Ar, ^{38}Ar, ^{39}Ar, ^{40}Ar), krypton (^{78}Kr, ^{80}Kr, ^{82}Kr, ^{83}Kr, ^{84}Kr, ^{86}Kr) and xenon (^{124}Xe, ^{126}Xe, ^{129}Xe, ^{130}Xe, ^{131}Xe, ^{132}Xe, ^{134}Xe, ^{136}Xe). Immediately after the gas is inlet into the mass spectrometer, they are scanned and peak centred for all the desired isotopes using a combination of a multi-collection and a peak jumping protocols. Helium data is collected with 100 collection cycles, and the remaining elements using 30 collection cycles. All isotopes are collected using a 4.19s integration time. Signals are calculated by using either exponential or linear regression lines back to time zero (time of inlet) depending on the fit of data to get the smallest statistical errors.

S2.3.2. Standards, blanks and corrections

It is critical to characterise the standards, blanks and required corrections when making noble gas measurements in order to ensure data reliability. We describe the methods and results for analysing standards, and the data corrections identified.

S2.3.2.1. Internal air standards

Internal air standards are run prior to processing unknown samples, and daily following both sample and ASW analysis. An air tank (pressure: 1010 mBar, temperature: 14 °C and humidity: 71%*)*, on the automated preparatory system (Figure 2.1), releases a known aliquot (between valves P8 and P9) of standard gas. This aliquot is gettered on two SAES NP-10 getters (one of which is set to operate) on the automated preparatory system and is then prepared and measured the same way as a sample (with the exception of He, which is not initially frozen down) on the automated preparatory system (see sections S2.3.1.2, S2.3.1.3.). The internal air standards are used to monitor and correct for changes in the machine performance, and account for any changes in machine sensitivity between analyses. Over a period of a week, the internal air standards variations are stable at 0.33% for ^{4}He, 0.64% ^{20}Ne, 0.66% ^{40}Ar, 1.2% ^{84}Kr and 0.92% for ^{132}Xe.

S2.3.2.2. Blank contribution and corrections

Due to the unknown and variable composition of produced waters, it is important to have low blank levels to ensure there is no significant contribution from residual or background gases. Three different blanks (preparatory system blank, procedural blanks and full system blank) are run during analysis to ensure the system was running with low blank contributions.

Preparatory system blanks are run daily on the automated preparatory system in the same way as the internal air standard, with the only difference being no air was released from the tank. Preparatory system blanks made up less than 0.05 % of the ASW signals. Procedural blanks involve following the protocols for both the gas purification system and automated preparatory system. These are run prior to first sample analysis and subsequently, once a week during sample analyses. They are used to ensure the systems (e.g., it is noted that the SAES NP-10 and GP-50 getters are a particular source of background gas that can affect blank levels) are sufficiently clean between samples. A maximum blank contribution to samples of less than 3% is required for the key indicator isotopes (^{4}He, ^{20}Ne, ^{36}Ar, ^{40}Ar, ^{82}Kr, ^{84}Kr, ^{86}Kr, ^{130}Xe, ^{132}Xe, ^{136}Xe). A 3% limit was chosen to be beneath the level of uncertainty associated with the ASWs. If the blanks have a higher signal than desired, the analysis is halted and the systems is baked and pumped on, in order to lower the backgrounds. Additional blanks are run until a desired level is reached. Full system blanks follow sample inlet and processing protocols, and also include the extraction system and an empty copper tube (only clamped at one side) attached to the system and pumped to vacuum. These experiments yield very similar results to the procedural blanks and therefore only procedural blanks are analysed regularly, as the slightly amended method of extraction could result in errors not seen within the samples.

S.2.3.2.3. $^{40}Ar^{++}$ and $^{44}CO_2{}^{++}$ corrections

Due to isobaric interferences within the mass spectrometer, both ^{20}Ne and ^{22}Ne signals must be corrected for contributions from $^{40}Ar^{++}$ and $^{44}CO_2{}^{++}$ respectively. The proportion of doubly charged ^{40}Ar was determined by inletting clean Ar gas and monitoring both $^{40}Ar^{+}$ and $^{40}Ar^{++}$ peaks (e.g., Ballentine et al., 1991). The size of the doubly-charged peak was calculated to be consistently

11.3% of the $^{40}Ar^{++}$. Argon background at mass 40 was then monitored during Ne isotope measurement to allow correction for the doubly-charged Ar contribution. The $^{44}CO_2^{++}$ is negligible compared to ^{22}Ne (<1%) and thus, no $^{44}CO_2^{++}$ correction was applied.

S2.3.3. Geological and production history Fruitvale

Fruitvale Oil Field is located on the Bakersfield arch, a westerly dipping faulted homocline the central part of which exhibits pronounced flattening (Hluza, 1965). The important formations for oil production and produced water disposal, in order of increasing depth are the Kern River Formation (Pleistocene), Etchegoin Formation (Pliocene), Chanac Formation (Pliocene-Miocene) and the Santa Margarita Sandstone Formation (Miocene) (Supplementary Figure S2.2.; Hluza, 1965, DOGGR, 2018). The Etchegoin and Santa Margarita Formations were both deposited under marine environments whilst the Chanac Formation was deposited in a fluvial environment and consist of siliciclastic deposits (Preston, 1931, Hluza, 1965). The oil is thought to have originated from the Monterey Formation to the west (Lillis and Magoon, 2007). Since 1929, oil has been mainly produced from the westerly dipping Chanac Formation between 960- 1350 m (DOGGR, 1998). This formation is made up of the Mason Parker, Martin and Kernco reservoirs (Hluza, 1965). These represent non-marine discontinuous sequences of fan deposits and the oil reservoirs are bound to the east by the Fairhaven normal fault (Hluza, 1965). There is also limited production from the basal Miocene Etchegoin Formation from the discontinuous Fairhaven sands, which formed in an estuarine depositional system. Samples for this study were taken from the central and eastern zones of the field, from wells producing in the Etchegoin, Chanac and Santa Margarita formations.

Enhanced oil recovery in Fruitvale began in the 1960's. The field has undergone both water flooding (since 1962) and cyclic steam injection (since 1964) (DOGGR, 1998). Between 1977 and 2018 over 87×10^6 m^3 of water has been injected for water and steam flooding of the reservoirs as well as produced water disposal (DOGGR, 2018).

Acknowledgments, Samples, and Data

This work was supported by a Natural Environment Research Council studentship to R.L.Tyne (Grant ref. NE/L002612/1) and the USGS (Grant ref. 15-080-250), as part of the California State Water Resource Control Board's, Oil and Gas Regional Groundwater Monitoring Program (RMP). Data can be accessed in Tables 2.1, 2.2, S2.3 and in the data release from Gannon et al. (2018). We thank the owners and operators at the Fruitvale Oil Field for access to wells. We thank Stuart Gilfillan and an anonymous reviewer for their constructive reviews as well as Marie Edmonds for editorial handling. We also thank Matt Landon and Myles Moore from the USGS who provided helpful comments on an earlier version of the manuscript.

Authorship Statement

I hereby give permission to Rebecca L Tyne to use our joint work as contribution towards her DPhil thesis to be submitted for examination at the University of Oxford.

I confirm that to the best of my knowledge, the author contribution statement below is accurate and Rebecca L Tyne's contribution towards the work is greater than that of any other co-author. Chapter author contribution statement:

The project was conceived by RLT, PHB, JTK and CJB. RLT managed the project and prepared the first draft of the manuscript. RLT, PHB, DJH, AGH and CJB developed the laboratory protocols. RLT, PHB and JTK collected the samples. RLT performed the noble gas isotopic analysis. MJS collated well information. Noble gas reconstructions were developed by RLT, PHB, DJB and CJB. All authors contributed to the final manuscript.

Chris J. Ballentine



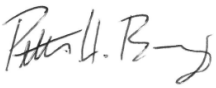
Date: 13/4/21

Justin T. Kulongoski



Date: 7/4/21

Peter H. Barry



Date: 6-4-2021

Michael J. Stephens

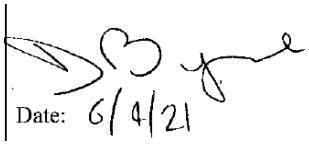


Date: 7/4/2021

Darren J. Hillegonds



David J. Byrne



Andrew G. Hunt

X

Andrew G Hunt, PhD
US Geological Survey

References

Ballentine, C.J., O'Nions, R.K., Oxburgh, E.R., Horvath, F., Deak, J. (1991). Rare gas constraints on hydrocarbon accumulation , crustal degassing and groundwater flow in the Pannonian Basin. *Earth and Planetary Science Letters* **105**, 229–246.

Ballentine, C.J., O'Nions, R.K., Coleman, M.L. (1996). A Magnus opus: Helium, neon, and argon isotopes in a North Sea oilfield. *Geochimica et Cosmochimica Acta*. **60**, 831–848.

Ballentine, C.J., Burgess, R., Marty, B. (2002). Tracing Fluid Origin, Transport and Interaction in the Crust, In: *Noble Gases in Geochemistry and Cosmochemistry.(*Eds: D. Porcelli, C.J. Ballentine,, R. Wieler) Reviews in Mineralogy and Geochemistry **47**. Geochemical Society, Mineralogical Society of America, Chapter 13, 539–614.

Barry, P.H., Lawson, M., Meurer, W.P., Warr, O., Mabry, J.C., Byrne, D.J., Ballentine, C.J. (2016). Noble gas solubility models of hydrocarbon charge mechanism in the Sleipner Vest gas field. *Geochimica et Cosmochimica Acta* **194**, 291–309.

Barry, P.H., Lawson, M., Meurer, W.P., Danabalan, D., Byrne, D.J., Mabry, J.C., Ballentine, C.J. (2017). Determining fluid migration and isolation times in multiphase crustal domains using noble gases. *Geology* **45**(9), 775-778.

Barry, P.H., Kulongoski, J.T., Landon, M.K., Tyne, R.L., Gillespie, J., Stephens, M., Byrne, D.J., Ballentine, C.J. (2018a). Tracing enhanced oil recovery signatures in casing gases using noble gases. *Earth and Planetary Science Letters* **496**, 57-67.

Barry, P.H., Lawson, M., Meurer, W.P., Cheng, A., Ballentine, C.J. (2018b). Noble gases in deep-water oils of the U.S. Gulf of Mexico. *Geochemistry Geophysics Geosystems* **19**.

Beyerle, U., Aeschbach-Hertig, W., Imboden, D.M., Baur, H., Graf, T., Kipfer, R. (2000). A mass spectrometric system for the analysis of noble gases and tritium from water samples. *Environmental Science and Technology*. **34**(10) 2042-2050.

Bosch, A., Mazor, E. (1988). Natural gas association with water and oil as depicted by atmospheric noble gases: case studies from the southeastern Mediterranean Coastal Plain. *Earth and Planetary Science Letters* **87**, 338–346.

Burnard, P. (2013). *The Noble Gases as Geochemical Tracers*. (Ed. P. Burnard). Advances in Isotope Geochemistry. Springer, Berlin, Heidelberg.

Byrne, D.J., Barry, P.H., Lawson, M., Ballentine, C.J. (2018a). Noble gases in conventional and unconventional petroleum systems. *Geological Society London Special Publ*ication **468**(1), 127–149.

Byrne, D.J., Barry, P.H., Lawson, M., Ballentine, C.J. (2018b). Determining gas expulsion vs retention during hydrocarbon generation in the Eagle Ford Shale using noble gases. *Geochimica et Cosmochimica Acta* **241**, 240-251.

Crovetto, R., Fernández-Prini, R., Japas, M. L. (1982). Solubilities of inert gases and methane in H_2O and in D_2O in the temperature range of 300 to 600 K. *Journal of Chemical Physics*. **76**, 1077-1086.

Darrah, T.H., Vengosh, A., Jackson, R.B., Warner, N.R., Poreda, R.J. (2014). Noble gases identify the mechanisms of fugitive gas contamination in drinking-water wells overlying the Marcellus and Barnett Shales. *Proceedings of the National Academy of Sciences* **111**, 14076–14081.

Darrah, T.H., Jackson, R.B., Vengosh, A., Warner, N.R., Whyte, C.J., Walsh, T.B., Kondash, A.J., Poreda, R.J. (2015). The evolution of Devonian hydrocarbon gases in shallow aquifers of the northern Appalachian Basin: Insights from integrating noble gas and hydrocarbon geochemistry. *Geochimica et Cosmochimica Acta* **170**, 321–355.

Division of Oil Gas and Geothermal Resources (DOGGR), (1998). California Oil and Gas Fields: Volume 1- Central California.TR11. California Department of Conservation, Sacramento, CA.

Division of Oil Gas and Geothermal Resources (DOGGR), (2017). GIS Mapping, DOGGR, Sacramento, CA. http://www.conservation.ca.gov/dog/maps/Pages/GISMapping2.aspx [Accessed online May 2017].

Division of Oil Gas and Geothermal Resources (DOGGR), (2018). Oil & Gas Online Data. Division of Oil, Gas, and Geothermal Resources.

http://www.conservation.ca.gov/dog/Online_Data/Pages/Index.aspx [Accessed October 23, 2018].

Fernández-prini, R., Alvarez, J.L., Harvey, A.H., Ferna, R. (2003). Henry's Constants and Vapor – Liquid Distribution Constants for Gaseous Solutes in H_2O and D_2O at High Temperatures Henry 's Constants and Vapor. *Journal of Physical and Chemical Reference Data* **32** , 903-916.

Gannon, R.S., Saraceno, J.F., Kulongoski, J.T., Teunis, J.A., Barry, P.H., Tyne, R.L., Kraus, T., Hansen, A.H., Qi, S.L. (2018). Produced Water Chemistry Data for the Lost Hills, Fruitvale, and North and South Belridge Study Areas, Southern San Joaquin Valley, California. 2016–17: U.S. Geological Survey Data Release.

Gilfillan, S.M. V., Ballentine, C.J., Holland, G., Blagburn, D., Lollar, B.S., Stevens, S., Schoell, M., Cassidy, M. (2008). The noble gas geochemsitry of natural CO_2 gas reservoirs from the Colorado Plateau and Rocky Mountain provinces, USA. *Geochimica et Cosmochimica Acta* **72**, 1174-1198..

Gilfillan, S.M.V., Haszeldine, R.S., Stuart, F.M., Gyore, D., Kilgallon, R., Wilkinson, M. (2014). The application of noble gases and carbon stable isotopes in tracing the fate, migration and storage of CO_2. *Energy Procedia*. **63**, 4123-4133.

Gilfillan, S.M. V., Sherk, G.W., Poreda, R.J., Haszeldine, R.S. (2017). Using noble gas fingerprints at the Kerr Farm to assess CO_2 leakage allegations linked to the Weyburn-Midale CO_2 monitoring and storage project. *International Journal of Greenhouse Gas Control* **63**, 215-225.

Györe, D., Stuart, F.M., Gilfillan, S.M.V., Waldron, S. (2015). Tracing injected CO_2 in the cranfield enhance oil recovery field (MS, USA) using He, Ne and Ar isotopes. *International Journal of Greenhouse Gas Control* **42**, 554-561.

Györe, D., Gilfillan, S.M.V., Stuart, F.M. (2017). Tracking the interaction between injected CO_2 and reservoir fluids using noble gas isotopes in an analogue of large scale carbon cpature and storage. *Applied Geochemistry* **78**, 116-128.

Harkness, J.S., Darrah, T.H., Warner, N.R., Whyte, C.J., Moore, M.T., Millot, R., Kloppmann, W., Jackson, R.B., Vengosh, A. (2017). The geochemistry of naturally occurring methane and saline groundwater in an area of unconventional shale gas development. *Geochimica et Cosmochimica Acta* **208**, 302-334.

Hillegonds, D J., Matsumoto, T., Manfred, J., Han, LF., Klaus, P, Wassenaar, L., Pradeep, A. (2013). Calibration of Dissolved Noble Gas Mass Spectrometric Measurements by an Air-Water Equilibration System. *EGU General Assembly* 2013, 7-12 April, Vienna, Austria.

Hluza, A.G., 1965. *Summary of operations, California oil fields.* Open File Report. Volume 51. California Department of Conservation, Sacramento, Ca.

Holland, G., Gilfillan, S.M.V. (2013). Application of noble gases to the viability of CO_2 storage. In: *The Noble Gases as Geochemical Tracers*. (Ed. P. Burnard). Advances in Isotope Geochemistry. Springer, Berlin, Heidelberg. 177-223.

Hunt, A.G. (2015). Noble Gas Laboratory's standard operating procedures for the measurement of dissolved gas in water samples: *U.S. Geological Survey Techniques and Methods* 5- A11. U.S. Geological Survey, Reston, Virginia

Kharaka, Y.K., Specht, D.J. (1988). The solubility of noble gases in crude oil at 25-100 ºC. *Applied Geochemistry* **3**, 137–144.

Lillis, P.G., Magoon, L.B. (2007). Petroleum Systems of the San Joaquin Basin Province—Geochemical Characteristics of Oil Types. In: *Petroleum Systems and Geological Assessment of oil and gas in the san Joaquin Basin Province, California.*(Ed. Scheirer A.H.) USGS professional paper 1713, Sacramento, Ca. Chapter 9.

Long, J.C.S., Feinstein, L.C., Dirkholzer, J., Jordan, P., Houseworth, J., Dobson, P.E., Herberger, M., Gautier, D.L. (2015). Historical and current application of well stimulation technology in California. In: *An Independent Scientific Assessment of Well Stimulation in California*, Volume 1. California Council on Science and Technology, Sacramento, Ca. Chapter 3.

McMahon, P. B., Kulongoski, J.T., Vengosh, A., Cozzarelli, I.M., Landon, M.K., Kharaka, Y.K., Gillespie, J.M., Davis, T.A. (2018). Regional Patterns in the geochemistry of oil-field water, southern San Joaquin Valley, California, USA. *Applied Geochemistry*. 98, 127-140.

Pinti, D.L., Marty, B. (1995). Noble gases in crude oils from the Paris Basin , France : Implications for the origin of fluids and constraints on oil-water-gas interactions. *Geochimica et Cosmochimica Acta* **59**, 3389–3404.

Preston, H.M. (1931). *Summary of operations, Calinforia oil field*, Vol 16. California Department of naturla resources. Division of oil and gas.

Prinzhofer, A. (2013). Noble gases in oil and gas accumulations. In: *The Noble Gases as Geochemical Tracers*. (Ed. P. Burnard). Advances in Isotope Geochemistry. Springer, Berlin, Heidelberg. 225–247

SAES Getters (1986). *Operating Instructions for SORB-AC cartridge pumps*. SAES Getters Group manufacturing company. Milan, Italy.

Scheirer, A.H., Magoon, L.B. (2007). Age, distribution, and stratigraphic relationship of rock units in the San Joaquin Basin Province, California. In: *Petroleum Systems and Geologic Assessment of Oil and Gas in the San Joaquin Basin Province, California.* .(Ed. Scheirer A.H.) U.S. Geological Survey Proffessional Paper 1713, Chapter 5.

Smith, S.P., Kennedy, B.M. (1983). The solubility of noble gases in water and in NaCl brine. *Geochimica et Cosmochimica Acta* **47**, 503–515.

Stephens, M.J., Shimabukuro, D.H., Gillespie, J.M., and Chang, W. (2018). Groundwater salinity mapping using geophysical log analysis within the Fruitvale and Rosedale Ranch oil fields: Kern County, California, USA. *Hydrogeology Journal*. **27**(2), 731-746.

Stout, V.L., Gibbons, M.D. (1955). Gettering of gas by titanium. *Journal of Applied Physics* **26**, 1488.

U.S. Geological Survey (2019). California Oil, Gas, and Groundwater (COGG) Program: at: https://ca.water.usgs.gov/projects/oil-gas-groundwater/index.html (accessed February, 2019).

Vengosh, A., Jackson, R.B., Warner, N., Darrah, T.H., Kondash, A. (2014). A Critical Review of the Risks to Water Resources from Shale Gas Development and Hydraulic Fracturing in the United States. *Environmental Science Technology* **16**, 6838.

Wagner, W., Pruss, A. (1992). International Equations for the Saturation Properties of Ordinary Water Substance . Revised According to the International Temperature Scale of 1990 . Addendum to J . International Equations for the Saturation Properties of Ordinary Water Substance . *Journal of Physical and Chemical Reference Data.* **893**, 1–6.

Weiss , R.F. (1968). Piggyback sampler for dissolved gas studies on sealed water samples. *Deep-Sea Research and Oceanographic Abstracts* **15**(6), 695-699.

Wright M. T., McMahon P. B., Landon M. K. and Kulongoski J. T. (2019) Groundwater quality of a public supply aquifer in proximity to oil development, Fruitvale oil field, Bakersfield, California. *Applied Geochemistry* **106**, 82–95.

Zhou Z., Ballentine C. J., Kipfer R., Schoell M. and Thibodeaux S. (2005) Noble gas tracing of groundwater/coalbed methane interaction in the San Juan Basin, USA. *Geochimica et Cosmochimica Acta* **69**, 5413–5428.

Chapter 3

Investigating the effect of enhanced oil recovery on the noble gas signature of casing gases and produced waters from selected California oil fields

R.L. Tyne[1], P.H. Barry[1,2], R. Karolytė[1], D.J. Byrne[1,4], J.T. Kulongoski[3], D.J. Hillegonds[1], C.J. Ballentine[1]

[1]Dept. of Earth Sci., University of Oxford, Oxford, UK. [2]Dept. of Marine Chem. and Geochem., Woods Hole Oceanographic Institution, Woods Hole, MA, USA. [3] USGS, California Water Science Center, San Diego, CA, USA. [4] CRPG-CNRS, Université de Lorraine, Nancy, France.

Contents

Abstract 80
3.1 Introduction 81
3.2 Geological context 83
3.3 Methods 84
3.3.1 Sample collection 84
3.3.2 Analytical techniques 88
3.3.3 Calculating noble gas concentrations within produced fluids 88
3.4 Results 90
3.4.1 Casing gas results 90
3.4.2 Produced fluid results 98
3.5 Discussions 99
3.5.1 Comparison of casing gas and produced fluids at the wellhead 99
3.5.2 Reconstructing noble gas concentrations in the reservoir oil 100
3.5.3 Determining pre-development reservoir characteristics 102
3.5.4 Assessing the effects of injection 106
3.6 Conclusions 112
S3.1 Supplementary figures 114
S3.2 Supplementary tables 119
S3.3 Supplementary information 120
Acknowledgments, samples, and data 125
Authorship statement 126
References 127

Abstract

In regions where water resources are scarce and in high demand, it is important to safeguard against contamination of groundwater aquifers by oil-field fluids (water, gas, oil). In this context, the geochemical characterisation of these fluids is critical, so that anthropogenic contaminants can be readily identified. The first step is characterising pre-development geochemical fluid signatures (i.e., those unmodified by hydrocarbon resource development). Once this is established, how these signals may have been perturbed by resource production, particularly in the context of enhanced oil recovery (EOR) techniques can be understood. Here, we present noble gas isotope data in fluids produced from oil wells in several water-stressed regions in California, USA, where EOR is prevalent. In oil-field systems, only casing gases are typically collected and measured for their noble gas compositions, even when oil and/or water phases are present, due to the relative ease of gas analysis. However, this approach relies on a number of assumptions in order to reconstruct the multiphase subsurface compositions. Here, we adopt a different approach and measure noble gases in both casing gas and produced fluid (oil-water-gas mixtures) samples from the Lost Hills, Fruitvale, Belridge (San Joaquin Basin, SJB) and Orcutt (Santa Maria Basin) oil fields, in order to fully characterise the distribution of noble gases within a multiphase hydrocarbon system. We find that measured concentrations in the casing gases agree well with those in the gas phase in the produced fluids and thus the two sample types can be used essentially interchangeably.

EOR signatures can readily be identified by their distinct air-derived noble gas elemental ratios (e.g., $^{20}Ne/^{36}Ar$), which are elevated compared to pre-development oil-field fluids, and conspicuously trend towards air values with respect to elemental ratios and overall concentrations. We reconstruct reservoir $^{20}Ne/^{36}Ar$ values using both casing gas and produced fluids and show that noble gas ratios in the reservoir are strongly correlated (r^2= 0.88-0.98) to the amount of water injected within ~500m of a well. We suggest that the $^{20}Ne/^{36}Ar$ increase resulting from injection is sensitive to the volume of fluid interacting with the injectate, the effective water-to-oil ratio, and the composition of the injectate. Defining both the pre-development and injection-modified hydrocarbon reservoir compositions are crucial for distinguishing the sources of hydrocarbons

observed in proximal groundwaters, and for quantifying the transport mechanisms controlling this occurrence.

3.1. Introduction

The environmental effects of oil production, enhanced oil recovery (EOR) techniques and hydraulic fracturing need to be established in order to safeguard nearby water resources. EOR is the injection of surface fluids (e.g., water, steam, CO_2) into a reservoir in order to increase oil production by means of displacing oil or lowering its viscosity. This is similar to, but distinct from, hydraulic fracturing - the injection of water, chemicals and sand to proliferate fractures in order to promote hydrocarbon production. There is growing concern about the effects of hydrocarbon production on overlying aquifers, which are particularly valuable resources in semi-arid regions such as California (e.g., EPA, 2015). The detection and quantification of oil-field fluids (oil, gas, produced fluids) within groundwater requires an understanding of the geochemical composition of the pre-development hydrocarbon reservoir (unmodified by hydrocarbon production) and the extent to which it may have been perturbed during production.

Noble gases are powerful conservative geochemical tracers of subsurface fluids that can be used to quantify volumes of water, gas and oil contributing to a particular multiphase fluid system (e.g., Bosch and Mazor, 1988; Ballentine et al., 1991, 1996, 2002). Once incorporated into subsurface fluids, noble gases are only fractionated by physical processes, such as phase partitioning and diffusion. Terrestrial noble gas reservoirs (atmosphere, crust and mantle) have distinct isotopic compositions, which allow fluids from each reservoir to be readily differentiated. Hydrocarbon phases are initially devoid of all atmospheric noble gases and gain their unique signatures by interactions with air-saturated waters (ASW), which inherit their geochemical signature via atmospheric equilibration at recharge (e.g., Ballentine and Hall, 1999; Aeschbach-Hertig et al., 1999; Kipfer et al., 2002). This subsequent redistribution – from water to oil – is solubility controlled and is a function of the thermodynamic conditions and the relative volumes involved. Noble gases have been successfully applied as tracers in hydrocarbon systems, and have provided essential information in developing our understanding of such systems (Zaikowski and Spangler,

1990; Ballentine et al., 1991; Pinti and Marty, 1995; Ballentine et al., 1996; Torgersen and Kennedy, 1999; Zhou et al., 2005; Gilfillan et al., 2009; Hunt et al., 2012; Darrah et al., 2015; Barry et al., 2016; 2017; 2018a; 2018b; Byrne et al., 2018, 2020). Furthermore, noble gases have also been shown to be useful tracers of thermogenic hydrocarbon gases in shallow aquifers (Darrah et al., 2014, 2015; Wen et al., 2017; Harkness et al., 2017) and for understanding the effects of EOR in hydrocarbon reservoirs (LaForce et al., 2014; Györe et al., 2015, 2017; Barry et al., 2018a). In hydrocarbon systems that have been perturbed by anthropogenic processes such as EOR and hydraulic fracturing, defining end-members for evaluating potential mixing with groundwater requires the determination of the pre-development reservoir noble gas compositions and how these signatures have evolved with production, as well as with the secondary effects of EOR.

However, there have been limited noble gas studies in oil dominated systems (Pinti and Marty, 1995; Ballentine et al., 1996; Torgersen and Kennedy, 1999; Györe et al., 2017; Barry et al., 2018a; 2018b) and these have mostly focused on casing gases that exsolve during production. Subsequent phase and reservoir reconstructions have been made using gas solubility in oil and assuming 100% of the noble gases have partitioned to the gas phase. However, the measured distribution of noble gases in the different phases from the same well has not been systemically explored and thus the biases involved in the assumptions for phase and reservoir reconstructions have never been comprehensively investigated. In order to validate these assumptions and methods, both the casing gases and produced fluids (oil-water-gas mixtures) must be fully characterised. The development of an extraction and purification method, and more precise analyses of noble gases allow for the characterisation of all noble gas concentrations and isotope ratios in these multi-phase samples, such that produced fluids can now be directly analysed (Chapter 2, Tyne et al., 2019). As a result, for the first time we are able to investigate the distribution of noble gases between casing gases and the phases that constitute produced fluids (i.e., oil, water and gas), allowing for the validity of previous assumptions to be investigated.

Specifically, this work compares noble gas distributions in casing gas and produced fluid samples from the Fruitvale, Lost Hills, Belridge and Orcutt Oil Fields in California. Casing gas results from

the Lost Hills Oil Field were reported in Barry et al. (2018a) and produced fluids from Fruitvale Oil Field were reported in Chapter 2 (Tyne et al., 2019). These data are used to: 1) compare the noble gas distribution within the reservoir fluids for various samples types, 2) reconstruct reservoir noble gas signatures, 3) establish pre-development reservoir noble gas signatures, 4) establish the effect of EOR injection on the noble gas distribution and 5) determine the controlling processes across multiple oil fields. This will provide a characterisation of both the pre-development and current reservoir endmembers, which are critical for distinguishing and quantifying any hydrocarbon fluids that may be present in overlying aquifers. This work is part of the California State Water Resources Control Board (SWRCB) Oil and Gas Regional Monitoring Program (RMP) to evaluate potential pathways, natural or anthropogenic, between hydrocarbon-bearing formations and groundwater resources (Taylor et al., 2014; California State Water Resources Control Board, 2020).

3.2. Geological context

The Fruitvale, Lost Hills and Belridge oil fields are located in Kern Country, at the southern end of the San Joaquin Basin (SJB) in the south of the Central Valley of California. The Orcutt oil field is distinct from the other fields in this study, being located within the Santa Maria Basin in coastal Santa Barbara County (Figure 3.1). A summary of the samples' site characteristics in each field can be found in Tables 3.1 and 3.2 and description of the oil fields can be found in the supplementary information (S3.3.1). All of these fields have been extensively injected with water, and sometimes steam, for EOR over the course of many decades. The Lost Hills, Belridge, and Fruitvale oil fields have similarly had extensive injections for produced water disposal and pressure management. Although > 90% of hydraulic fracturing in California occurs in the Lost Hills and Belridge (North and South) oil fields, hydraulic fracturing accounted for <0.5% of total water volume injection during 2014-17 (McMahon et al., 2018). Hydraulic fracturing has also been allegedly tested in the Orcutt Oil Field (Kamori and Hauksson, 1992). Volumes of injection for EOR and produced water disposal are orders of magnitude larger than volumes of injection for hydraulic fracturing in these fields. No hydraulic fracturing is known to have occurred in the Fruitvale Oil Fields.

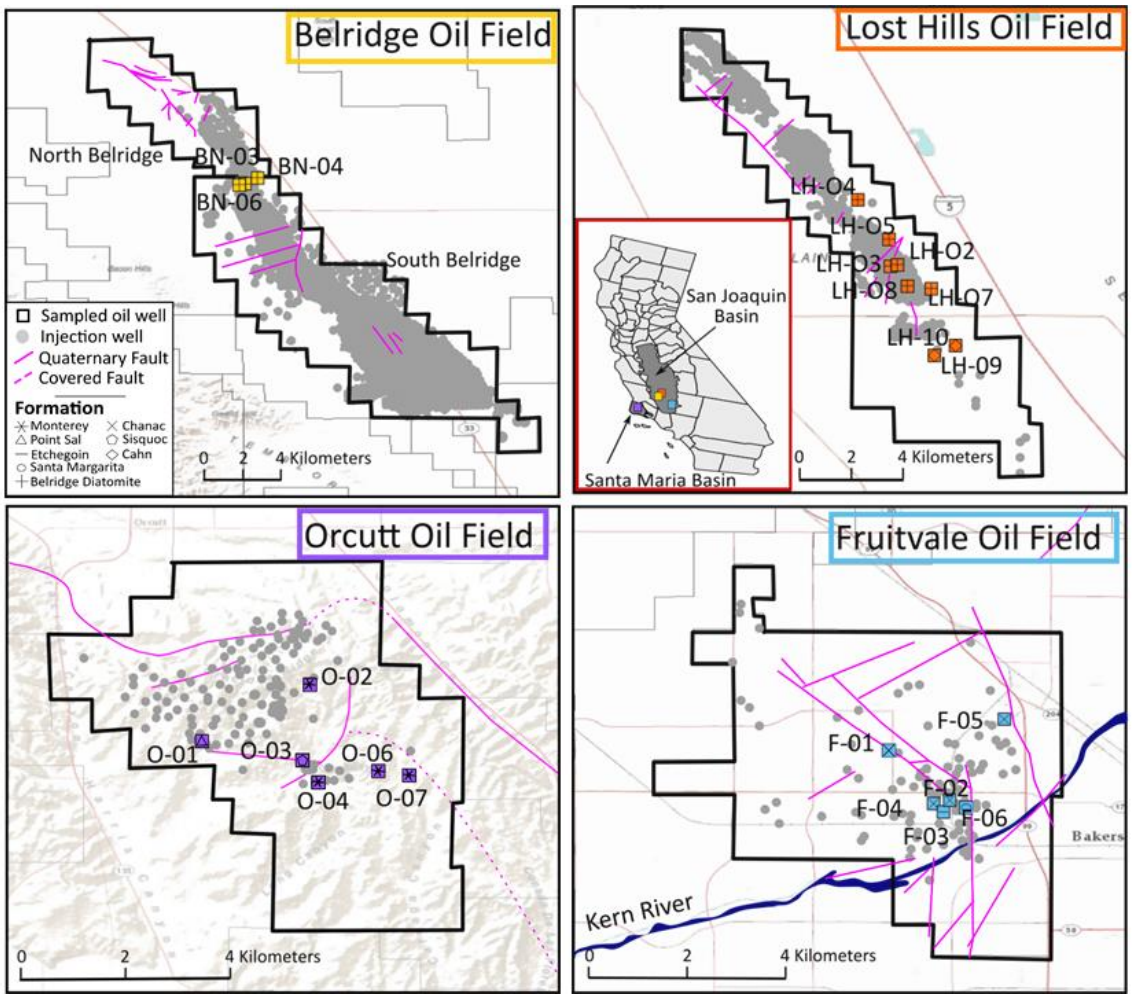


Figure 3.1: Location of study oil fields and sampling sites (coloured squares). Injection wells (grey circles) are those used for water flooding, water disposal, steam flooding, and water and cyclic steam injection (CalGEM, 2020a). Producing formation is indicted by a symbol for each well; these symbols are consistent throughout the manuscript. Oil field boundaries and quaternary and major inactive faults have been sourced from DOGGR (2017) and USGS (2019) respectively. Topography is from ESRI (2020).

3.1. Methods

3.3.1. Sample collection

During 2016, 11 casing gas and 12 produced fluid samples were collected from the Lost Hills, Fruitvale and Belridge oil fields. A further six pairs of casing gas and produced fluid samples were collected from the Orcutt Oil Field in 2018. All samples were collected as part of the RMP at wells that are close to EOR injection (within 500m) and at wells more than 500m from injection. Produced fluids are oil-water-gas mixtures taken directly from the well discharge points. Gases exsolve from

Sample	COGG ID	Site ID	Sample Type	Producing member (Reservoir)	Age
Fruitvale					
F1	4_FRUT_PW01	352336119043201	PF	Chanac	Pliocene-Miocene
F2	4_FRUT_PW02	352256119034201	PF	Chanac	Pliocene-Miocene
F3	4_FRUT_PW03	352246119034801	PF	Etchegoin	Pliocene
F4	4_FRUT_PW04	352253119035701	PF	Chanac	Pliocene-Miocene
F5	4_FRUT_PW05	352401119025901	PF	Chanac	Pliocene-Miocene
F6	4_FRUT_PW06	352250119033001	PF	Santa Margarita	Miocene
Lost Hills					
LH2	4_LOST_PW02	353703119432701	CG, PF	Diatomite	Miocene
LH3	4_LOST_PW03	353704119433501	CG, PF	Diatomite	Miocene
LH4	4_LOST_PW04	353838119442901	CG, PF	Diatomite	Miocene
LH5	4_LOST_PW05	353740119434001	CG, PF	Diatomite	Miocene
LH7	4_LOST_PW07	353622119425901	CG	Diatomite	Miocene
LH8	4_LOST_PW08	353628119431201	CG	Diatomite	Miocene
LH9	4_LOST_PW09	353502119420001	CG, PF	Cahn	Miocene
LH10	4_LOST_PW10	353447119423101	CG	Cahn	Miocene
Belridge					
BN3	4_BELN_PW03	353050119455701	CG	Diatomite	Miocene
BN4	4_BELN_PW04	353053119454601	CG	Diatomite	Miocene
BN6 (S)	4_BELN_PW06	353048119455901	CG	Diatomite	Miocene
Orcutt					
O1	3_ORCT_PW01	344910120251501	CG, PF	Point Sal	Miocene
O2	3_ORCT_PW02	344959120235101	CG, PF	Monterey	Miocene
O3	3_ORCT_PW03	344855120240101	CG, PF	Sisquoc	Pliocene-Miocene
O4	3_ORCT_PW04	344840120234901	CG, PF	Monterey	Miocene
O6	3_ORCT_PW06	344845120223701	CG, PF	Monterey	Miocene
O7	3_ORCT_PW07	344848120230101	CG, PF	Monterey	Miocene

Table 3.1: Sample type and site identification.

Sample	API	Measured volumes within sample tube			Injected volume within 500m^	Reservoir average		EOR types
		Oil (g)	Water (g)	Gas (cm^3)	m^3	WOR*	GOR*	
Fruitvale								
F1	18.5	12.9	0.0	0.5	3292010	0.5	11.19	Cyclic Steam (since 1964), water flooding (since 1962) and produced water disposal (DOGGR, 1998, 2018).
F2	18.5	12.4	0.0	0.8	9714280	0.5	11.19	
F3	18.5	12.3	0.5	0.5	3005000	2.3	11.19	
F4	18.5	12.9	0.0	0.4	6319980	0.5	1	
F5	18.5	12.9	0.0	0.4	0	0.5	11.19	
F6	16.7	12.7	0.0	0.7	3400770	2.2	4.63	
Lost Hills								
LH2	23.1	10.0	2.0	1.4	41511720	1.6	107.6	Combination of water flooding, steam flooding, CO2 injection and hydraulic fracturing since 1962 (Land, 1984)
LH3	23.1	12.1	0.0	0.1	46507300	1.6	107.6	
LH4	23.1	12.5	0.0	0.8	50670	0.5	107.6	
LH5	21.5	10.0	2.4	1.0	21505650	1.6	107.6	
LH7	23.1	0.0	0.1	13.2	32348780	1.6	107.6	
LH8	23.1				2511690	1.6	107.6	
LH9	23.1	5.2	0.5	7.5	0	4.2	650	
LH10	23.1				1205850	4.2	650	
Belridge								
BN3	27.2				36351580	5.5	625	Primarily water flooding (56% in South Belridge, 98% North Belridge), produced water disposal and well stimulation (McMahon et al., 2018).
BN4	27.2				22413710	5.5	625	
BN6 (S)	27.2				32763270	5.5	625	

Table 3.2: Well, fluid and enhance oil recovery (EOR) information for the sampled sites. Sampled oil wells API are sourced from CalGEM (2020). A 15% uncertainty is given to these values to reflect uncertainty with using average values. ^between 1977 and 2017. * WOR and GOR are the water to oil and gas to oil ratios respectively and the average WOR and GOR of the sampled wells for each formation within a field, as calculated from production logs (DOGGR, 2018).

Sample	API	Measured volumes within sample tube			Injected volume within 500m^	Reservoir average		EOR types
		Oil (g)	Water (g)	Gas (cm^3)	m^3	WOR*	GOR*	
Orcutt								
O1	22.9	9.0	0.0	4.3	98195116	43.8	650	
O2	22.9	13.1	0.0	0.4	0	2.9	6	
O3	23.9	0.0	6.2	6.4	1986664	1.8	170	Primarily Cyclic steam injection(since 2009) and water flooding
O4	21.4	7.6	0.6	5.1	16690172	0.2	15	
O6	21.4	0.5	0.0	12.7	0	0.2	15	
O7	21.4	13.5	0.3	0.1	3777560	0.2	15	

Table 3.2 continued.

subsurface fluids and travel up the well annulus during production and are known as casing gases. Sample types for each field can be found in Table 3.1.

Produced fluid samples were collected in 3/8" refrigeration-grade copper tubes with stainless steel clamps using methods previously described (Chapter 2, Tyne et al., 2019). The Cu tubes were connected to the wellhead sampling point using reinforced PTFE tubing and hose clamps. A 'T-connection' was fitted at the wellhead to ensure the tubing did not become over pressurised once the Cu tubes were sealed. Cu tubes were flushed with produced fluids prior to sampling. Casing gases were also collected in Cu tubes using standard sampling methods using a two-stage regulator attached to the well head which stepped the pressure down to 1-2 bars (Burnard, 2013). Cu tubes were flushed with casing gases for 10 minutes with the end submerged into water to prevent any backflow before being sealed with stainless steel clamps (Weiss, 1968).

3.3.2. Analytical techniques

Noble gas analyses were conducted in the Noble Laboratory at the University of Oxford, UK, using two noble gas mass spectrometers interfaced to a dedicated hydrocarbon extraction and purification line, as well as a dedicated offline fluid extraction system. Gases were initially extracted from the produced fluids using an offline double capillary method to quantitatively isolate noble gases into a transfer vessel, while effectively removing all water, oil, and less volatile hydrocarbons (Chapter 2, Tyne et al., 2019). Relative volumes of gas, water and oil, as well as the full tube volume, were then recorded. The extracted gases and casing gases were then purified of their hydrocarbons and other reactive gases and analysed on a Thermo Helix SFT and Thermo Argus IV. Full procedures can be found in Chapter 2 (Barry et al., 2016, 2018a; Tyne et al., 2019).

3.3.3. Calculating noble gas concentrations within produced fluids

In order to compare the noble gas concentrations in the multi-phase produced fluids and casing gases at the wellhead, the concentration of noble gas within each phase of the produced fluid need to be calculated from the measured total noble gas abundance . The abundance of noble gas *i* in the oil ($[i]_o$), gas ($[i]_g$) and water ($[i]_w$) can be calculated relative to each other at the time of sampling using their relative solubilities (parameterised by Henry's Constant for each element), production

temperatures, sampling salinity and oil density (Eq. 3.1 and 3.2). Production temperatures, sample salinity and oil density can be found in Gannon et al. (2018) and Seitz et al. (2021).

$$[i]_o = \frac{[i]_g \times \mathrm{V_o}}{\mathrm{K^i_{go}} \times \mathrm{V_g}} \quad \text{(Eq. 3.1)}$$

$$[i]_w = \frac{[i]_g \times \mathrm{V_w}}{\mathrm{K^i_{gw}} \times \mathrm{V_g}} \quad \text{(Eq. 3.2)}$$

V_o, V_g and V_w are the volumes of oil, gas, and water respectively that are measured in the sample tube. K^i_{gw} and K^i_{go} are the Henry's Constants for species *i* between gas and water and gas and oil respectively. K^i_{gw} and K^i_{go} are temperature, salinity and pressure dependent and can be calculated as in Crovetto et al. (1982), Kharaka and Specht (1983) and Fernández-Prini et al. (2003). Using the total abundance of noble gases measured within the produced fluid and the relative volumes of each phase at the wellhead, the concentration in each phase can be calculated (equations 3.3-3.5)(Chapter 2; Tyne et al., 2019).

$$\mathrm{C^i_g} = \frac{[\mathrm{i}]_m \times [i]_g \times 22400}{([i]_g + [i]_o + [i]_w) \times \mathrm{GOR} \times \mathrm{V}_o} \quad \text{(Eq. 3.3)}$$

$$\mathrm{C^i_o} = \frac{[\mathrm{i}]_m \times [i]_o}{([i]_g + [i]_o + [i]_w) \times \mathrm{V}_o} \quad \text{(Eq. 3.4)}$$

$$\mathrm{C^i_w} = \frac{[\mathrm{i}]_m \times [i]_w}{([i]_g + [i]_o + [i]_w) \times \mathrm{WOR} \times \mathrm{V}_o} \quad \text{(Eq. 3.5)}$$

Where C_g^i, C_o^i and C_w^i are the concentration in the gas (cm^3/cm^3), oil (mol/g) and water (mol/g) phase respectively in cm^3/cm^3. $[i]_m$ is the total abundance of noble gas species *i* measured in the sample. The variable nature of the produced fluid compositions at the wellhead means that the water-to-oil ratio (WOR) and gas-to-oil ratio (GOR) are not consistent during sampling and are not representative of the average GOR and WOR for production. Therefore, instead of using V_w and V_g to calculate the concentrations, the average time integrated GOR and WOR relative to V_o (Table 3.2) are used. If one phase is not present within the produced fluid collected, the concentration in the missing phase can be calculated based on phase equilibrium under wellhead conditions. The

calculated concentration in the gas phase can then be directly compared to that measured in the casing gas. From the concentration in the casing gases, the expected concentrations in the oil and water phase can also be calculated based on relative solubility.

3.2. Results

3.4.1. Casing gas results

Casing gases were collected from the Lost Hills, Belridge and Orcutt oil fields; measured concentrations can be found in Table 3.3 and isotope ratio data can be found in Table 3.4, as well in USGS data reports (Gannon et al 2018, Seitz, et al., 2021).

Measured helium (^{4}He) concentrations in the casing gases across the sites vary from 4.8±0.4 x10^{-8} to 3.3±0.1 x10^{-5} cm^3(STP)/cm^3 (where STP is standard temperature and pressure; Figure 3.2). Samples from the SJB (Lost Hills and Belridge) have helium isotope ratios (^{3}He/^{4}He) relative to air (R_A= 1.4 x10^6) of 0.013±0.001 to 0.06±0.003 R_A, which suggests that they are dominated by radiogenic ^{4}He (where the radiogenic production ^{3}He/^{4}He value = 0.02R_A). However, in the Orcutt Field, ^{3}He/^{4}He ranges from 0.051±0.001 to 0.572±0.006R_A, suggesting a mantle helium contribution. Using the expected R_A from radiogenic production and assuming a mantle helium isotopic composition of 6.1±2.1 R_A (Day et al., 2015), the Orcutt samples are predicted to have up to a 9% mantle helium contribution. The most elevated helium isotope ratios are found in samples O-01, O-02, and O-03, to the west of the active faults within the field (Figure 3.1d), suggesting that these faults are acting as a conduit for mantle derived fluids (Kulongoski et al., 2003; 2005; 2013). Fluid migration along a fault is in agreement with findings from Hummel, 2009, who found that the activation and reactivation of faulting within the Orcutt Field provided conduits for fluid migration.

Across the three fields, neon (^{20}Ne) concentrations range from 1.85±0.04 x10^{-9} to 28.6±0.4 x10^{-9} cm^3(STP)/cm^3. Measured ^{20}Ne/^{22}Ne and ^{21}Ne/^{22}Ne ratios vary between 9.38±0.05 and 10.2±0.1 and 0.0283±0.006 and 0.0305±0.002. Deviations from the atmospheric ^{20}Ne/^{22}Ne (9.8) and ^{21}Ne/^{22}Ne (0.0290) can be attributed to mass fractionation effects.

Measured argon isotopes ($^{40}Ar/^{36}Ar$) values are above the atmospheric value (298.56 (Lee et al., 2006)), with measured values between 304.8±0.4 to 501.5±0.6, showing a resolvable radiogenic ^{40}Ar concentrations in each of the oil fields. Measured $^{38}Ar/^{36}Ar$ values are predominantly air-like. Argon (^{36}Ar) concentrations in the casing gases range from 10.0±0.1 to 219±2 x10^{-9} cm^3(STP)/cm^3. Measured krypton and xenon isotope ratios are indistinguishable from air (Table 3.4). Krypton (^{84}Kr) concentrations from the Lost Hills, Orcutt and Belridge casing gases range from 1.42±0.03 to 12.2±0.3 x10^{-9} cm^3(STP)/cm^3. The xenon (^{130}Xe) concentrations in the three fields range from 111±2 to 529±11 x10^{-12} cm^3(STP)/cm^3.

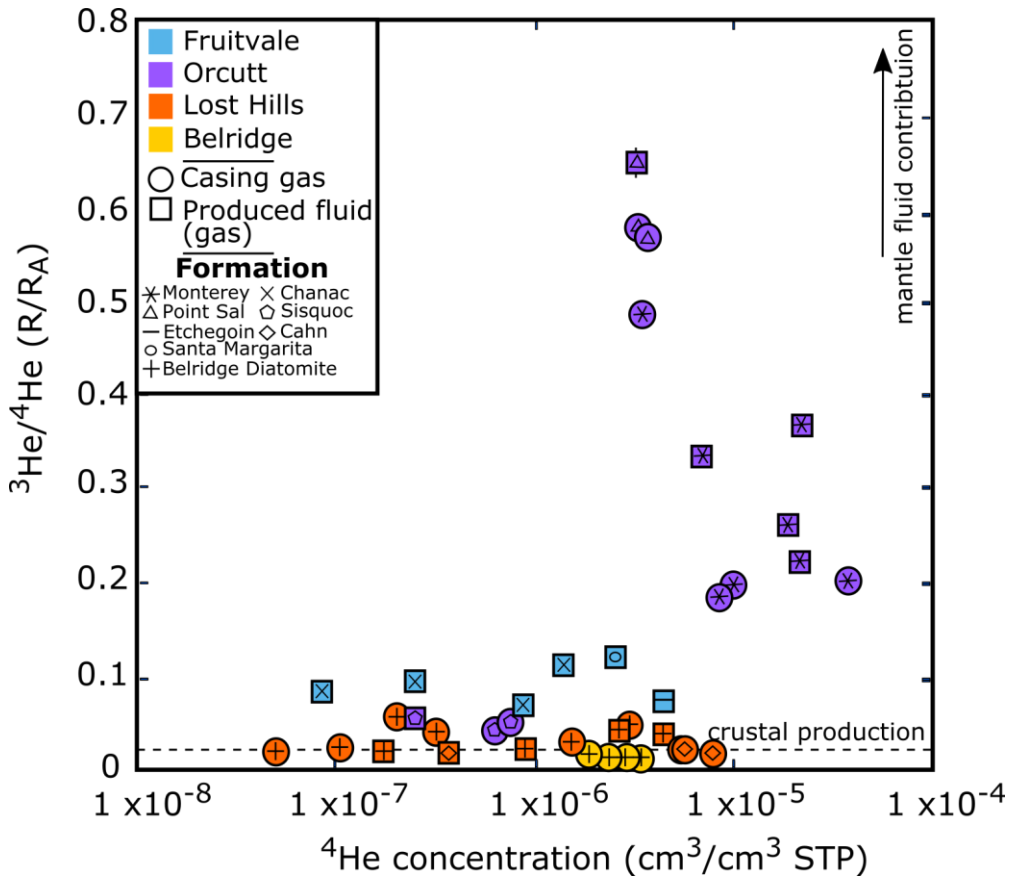


Figure 3.2: Helium (^4He) concentrations and isotope data ($^3He/^4He$) for casing gas and produced fluid samples. Helium isotopes are normalised to air (where air =1R_A). With the exception of the Orcutt Field, all fields are radiogenic in their helium isotopes. The Orcutt Field has more elevated helium isotopes likely due to a mantle influx from its proximity to faults (e.g. Kulongoski et al., 2013). 1σ uncertainties are less than 5% and within symbol size for most samples.

Sample	Casing gas (cm^3(STP)cm^3)									
	^{4}He ($x10^{-6}$)	±	^{20}Ne ($x10^{-9}$)	±	^{36}Ar ($x10^{-9}$)	±	^{84}Kr ($x10^{-9}$)	±	^{130}Xe ($x10^{-12}$)	±
Lost Hills										
LH2^	0.187	0.004	13.5	0.27	70	1	4.10	0.08	253	5
LH3^	0.345	0.006	10.3	0.21	50	1	2.57	0.05	111	2
LH4^	2.95	0.06	5.83	0.12	40	1	6.27	0.13	292	6
LH5^	1.48	0.03	24.0	0.5	90	2	4.39	0.09	266	6
LH7^	0.048	0.004	2.67	0.03	10	1	2.49	0.05	323	6
LH8^	0.148	0.002	2.30	0.05	10	1	1.42	0.03	323	6
LH9^	7.53	0.15	2.36	0.05	20	1	4.56	0.09	219	5
LH10^	5.31	0.11	1.85	0.04	20	1	3.70	0.07	182	3
LH10^	5.36	0.11	1.90	0.04	20	1	3.67	0.07	179	3
Belridge										
BN3	2.6	0.1	5.01	0.07	21.9	0.2	5.72	0.12	289	6
BN4	2.9	0.1	3.64	0.05	16.6	0.1	6.89	0.15	454	9
BN6 (S)	2.1	0.1	4.52	0.07	24.6	0.2	5.41	0.12	324	7
BN6 (S)	1.9	0.1	4.02	0.06	22.3	0.2	4.81	0.10	281	6
Orcutt										
O1	3.5	0.1	23.1	0.3	143	1	12.2	0.3	529	11
O2	3.3	0.1	15.1	0.2	63.3	0.5	3.85	0.08	129	3
O2	3.3	0.1	11.2	0.2	61.4	0.5	3.25	0.07	124	3
O3	0.71	0.03	17.8	0.3			4.91	0.11	290	6
O4	9.1	0.4	11.9	0.2	144	1	10.3	0.2	271	5
O6	33	1	28.6	0.4	219	2	10.8	0.2	223	5
O7	6.8	0.3	9.72	0.14	122	1	8.34	0.18	220	4

Table 3.3: Measured noble gas (He, Ne, Ar, Kr, Xe) in the casing gases and each phase of the produced fluids at each of the sampling localities. *PW data previously reported in Tyne et al. (2019). ^Casing gas measurements previously reported in Barry et al. (2018a). Data can be found in USGS data reports (Gannon et al., 2018; Seitz et al., 2021). For the Gannon et al. (2018) data was recorded in cm^3/g (total fluid) at standard temperature and pressure; these values can be converted to the total amount of noble gases in the Cu tube ($[i]t$) by multiplying by ($Vw+Vo$). Concentrations in each phase can then be calculated as in Chapter 2 (Tyne et al., 2019).

Sample	Produced fluid: Gas (cm^3(STP)cm^3)									
	^{4}He ($x10^{-6}$)	±	^{20}Ne ($x10^{-9}$)	±	^{36}Ar ($x10^{-9}$)	±	^{84}Kr ($x10^{-9}$)	±	^{130}Xe ($x10^{-12}$)	±
Fruitvale										
F1*	0.24	0.01	1.01	0.05	6.48	0.24	1.97	0.10	218	15
F2*	0.86	0.02	31.2	2.4	76.8	4.8	7.44	0.48	2800	40
F3*	4.32	0.24	40.8	2.4	158	7	21.4	1.0	486	31
F4*	1.32	0.05	26.4	2.4	91.2	4.8	19.0	1.0	896	72
F5*	0.084	0.002	1.22	0.07	15.1	0.7	4.80	0.24	503	28
F6*	2.40	0.07	137	7	816	48	36.0	2.4	341	19
Lost Hills										
LH3	4.39	0.16	20.6	1.0	79.8	3.4	11.6	1.0	734	42
LH4	2.53	0.09	31.9	1.6	250	11	45.1	3.7	2490	150
LH5	0.84	0.03	2.90	0.14	15.1	0.7	4.89	0.41	545	32
LH7	0.17	0.01	1.32	0.06	6.05	0.26	1.14	0.09	107	6
LH9	0.35	0.01	0.86	0.04	4.09	0.18	0.74	0.06	31.8	1.5
Orcutt										
O1	3.14	0.09	11.3	0.1	34.3	1.4	2.49	0.25	39.4	3.0
O2	6.75	0.20	90.6	0.9	663	27	44.3	4.4	928	84
O2			84.9	0.9	669	27	37.8	3.8	726	66
O3	0.23	0.01	4.06	0.04	30.3	1.2	2.71	0.27	163	15
O4	21.1	0.6	17.4	0.2	557	22	25.5	2.6	592	53
O6			32.7	0.3	222	9	22.1	2.2	333	30
O7	18.0	0.5	32.9	0.3	377	15	2.27	0.23	609	55

Table 3.3. Continued

Sample	Produced fluid: Oil (mol/g_{oil})									
	^{4}He ($x10^{-15}$)	±	^{20}Ne ($x10^{-15}$)	±	^{36}Ar ($x10^{-15}$)	±	^{84}Kr ($x10^{-15}$)	±	^{130}Xe ($x10^{-15}$)	±
Fruitvale										
F1*	63	3	0.22	0.01	19	1	16	1	30	2
F2*	250	10	7.4	0.4	230	10	56	3	37	2
F3*	1200	49	10	1	470	20	160	10	150	10
F4*	380	20	6.4	0.3	270	10	140	10	120	10
F5*	25	1	0.30	0.01	45.0	1.7	36	2	43	3
F6*	750	30	35	2	2500	100	260	10	78	5
Lost Hills										
LH3	152	6	0.62	0.03	25.4	1.1	9.93	0.82	11.4	0.7
LH4	90.5	3.3	0.994	0.049	80.5	3.5	38.7	3.2	38.6	2.2
LH5	28.3	1.0	0.084	0.004	4.76	0.21	4.10	0.34	7.95	0.46
LH7	6.24	0.23	0.043	0.002	1.97	0.09	0.98	0.08	1.66	0.10
LH9	12.6	0.5	0.025	0.001	1.31	0.06	0.64	0.05	0.48	0.03
Orcutt										
O1	44.7	1.3	0.158	0.002	1.02	0.04	0.115	0.011	0.018	0.002
O2	201	6	2.40	0.02	158	6	26.6	2.7	9.59	0.86
O2	629	18	2.25	0.02	160	6	22.7	2.3	7.50	0.68
O3	6.6	0.2	0.101	0.001	8.89	0.36	2.27	0.23	2.60	0.23
O4	37400	1100	0.456	0.005	52.3	2.1	14.4	1.4	5.63	0.51
O6	762	22	1.12	0.01	129	5	10.7	1.1	2.59	0.23
O7	489	14	0.767	0.008	93.8	3.8	1.47	0.15	6.85	0.62

Table 3.3. Continued

Sample	Produced fluid: Water (mol/g_{water})									
	^{4}He ($x10^{-15}$)	±	^{20}Ne ($x10^{-15}$)	±	^{36}Ar ($x10^{-15}$)	±	^{84}Kr ($x10^{-15}$)	±	^{130}Xe ($x10^{-15}$)	±
Fruitvale										
F1*	40	2	0.19	0.01	36	2	2	0.1	2.5	0.1
F2*	140	10	5.6	0.3	38	2	6.5	0.3	2.7	0.2
F3*	700	30	7.7	0.4	81	4	19	1	11	1
F4*	220	10	4.9	0.2	46	2	17	1	8.5	1
F5*	14	1	0.22	0.01	7.7	0.4	4.2	0.2	3.2	0.2
F6*	410	20	25	1	380	20	28	1	5.5	0.3
Lost Hills										
LH3	77.8	2.9	0.405	0.020	4.33	0.19	1.09	0.09	0.756	0.044
LH4	45.2	1.7	0.628	0.031	13.4	0.6	4.15	0.34	2.48	0.14
LH5	15.0	0.6	0.057	0.003	0.803	0.035	0.450	0.037	0.541	0.031
LH7	3.04	0.11	0.026	0.001	0.316	0.014	0.102	0.008	0.103	0.006
LH9	6.28	0.23	0.016	0.001	0.218	0.009	0.068	0.006	0.031	0.002
Orcutt										
O1	44.7	1.3	0.158	0.002	1.02	0.04	0.115	0.011	0.018	0.002
O2	90.6	2.6	1.29	0.01	23.3	0.9	2.60	0.26	0.557	0.05
O2	284	8	1.21	0.01	23.6	0.9	2.22	0.22	0.435	0.039
O3	6.57	0.19	0.134	0.001	3.09	0.12	0.499	0.050	0.343	0.031
O4	17000	500	0.244	0.002	7.44	0.30	1.41	0.14	0.330	0.03
O6	284	8	0.433	0.004	15.4	0.6	0.946	0.095	0.136	0.012
O7	253	7	0.504	0.005	15.4	0.6	0.159	0.016	0.454	0.041

Table 3.3. Continued

Sample	Casing Gas $^{3}He/^{4}He$ (R/R_A)	±	$^{20}Ne/^{22}Ne$	±	$^{21}Ne/^{22}Ne$	±	$^{40}Ar/^{36}Ar$	±	$^{86}Kr/^{84}Kr$	±	$^{132}Xe/^{130}Xe$	±
Lost Hills												
LH2	0.060	0.003	0.0288	0.0002	9.76	0.05	307.1	1.5	0.291	0.001	6.57	0.03
LH3	0.042	0.002	0.0287	0.0002	9.68	0.05	307.6	1.5	0.292	0.001	6.58	0.03
LH4	0.048	0.002	0.0293	0.0002	9.79	0.05	310.6	1.6	0.292	0.001	6.57	0.03
LH5	0.030	0.002	0.0283	0.0002	9.55	0.05	308.6	1.5	0.385	0.002	6.57	0.03
LH7	0.018	0.001	0.0303	0.0002	9.38	0.05	332.3	1.7	0.292	0.001	6.57	0.03
LH8	0.024	0.001	0.0296	0.0002	10.2	0.1	304.9	1.5	0.291	0.001	6.56	0.03
LH9	0.018	0.001	0.0303	0.0002	9.38	0.05	332.3	1.7	0.292	0.001	6.57	0.03
LH10	0.019	0.001					333.6	1.7	0.292	0.001	6.58	0.03
LH10	0.019	0.001	0.0305	0.0002	9.78	0.05	333.9	1.7	0.291	0.001	6.58	0.03
Belridge												
BN3	0.014	0.001	0.0289	0.0002	9.80	0.05	501.5	0.6	0.301	0.001	6.62	0.07
BN4	0.015	0.001	0.0299	0.0002	10.2	0.1	291.8	0.4	0.298	0.001	6.54	0.07
BN6 (S)	0.013	0.001	0.0292	0.0002	10.1	0.1	292.7	0.4	0.300	0.001	6.55	0.07
BN6 (S)	0.014	0.001	0.0287	0.002	10.0	0.1	304.8	0.4	0.301	0.001	6.59	0.07
Orcutt												
O1	0.572	0.006	0.0293	0.0001	9.89	0.05	348.6	0.8	0.301	0.001	6.63	0.01
O2	0.489	0.005	0.0292	0.0001	10.0	0.1	372.8	0.9	0.301	0.001	6.63	0.01
O2	0.483	0.005	0.0292	0.0001	9.93	0.05	311.1	0.7	0.301	0.001	6.57	0.01
O3	0.051	0.001	0.0293	0.0001	10.0	0.1			0.297	0.001	6.53	0.01
O4	0.199	0.002	0.0295	0.0001	9.85	0.05	336.8	0.8	0.301	0.001	6.58	0.01
O6	0.208	0.002	0.0295	0.0001	9.77	0.05	333.5	0.8	0.298	0.001	6.55	0.01
O7	0.186	0.002	0.0296	0.0001	9.97	0.05	326.1	0.7	0.299	0.001	6.55	0.01

Table 3.4: Measured noble gas (He, Ne, Ar, Kr, Xe) isotope ratios in the casing gases and produced fluids at each of the sampling localities

Sample	Produced fluid											
	$^{3}He/^{4}He$ (R/R_A)	±	$^{20}Ne/^{22}Ne$	±	$^{21}Ne/^{22}Ne$	±	$^{40}Ar/^{36}Ar$	±	$^{86}Kr/^{84}Kr$	±	$^{132}Xe/^{130}Xe$	±
Fruitvale												
F1	0.090	0.001	0.0298	0.0004	9.80	0.14	370.0	6.7	0.300	0.005	6.69	0.11
F2	0.068	0.001	0.0290	0.0004	10.1	0.1	354.7	6.4	0.302	0.005	6.68	0.11
F3	0.072	0.001	0.0290	0.0004			305.4	5.5	0.302	0.005		
F4	0.108	0.001	0.0293	0.0004	10.3	0.1	351.8	6.3	0.301	0.005	6.67	0.11
F5	0.082	0.001	0.0301	0.0005	10.0	0.1	303.3	5.5	0.302	0.005		
F6	0.117	0.002	0.0290	0.0004	9.90	0.14	294.1	5.3	0.303	0.005		
Lost Hills												
LH3	0.042	0.001	0.0310	0.0002	9.96	0.01	299.5	6.9	0.304	0.003	6.62	0.03
LH4	0.023	0.001	0.0284	0.0002	10.2	0.1	310.7	7.1	0.303	0.007	6.60	0.07
LH5	0.020	0.001	0.0309	0.0002	9.99	0.01	289.8	6.7	0.302	0.007	6.63	0.07
LH7	0.042	0.001	0.0278	0.0002	10.2	0.1	479.3	11.0	0.301	0.007	6.62	0.07
LH9	0.014	0.001	0.0297	0.0002	10.1	0.01	320.4	7.4	0.304	0.003	6.60	0.03
Orcutt												
O1	0.648	0.018	0.0294	0.0004	10.4	0.2	359.8	0.8	0.308	0.001	6.60	0.02
O2	0.336	0.009	0.0295	0.0004	10.2	0.2	301.9	0.7	0.307	0.001	6.54	0.02
O2	0.370	0.01	0.0293	0.0004	10.0	0.2	321.1	0.7	0.305	0.001	6.52	0.02
O3	0.052	0.001	0.0295	0.0004	10.4	0.2			0.308	0.001	6.57	0.02
O4	0.241	0.007	0.0297	0.0004	10.1	0.2	318.1	0.7	0.309	0.001	6.59	0.02
O6	0.218	0.006	0.0297	0.0004	9.81	0.21	315.7	0.7	0.308	0.001	6.58	0.02
O7	0.262	0.007	0.0294	0.0004	10.5	0.2	335.8	0.8	0.307	0.001	6.60	0.02

Table 3.4: Continued

3.4.2. Produced fluid results

Produced fluids were collected from the Fruitvale, Lost Hills and Orcutt oil fields. Wellhead concentrations from each phase of the produced fluids are reported in Table 3.3. These have been calculated following methods described in section 3.3.3 and in more detail in Chapter 2 (Tyne et al., 2019). Due to solubility within elements being approximately the same for all isotopes, differences in the noble gas isotope ratios between the phases are expected to be negligible (Table 3.4). Within an oil-water system, higher noble gas concentrations are expected in the oil phase compared to the water phase (Chapter 2; Ballentine, et al., 1996; Tyne et al., 2019). During production, gases exsolve from the denser fluids and typically exhibit the highest noble gas concentrations of all three phases. We observe this partitioning trend within the produced fluids, where the gas phase concentrations are >2 orders of magnitude higher than oil concentrations, which contain approximately twice the amount of noble gases as the water phase (Table 3.3).

The ^{4}He concentration within the exsolved gases in the produced fluid samples range from 0.084±0.002 to 21.1±0.6 $x10^{-6}$ $cm^3(STP)/cm^3$, with the largest ^{4}He concentration range within the Orcutt field (Figure 3.2). The ^{4}He concentrations calculated in the oil and water phases were significantly lower at 6.24±0.23 to 37400±1100 $x10^{-15}$ mol/g_{oil} and 3.04±0.11 to 17000±500 $x10^{-15}$ mol/g_{water} respectively. Similarly to the casing gases, the $^{3}He/^{4}He$ in the produced fluids from Lost Hills are strongly radiogenic (0.014±0.001 to 0.042±0.001R_A). Fruitvale has a slightly less radiogenic signature (0.068±0.001 to 0.17±0.002R_A), whilst Orcutt again shows a variable mantle contribution with $^{3}He/^{4}He$ ranging from 0.052±0.001 to 0.648±0.08R_A in agreement with the casing gases.

Neon (^{20}Ne) concentrations vary from 0.086±0.004 to 90.6±0.9 $x10^{-9}$ $cm^3(STP)/cm^3$ in the gas phase of the produced fluids. Concentrations of ^{20}Ne in the oil and water phases within the sample fields are between 0.025±0.001 to 35±1 $x10^{-15}$ mol/g_{oil} and 0.016±0.001 to 7.7±0.4 $x10^{-15}$ mol/g_{water}, respectively. $^{20}Ne/^{22}Ne$ and $^{21}Ne/^{22}Ne$ ratios within the produced fluids are in agreement with the casing gases at 9.80±0.14 to 10.5±0.2 and 0.0278±0.0002 to 0.0310±0.0002 respectively.

Fruitvale, Lost Hills and Orcutt ^{36}Ar concentrations in gas, oil and water phases are 4.09±0.18 to 816±48 x10^{-9} cm^3(STP)/cm^3, 1.02±0.04 to 2500±100 x10^{-15} mol/g_{oil} and 0.218±0.009 to 380±20 x10^{-15} mol/g_{water} respectively. $^{40}Ar/^{36}Ar$ values are between 294±5 and 479±11, and are consistent with a radiogenic ^{40}Ar present in some samples.

Krypton isotopic ratios ($^{86}Kr/^{84}Kr$) are agreement with the air value (0.303) at 0.300±0.005 to 0.309±0.001 and consistent with the casing gas results. The ^{84}Kr concentrations are 0.115±0.011 to 260±10 x10^{-15} mol/g_{oil} in the oil phase, 0.74±0.06 to 45.1±3.7 x10^{-9} cm^3(STP)/cm^3 in the gas phase and 0.102±0.0008 to 28±1 x10^{-15} mol/g_{water} in the water phase.

Measured $^{132}Xe/^{130}Xe$ in the produced fluids across the fields are 6.52±0.02 to 6.69±0.11, consistent with both the casing gas values and air. Within the gas phase, the produced fluids had ^{130}Xe concentrations of 31.8±1.5 to 2800±40 cm^3(STP)/cm^3 and 0.018±0.002 to 150±10 x10^{-15} mol/g_{oil} within the oil phase. The ^{130}Xe concentrations within the water in the produced fluids were 0.018±0.002 to 11±2 x10^{-15} mol/g_{water}.

3.3. Discussion

Casing gas and produced fluid data from the Fruitvale, Lost Hills, Belridge and Orcutt oil fields in California are used to: 1) compare the noble gas abundance in the casing gas and gas phase of the produced fluids at the wellhead (Section 3.5.1.), 2) reconstruct the noble gas distribution within the reservoir system for both the casing gases and produced fluids (Section 3.5.2.), 3) characterise pristine reservoir noble gas signatures (Section 3.5.3.), 4) quantify the effects of EOR injection on the noble gas distribution (Section 3.5.4.), and 5) determine the controlling processes, across multiple oil fields (Section 3.5.4.).

3.5.1. Comparison of casing gas and produced fluids at the wellhead

In this study, we collected both casing gases and produced fluids from the Lost Hills and Orcutt oil fields, which allow the distribution of noble gases between the casing gas and produced fluid (oil-water-gas) phases to be investigated for the first time. The abundances in measured casing gas samples can be directly compared to the gas phase in the produced fluids (calculated as in Section

3.3.3.) under sampling conditions (Table 3.3). By comparing the two, we are able to rigorously test the assumptions (e.g., equilibrium) used for both the casing gas and produced fluids and determine whether these two sample types can be used interchangeably.

On average, measured ^{20}Ne concentrations in Lost Hills casing gases are 2.8±3.3 times those exsolved from the produced fluid (Figure 3.3), with two samples having lower ^{20}Ne concentrations than in the produced fluid gases. A similar offset is seen for ^{36}Ar (2.6±2.6 times greater in the casing gas) (Table 3.3, Supplementary Figure S3.2) at Lost Hills and in the Orcutt Oil Field (1.2±1.5 and 5.5±4.7 times greater in the gases within the produced fluids than casing gas for ^{20}Ne and ^{36}Ar respectively) (Figure 3.3, Supplementary Figure S3.2). We attribute the variance in the data to differences in production practices both between wells and between casing gases and produced fluids, which may affect the assumptions used. Further interrogation of these assumptions using a larger dataset is needed to fully understand this variance. The agreement between casing gas samples and gases exsolved from produced fluids at wellheads confirms that assumptions for both sample types are reasonable and that either casing gas or produced fluids can be used to determine the noble gas composition of a reservoir.

3.5.2. Reconstructing noble gas concentrations in the reservoir oil

In hydrocarbon systems that consist predominantly of oil and water (at reservoir conditions), fluids brought to the surface during production will exsolve gases due to decompression. The noble gas content in the denser (i.e., oil and water) phases within the reservoir can be reconstructed, by taking into account this exsolution during extraction. Previous reconstructions of the oil phase from casing gases have assumed that 100% of the gas phase is derived from the oil (Barry et al., 2018a). However, it is probable that gases have also exsolved from the produced water. Here, we assume the amount of noble gases is constant between the bottom of the well and wellhead and the noble gases are distributed between the water and oil phases. Predicted WOR were made based on production data for the field and can be found in Table 3.2.

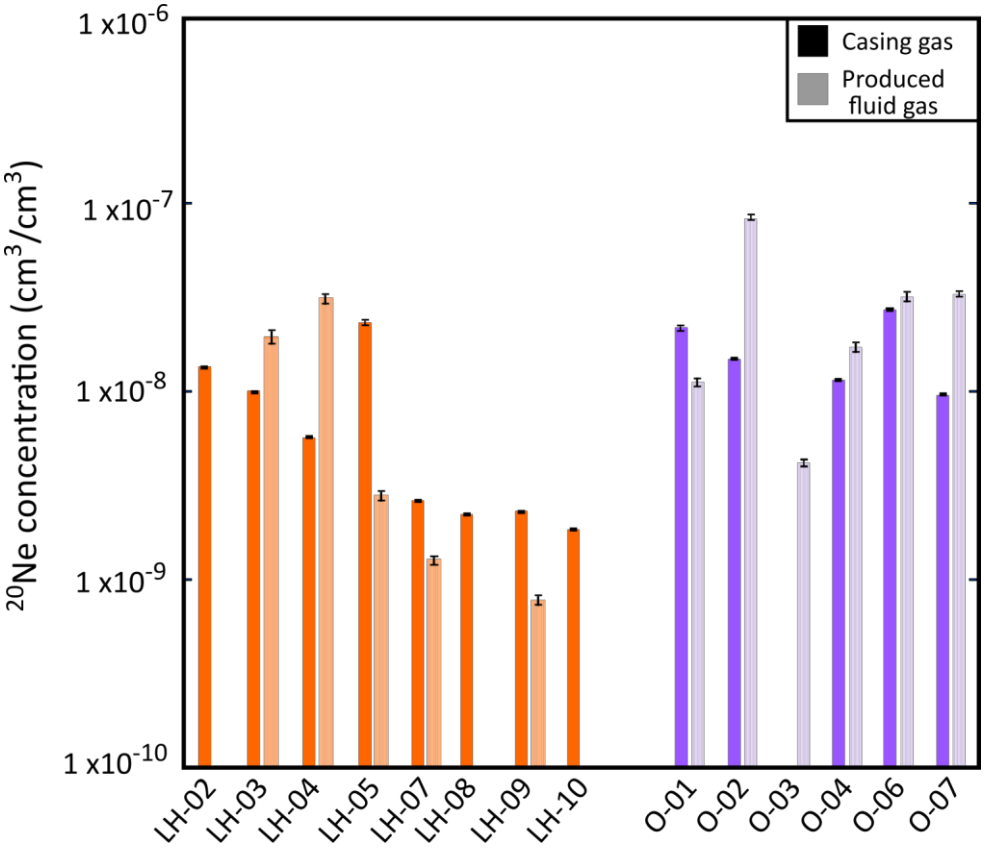


Figure 3.3: Comparison of the ^{20}Ne concentration measured in the casing gases and in the gaseous phase of the produced fluid samples, where the darker bars are for the casing gas samples and lighter bars are the gaseous phase in the produced fluids. 1σ uncertainties are shown and are less than 5%. ^{20}Ne concentrations in both sample types are in broad agreement.

The total amount of a noble gas (n^i_t) is calculated by multiplying the calculated wellhead concentration by the relative volumes produced over a set time frame (Eq. 3.6).

$$n_t^i = C_o^i \times V_o + \frac{C_g^i \times V_g}{22400} + C_w^i \times V_w \qquad \text{(Eq. 3.6)}$$

V_g/V_o (GOR) and V_w/V_o (WOR) are measured at the wellhead and can vary significantly over short timescales due to variation in production techniques. Here, we use the average time-integrated GOR and WOR values (with an assumed 15% error) for each formation (Table 3.2), which are likely more representative of the true values in the reservoir.

The concentration of a given noble gas, originally in the oil (C^i_{or}, mol/g_{oil}) and water (C^i_{wr}, mol/g_{water}) phases at reservoir temperature and pressure (RTP) can be estimated using equations 3.7 -3.9.

$$C_{or}^{i} = \frac{F \times n_t^i}{V_o} \quad \text{(Eq. 3.7)}$$

$$C_{wr}^{i} = \frac{F \times n_t^i}{V_w} \quad \text{(Eq. 3.8)}$$

$$F = \frac{n_{or}^i}{n_{or}^i + \frac{V_w \times K_{gw}^i \times n_{or}^i}{V_o \times K_{go}^i}} \quad \text{(Eq. 3.9)}$$

where F is the proportion of noble gas *i* in the oil phase. K^i_{gw} and K^i_{go} are the Henry's Constants for a given noble gas *i* under reservoir conditions. n^i_{or} is the amounts of *i* within the reservoir, as only relative proportions are needed any value can be used. Where needed WOR were used instead of absolute volumes. Calculated concentrations within the reservoirs from both casing gases and produced fluids can be found in Table 3.5.

3.5.3. Determining pre-development reservoir characteristics

In order to trace hydrocarbon contributions to shallow aquifers, it is important to first determine pre-development reservoir characteristics, as well as an understanding of how this composition has been perturbed during production (i.e., due to EOR). As described in section 3.5.2, concentrations of noble gases within the oil and water in the reservoir can be reconstructed based on their solubility at depth (Table 3.5).

Atmosphere-derived noble gases (e.g., ^{20}Ne, ^{36}Ar, ^{84}Kr, ^{130}Xe) enter the subsurface dissolved in groundwater either during natural aquifer recharge or anthropogenically during injection. Krypton and xenon concentrations across all fields measured here are in excess of those predicted by solubility (Supplementary Figure S3.3), as is commonly observed in hydrocarbon systems (e.g., Torgersen and Kennedy, 1999; Zhou et al., 2005; Barry et al., 2016, 2018a; Wen et al., 2017; Byrne et al., 2018). This excess is likely derived from sediments but the processes controlling heavy noble gas excesses are not well-understood (Torgersen and Kennedy, 1999; Zhou et al., 2005; Barry et al., 2016). As a result, we consider only the light atmospheric gases (^{20}Ne, ^{36}Ar, which have no

significant subsurface sources) in the following mixing models to evaluate the effects of injection on hydrocarbon reservoir noble gas signatures.

The solubilities of noble gases in groundwater are a function of the recharge conditions (temperature, salinity and recharge elevation, Supplementary Table S3.1) and generally increase with mass, allowing the initial noble gas inventory to be calculated (Ballentine and Hall, 1999; Aeschbach-Hertig et al., 1999; Kipfer et al., 2002). As oil migrates from source to the reservoir, any contact with formation waters will result in the partitioning of noble gases into the oil phase based on their relative solubility under reservoir conditions and Specific Gravity of oil (where S_g= *141.5/(API + 131.5)*)(Supplementary Table S3.1).

During initial charging of the reservoir (i.e., high WOR) the oil will be at its most fractionated (i.e., have the lowest $^{20}Ne/^{36}Ar$, '1st bubble' composition) and as the system evolves (i.e., oil is produced) and/or more oil-water interaction occurs (WOR decreases), the $^{20}Ne/^{36}Ar_{oil}$ will increase towards $^{20}Ne/^{36}Ar_{ASW}$ (Figure 3.4a), and concentrations of the noble gases in the oil will decrease due to dilution. Assuming a closed system equilibrium, the relative volumes of water that have exchanged with the oil can therefore be derived (Eq. 3.10 after Ballentine et al., 1996; Barry et al., 2016; 2018a) to predict the relative pre-development WOR within each reservoir.

$$WOR = \frac{[i]_{asw}}{[i]_{oil}} - \frac{K^i_{go}}{Sg \times K^i_{gw}} \qquad \text{(Eq. 3.10)}$$

$[i]_{asw}$ is the amount of noble gas *i* in the formation water calculated from its recharge conditions (in mol/g) and $[i]_{oil}$ is the amount of noble gas *i* in the oil phase (mol/g). Henry's Constant's (K^i_{go} and K^i_{gw}) were calculated under reservoir conditions (temperature, salinity and pressure) and S_g is the specific gravity of oil in g/cm^3. Sample API's can be found in Table 3.2.

Assuming that the oil and water phases are in direct contact and the reservoir is in equilibrium, the pre-development concentrations of ^{20}Ne and ^{36}Ar within the hydrocarbon reservoir for different WOR's can be estimated by rearranging Eq. 3.11 (Barry et al., 2018a).

Sample	Casing gas (mol/g_{oil})						Produced fluid (mol/g_{oil})					
	^{4}He ($x10^{-9}$)	^{20}Ne ($x10^{-12}$)	^{36}Ar ($x10^{-12}$)	^{84}Kr ($x10^{-12}$)	^{130}Xe ($x10^{-12}$)	$^{20}Ne/^{36}Ar$	^{4}He ($x10^{-9}$)	^{20}Ne ($x10^{-12}$)	^{36}Ar ($x10^{-12}$)	^{84}Kr ($x10^{-12}$)	^{130}Xe ($x10^{-12}$)	$^{20}Ne/^{36}Ar$
Fruitvale												
F1							2.28	8.95	85.9	25.0	18.1	0.10
F2							1.41	46.9	176	16.1	4.03	0.27
F3							3.26	28.4	301	36.1	13.4	0.09
F4							2.14	40.7	208	41.7	12.7	0.20
F5							0.86	11.6	219	65.2	29.3	0.05
F6							0.39	18.8	335	13.3	1.81	0.06
Lost Hills												
LH2	0.586	38.1	278	17.2	7.35	0.14						
LH3	0.879	29.1	198	10.8	3.23	0.15	14.4	65.1	355.0	54.4	24.1	0.18
LH4	0.544	1.08	8.41	1.35	0.421	0.13	0.53	6.64	59.4	10.9	4.09	0.11
LH5	4.32	65.9	357	18.4	7.72	0.18	2.71	8.98	67.3	23.0	17.9	0.13
LH7	1.49	8.55	45.6	11.9	10.7	0.19	0.56	4.22	27.3	5.44	3.59	0.15
LH8	0.019	0.43	2.10	0.31	0.47	0.20						
LH9	62.8	18.6	288	74.0	26.3	0.06	3.31	7.11	66.5	13.6	4.31	0.11
LH10	44.4	14.6	288	60.1	21.9	0.05						
LH10	45.2	15.0	288	59.6	21.6	0.05						

Table 3.5: Noble gas (He, Ne, Ar, Kr, Xe) in the reservoir predicted from both casing gases and produced fluids at each of the sampling localities. A 15% errors apply to concentrations based on the uncertainty from GOR and WOR estimates.

Sample	Casing gas (mol/g_{oil})						Produced fluid (mol/g_{oil})					
	^{4}He ($x10^{-9}$)	^{20}Ne ($x10^{-12}$)	^{36}Ar ($x10^{-12}$)	^{84}Kr ($x10^{-12}$)	^{130}Xe ($x10^{-12}$)	$^{20}Ne/^{36}Ar$	^{4}He ($x10^{-9}$)	^{20}Ne ($x10^{-12}$)	^{36}Ar ($x10^{-12}$)	^{84}Kr ($x10^{-12}$)	^{130}Xe ($x10^{-12}$)	$^{20}Ne/^{36}Ar$
Belridge												
BN3	26.0	47.5	421	104	38.2	0.11						
BN4	15.3	18.0	244	91.4	46.4	0.07						
BN6 (S)	24.2	50.6	500	106	44.4	0.10						
BN6 (S)	21.5	45.0	454	93.9	38.8	0.10						
Orcutt												
O1	3.54	23.4	150	12.9	3.74	0.16	4.53	16.3	130	12.3	1.90	0.13
O2	9.32	43.2	182	11.1	2.46	0.24	0.73	9.43	112	8.15	1.22	0.08
O2	9.45	31.9	176	9.34	2.35	0.18	2.30	8.82	113	6.96	0.957	0.08
O3	2.17	54.1	n.d.	15.1	5.84	n.d.	0.89	14.4	166	16.1	6.78	0.09
O4	4.85	6.29	80.2	5.79	1.01	0.08	2520	34.4	462	53.4	8.21	0.07
O6	33.1	28.4	229	11.4	1.55	0.12	9.86	15.2	272	10.9	1.09	0.06
O7	3.78	5.34	70.4	4.85	0.85	0.08	9.94	18.0	218	1.32	2.36	0.08

Table 3.5: Continued.

$$[i]_{oil} = \frac{[i]_{asw}}{WOR + \frac{K^i_{go}}{Sg \times K^i_{gw}}} \quad \text{(Eq. 3.11)}$$

$[i]_{oil}$ is calculated for each reservoir using a fixed specific gravity assumption, solubility coefficients and noble gas concentrations in the ASW (based on the unique estimated recharge conditions in each reservoir; Supplementary Table S3.1). The volume of injected water for each injection well within a 500m radius of the sampled wells has been recorded and aggregated since 1977. Samples which have not been subjected to injection within 500m display $^{20}Ne/^{36}Ar$ and noble gas concentrations consistent with those calculated for a pristine system (Figure 3.4, Supplementary Figure S3.5).

3.5.4. Assessing the effects of injection

During injection, noble gases are redistributed from the injected fluids into the reservoir oil, effectively altering the pre-development system. Samples exposed to injection within 500m have elevated $^{20}Ne/^{36}Ar$ and ^{20}Ne and ^{36}Ar concentrations compared to those predicted for the pre-development reservoir (Figure 3.4a, Supplementary Figure S3.5), in agreement with previous findings (Barry et al., 2018a). This distinct injection signature allows us to differentiate between those samples which have been affected by EOR (i.e., have elevated $^{20}Ne/^{36}Ar$, ^{20}Ne and ^{36}Ar concentrations) and pristine samples, which are characterised by equilibrium exchange (Eq. 3.10). These results emphasise the importance of characterising both the endmember (injectate and pre-development reservoir) composition and how this has perturbed the system over time to better distinguish the source of any hydrocarbon contributions identified in the groundwater.

Within the Lost Hills and Orcutt oil fields, the relationship of $^{20}Ne/^{36}Ar$ in reservoir oil vs injection volume for both the produced fluids and casing gases can be seen in Supplementary Figure S3.4. We note that there is a similar relationship between oil values calculated from the casing gases and the produced fluids at Lost Hills. However, at Orcutt, elevated $^{20}Ne/^{36}Ar$ and $^{3}He/^{4}He$ in the O-02 and O-06 casing gas samples compared to in the produced fluids suggests significant air. Therefore, where both sample types are available, the produced fluid data appears to yield more robust results.

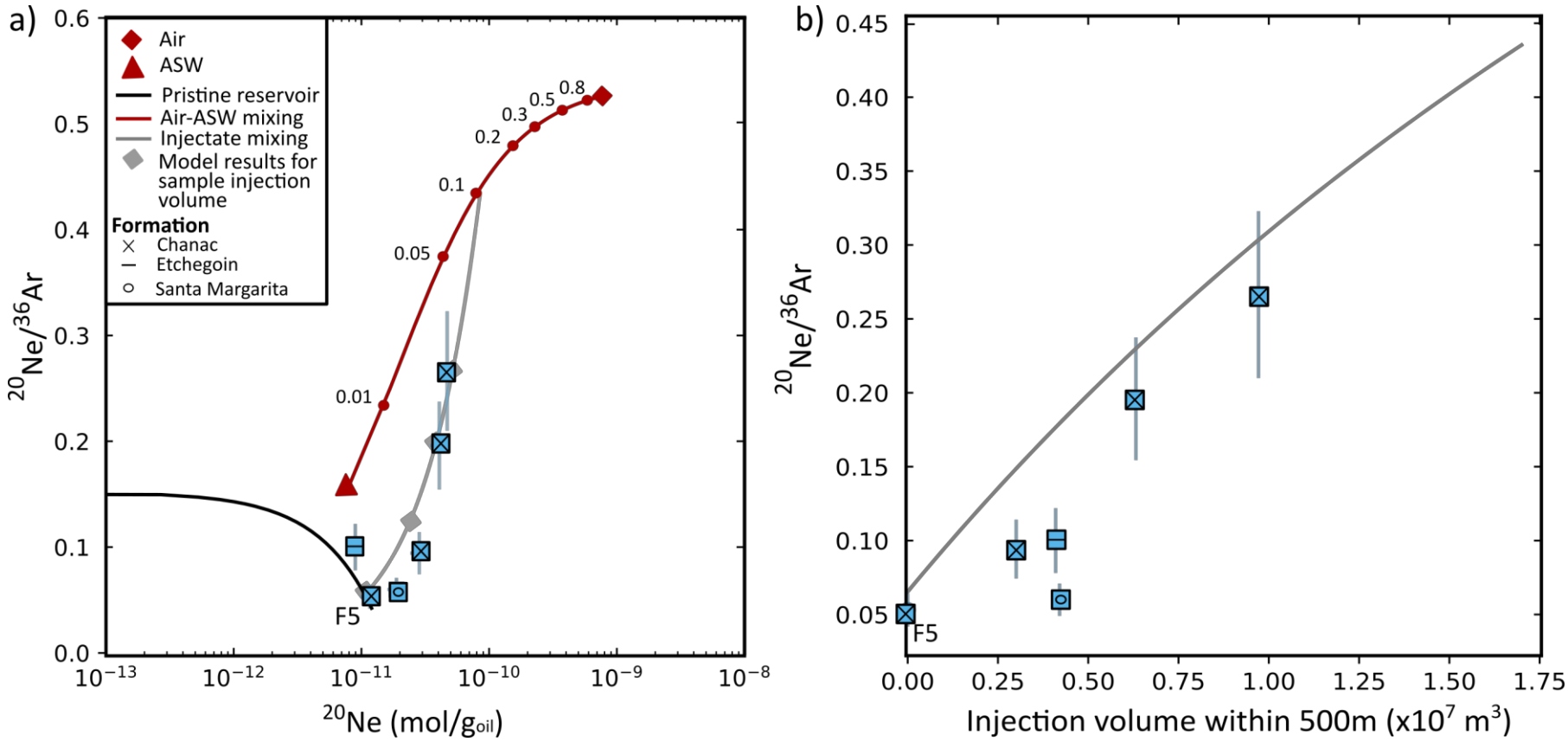


Figure 3.4: Noble gas mixing models for the Fruitvale Oil Field, showing solubility partitioning and the effects of injection. a) Fruitvale samples as a function of their $^{20}Ne/^{36}Ar$ vs. ^{20}Ne concentration in oil. The solid black line represents the predicted pristine hydrocarbon evolution for the reservoir conditions within the Fruitvale Oil Field and the red line represents the range of possible injectate compositions (as a function of F_{air}) given in oil equivalent concentrations. Solid grey line represents the predicted mixing and reservoir evolution between the pristine reservoir and injectate using best fit V_t and F_{air} parameters, with grey diamonds indicating model results for known sample injection

volumes. Sample F5, which has seen no injection falls on the pristine reservoir evolution. b) $^{20}Ne/^{36}Ar$ as a function of injected water volume within 500m. Corresponding modelled injection evolution is shown by the grey line.

Location	Pearson's R		Injection model							
	R-value	p-value	*d.f.*	Chi-2	p-value	F_{air}	±	Vt	±	WOR
Fruitvale	0.95	0.0032	6	9.53	0.15	0.11	0.04	$1.73x10^{7}$	$7.1x10^{6}$	8.96
Belridge	0.98	0.0030	6	43.7		1	16	$1.19x10^{9}$	$1.95x10^{10}$	27
Lost Hills	0.99	0.0075	5	39.0		0		$1.00x10^{12}$		1
Orcutt	0.88	0.0195								

Table 3.6: Summary of injection model (Eq. 3.12 and 3.13) findings, using a non-linear least squares minimisation for each field. The minimisation is carried out using the Levenberg-Marquardt algorithm (Marquardt, 1963). d.f.= degrees of freedom. F_{air}= fraction of noble gases derived from air in the injected fluids.

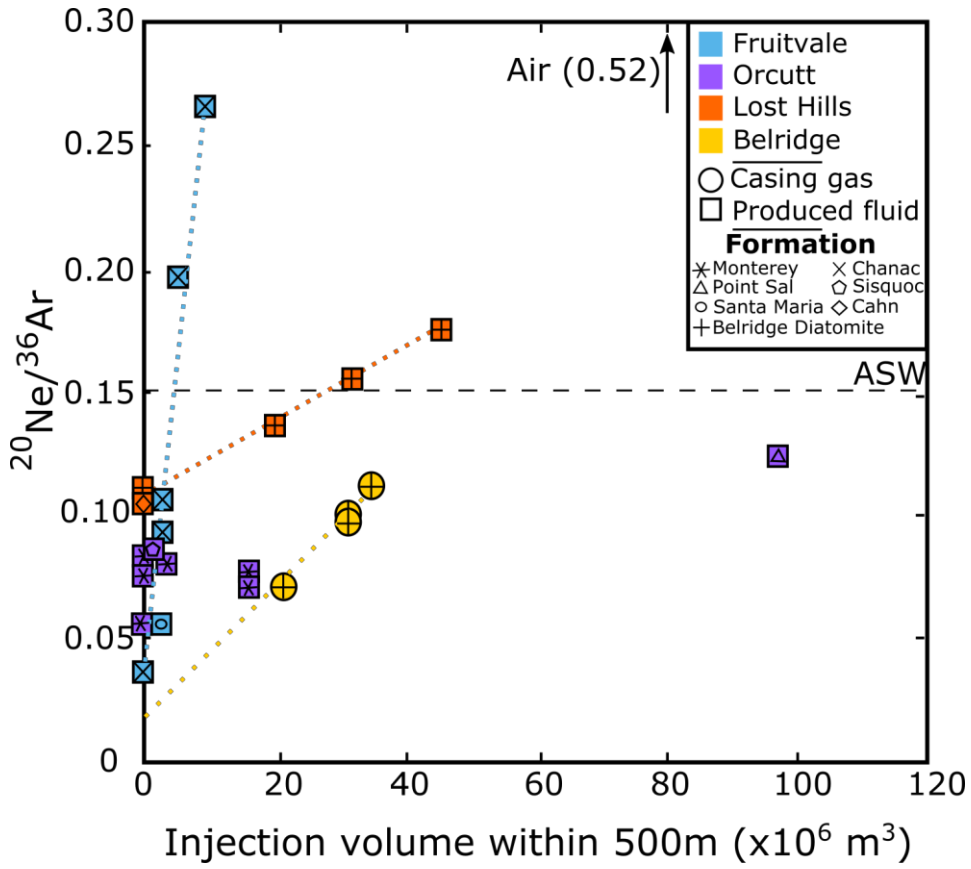


Figure 3.5: Atmospheric noble gas ratio ($^{20}Ne/^{36}Ar$) in the reservoir oil vs. volume of injected fluids (x10^6) within 500m of the sampled well. 1σ uncertainties encompassed by symbol sizes. There is a clear positive correlation between the injected volume and response in the atmospheric noble gas ratio (as denoted by the dashed lines), and the sensitivity of this response (increase in $^{20}Ne/^{36}Ar$) appears different between the fields, with the most sensitive response (steepest slope) occurring within the Fruitvale Oil Field.

The calculated $^{20}Ne/^{36}Ar$ values in reservoir oil within the samples are strongly correlated to injected volume (within 500m; Figure 3.4b, Figure 3.5). This relationship is statistically significant at a 95% confidence level in all the sampled fields (Pearson's R correlation Fruitvale p= 0.0032, Lost Hills p=0.0030, Belridge p=0.0075 and Orcutt p=0.0195, Table 3.6). This implies that the noble gas composition of the reservoir during production is impacted by injection, and thus, the expected composition of a well, where other samples have been characterised, can be predicted based on its injection volume within 500m. However, the response (i.e., increase in $^{20}Ne/^{36}Ar$) to the injected water differs between fields, with the Fruitvale Field's response being much greater than in the other fields (Figure 3.5).

In previous studies, injected fluids have been assumed to be 'air-like' based upon measured injectate gases having elevated $^{20}Ne/^{36}Ar$ and elevated ^{20}Ne and ^{36}Ar concentrations (Barry et al., 2018a). However, in all sampled fields, the injected fluids are predominantly recycled produced waters and other sources, with contributions from groundwater (McMahon et al., 2018; CalGEM, 2020a).

Produced waters have inherently low noble gas concentrations as a result of stripping into the oil phase and therefore cannot account for the elevated concentrations observed within the injected samples. We propose that during the injection process, de-oiled produced waters equilibrate with 'head space' air to reach ASW conditions, and additional entrapped air bubbles cause both the elevated concentrations and observed ratios. The injected material composition can therefore be modelled as a two-component mixture between air and ASW (Eq. 3.12).

$$[i]_{inj} = [i]_{ASW} \times (1 - F_{air}) + [i]_{air} \times F_{air} \qquad \text{(Eq. 3.12)}$$

where F_{air} is the fraction of air in the mixture, and $[i]_{inj}$, $[i]_{ASW}$, $[i]_{air}$ are the concentration of noble gas *i* in the injectate, ASW (assumed at 15 °C) and air respectively.

As there is no evidence of gas caps in the sampled fields, we assume that the injected material will mix with the oil within the reservoir and can therefore be treated as binary mixing between the pristine system oil and the injectate:

$$[i]_{res} = [i]_{pris} \times F_{pris} + [i]_{inj} \times F_{inj} \qquad \text{(Eq. 3.13)}$$

where $[i]_{inj}$, $[i]_{pris}$, $[i]_{res}$ are the concentration of noble gas *i* in the injectate, pristine oil and reservoir after injection. The concentration of *i* in the 'pristine' oil is a function of the WOR of the system and can be calculated by rearranging equation 3.10. Although we recognise that there is likely a range in pre-development reservoir compositions, we assume a common endmember, which has not been subjected to any injection (e.g., sample F5 for the Chanac reservoir at Fruitvale), and the WOR of this sample is assumed to be representative of all pre-development system WORs within the field. In fields where an unaltered sample is not available, we used the calculations to find a best-fit WOR. F_{pris} *and* F_{inj} are the fraction of pristine oil and injectate, respectively and $F_{pris} + F_{inj} = 1$. They can be calculated using the following: $F_{inj} = V_{inj}/(V_{oil}+V_{inj})$ and $F_{pris} = V_{oil}/(V_{oil}+V_{inj})$.

By iteratively calculating the effects of injection in this way for differing F_{air}, which determines the composition of injectate, and $V_{oil,,}$ we are able to determine these parameters and their associated uncertainties using non-linear least squares minimisations for each field. The minimisation is carried out using the Levenberg-Marquardt algorithm (Marquardt, 1963), and an associated Chi-Squared value is calculated. V_{oil} and F_{air} are shared parameters between samples from the same formations, while V_{inj} is the known amount of injectate, assumed to be different for each well. Within the Fruitvale system, at 85% probability, we find that samples influenced by EOR are consistent with modelled mixtures of injectate with a best-fit fraction of air of 0.11±0.04, a total volume of oil and injectate mixture of 1.7±0.7 x 10^7 m^3, and assuming a pristine composition of sample F5 (Figure 3.4, Table 3.6). This novel noble gas approach allows us to derive an estimated oil volume for which the known volume of injected fluids must have come into contact with within the reservoir. Within the Fruitvale Oil Field, this volume of oil is 2 orders of magnitude less than maximum predictions based on simple reservoir reserve estimates and size (~2 x10^9 m^3; DOGGR, 1991a). This difference suggests that the injected water has had restricted interaction with the reservoir fluids. A combination of the V_{oil} and F_{air} will control how the system responds to injection and how it will evolve during production.

The same model was applied to both the Belridge and Lost Hills oil fields (Supplementary Figure S3.5). For samples collected within the Belridge Oil Field, we predict that the injectates have a more 'air–like' composition than at Fruitvale (Supplementary Figure S3.5, Table 3.6) and that the volume of oil exposed to the injectate (within 500m of the well) is 2 orders of magnitude greater than at Fruitvale, causing the smaller increase in $^{20}Ne/^{36}Ar$ with the same injected volume, (Figure 3.5, Table 3.6). In the Lost Hills Oil Field, the injectate fluid appears to have a larger ASW contribution and more variable pristine WOR (Supplementary Figure S3.5). However, the calculated results for the Belridge and Lost Hills oil fields were not statistically significant. It is likely that the variability within these reservoirs could be a result of: (1) differences in the injectate compositions between different injection processing tanks and injection wells; (2) differences in the ease of noble gas circulation within the field (i.e., permeability and porosity), where higher

permeability and porosity would increase circulation and allow for a greater volume of water per bulk unit and thus, a higher effective WOR; (3) differences in migration distances, as oils with longer migration distance are likely to have been exposed to greater volumes of water; (4) geo-compartmentalisation, whereby some stratigraphic units will have been subjected to greater volumes of water than others since flow is restricted by geological conditions and features such as faults; and (5) human induced variability as a result of production history. It is important to note here that these explanations are not mutually exclusive and each of these will have implications on the reservoir processes. No model has been constructed for the Orcutt field due to its large degree of geo-compartmentalisation driven by quaternary faulting across the field.

By modelling the injection within the reservoir, we are able to develop a broad reconnaissance-level understanding of the composition of the injectate and how the injectate has interacted with the pristine reservoir. As a result, the secondary overprinting of noble gas signatures by injection can be quantified. This allows for the characterisation of both the pristine reservoir and how this pristine reservoir has been perturbed and evolved with the addition of these injected fluids.

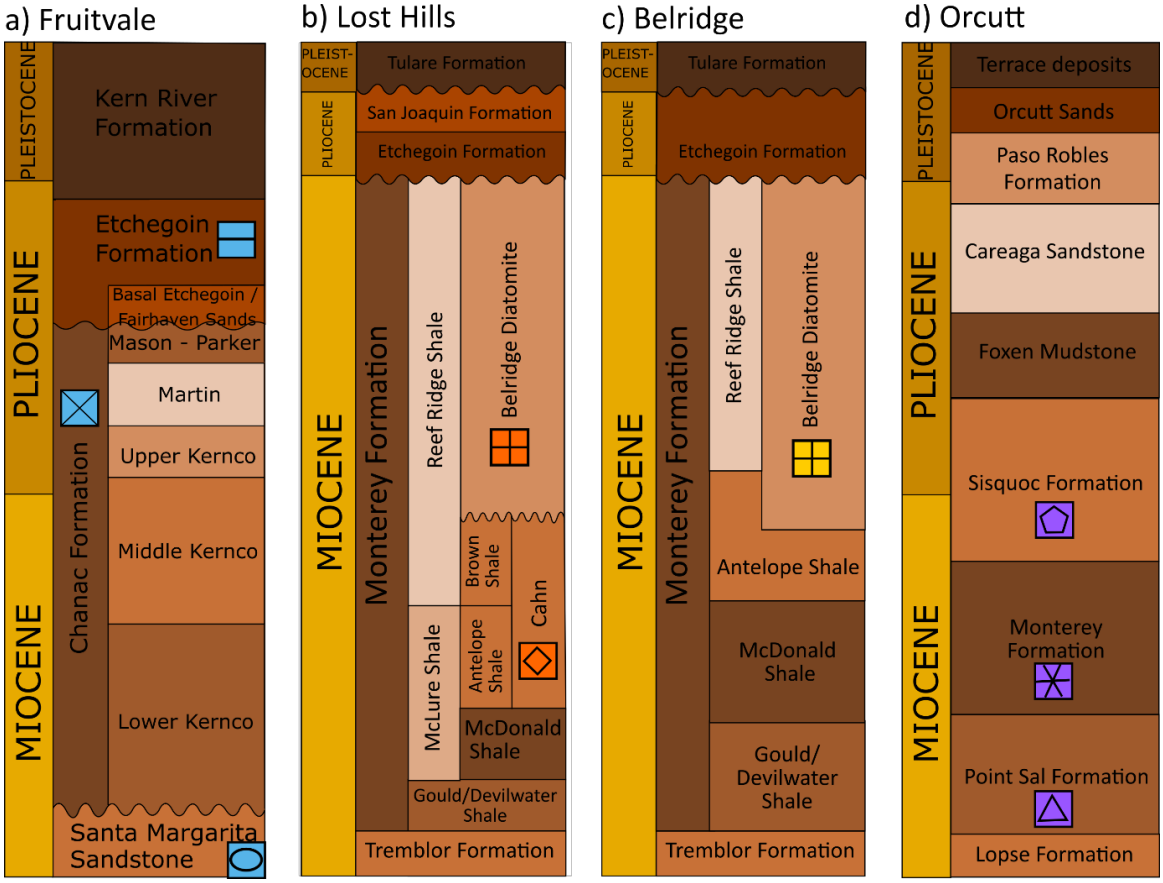
3.4. Conclusions

We present noble gas data from both casing gases and produced fluids across four oil fields (Fruitvale, Lost Hills, Orcutt and Belridge) in California, which have been subjected to variable degrees of EOR. Collecting both casing gas and produced fluid samples enables a comparison, for the first time, of these two samples types with regards to their noble gas concentrations. Concentrations of noble gases were on average 3.0±1.8 times greater in the casing gases, validating previous methods of phase and reservoir reconstructions that rely on casing gas compositions. This validation allows for direct comparison of fields where only singular sample types are available, regardless of sample type.

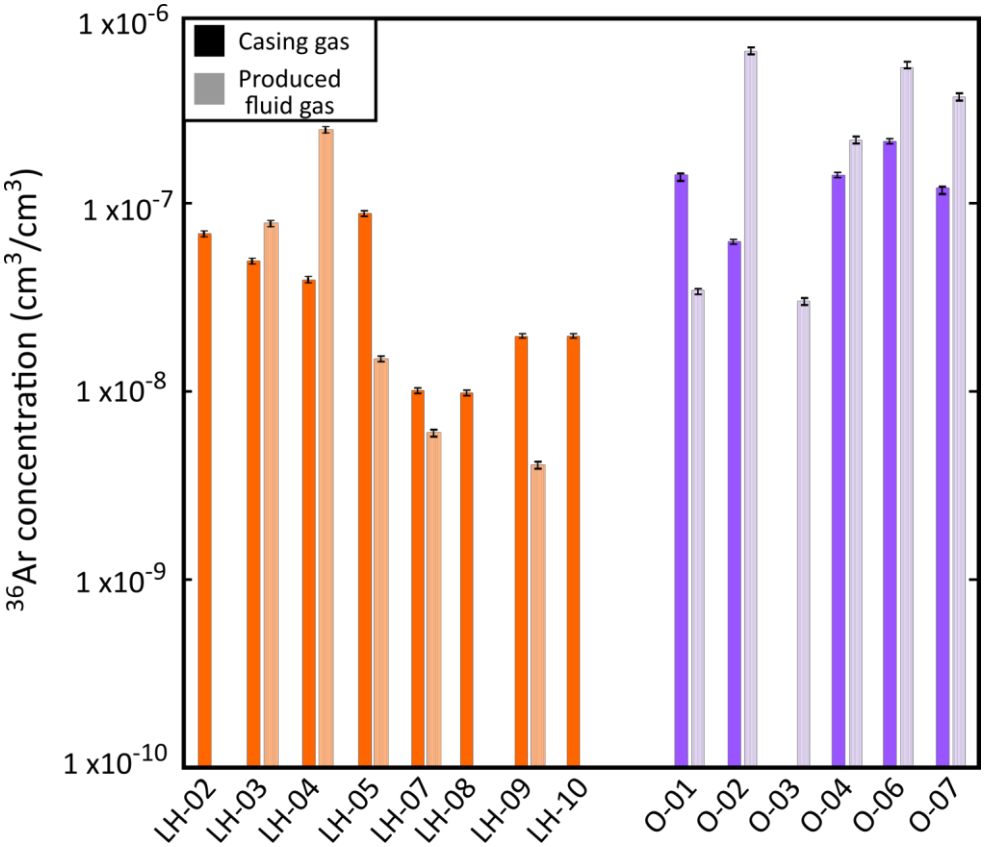
We find that $^{20}Ne/^{36}Ar$ in each of the sampled fields has a strong positive correlation with the injected volume within 500m of the sampled wells. The sensitivity of this correlation is, however, not consistent between fields, and the Fruitvale Oil Field $^{20}Ne/^{36}Ar$ values are higher as a result of

injection than the Lost Hills, Belridge and Orcutt oil fields. By developing a mixing model between the injected fluid and pristine system compositions we determine both the fraction of air injected and initial oil volume interacting with the injection fluids, which allows us to investigate how the pristine system has been perturbed during production. We conclude that the injectate composition and volume of oil are likely to be the primary controls on the magnitude of increase of $^{20}Ne/^{36}Ar$ with injection volume. This observation may help to develop a tool to quantify interaction between the injectate and reservoir fluids, however further work is needed to characterise the composition of the injectate fluids and range in possible initial WOR's within a reservoir. Understanding the composition of the pristine hydrocarbon reservoir and how it evolves with injection is critical in determining baseline endmembers for future forensic studies of groundwater quality.

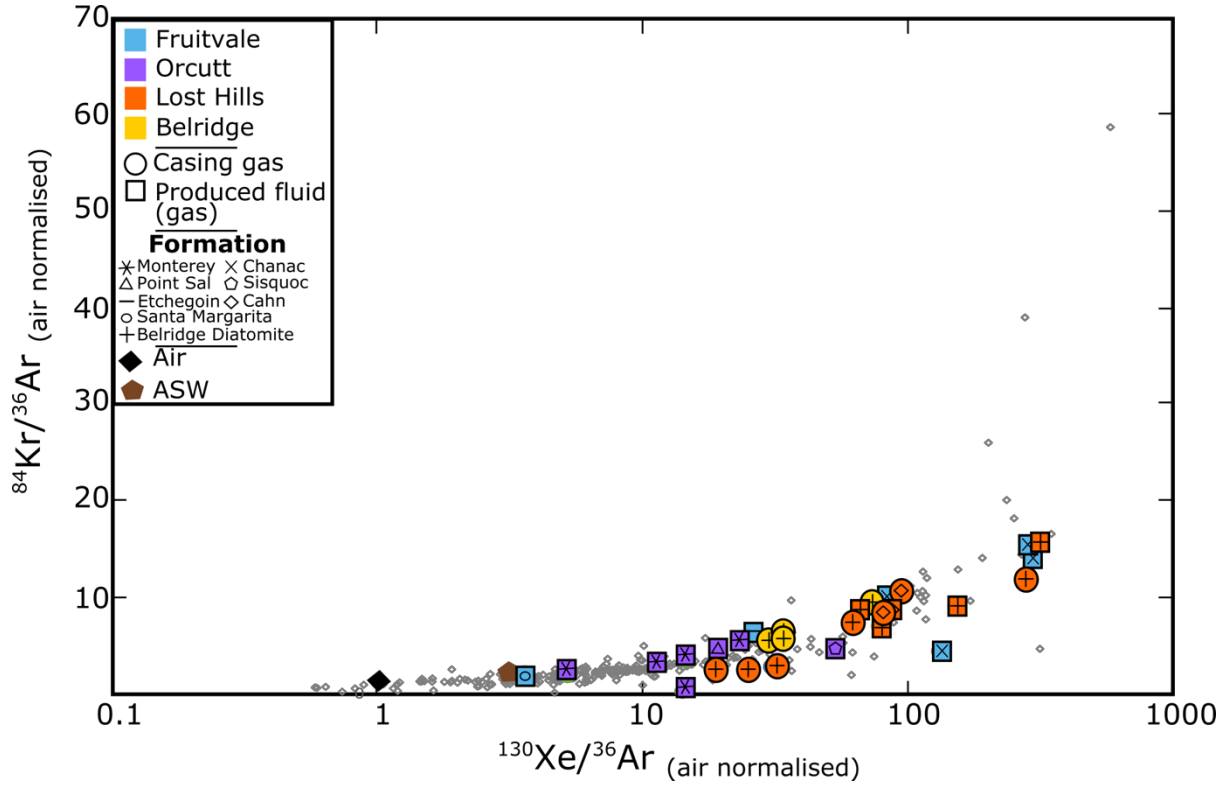
S3.1. Supplementary figures



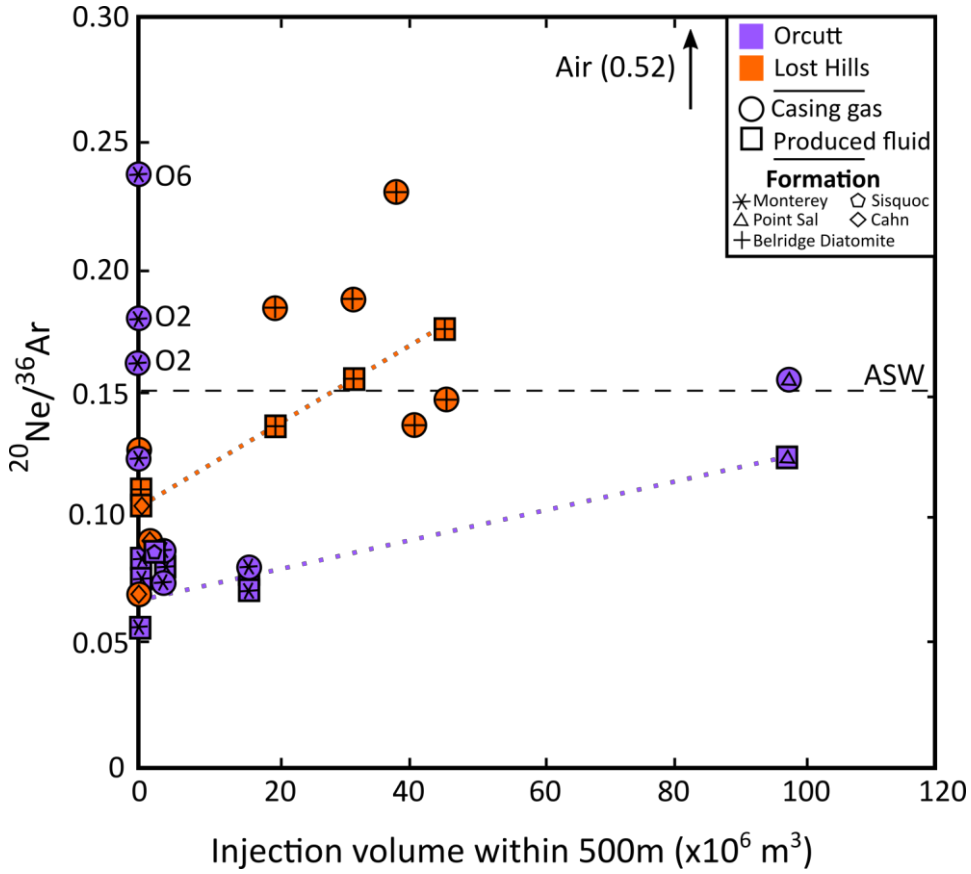
Supplementary Figure S3.1: Stratigraphic columns for the Fruitvale (a), Lost hills (b), Belridge (c) and Orcutt (d) oil fields. Intervals where samples have been taken have been indicated, and the symbols displayed are used throughout the figures.



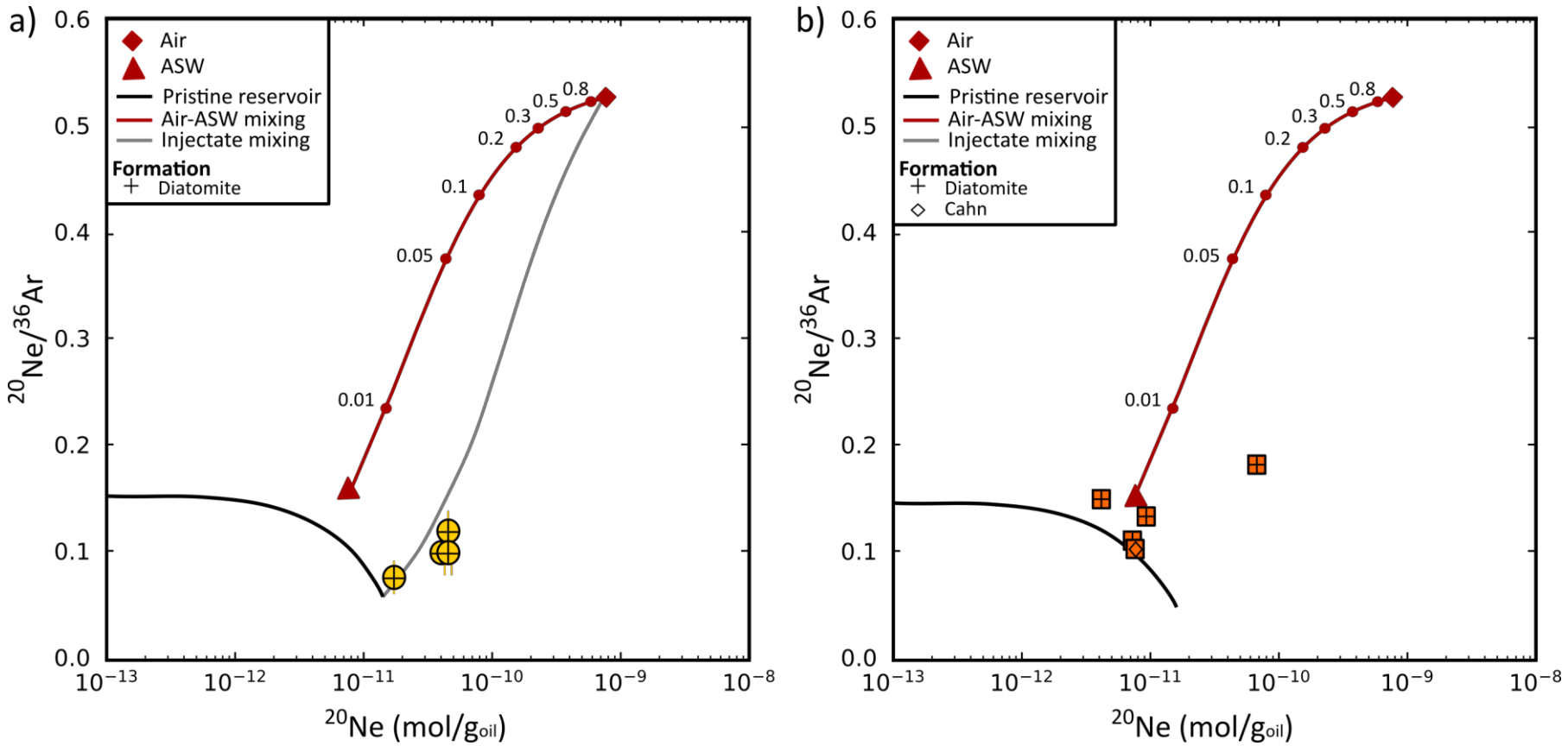
Supplementary Figure S3.2: Comparison of the ^{36}Ar concentration measured in the casing gases and in the gaseous phase of the produced fluid samples. Darker bars represent casing gas samples and lighter bars are the gaseous phase in the produced fluids. 1σ uncertainties are shown and are less than 5%. ^{36}Ar concentrations in both sample types are in broad agreement.



Supplementary Figure S3.3: Heavy noble gas (^{84}Kr and ^{130}Xe) relative to ^{36}Ar, normalised to the air ratios in study samples and in historical data. Data shows a clear excess in Kr and Xe, which is particularly noticeable in the San Joaquin Basin samples (Belridge, Lost Hills and Fruitvale). For reference, air is denoted by the black diamond and ASW by the brown pentagon. Organic rich sediments have measured Kr and Xe excesses of 0.7-1658 (Bogard et al., 1965; Torgersen and Kennedy, 1999) and 4-45000 (Bogard et al., 1965; Podosek et al., 1980) respectively. Small unfilled diamonds symbols represent previous Kr and Xe gas data from: Hearn et al., 1990; Hiyagon and Kennedy, 1992; Pinti and Marty, 1995; Torgersen and Kennedy, 1999; Holland and Ballentine, 2006; Gilfillan et al., 2008; Ma et al., 2009; Lowenstern et al., 2014; Barry et al., 2016, 2018a; Wen et al., 2017; Heard et al., 2018; Byrne et al., 2018, 2020.



Supplementary Figure S3.4: Atmosphere-derived Noble gas ratios ($^{20}Ne/^{36}Ar$) in the reservoir oil vs. volume of injected fluids (x10^6) within 500m of the sampled wells for both the produced fluids and casing gases at Lost Hills and Orcutt. Higher $^{20}Ne/^{36}Ar$ indicate more atmospheric composition. 1σ uncertainties are within the size of the symbols. Both the casing gases and produced fluids at Lost Hills show the same positive correlation, however in the Orcutt casing gases (Purple circles) we see 3 samples from 2 sites (O2 and O6) that have not seen injection within 500m and have higher $^{20}Ne/^{36}Ar$ ratios than could be accounted for by solubility, thus, these are thought to be air contaminated.



Supplementary Figure S3.5: $^{20}Ne/^{36}Ar$ vs. ^{20}Ne concentration in the reservoir, with modelled injection in the Belridge (a) and Lost Hills (b) oil fields. The solid black line represents the predicted pristine hydrocarbon evolution for the reservoir conditions within each field and the red line represents the range of possible injectate compositions (as a function of F_{air}) where the concentrations are in oil equivalents. Solid grey line represents the predicted mixing and reservoir evolution between the pristine reservoir and injectate using best fit V_t and F_{air} parameters. No pristine reservoir- injectate line is shown for the Lost Hills fields, which is due to difficulties in fitting the model over a large range of pristine WOR within the reservoir. Within the Lost Hills Oil Field, sample LH9 (which has had no injection within 500m) falls on the pristine reservoir evolution (solid black line).

S3.2. Supplementary tables

Producing member (Reservoir)	Recharge conditions Temperature (°C)	Salinity (M)	Elevation (m)	Reservoir conditions Temperature (°C)	Salinity (M)
Fruitvale					
Etchegoin	16	0	123	51	0.095
Chanac	16	0	123	51	0.095
Santa Margarita	16	0	123	51	0.095
Lost Hills					
Diatomite	17	0	0	57	0.57
Cahn	17	0	0	57	0.57
Belridge					
Diatomite	17	0	0	44	0.54
Orcutt					
Sisquoc	17	0	109	42	0.18
Monterey	17	0	109	60	0.72
Point Sal	17	0	109	74	0.48

Supplementary Table S3.1: Recharge and conditions for each oil field. Recharge conditions are sourced from average annual temperatures and elevations (Chapter 2; Barry et al., 2018a, Tyne et al., 2019). Reservoir conditions for Lost Hills are from Barry et al. (2018a). Sources for reservoir conditions in other fields have been cited within the text or can be found within Gannon et al. (2018) and Seitz et al. (2021).

S3.3. Supplementary information

S3.3.1. Geological history

S3.3.1.1. Fruitvale geological and production history

The Fruitvale Oil Field is located on the southern edge of the Bakersfield arch (a faulted southwest dipping homocline) and has been in production since 1928 (Preston, 1931). The stratigraphy of interest in order of increasing depth are the Kern River Formation (Pleistocene), Etchegoin Formation (Pliocene), Chanac Formation (Pliocene-Miocene) and the Santa Margarita Sandstone Formation (Miocene) (Hluza, 1965; CALGEM, 2020a) (Supplementary Figure S3.1a). Oil is mostly produced from the Chanac Formation, which consists of the Mason Parker, Martin and Kernco reservoirs, and are non-marine discontinuous fan deposits (Hluza, 1965; DOGGR, 1998). There is also limited production from marine deposits of the basal Etchegoin Formation and Santa Margarita Sandstone. The oil is thought to have originated from the Monterey Formation to the west of the field (Lillis and Magoon, 2007). A detailed geological history can be found in Hluza 1965.

The reservoir has a relatively low salinity of 0.095 M in comparison to other oil-fields due to significant recharge over geological timescales from the Kern River and other streams draining the Sierra Nevada (McMahon et al., 2018). Average reservoir temperature is thought to be 51.3^{o}C (CALGEM, 2020b). Oil density (relative to water; given in American Petroleum Institute (API) gravity units) is 18.5^{o} in the Chanac and Etchegoin and 16.7^{o} in the Santa Margarita reservoir. Porosity within the reservoirs is ~ 25% (Stephens, et al., 2019). Permeability within the Chanac Formation is between 2-3mD, however, permeability is significantly higher in the Santa Margarita Formation where it averages 975mD (EPA, 2016). There is no evidence of gas cap formation (DOGGR 1998; CALGEM, 2020a). Average field parameters can be found in Supplementary Table S3.1.

Injection of fluids for both water disposal and EOR began in the 1960's, with a combination of water flooding (since 1962), cyclic steam injection (since 1964) and water disposal. Over 87 million m^3 of water was injected between 1977 and 2018 (CALGEM, 2020b). The majority of the injected water is produced water from the oil wells, however there is a small proportion of wastewater from

refineries (Wright et al., 2019). Injection has not caused any significant change in reservoir salinity (Stephens et al., 2019). A combination of the long production-injection history at the Fruitvale Field has resulted in temporal variations in the overall hydrocarbon and produced water production volumes (McMahon et al., 2018). For sample wells that have seen injection, injected volumes are between 3.01 and 9.71 $x10^6$ m^3.

S3.3.1.2. Lost Hills geological and production history

Oil production at Lost Hills began in 1910. The oil field is located on an asymmetrical northwest doubly plunging anticline that formed from a fault bend fold initiated by a step in the Lost Hills thrust fault (Medeweff, 1989). The stratigraphy of the anticline with increasing depth is: alluvium; Tulare Formation (Pleistocene, fluvial sands and clays); Upper Etchegoin Formation (Pliocene, marine diatomaceous sands and clays); Lower Etchegoin Formation (Pliocene, low permeability marine diatomaceous sands and clays) and; Monterey Formation (Miocene Belridge Diatomite /brown shales of the reef ridge shale and the Cahn Cherts) (Supplementary Figure S3.1b). A detailed geological history for the field can be found in Land, 1984.The source rock is believed to be within the Miocene Monterey Formation, (Philippi, 1965, Kruge and Williams, 1982; Kruge, 1986). Most of the hydrocarbons found within the formation are solvent extractable, which suggest that the hydrocarbons have migrated from a different source or they were formed at relatively low thermal maturity (Claypool et al., 1979). The Belridge Diatomite (304-914m deep) is the main reservoir unit, however, there is additional production in both deeper and shallower units, such as the deeper Cahn Cherts. During production, no separate gas phase has been encountered in either reservoir (CALGEM, 2020a, 2020b).

The permeability and porosity in the Belridge Diatomites are variable due to changes in clay, sand and silt content across the formation and the transition of the silica in the diatoms and microplankton from Opal-A to Opal CT, due to dissolution and re-precipitation (Mizutani, 1977; Pisciotto and Garrison, 1981; Soutar et al., 1981). However, in general they have high porosity (up to 65%) and low permeability (~0.1mD; Barry et al., 2018a), which results in some difficulties during extraction and a high density of wells required. Variability in porosity and other reservoir properties, along

with reservoir evolution with production and EOR have resulted in a reservoir temperature range between 44-69ºC and salinities from 0.54M to 0.6M (Supplementary Table S3.1) (CALGEM, 2020a). Oil density is homogenous across the wells sampled at 23.1º, with the exception of LH-O5, which is 21.5º.

In Lost Hills, the Belridge Diatomite has undergone a mixture of water flooding, CO_2 flooding and hydraulic fracturing since 1962 and the Tulare formation has been steam flooded since 1964 (Land, 1984). The breakthrough time for this these fluids to the producing wells has been shown to be less than a month (Zhou et al, 2002). Production within the Diatomite is also commonly stimulated by hydraulic fracturing (Jordan and Heberger, 2014). Water disposal at Lost Hills has also increased from 160000m^3/yr in 1973 to 4.8 million m^3 in 2009 (Gillespie et al., 2019). This disposal was initially into both the Tulare and Etchegoin formation, however from 1990 disposal was solely into the Etchegoin Formation. With the exception of LH-09, all wells have been subjected to some EOR fluid injection within 500m of the well; the amount of injected fluid to these wells varies between $5.1x10^4$ - $4.7x10^7$ m^3. Injected volumes in the field have only been digitised since 1977, however it is believed injection prior to this only accounts for 2% of the total injection in the field.

S3.3.1.3. Belridge geological and production history

Oil was discovered at Belridge between 1911 (South Belridge) and 1912 (North Belridge). The fields were developed on an elongated anticline. Oil and gas producing wells penetrate into the Tulare (Pleistocene), Diatomite (Miocene Monterrey) and Temblor (Oligocene) formations (Supplementary Figure S3.1c). A more detailed geological history can be found in Miller et al. (1990), Taylor and Soule (1993), Hill et al. (1995), Fredrich et al. (2000) and Allan and Lalicata (2011). Hydrocarbons in the Temblor Formation are thought to be from Eocene source rocks, whereas oils in the Diatomite and Tulare formations are thought to have been sources from the Monterey Shales to the east of the field (Allan and Lalicata, 2011).

Similarly to within Lost Hills, changes in clay, sand and silt content across the formation and the transition from Opal-A to Opal CT of silica in the diatoms and microplankton, have caused variable porosity and permeability within the Diatomite Formation (Mizutani, 1977; Pisciotto and Garrison,

1981; Soutar et al., 1981). Average effective porosity in the Diatomite reservoir is 36.7- 55.4% and permeability between 0.1-1mD (Allan and Lalicata, 2012). Within the Tulare Formation porosity ranges from 30-40% and permeability from 35- 4000mD (EPA, 2019). Porosity in the Temblor Formation is between 10 and 40% and permeability varies from 7-10,000mD (Downey and Clinkenbeard, 2005). Oil density within the sampled Diatomite Formation range from 22.2° to 32° (Table 3.2), while the shallower formations are expected to have heavier oil (11-15°; Smith, 2012). Measured reservoir fluid salinity were 0.54 -0.65M and temperatures were 44.8-99.4°C with the average temperature of 60.8°C (Supplementary Table S3.1; Gannon et al., 2018). Production data is not consistent with a gas cap present in the Diatomite reservoirs (DOGGR, 1998, CALGEM 2020a).

South Belridge has been subjected to steam and water flooding and hydraulic fracturing (DOGGR, 1998). The field has seen the largest total volume of water and steam injection of the sampled fields (~1400 million m^3 from 1960-2017; DOGGR 2018). Water disposal is almost entirely into the Tulare Formation. 98.2% of injection in the North Belridge Oil Field is for EOR. The sampled wells form Belridge have injected volumes of between 2.24 to 3.64 $x10^7 m^3$ water within 500m (DOGGR 2018)

S3.3.1.4. Orcutt geological and production history

Oil was first discovered in the Orcutt Oil Field in 1901, and the production in the field began shortly after (Isaacs, 1992). It was originally named the 'Santa Maria' Oil Field and changed its name to 'Orcutt' due to the discovery of a much larger field nearby. The Santa Maria basin is defined by west-northwest trending open fold and some narrow closely spaced fold, with sub parallel Cenozoic age faults (Namson and Davis, 1990). The Orcutt Oil Field lies on one of these anticlines, known as the Orcutt Anticline which is a broad flat crested asymmetrical anticline and is likely a fault bend fold from the Pruisana –Solom Thrust (Namson and Davis, 1992). Additional second order folds, which initiated 6-3Ma, are present because of continued shortening (Woodring and Bramlette, 1950; Isaacs, 1992; Namson and Davis, 1992). Notably, there are numerous west-northwest trending high angle faults cut the anticline, the most important being the Orcutt Fault, which is a

reactivated normal fault, which have created an ideal trap for the oil. The stratigraphy of interest in ascending order consists of: 1) Early-mid Miocene Point Sal Formation (marine facies consisting of siltstone mudstone and thin sandstones); 2) Miocene Monterey Formation (shale, cherts and diatoms); 3) Late Miocene- Early Pliocene Sisquoc Formation (diatom rich and includes Tinsquaic sandstone and the basin facies); 4) Mid-Late Pliocene Foxon Formation (mud and silt stones); 5) Late Pliocene-Pleistocene Paso Robles (sand gravel and clays) 6) Recent Pleistocene deposits (Orcutt sands, terraces and alluvium) (Supplementary Figure S3.1d) Woodring and Bramlette, 1950; Isaacs, 1992) . The Monterey Formation consists of 3 members, i) lower phospahtic shale and porcelaneous shale, ii) mid chert and cherty shales, iii) upper-procelaneous shale and diatomaceous strata). Oil is thought to have been generated in Monterey Formation within the syncline between the Orcutt and Lompoc oil fields, where they diagenetic grade and thermal maturity potential is greatest (Pisciotto, 1981; Isaacs and Tomson, 1990). Within the Orcutt Oil Field, most of the production is from the fractured rocks within the Monterey Formation (75%), with limited production from other fractured rocks (2%). The remaining production is from the Point Sal Formation and Sisquoc Formation which act as conventional reservoirs (Crawford, 1971; DOGGR, 1991a, 1991b).

Reservoir temperatures vary from 49-71^{o}C across the reservoir, due to changes in reservoir properties (e.g., porosity) and differential production and EOR. Oil density is also variable between 14- 27.5^{o} across the reservoir; however, the samples were largely homogenous at 21.4^{o} with only O-02 at 22.9^{o} (Table 3.2). Well logs from the Orcutt Oil Field give average temperatures for the Monterey Formation at 60ºC, Point Sal Formation at 74ºC and Sisquoc Formation at 42ºC. Salinities in the formation waters are 0.72M, 0.48M and 0.18M for the Monterey, Point Sal and Sisquoc respectively (CALGEM, 2020a, Seitz 2021). Porosity in the different formations vary from 15-70% and permeability is thought to be ~5-10mD (Beyer et al., 1985; Carpenter, 2016) There is no evidence for gas nor a secondary gas cap within the field (CALGEM, 2020b).

Cyclic steam injection into the Diatomite in the Monterey Formation at Orcutt began in 2005 and now 96 wells in the field are using this technique (Land, 1984; Elias et al., 2010; Pacific Coast Oil

Trust, 2020). During this process, steam is injected into the reservoir and left to soak for a few days before the well is produced by flowing the hot oil and water to the surface, and repeated. Additionally, since 2009, the Sisquoc Formation has been water flooded in order to maintain reservoir pressure. O-02 and O-06 have not been affected by injection, the remaining wells have with between $2.0x10^6$ – $9.8x10^7 m^3$ injected within 500m of the wells. Hydraulic fracturing was allegedly trialled in the field in 1991 (Kamori and Hauksson, 1992).

Acknowledgements, Samples and Data

This work was supported by a Natural Environment Research Council studentship to R.L.Tyne (Grant ref. NE/L002612/1) and the USGS (Grant ref. 15-080-250), as part of the California State Water Resource Control Board's, Oil and Gas Regional Groundwater Monitoring Program (RMP). Data can be accessed in Tables 3.2-3.4 and in the data release from Gannon et al. (2018) and Seitz et al. (2021). We thank the owners and operators at the Fruitvale, Lost Hills, Belridge and Orcutt Oil Fields for access to wells. We also thank Matt Landon and Jennifer Harkness from the USGS who provided helpful comments on an earlier version of the manuscript.

Authorship Statement

I hereby give permission to Rebecca L. Tyne to use our joint work as contribution towards her DPhil thesis to be submitted for examination at the University of Oxford.

I confirm that to the best of my knowledge, the author contribution statement below is accurate and Rebecca L. Tyne's contribution towards the work is greater than that of any other co-author.

Chapter author contribution statement:

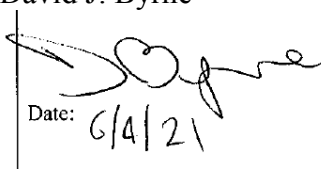
The project was conceived by RLT, PHB, JTK and CJB. RLT managed the project and prepared the first draft of the manuscript. RLT, PHB, JTK and CJB collected the samples. RLT and PHB performed the noble gas isotopic analysis, supported by DJH and DJB. Noble gas reconstructions and models were developed by RLT, PHB, RK, DJB and CJB. All authors contributed to the final manuscript.

Chris J. Ballentine



Date: 13/04/2021

David J. Byrne



Peter H. Barry



Date: 6-4-2021

Justin T. Kulongoski



Date: 7/4/2021

Rūta Karolytė



Date: 7/4/2021

Darren J. Hillegonds



References

Aeschbach-Hertig W., Peeters F., Beyerle U. and Kipfer R. (1999) Interpretation of dissolved atmospheric noble gases in natural waters. *Water Resources Research* **35**, 2779–2792.

Allan M. E. and Lalicata J. J. (2012) The Belridge Giant Oil Field - 100 Years of History and a Look to a Bright Future. *Search and Discovery Article, 20124*.

Ballentine, C.J., Burgess, R., Marty, B. (2002). Tracing Fluid Origin, Transport and Interaction in the Crust. In: *Noble Gases in Geochemistry and Cosmochemistry.(*Eds: D. Porcelli, C.J. Ballentine,, R. Wieler) Reviews in Mineralogy and Geochemistry **47**. Geochemical Society, Mineralogical Society of America, Chapter 13, 539–614.

Ballentine C. J. and Hall C. M. (1999) Determining paleotemperature and other variables by using an error-weighted, nonlinear inversion of noble gas concentrations in water. *Geochimica et Cosmochimica Acta* **63**, 2315–2336.

Ballentine C. J., O'Nions R. K. and Coleman M. L. (1996) A Magnus opus: Helium, neon, and argon isotopes in a North Sea oilfield. *Geochimica et Cosmochimica Acta* **60**, 831–849.

Ballentine C. J., O'Nions R. K., Oxburgh E. R., Horvath F. and Deak J. (1991) Rare gas constraints on hydrocarbon accumulation, crustal degassing and groundwater flow in the Pannonian Basin. *Earth and Planetary Science Letters* **105**, 229–246.

Barry P.H., Kulongoski J. T., Tyne R. L., Landon M. K., Gillespie J. M., Stephens M. J., Hillegonds D. J., Byrne D. J. and Ballentine C. J. (2018a) Tracing enhanced oil recovery signatures in casing gases from the Lost Hills oil field using noble gases. *Earth and Planetary Science Letters* **496**, 57–67.

Barry P. H., Lawson M., Meurer W. P., Cheng A. and Ballentine C. J. (2018b) Noble Gases in Deepwater Oils of the U.S. Gulf of Mexico. *Geochemistry, Geophysics, Geosystems* **19**, 4218–4235.

Barry, P.H., Lawson, M., Meurer, W.P., Danabalan, D., Byrne, D.J., Mabry, J.C. and Ballentine, C.J. (2017). Determining fluid migration and isolation times in multiphase crustal domains using noble gases. *Geology*, ***45***(9), 775-778.

Barry P. H., Lawson M., Meurer W. P., Warr O., Mabry J. C., Byrne D. J. and Ballentine C. J. (2016) Noble gases solubility models of hydrocarbon charge mechanism in the Sleipner Vest gas field. *Geochimica et Cosmochimica Acta* **194**, 291–309.

Beyer, L.A., Robbins, S.L., Clutsom, F.G., (1985) Basic data and preliminary density and porosity profiles for twelve borehole gravity surveys made in the Lost Angeles, San Joaquin, Sana Maria and Ventura Bains, California. USGS Report 85-42.

Bogard D. D., Rowe M. W., Manuel O. K. and Kuroda P. K. (1965) Noble gas anomalies in the mineral thucholite. *Journal Geophysical. Research* **70**, 703–708.

Bosch, A., Mazor, E., 1988. Natural gas association with water and oil as depicted by atmospheric noble gases: case studies from the southeastern Mediterranean Coastal Plain. *Earth Planetary Science Letters* **87**, 338–346.

Burnard, P., 2013. *The Noble Gases as Geochemical Tracers*. (Ed. P. Burnard). Advances in Isotope Geochemistry. Springer, Berlin, Heidelberg.

Byrne D. J., Barry P. H., Lawson M. and Ballentine C. J. (2018) Determining gas expulsion vs retention during hydrocarbon generation in the Eagle Ford Shale using noble gases. *Geochimica et Cosmochimica Acta* **241**, 240–254.

Byrne D. J., Barry P. H., Lawson M. and Ballentine C. J. (2020) The use of noble gas isotopes to constrain subsurface fluid flow and hydrocarbon migration in the East Texas Basin. *Geochimica et Cosmochimica Acta* **268**, 186–208.

CalGEM (2020a) *Online Production and Injection Data*., California Department of Conservation, CalGEM publication. Available at: ftp://ftp.consrv.ca.gov/pub/oil/Online_Data/Production_Injection_Data. [Accessed June 2020]

CALGEM (2020b) *Online Well data*. Available at: https://secure.conservation.ca.gov/WellSearch.

California State Water Resources Control Board (2020) Water quality in areas of oil and gas production – Regional Groundwater Monitoring. California State Water Resources Control

Board, Available at: https://www.waterboards.ca.gov/water_issues/programs/groundwater/sb4/regional_monitoring/. [Accessed December 2020]
Carpenter, C. (2016) Case Study: Steam-Injection Step Rates Tests Run in the Orcutt Oil Field. *Journal of Petroleum Technology* **68**(06) 78-79.
Claypool G. E., Baysinge J. P., Lubeck C. M. and Love A. H. (1979) *Organic geochemistry*., USGS.
Crawford F. D. (1971) Petroleum Potential of Santa Maria Province, California: Region **2**(128) 316–328.
Crovetto, R., Fernández-Prini, R., Japas, M. L. (1982) Solubilities of inert gases and methane in H_2O and in D_2O in the temperature range of 300 to 600 K. *Journal Chemical Physics* **76**, 1077-1086.
Darrah T. H., Jackson R. B., Vengosh A., Warner N. R., Whyte C. J., Walsh T. B., Kondash A. J. and Poreda R. J. (2015) The evolution of Devonian hydrocarbon gases in shallow aquifers of the northern Appalachian Basin: Insights from integrating noble gas and hydrocarbon geochemistry. *Geochimica et Cosmochimica Acta* **170**, 321–355.
Darrah T. H., Vengosh A., Jackson R. B., Warner N. R. and Poreda R. J. (2014) Noble gases identify the mechanisms of fugitive gas contamination in drinking-water wells overlying the Marcellus and Barnett Shales. *Proceedings of the National Academy of Sciences* **111**, 14076–14081.
Division of Oil Gas and Geothermal Resources (DOGGR), (2017). GIS Mapping, DOGGR, Sacramento, CA. http://www.conservation.ca.gov/dog/maps/Pages/GISMapping2.aspx (Accessed online May 2017).
DOGGR (1991a) *California oil and gas fields*. California Department of Conservation, DOGGR publication.
DOGGR (1991b) *76th Annual Report of the State Oil and Gas Supervisor*., California Department of Conservation, DOGGR publication.
DOGGR (1998) *California oil and gas fields volume 1-Central California*., California Department of Conservation, DOGGR publication. Available at: ftp://ftp.consrv.ca.gov/pub/oil/publications/Datasheets/Dtasheet_vol_1.pdf. [Accessed January 2020]
DOGGR (2018). Oil & Gas Online Data. California Department of Conservation, DOGGR publication. Available at: http://www.conservation.ca.gov/dog/Online_Data/Pages/Index.aspx. [Accessed May 2018]
Downey, C. and Clinkenbeard, J.C. (2005) An Overview of geological carbon sequestration potential in California. CGS Special report. West Coast Regional Carbon Sequestration Partnership. California Geological Survey Sacramento. Available at: https://www.osti.gov/servlets/purl/903323
Elias R., Wilson M. L., Vassilellis G. D. and Bust V. K. (2010) Successful Thermal Recovery of Heavy Oil from an Ultratight Reservoir Renews Development of the 100-Year-Old Orcutt Oil Field. In: *SPE Annual Technical Conference and Exhibition*. Society of Petroleum Engineers. Available at: https://www.onepetro.org/conference-paper/SPE-135520-MS [Accessed June 3, 2019].
EPA, (2015). Assessment of the Potential Impacts of Hydraulic Fracturing for Oil and Gas Drinking Water Resources. External Review Draft, EPA/600/R-15/047, June 2015.
EPA. (2016) Aquifer exemption record of decision. South Belridge Oil Field-Tulare Formation Available at: https://www.epa.gov/sites/production/files/2017-02/documents/fruitvale_rod.pdf [Accessed November 2020]
EPA. (2019) Aquifer exemption record of decision. Santa Margarita Formation of the Fruitvale Oil Field. Available at: https://www.epa.gov/sites/production/files/2020-03/documents/epa_rod_south_belridge_ae-2020-03-13.pdf [Accessed November 2020]
ESRI, 2020. World Topographic map. https://www.arcgis.com/home/item.html?id=30e5fe3149c34df1ba922e6f5bbf808f [Accessed October 2019]
Fernández-prini, R., Alvarez, J.L., Harvey, A.H., Ferna, R. (2003) Henry 's Constants and Vapor – Liquid Distribution Constants for Gaseous Solutes in H_2O and D_2O at High Temperatures

Henry 's Constants and Vapor. *Journal of Physical and Chemical Reference Data* **32** , 903-916.

Fredrich, J.T., Arguello, J.G. (2000). Geomechanical modelling of reservoir compaction, surface subsidence, and casing damage at the Belridge Diatomite field. *SPE Reservoir Evaluation & Engineering* **3**(04), 348–359.

Gannon, R.S., Saraceno, J.F., Kulongoski, J.T., Teunis, J.A., Barry, P.H., Tyne, R.L., Kraus, T.E.C., Hansen, A.M., and Qi, S.L. (2018) Produced water chemistry data for the Lost Hills, Fruitvale, and North and South Belridge study areas, Southern San Joaquin Valley, California: U.S. Geological Survey data release.

Gilfillan S. M. V., Ballentine C. J., Holland G., Blagburn D., Lollar B. S., Stevens S., Schoell M. and Cassidy M. (2008) The noble gas geochemistry of natural CO_2 gas reservoirs from the Colorado Plateau and Rocky Mountain provinces, USA. *Geochimica et Cosmochimica Acta* **72**, 1174–1198.

Gilfillan S. M. V., Lollar B. S., Holland G., Blagburn D., Stevens S., Schoell M., Cassidy M., Ding Z., Zhou Z., Lacrampe-Couloume G. and Ballentine C. J. (2009) Solubility trapping in formation water as dominant CO_2 sink in natural gas fields. *Nature* **458**, 614–618.

Gillespie J. M., Davis T. A., Stephens M. J., Ball L. B. and Landon M. K. (2019) Groundwater salinity and the effects of produced water disposal in the Lost Hills–Belridge oil fields, Kern County, California. *Environmental Geosciences* **26**, 73–96.

Graham D. W. (2002) Noble Gas Isotope Geochemistry of Mid-Ocean Ridge and Ocean Island Basalts: Characterization of Mantle Source Reservoirs. In: *Noble Gases in Geochemistry and Cosmochemistry.*(Eds: D. Porcelli, C.J. Ballentine,, R. Wieler) Reviews in Mineralogy and Geochemistry **47**. Geochemical Society, Mineralogical Society of America, Chapter 8, 247–317.

Györe D., Gilfillan S. M. V. and Stuart F. M. (2017) Tracking the interaction between injected CO_2 and reservoir fluids using noble gas isotopes in an analogue of large-scale carbon capture and storage. *Applied Geochemistry* **78**, 116–128.

Györe D., Stuart F. M., Gilfillan S. M. V. and Waldron S. (2015) Tracing injected CO_2 in the Cranfield enhanced oil recovery field (MS, USA) using He, Ne and Ar isotopes. *International Journal of Greenhouse Gas Control* **42**, 554–561.

Harkness J. S., Darrah T. H., Warner N. R., Whyte C. J., Moore M. T., Millot R., Kloppmann W., Jackson R. B. and Vengosh A. (2017) The geochemistry of naturally occurring methane and saline groundwater in an area of unconventional shale gas development. *Geochimica et Cosmochimica Acta* **208**, 302–334.

Heard A. W., Warr O., Borgonie G., Linage B., Kuloyo O., Fellowes J. W., Magnabosco C., Lau M. C. Y., Erasmus M., Cason E. D., van Heerden E., Kieft T. L., Mabry J. C., Onstott T. C., Sherwood Lollar B. and Ballentine C. J. (2018) South African crustal fracture fluids preserve paleometeoric water signatures for up to tens of millions of years. *Chemical Geology* **493**, 379–395.

Hearn E. H., Kennedy B. M. and Truesdell A. H. (1990) Coupled variations in helium isotopes and fluid chemistry: Shoshone Geyser Basin, Yellowstone National Park. *Geochimica et Cosmochimica Acta* **54**, 3103–3113.

Hill, D.W., Sande, J.J., Doe, P.H. (1995) Oil gravity distribution in the diatomite at South Belridge Field, Kern County, CA: Implications for oil sourcing and migration. *AAPG Bulletin* **79**(4)

Hiyagon H. and Kennedy B. M. (1992) Noble gases in CH_4-rich gas fields, Alberta, Canada. *Geochimica et Cosmochimica Acta* **56**, 1569–1589.

Holland G. and Ballentine C. J. (2006) Seawater subduction controls the heavy noble gas composition of the mantle. *Nature* **441**, 186–191.

Hluza A. G. (1965) *Main area of Fruitvale oil field*: California division of oil and gas. Summary of Operations, **51**(2)

Hummel, 2009. The Orcutt Oil Field: How stratigraphic Relationships Reflect the Structural and Tectonic History. AAPG Search and Discovery article (9088). Pacific Section Meeting, Ventura, California, May 3-5.

Hunt A. G., Darrah T. H. and Poreda R. J. (2012) Determining the source and genetic fingerprint of natural gases using noble gas geochemistry: A northern Appalachian Basin case study. *AAPG Bulletin* **96**, 1785–1811.

Isaacs C. M. (1992) *Preliminary petroleum geology background and well data for oil samples in the cooperative Monterey organic geochemistry study, Santa Maria and Santa Barbara-Ventura basins- California.*, USGS open file report, 92-539-F

Isaacs C. M. and Tomson J. H. (1990) *Reconnaissance study of petroleum source-rock characteristics of core samples from the Sisquoc and Monterey Formations in a north-south subsurface transect across the onshore Santa Maria basin and in surface sections along the Santa Barbara-Ventura coast, Southern California*., USGS open file report, 89-108.

Jordan P. D. and Heberger M. G. (2014) Historic and Current Application of Well Stimulation Technology in California. In *Advanced Well Stimulation Technologies in California US Bureau of Land Management)*.California Council on Science and Technology Lawrence Berkeley National Laboratory Pacific Institute. Sacramento, Ca.

Kamori, H. and Hauksson, E. (1992) A slow earthquake in the Santa Maria Basin, California. *Bulletin of the Seismological Society of America*. **82**(5), 2087-2096.

Kharaka, Y.K., Specht, D.J., 1988. The solubility of noble gases in crude oil at 25-100 ºC. *Applied Geochemistry* **3**, 137–144.

Kipfer R., Aeschbach-Hertig W., Peeters F. and Stute M. (2002) Noble gases in Lakes and Groundwaters. In: *Noble Gases in Geochemistry and Cosmochemistry.(*Eds: D. Porcelli, C.J. Ballentine,, R. Wieler) Reviews in Mineralogy and Geochemistry **47**. Geochemical Society, Mineralogical Society of America, Chapter 14, 615–700.

Kruge M. A. (1986) Biomarker geochemistry of the Miocene Monterey Formation, West San Joaquin Basin, California: Implications for petroleum generation. *Organic Geochemistry* **10**, 517–530.

Kruge M. A. and Williams L. A. (1982) Silica diagenesis in the Monterey Formation (Miocene) in the Lost Hills oil field, San Joaquin Valley, California. *AAPG Bulletin*, 37–42.

Kulongoski, J. T., D. R. Hilton, and J. A. Izbicki (2003), Helium isotope studies in the Mojave Desert, California: implications for ground-water chronology and regional seismicity, *Chemical Geology* **202**(1-2), 95-113.

Kulongoski, J. T., D. R. Hilton, and J. A. Izbicki (2005), Source and movement of helium in the eastern Morongo groundwater Basin: The influence of regional tectonics on crustal and mantle helium fluxes, *Geochimica et Cosmochimica Acta*, **69**(15), 3857-3872.

Kulongoski, J. T., D. R. Hilton, P. H. Barry, B. K. Esser, D. Hillegonds, and K. Belitz (2013), Volatile fluxes through the Big Bend section of the San Andreas Fault, California: Helium and carbon-dioxide systematics, *Chemical Geology* **339**, 92-102.

LaForce T., Ennis-King J., Boreham C. and Paterson L. (2014) Residual CO_2 saturation estimate using noble gas tracers in a single-well field test: The CO_2CRC Otway project. *International Journal of Greenhouse Gas Control* **26**, 9–21.

Land P. E. (1984) *Lost Hills Oil Field*., California Department of Conservation, Division of Oil and Gas (TR32)

Lee J.-Y., Marti K., Severinghaus J. P., Kawamura K., Yoo H.-S., Lee J. B. and Kim J. S. (2006) A redetermination of the isotopic abundances of atmospheric Ar. *Geochimica et Cosmochimica Acta* **70**, 4507–4512.

Lillis P. G. and Magoon L. B. (2007) *Petroleum systems of the San Joaquin Basin Province, California - geochemical characteristics of oil types.* In: Petroleum systems and geologic assessment of oil and gas in the San Joaquin Basin Province, California, Reston, VA. Chapter 9.

Lowenstern J. B., Evans W. C., Bergfeld D. and Hunt A. G. (2014) Prodigious degassing of a billion years of accumulated radiogenic helium at Yellowstone. *Nature* **506**, 355–358.

Ma L., Castro M. C. and Hall C. M. (2009) Atmospheric noble gas signatures in deep Michigan Basin brines as indicators of a past thermal event. *Earth and Planetary Science Letters* **277**, 137–147.

Marquardt D. W. (1963) An Algorithm for Least-Squares Estimation of Nonlinear Parameters. *Journal of the Society for Industrial and Applied Mathematics* **11**, 431–441.

McMahon P. B., Kulongoski J. T., Vengosh A., Cozzarelli I. M., Landon M. K., Kharaka Y. K., Gillespie J. M. and Davis T. A. (2018) Regional patterns in the geochemistry of oil-field water, southern San Joaquin Valley, California, USA. *Applied Geochemistry* **98**, 127–140.

Medeweff D. A. (1989) Growth Fault-Bend Folding at Southeast Lost Hills, San Joaquin Valley, California. *AAPG Bulletin* **73**.

Miller, D.D., McPherson, J.G., Covington, T.E. (1990) Fluviodeltaic reservoirs, South Belridge Field, San Joaquin Valley, California. *Casebooks in Earth Science: Sandstone Petroleum reservoirs.* (Eds: Barwis, McPherson, Studlick). Springer. New York.

Mizutani S. (1977) Progressive ordering of cristobalitic silica in the early stage of diagenesis. *Contributions to Mineralogy and Petrology* **61**, 129–140.

Namson J. and Davis T. L. (1992) *Late Cenozoic thrust ramps of southern California*. Final Report for 1991 Contract. Southern California Earthquake Center., Southern California Earthqake centre.

Pacific Coast Oil Trust (2020) Pacific Coast Oil Trust - Trust Overview - Properties Overview. *Properties overview*. Available at: http://royt.q4web.com/trust-overview/properties-overview/default.aspx [Accessed October 7, 2020].

Philippi G. T. (1965) On the depth, time and mechanism of petroleum generation. *Geochimica et Cosmochimica Acta* **29**, 1021–1049.

Pinti D. L. and Marty B. (1995) Noble gases in crude oils from the Paris Basin, France: Implications for the origin of fluids and constraints on oil-water-gas interactions. *Geochimica et Cosmochimica Acta* **59**, 3389–3404.

Pisciotto K. A. (1981) Diagenetic trends in the siliceous facies of the Monterey Shale in the Santa Maria region, California. *Sedimentology* **28**, 547–571.

Pisciotto K. A. and Garrison R. E. (1981) Lithofacies and Depositional Environments of the Monterey Formation, California. In: *The Monterey Formation and related siliceous rocks of California.* Pacific Society of Economic Palaeontologist and Mineralogists. 97–122.

Podosek F. A., Honda M. and Ozima M. (1980) Sedimentary noble gases. *Geochimica et Cosmochimica Acta **44**, 1875–1884.*

Preston H. M. (1931) *Summary of Operations, California Oil Fields*, DOGGR, California Department of Natural Resources.

Seitz, N.O., Kulongoski, J.T., Marcusa, J.A. Marcusa, and Qi, S.L., 2021, Produced water chemistry data collected from the Orcutt oil field, 2018, Santa Barbara County, California: U.S. Geological Survey.

Soutar A., Johnson S. R. and Baumgartner T. R. (1981) In Search of Modern Depositional Analogues to the Monterey Formation. In: *The Monterey Formation and related siliceous rocks of California.* Pacific Society of Economic Palaeontologist and Mineralogists. 123-147.

Smith, T. (2012) The Many Lives of Belridge. *History of Oil North America (GEOExPro)* **9**(2).

Stephens M. J., Shimabukuro D. H., Gillespie J. M. and Chang W. (2019) Groundwater salinity mapping using geophysical log analysis within the Fruitvale and Rosedale Ranch oil fields, Kern County, California, USA. *Hydrogeology Journal* **27**, 731–746.

Taylor K. A., Fram M. S., Landon M. K., Kulongoski J. T. and Faunt C. C. (2014) *Oil, Gas, and Groundwater Quality in California—a discussion of issues relevant to monitoring the effects of well stimulation at regional scales*. Prepared in Cooperation with the California State Water Resources Control Board ftp://ftp.consrv.ca.gov/pub/oil/SB4EIR/docs/Taylor_et_al_2014.pdf

Taylor K. A., Fram M. S., Landon M. K., Kulongoski J. T. and Faunt C. C. (2014) *Oil, Gas, and Groundwater Quality in California—a discussion of issues relevant to monitoring the effects of well stimulation at regional scales*. Prepared in Cooperation with the California State Water Resources Control Board ftp://ftp.consrv.ca.gov/pub/oil/SB4EIR/docs/Taylor_et_al_2014.pdf [Accessed November 2018]

Torgersen T. and Kennedy B. M. (1999) Air-Xe enrichments in Elk Hills oil field gases: role of water in migration and storage. *Earth and Planetary Science Letters* **167**, 239–253.

Tyne R. L., Barry P. H., Hillegonds D. J., Hunt A. G., Kulongoski J. T., Stephens M. J., Byrne D. J. and Ballentine C. J. (2019) A Novel Method for the Extraction, Purification, and Characterization of Noble Gases in Produced Fluids. *Geochemistry, Geophysics, Geosystems* **20**, 5588–5597.

USGS, 2019, Active quaternary faults, California. Available at: https://www.usgs.gov/natural-hazards/earthquake-hazards/faults?qt-science_support_page_related_con=4#qt-science_support_page_related_con [Accessed October 2019]

Weiss , R.F., 1968. Piggyback sampler for dissolved gas studies on sealed water samples. *Deep-Sea Research and Oceanographic Abstracts* **15**(6), 695-699.

Wen T., Castro M. C., Nicot J.-P., Hall C. M., Pinti D. L., Mickler P., Darvari R. and Larson T. (2017) Characterizing the Noble Gas Isotopic Composition of the Barnett Shale and Strawn Group and Constraining the Source of Stray Gas in the Trinity Aquifer, North-Central Texas. *Environmental Science & Technology* **51**, 6533–6541.

Woodring W. P. and Bramlette M. N. (1950) *Geology and Palaeontology of the Santa Maria district, California*, USGS professional paper **222**. Washington DC.

Wright M. T., McMahon P. B., Landon M. K. and Kulongoski J. T. (2019) Groundwater quality of a public supply aquifer in proximity to oil development, Fruitvale oil field, Bakersfield, California. *Applied Geochemistry* **106**, 82–95.

Zaikowski A. and Spangler R. R. (1990) Noble gas and methane partitioning from ground water: An aid to natural gas exploration and reservoir evaluation. *Geology* **18**, 72.

Zhou Z., Ballentine C. J., Kipfer R., Schoell M. and Thibodeaux S. (2005) Noble gas tracing of groundwater/coalbed methane interaction in the San Juan Basin, USA. *Geochimica et Cosmochimica Acta* **69**, 5413–5428.

Chapter 4

Rapid microbial methanogenesis during CO_2 storage in hydrocarbon reservoirs

R.L. Tyne[1], P.H. Barry[1,2], M. Lawson[3], D.J. Byrne[4], O. Warr[5], H.Xie[6], D.J. Hillegonds[1], M. Formolo[7], Z.M. Summers[8],B. Skinner[7], J.M. Eiler[6], C.J. Ballentine[1]

[1] Dept. of Earth Sci., University of Oxford, Oxford, UK [2] Dept. of Marine Chem. and Geochem., Woods Hole Oceanographic Institution, Woods Hole, MA, USA [3] ExxonMobil Upstream Business Development, Spring, TX, USA [4] CRPG-CNRS, Université de Lorraine, Nancy, France [5] Dept. Earth Sciences, University of Toronto, Canada [6] Div. of Geological and Planetary Sci., California Institute of Technology, Pasadena, California, USA [7] ExxonMobil Upstream Integrated Solutions, Spring, TX, USA [8] ExxonMobil Research and Engineering Co., NJ, USA

Contents

Abstract			134
4.1	Main text		134
4.2	Methods		144
	4.2.1	Modelling	144
	4.2.2	Sample collection and analysis	145
S4.1	Supplementary figures		147
S4.2	Supplementary tables		153
S4.3	Supplementary information		157
Acknowledgments			169
Authorship statement			170
References			171

Abstract

Carbon capture and storage (CCS) is a key technology to mitigate the environmental impact of CO_2 emissions. An understanding of the potential trapping and storage mechanisms is required to provide confidence in safe and secure CO_2 geologic sequestration (Leung et al., 2014; Bui et al., 2018). Depleted hydrocarbon reservoirs have significant CO_2 storage potential (Stewart and Haszeldine, 2014; Leung et al., 2014) and numerous hydrocarbon reservoirs have undergone CO_2 injection as a means of enhanced oil recovery (CO_2-EOR), providing an opportunity to evaluate the (bio)geochemical behaviour of injected carbon. Here, we present noble gas, stable isotope, clumped isotope and gene sequencing analysis from a CO_2-EOR project in the Olla Oil Field (Louisiana, USA). We show that most of the injected CO_2 remained dissolved in the formation waters after the EOR project, but microbial methanogenesis converted as much as 13-19 % of the remaining fraction of CO_2 to CH_4. We calculate the first *in-situ* microbial methanogenesis rate from within a natural system, yielding 73-109 mmol CH_4/m^3(STP)/yr for the Olla Field. Similar geochemical trends in both injected and natural CO_2 fields suggest that microbial methanogenesis may be a significant sink of CO_2 in these types of systems globally. For CO_2 sequestration sites within the environmental window for microbial methanogenesis, conversion to CH_4 should be considered in site selection.

4.1. Main text

A promising method for reducing current greenhouse gas emission rates is CCS. Long-term CCS is effective when a geological reservoir is conducive to long-term CO_2 storage. Trapping mechanisms include structural/stratigraphic trapping in stable geologic configurations, dissolution into pore fluids (solubility trapping (Gilfillan et al., 2009)), carbonate mineralisation (precipitation/mineral trapping (Baines and Worden, 2004; Zevenhoven et al., 2006; Matter et al., 2016)) or adsorption (e.g., onto coal (Yee et al., 1993; Bachu, 2000; Busch et al., 2004)). Typically, during CO_2-EOR, a proportion of the injected CO_2 remains within the reservoir post-injection (Stewart and Haszeldine, 2014), providing an analogue for investigating and quantifying processes within CCS sites, over the decadal timescales associated with these processes.

Here, we investigate the behaviour of CO_2 within the Olla Oil Field, Louisiana (Figure 4.1), which was CO_2-EOR flooded in the 1980's and compare it with the adjacent Nebo-Hemphill Oil Field, which is in close proximity, has a similar geologic history, but was never subjected to CO_2-EOR (Supplementary Information S4.3.1.). Approximately $9x10^7$ m^3(STP) of injected CO_2 is estimated to have remained in the Olla Field post-injection, which represents approximately 30% of the total injected CO_2 (Moffet, 1990). The injected CO_2 was sourced from the Black Lake Oil Field, which is located adjacent to the Sabine Island Complex, a basement high and likely conduit for mantle-derived fluids (Byrne et al., 2020). Although the Olla Field has been geochemically characterised by several previous studies (McIntosh et al., 2010; Shelton et al., 2014, 2016a), this study is unique in integrating noble gas, stable isotope, clumped isotope and microbiological data to specifically investigate the fate of the injected CO_2. Notably, previous studies suggested microbial hydrocarbon degradation and methanogenesis may occur within both the Olla and Nebo-Hemphill fields (McIntosh et al., 2010; Shelton et al., 2014, 2016a). Microbial methanogenesis usually operates by either acetate fermentation or CO_2 consumption (hydrogenotrophic methanogenesis, Eq.4.1); the latter mechanism is most relevant to this study. Hydrogenotrophic methanogenesis results in ^{13}C enrichment of residual CO_2 and the formation of CH_4 initially ^{13}C depleted compared to the source CO_2 but evolves to a more enriched ^{13}C content with continued CO_2 consumption.

$$CO_2+4H_2 \rightarrow CH_4+2H_2O \qquad \text{(Eq. 4.1)}$$

Given the close proximity and comparable geologic history (including hydrocarbon production from similar reservoirs, Supplementary Information S4.3.1 and S4.3.2), we assume that Nebo-Hemphill and Olla had comparable geochemical compositions, prior to CO_2-EOR at the Olla. Despite CO_2 injection ceasing over 30 years ago, present day CO_2 concentrations within the Olla Field are significantly greater (18±12 mol%) than at Nebo-Hemphill (1.02±0.69 mol%). We also observe a higher $\delta^{13}C_{VPDB}$ of CO_2 at Olla (13.5±3.4‰) compared to both Nebo-Hemphill (4.8±4.9‰) and the injected CO_2 (0.85±0.92‰)(McIntosh, et al., 2010). This demonstrates that injection alone cannot account for the higher δ^3C of CO_2 values at Olla, requiring integration of complimentary datasets to evaluate additional *in-situ* processes.

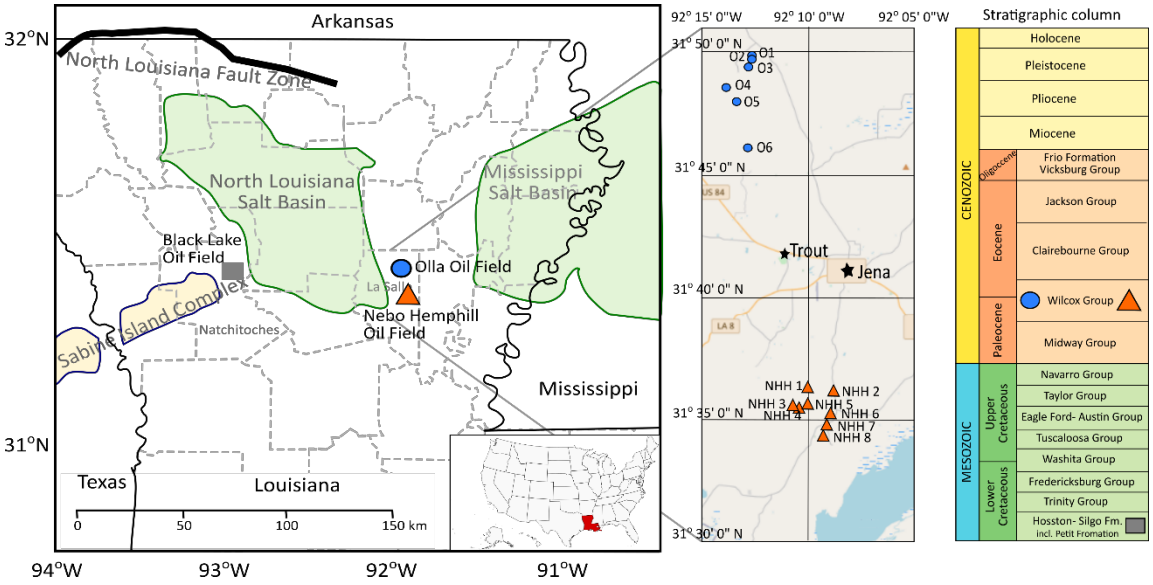


Figure 4.1: Map of study area showing locations of the Olla and Nebo-Hemphill oil fields as well as the Black Lake Oil Field, from which the injected CO_2 was sourced. Only the Olla Field contains injected CO_2. The inset on the right shows an expanded view with individual sample locations (nearby urban areas are denoted by stars) and a stratigraphic column showing the relative lithologic units (McIntosh et al., 2010).

Due to their inert nature, noble gases provide a powerful tool for tracing and quantifying physico-chemical processes associated with CO_2 injection (Ballentine et al., 1991; Ballentine and Burnard, 2002; Ballentine and Sherwood Lollar, 2002; Gilfillan et al., 2008, 2009; LaForce et al., 2014; Györe et al., 2015; Sathaye et al., 2016; Shelton et al., 2016b; Barry et al., 2018a, 2018b; Byrne et al., 2020). The average air-corrected helium isotope ($^3He/^4He$) ratio relative to the atmospheric ratio (R/R_A where $R = {}^3He/^4He_{sample}$ and $R_A = {}^3He/^4He_{air}$) was determined for the Olla and Nebo-Hemphill fields to be $1.76\pm0.31R_A$ and $0.46\pm0.12R_A$ respectively (Supplementary Figure S4.3.1, Supplementary Table S4.1). The elevated He isotope values associated with the Olla Field require an increased contribution of mantle-derived noble gases, which is supported by additional noble gas data (Supplementary Table S4.1, Supplementary Information S4.3.3). We associate this enhanced mantle component with the CO_2 injected during EOR, which was sourced from Black Lake Field.

In addition to characterising fluid origin, a combined noble gas and CO_2 isotope approach provides insight into processes associated with CO_2 trapping (e.g., Gilfillan et al., 2009) or methanogenesis

following injection. ^{3}He is inert and insoluble, with no significant sources within the crust. As such, variations in $CO_2/^{3}He$ post-injection are directly attributable to the addition or removal of CO_2 within the system (Sherwood Lollar et al., 1997; Gilfillan et al., 2008, 2009). While two samples at Olla (O5 and O6) have $CO_2/^{3}He$ within the mantle range ($2\pm1x10^{9}$), consistent with injection of mantle derived fluids into the Olla Field, the majority of the ratios are lower and indicate CO_2 trapping/methanogenesis (Figure 4.2a, Supplementary Table S4.1). The difference between the highest $CO_2/^{3}He$ (O5, considered most pristine sample) and the remaining samples provides a conservative estimate of post-injection CO_2 trapping in the majority of samples of between 39-89%.

A decrease in the $CO_2/^{3}He$ alongside increasing ^{4}He and ^{20}Ne concentrations is observed within the Olla Field (Supplementary Figure S4.2, Supplementary Information S4.3.4.). In the subsurface ^{4}He is produced via radiogenic decay of U and Th and accumulates in formation water (Ballentine and Burnard, 2002), which also contains the atmosphere-derived ^{20}Ne. Anti-correlation of $CO_2/^{3}He$ with ^{4}He and ^{20}Ne is observed in natural CCS analogues globally (Gilfillan et al., 2009). These indicate that the extent of water contact controls the magnitude of CO_2 trapping via dissolution or precipitation of CO_2 (Gilfillan et al., 2009; Sathaye et al., 2016). Within the observed pH range (7.0±0.5) at Olla, dissolution will dominate over precipitation as a trapping mechanism for CO_2 (Gilfillan et al., 2009; Shelton et al., 2014). However, as described above, $\delta^{13}C$ of CO_2 in the Olla gases is also significantly more enriched (7.05-16.4‰$_{VPDB}$, Supplementary Table S4.1) than can be explained by these processes alone (Figure 4.2a).

Independent of the source of the injected CO_2, such positive $\delta^{13}C$ values suggest significant modification from a starting composition that is unlikely to be heavier than 2‰ (Clark and Fritz, 1997; Wycherley et al., 1999). Notably, sorption to coal, hydrocarbon biodegradation and subsequent consumption and mixing processes could result in an increase in $\delta^{13}C$ of CO_2 (Prinzofer and Huc, 1995; Prinzofer and Pernaton, 1997). However, even from the most pristine sample (O5), it is unlikely that any of these processes could generate a fluid with the elevated concentrations of the isotopically enriched CO_2 observed at Olla (Supplementary Information S4.3.4.).

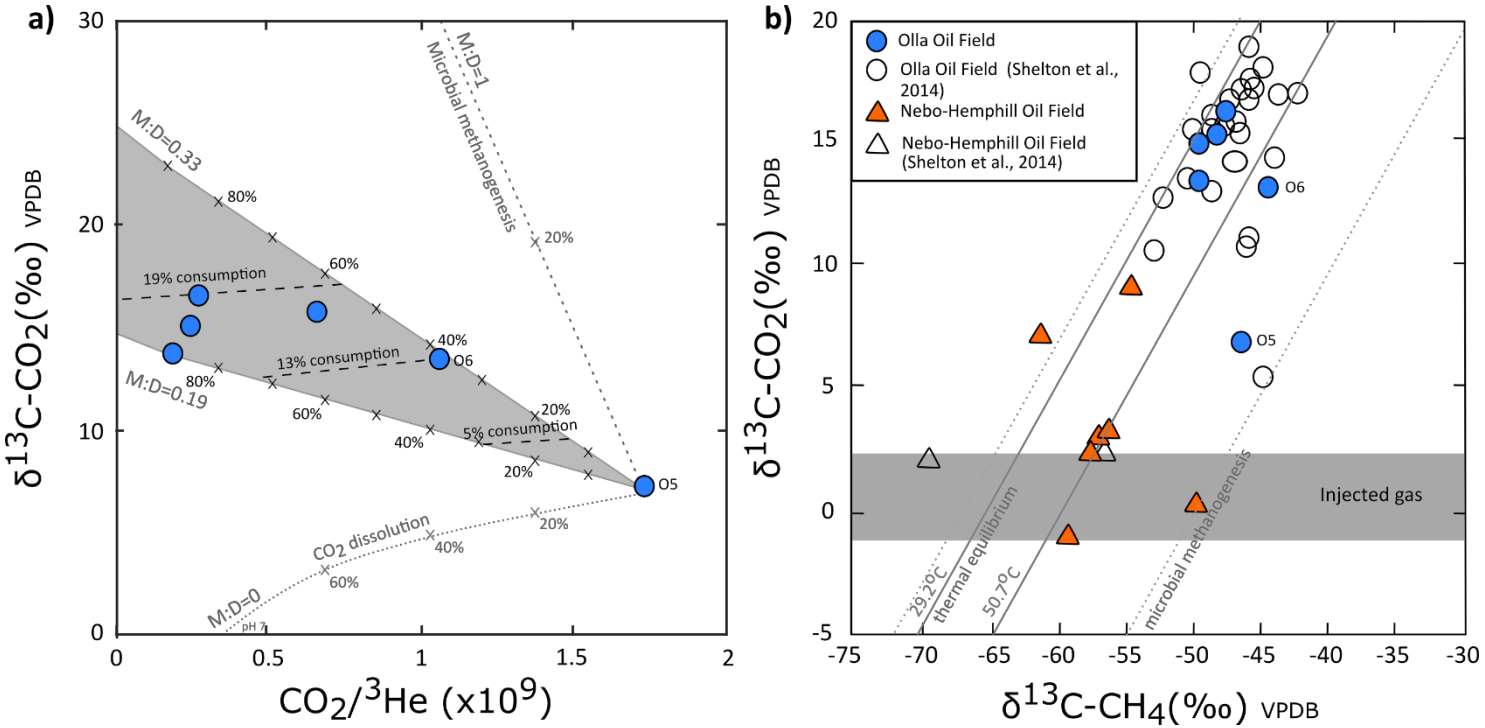


Figure 4.2: $\delta^{13}C$ of CO_2 in the Olla (CO_2 injected field) samples as a function of (a) $CO_2/^3He$ and (b) $\delta^{13}C$ of CH_4. 1σ level of uncertainty is within symbol size. (a) Dashed lines show endmember methanogenesis and dissolution (pH=7) fractionation trajectories. Tick marks represent the total amount of CO_2 trapping within the system, relative to sample O5. The shaded region represents trapping by the combination of both microbial methanogenesis and dissolution. The upper and lower methanogenesis:dissolution ratios (M:D) are 0.33 and 0.19 respectively, showing dissolution to account for approximately three times more CO_2 removal (M:D=0.26) than microbial methanogenesis. Lines labelled 'consumption' show the proportion of original CO_2 that has been removed by net microbial methanogenesis. (b) The shaded region represents the CO_2 isotopic composition of the injectate from the Black Lake field into the Olla system. Olla data is consistent with thermal re-equilibration with both reservoir temperatures (solid lines) and microbial methanogenesis (dotted lines).

Further constraints on the origins and histories of the studied gases are provided by the molecular-average and clumped isotope compositions of the associated CH_4. We observe relatively high $\delta^{13}C$ of CO_2 (13.6±3.2‰) and $\delta^{13}C$ of CH_4 (-47.7±1.7‰) in the Olla Field compared to those observed at Nebo-Hemphill (3.5±3.6‰ and -56.4±3.6‰ for CO_2 and CH_4 respectively) (Figure 4.2b, Supplementary Table S4.1). In the absence of other data, the higher $\delta^{13}C$ of CH_4 from the Olla samples compared with data from Nebo-Hemphill could be interpreted as evidence that the Olla Field contains a higher proportion of thermogenic gas, or thermogenic gas of higher thermal maturity, whereas the Nebo-Hemphill Field contains more microbial gas or thermogenic gas of lower thermal maturity. Using the multi-faceted approach applied in this study, a better-fit model can be formulated: Olla is assumed to have had a pre-EOR composition resembling Nebo-Hemphill, but following CO_2-EOR, microbial activity converted significant amounts of injected CO_2 to CH_4. This results in the observed higher $\delta^{13}C$ values of CH_4 and an increase in the $\delta^{13}C$ of residual CO_2. We arrive at this conclusion based on the following observations.

First, we report an offset between the $\delta^{13}C$ of CH_4 and $\delta^{13}C$ of CO_2 of 53.7-64.4‰ in the Olla Field and 50.8-68.1‰ at Nebo-Hemphill (Figure 4.2b). The observed carbon isotope fractionations between co-existing CO_2 and CH_4 are consistent with thermodynamic isotopic equilibrium at temperatures between 44.6-76.3°C at Olla and 29.8-85.3°C at Nebo-Hemphill (Bottinga, 1969), which overlap the present-day reservoir temperatures within these fields (29.2-50.7°C and 29.7-57.1°C respectively), suggesting the systems are approaching isotopic equilibrium under current reservoir conditions (Supplementary Information S4.3.5.). The carbon isotopes within the system appear to be approaching equilibrium under reservoir conditions as a result of microbial cycling of carbon (i.e., methanogenesis and anaerobic oxidation of methane (AOM)). Equilibrium with reservoir conditions between $\delta^{13}C$ of CO_2 and CH_4 has previously been observed under similar geological settings (Thiagarajan et al., 2020a).

Second, we observe a range in the two measurable clumped isotopologues of methane ($\Delta^{13}CH_3D$ and $\Delta^{12}CH_2D_2$) at Olla of 3.45-5.62‰ and 9.13-12.4‰ (Figure 4.3, Supplementary Table S4.2),

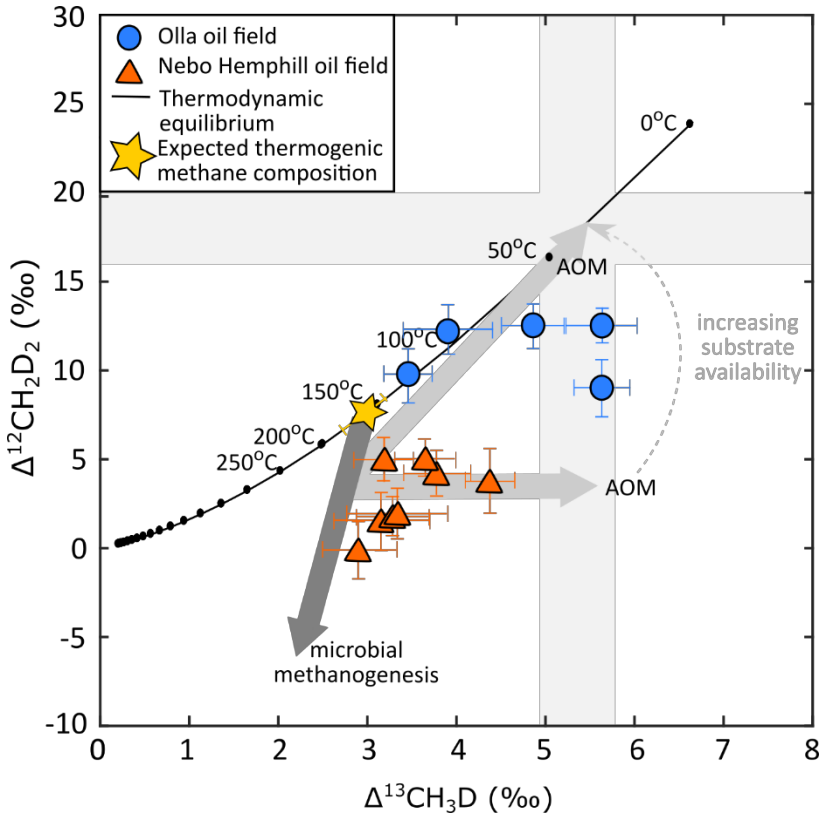


Figure 4.3: $\Delta^{12}CH_2D_2$ vs $\Delta^{13}CH_3D$ of the measured Olla (blue circles) and Nebo-Hemphill (orange triangles) samples. 1σ level of uncertainty is shown on the measured samples. Clumped isotopologue space illustrates whether measured methane is at internal thermodynamic equilibrium (black line) or not. The thermodynamic equilibrium curve is calculated following ref[36]. The shaded cross represents thermal equilibration to current reservoir temperatures in each isotopologue. Arrows represent the theoretical trends for methanogenesis and anaerobic oxidation of methane (AOM)(Young, 2017).

which correspond to apparent temperature ranges of 29^{+14}_{-12} to 128^{+17}_{-16}°C and 87^{+13}_{-11} to 132^{+30}_{-23}°C respectively, which are approaching equilibrium with current reservoir conditions. Clumped isotope compositions provide a unique and independent constraint on the origin of methane in petroleum systems (Stolper et al., 2014, 2015; Douglas et al., 2017; Stolper et al., 2018; Giunta et al., 2019; Young, 2019). Thermogenic methane appears to dominantly form under internal isotopic equilibrium (Stolper et al., 2015; Douglas et al., 2017) whilst microbial methane has been shown to be highly variable in its clumped isotope compositions, with both non-equilibrium (Giunta et al., 2019; Young, 2019) and apparent equilibrium signatures reported in samples obtained from the deep subsurface (Wang et al., 2015; Douglas et al., 2017; Gruen et al., 2018;

Giunta et al., 2019; Cao et al., 2019; Young, 2019; Thiagarajan et al., 2020a; Ono et al., 2021). For Olla, we expect the temperature for thermogenic methane generation to have exceeded 163±18°C from independent maturity constraints provided by biomarkers (Sweeney and Burnham, 1990). Two samples from Olla (O4, O6) appear to be in internal isotopic equilibrium (~120 and ~95°C) but have lower apparent temperatures than expected for pure thermogenic methane. These temperatures are consistent with a component of microbial methane formed at or close to equilibrium with current reservoir conditions. The remaining samples have $\Delta^{13}CH_3D$ apparent temperatures of $28.7^{+13.6}_{-12.3}$ to $74.0^{+16.8}_{-15.0}$°C, within error of the present-day reservoir temperature for these fluids (Supplementary Table S4.2, Supplementary Information S4.3.5.), consistent with *in-situ* microbial methanogenesis and AOM. Furthermore, these samples exhibit deficits in $\Delta^{12}CH_2D_2$ consistent with fluids that are dominated by microbial methane (Head et al., 2003; Giunta et al., 2019; Young, 2019) in a system approaching equilibrium via active methanogenesis and AOM. In contrast, the $\Delta^{13}CH_3D$ based temperatures of $77.9^{+13.5}_{-12.3}$ to 166^{+34}_{-29}°C at Nebo-Hemphill suggest that these fluids are dominated by thermogenic methane, although similarly to Olla, the $\Delta^{12}CH_2D_2$ clumped isotopologues also suggest some contribution of microbial methane.

Third, we identify evidence for the biodegradation of hydrocarbons in the molecular geochemistry of oils produced from both the Olla and Nebo-Hemphill fields (Supplementary Information S4.3.2.). In the case of Olla, we also report heavy $\delta^{13}C$ of propane (Supplementary Figure S4.4, Supplementary Table S4.4). The presence of oils co-existing with propane in these reservoirs preclude the possibility of high-temperature cracking as the cause of the positive $\delta^{13}C$ values and suggests that the propane has been subjected to biodegradation, consistent with low temperature microbial activity within the field.

Fourth, SSU rRNA gene sequencing of microbial communities sampled from produced waters from two wells within each field alongside previous microbiology analysis in these fields (Shelton et al., 2018), identify the presence of hydrogenotrophic methanogens, methanol/methylotrophic methanogens and anaerobic methanotrophs (ANME)-assigned sequences (Supplementary Figure

S4.5). As well as ANME's being associated with AOM, it has been proposed that some methanogens are also capable of performing methanogenesis in reverse (Boetius et al., 2000), consuming CH_4 and generating CO_2. This diverse microbial consortia is capable of producing and consuming both CO_2 and CH_4, evolving the system to intra- and inter-molecular equilibrium through a combination of hydrogenotrophic methanogenesis and AOM.

The integration of independent geochemical and microbiological constraints we provide here overwhelmingly supports our assertion that injected CO_2 is being consumed at Olla by microbial methanogenesis. To our knowledge, this study represents the first identification of these microbial processes associated with the injection of CO_2 into the deep subsurface operating on such short (decadal) timescales and at such scale.

To quantify the impact of these microbial processes on the Olla Field, we have constructed a model which considers both dissolution and microbial methanogenesis (Figure 4.2a, Section 4.2). Using O5 as our most pristine sample (i.e., highest $CO_2/^3He$) we find that in order to match the isotopic composition of CO_2 with its corresponding $CO_2/^3He$, dissolution must account for 3.1±1.1 times more CO_2 removal than hydrogenotrophic methanogenesis. From this model, microbial methanogenesis is estimated to have consumed a minimum of between 13 to 19% of the post-injection CO_2, depending on sample location, while dissolution is responsible for up to an additional 74% CO_2 solubility trapping. This estimate is independently confirmed when CO_2 concentrations are compared to $\delta^{13}C$ of CO_2 (Supplementary Figure S4.6). Based on the elevated $\delta^{13}C$ of CO_2, we recognise that our most pristine sample has likely also undergone a significant degree of modification, consistent with our estimate being conservative and that CO_2 concentrations post-injection were likely to be higher and variable across the field.

Our combined noble gas and stable isotope approach in the Olla Field allows estimates of *in-situ* microbial methanogenesis rates from within a natural system to be calculated for the first time. By extrapolating our results over the 29 years between the cessation of injection and sampling, and assuming 13-19% microbial consumption of CO_2 since injection (from the hybrid methanogenesis-dissolution model, Figure 2) with the remaining injected CO_2 volume ($9x10^7$

m^3(STP) (Moffet, 1990)), we calculate that a minimum of 1.15-1.72x10^7 m^3(STP) of microbial CH_4 has been produced at a minimum rate of 73-109 mmol CH_4/m^3(STP)/yr. Previous estimates for CO_2 reduction following methanogenic oil degradation by hydrogenotrophic methanogens from lab cultures at similar temperatures are significantly lower (~0.01-0.15 mmol CH_4/m^3(STP)/yr (Gray et al., 2009)) by comparison.

This identification and quantification of CO_2-EOR-related microbial methanogenesis at Olla has significant implications, and warrants reconsideration of reservoir processes at similar sites worldwide. The fate of injected CO_2 in other oil fields (e.g., Lost Hills, CA, USA (Perri, 2003; P.H. Barry et al., 2018a)) has never been systematically explored using this integrated approach. Similarly, to Olla, the Lost Hills Field has elevated $\delta^{13}C$ of DIC (20.16-23.61‰ (Gannon et al., 2018)) compared to the injected $\delta^{13}C$ of CO_2 (-30.1‰ (Perri, 2003)) and the fractionation between $\delta^{13}C$ of DIC and CH_4 suggests the Lost Hills system is approaching equilibrium with current reservoir conditions. An inverse correlation between the $\delta^{13}C$ of the post-injection residual CO_2 and concentration is consistent with microbial methanogenesis. Additionally, data from Nebo-Hemphill as well as naturally CO_2-rich hydrocarbon systems in the Pannonian Basin, Hungary, also appears consistent with significant microbial methanogenesis based on the $CO_2/^3He$ and $\delta^{13}C$ of CO_2 (Supplementary Figure S4.7, Supplementary Information S4.3.6 and S4.3.7). These examples suggest that hydrogenotrophic methanogenesis likely occurs in both natural and injection-perturbed systems when reservoirs have favourable physical and chemical conditions.

We conclude that although methanogenesis is not the dominant CO_2 sink, it can represent a substantial process within both natural and perturbed CO_2 fields and may be significantly more prevalent than previously considered. Even with the most conservative estimates of CO_2 conversion by methanogenesis in the Olla Field, we find that, to date, as much as 13 to 19% of the emplaced CO_2 in sampled sections of the field has been consumed by methanogens. This is less than the amount of CO_2 that has been dissolved into water, but similarly occurs at rates that are significant on engineering timescales. Depleted hydrocarbon reservoirs have the second largest CO_2 storage potential (Stewart and Haszeldine, 2014; Leung et al., 2014) after deep saline

aquifers. If physicochemical and environmental conditions within these reservoirs (e.g., low temperature, low salinity, high substrate availability) are conducive to microbial methanogenesis, we suggest that these microbial processes should be considered as a criteria in future CCS site selection to ensure low-risk long-term storage, and that integrated studies like this may provide an opportunity to monitor CO_2 storage and the processes that may operate as a consequence of it.

4.2. Methods

4.2.1 Modelling

Here, we provide extra details of the $\delta^{13}C$-CO_2 fractionation modelling of methanogenesis, and dissolution. In our models (Figure 4.2a, Supplementary Figure S4.6) we use the sample with the highest measured $CO_2/^3He$ (O5) as a reference point to calculate the change in $CO_2/^3He$ and $\delta^{13}C$-CO_2 with CO_2 processing (i.e., methanogenesis, dissolution). We assume there is no ^3He loss with dissolution or methanogenesis and therefore changes in the fraction of the CO_2 cause changes in the $CO_2/^3He$.

Dissolution is modelled as open system Rayleigh fractionation (Gilfillan et al., 2009).

$$\delta^{13}C_{CO2} = \delta^{13}C_{CO2i} \times f^{(\alpha-1)} \quad \text{(Eq. 4.2)}$$

Where f is the fraction of the original CO_2 trapped, $\delta^{13}C_{CO2}$ and $\delta^{13}C_{CO2i}$ are the carbon isotopic composition of the CO_2 for post-dissolution and in the initial CO_2 respectively, and α is the fractionation factor. The fractionation factor for dissolution (α_d = 1.0038±0.0012) was calculated based on the average measured pH (Shelton et al., 2014). Precipitation curves (Figure 4.2a) can be modelled in the same way using fractionation factors (α_p= 1.0086±0.0012) calculated for the current reservoir temperature (Clark and Fritz, 1997).

From consideration of the carbon isotopes, which appear to be approaching equilibrium under current reservoir conditions, net methanogenesis has been modelled as a closed system equilibrium process (Eq.4.2, Figure 4.2a). The fractionation resulting from this cycling, α_m, is 0.9363±0.003, which is consistent with thermal equilibration at current reservoir temperatures (Bottinga, 1969).

$$\delta^{13}C_{CO2} = \delta^{13}C_{CO2i} - (\alpha_m - 1)(1 - f) \times 1000 \quad \text{(Eq. 4.3)}$$

Within the Olla Field, it is likely that there is a combination of both microbial cycling and dissolution. As a result, the net effect of microbial methanogenesis and dissolution can be described using Eq. 4.3.

$$\delta^{13}C_{CO2} = \delta^{13}C_{CO2i} \times f^{(\alpha_A - 1)} - (\alpha_A - 1)(1 - f) \times 1000 \quad \text{(Eq. 4.4)}$$

where f is the fraction of CO_2 trapped/converted and α_A is the apparent fractionation factor for the system. α_A depends on the degree of dissolution compared to methanogenesis and is described as:

$$\alpha_A = F_d\alpha_d + (1 - F_d)\alpha_m \text{ (Van Breukelen, 2007)} \quad \text{(Eq. 4.5)}$$

F_d is the fraction of CO_2 trapped due to dissolution.

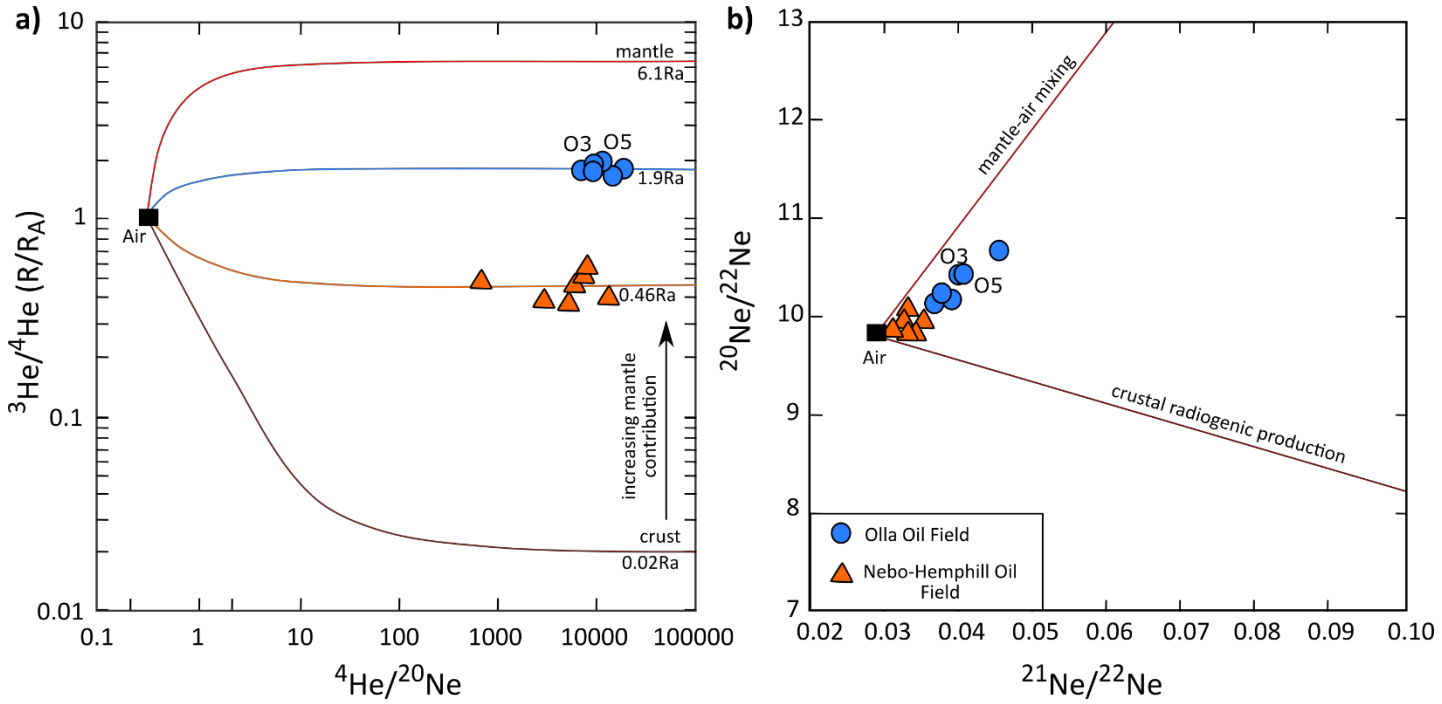
4.2.2 Sample collection and analysis

Samples for bulk gas composition, stable isotope, noble gas and clumped isotope analysis were collected using standard techniques (Weiss, 1968; Burnard, 2013; Byrne et al., 2020; Thiagarajan et al., 2020a, 2020b). Noble gas isotope determination was conducted in the Noble Laboratory at the University of Oxford, where the analysis of hydrocarbon gases is well established (Chapter 2; Barry et al., 2016, 2018a, 2018b; Byrne et al., 2018, 2020; Tyne et al., 2019). For bulk composition and C and H stable isotope analysis, gas cylinders were shipped to Isotech Inc. in Champaign, Illinois, USA. Standard procedures for these are described in Thiagarajan et al. (2020a, 2020b). Methane clumped isotopologues were determined at the California Institute of Technology following the procedures described in Thiagarajan et al. (2020a, 2020b).

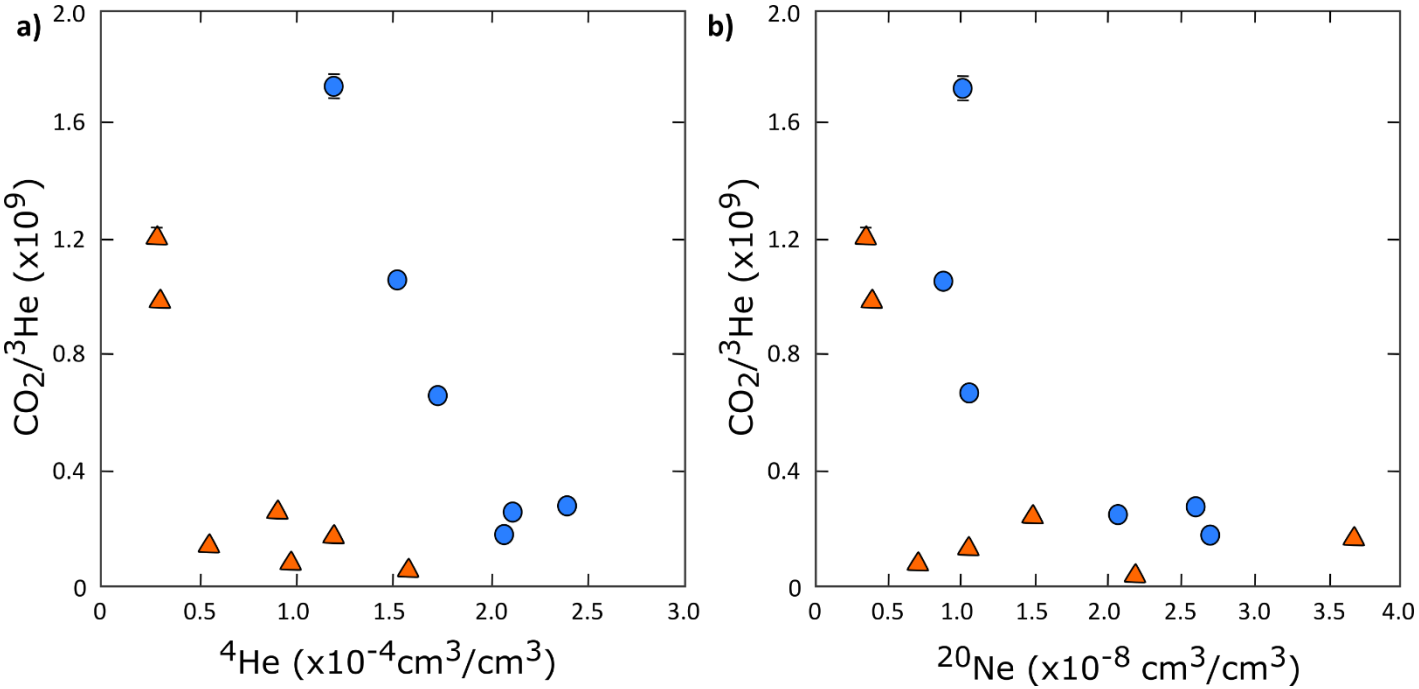
Microbiological analysis was conducted at an internal ExxonMobil Research and Engineering Company Facility. Produced water samples were collected and filtered immediately from wells O1, O4, NHH3 and NHH6. Water was passed through 0.22µm SVGPL10 RC Sterivex GP filters (EMD Milipore) until filters clogged in the following amounts: O1 1350mL, O4 1350mL, NHH3 1750mL, NHH6 300mL. Filters were stored on ice immediately and stored at -80ºC until DNA extraction. DNA was extracted from the Sterivex filters using the DNeasy PowerWater Sterivex Kit (Qiagen). The SSU rRNA gene was amplified with V4V5 specific primers

(www.vampls.mbl.edu) targeting Bacteria: Forward Primer (518F) CCAGCAGCYGCGGTAAN, Reverse Primers (926R) CCGTCAATTCNTTTRAGT, CCGTCAATTTCTTTGAGT, CCGTCTATTCCTTTGANT. A second set of amplifications were performed using V4V5 specific primers targeting Archaea: Forward Primers (517F) GCCTAAAGCATCCGTAGC, GCCTAAARCGTYCGTAGC, GTCTAAAGGGTCYGTAGC, GCTTAAAGNGTYCGTAGC, GTCTAAARCGYYCGTAGC; Reverse Primer (958R) CCGGCGTTGANTCCAATT. Illumina MiSeq 250bp paired end sequencing was performed by Genewiz Inc. (South Plainfield, NJ, USA). Microbiome bioinformatics were performed with QIIME 2 2017.4(Bolyen et al., 2019). Raw sequence data were demultiplexed and quality filtered using the q2-demux plugin followed by denoising with DADA2 (Callahan et al., 2016). Amplicon sequence variants (ASVs) were aligned with mafft and used to construct a phylogeny with fasttree2 (Katoh et al., 2002; Price et al., 2010). Taxonomy was assigned to ASVs using the q2-feature-classifier (Bokulich et al., 2018) classify-sklearn Naïve Bayes taxonomy classifier against the Greengenes 13_8 99% OTUs reference sequences (McDonald et al., 2012).

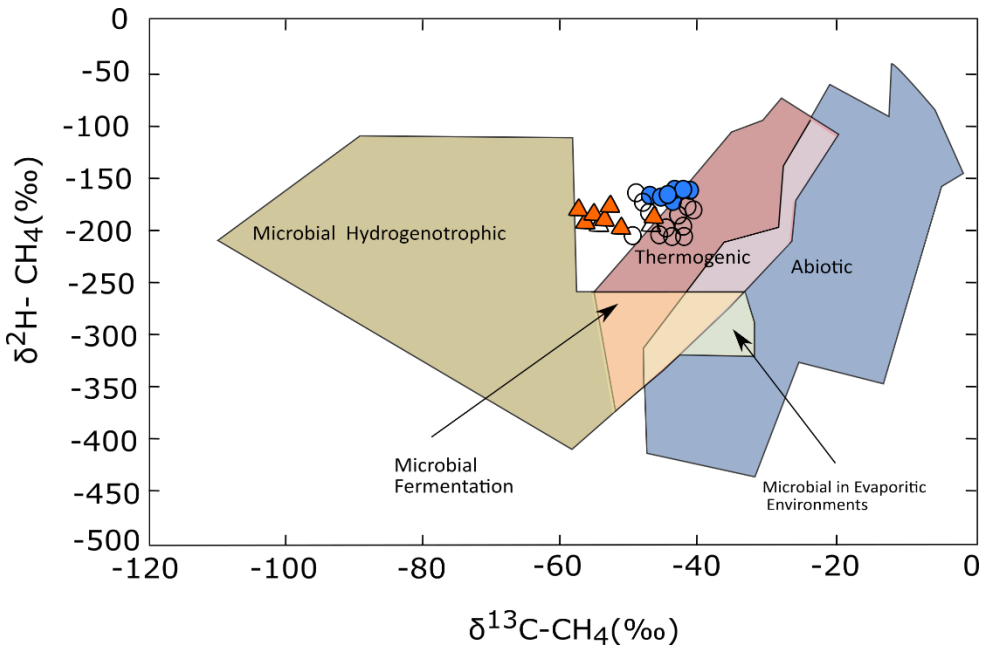
S4.1. Supplementary figures



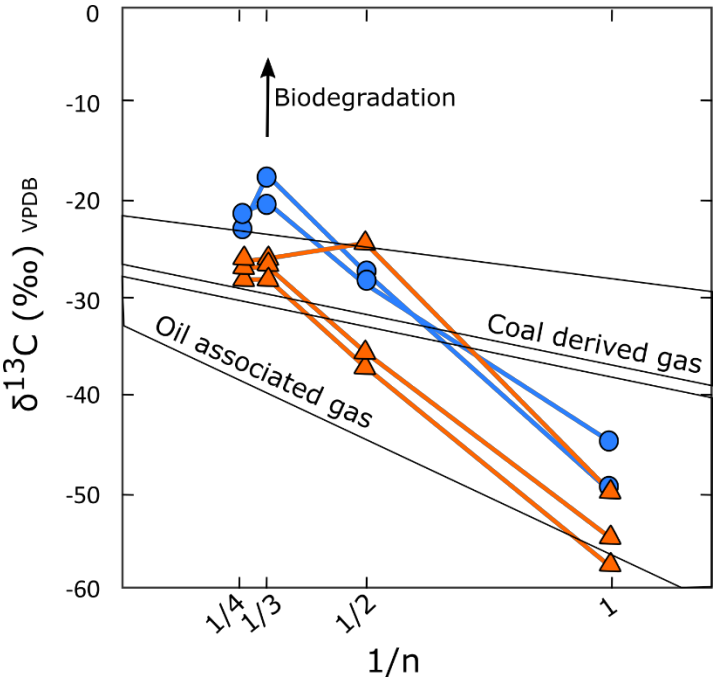
Supplementary. Figure S4.1: Relationship between noble gas isotopic ratios in the Olla (blue circles) and Nebo-Hemphill (orange triangles) oil fields. Both fields show a resolvable mantle component that is significantly greater in the Olla Field. One standard deviation error bars are within symbol size. a) Helium isotopic ratios vs. $^4He/^{20}Ne$ ratio. Air corrected helium isotopes are reported relative to air ($R_A = 1.4 \times 10^{-6}$). All samples are in excess of typical radiogenic production ($0.02R_A$), requiring a mantle contribution. High $^4He/^{20}Ne$ indicates negligible air contamination in the samples. b) Three neon isotope plot. The crustal production line reflects the observed trend in typical crustal fluids (Kennedy et al., 1990). The mantle-air line represents mixing between air and a MORB-like endmember (Ballentine et al., 2005). Data are consistent with mixing between air and a mantle-rich component. In both helium and neon isotopes, the mantle signal is stronger in the Olla Field.



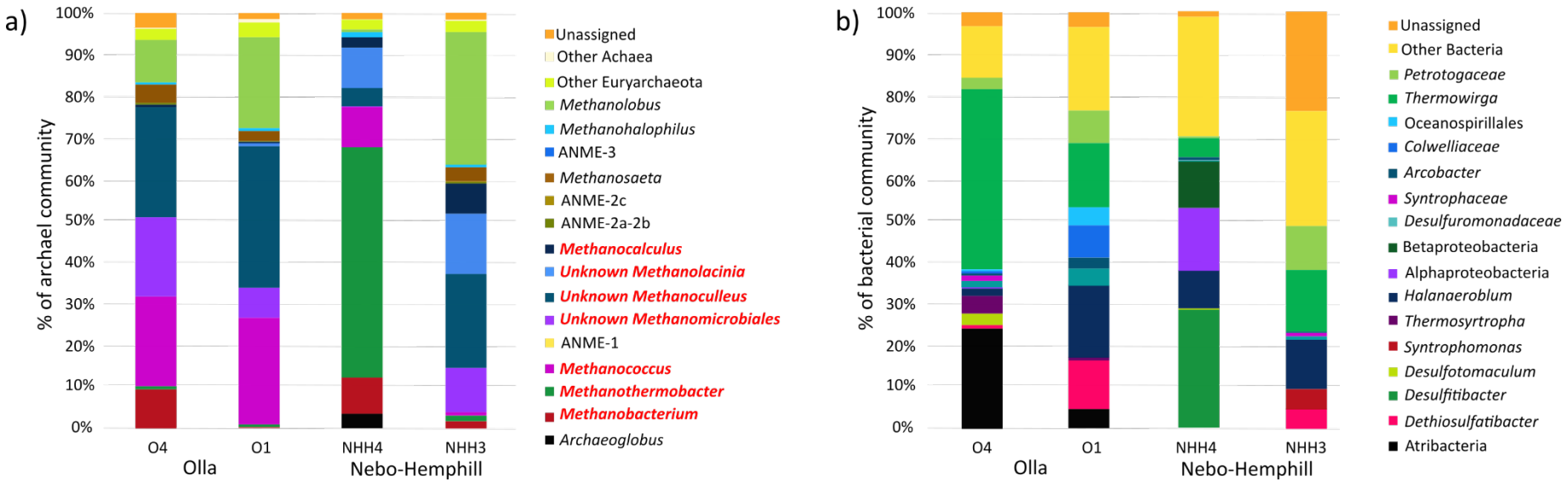
Supplementary Figure S4.2: $CO_2/^3He$ variation vs. a) ^4He and b) ^{20}Ne abundances in the Olla (blue circles) and Nebo-Hemphill (orange triangles) oil fields. 1σ level of uncertainty is shown on the measured samples. A negative correlation between ^4He, which accumulates in formation waters as a function of time and ^{20}Ne (which is groundwater derived) and $CO_2/^3He$, has been interpreted in other CO_2-rich natural gas fields to support the importance of the formation water in controlling CO_2 removal (Gilfillan et al., 2009).



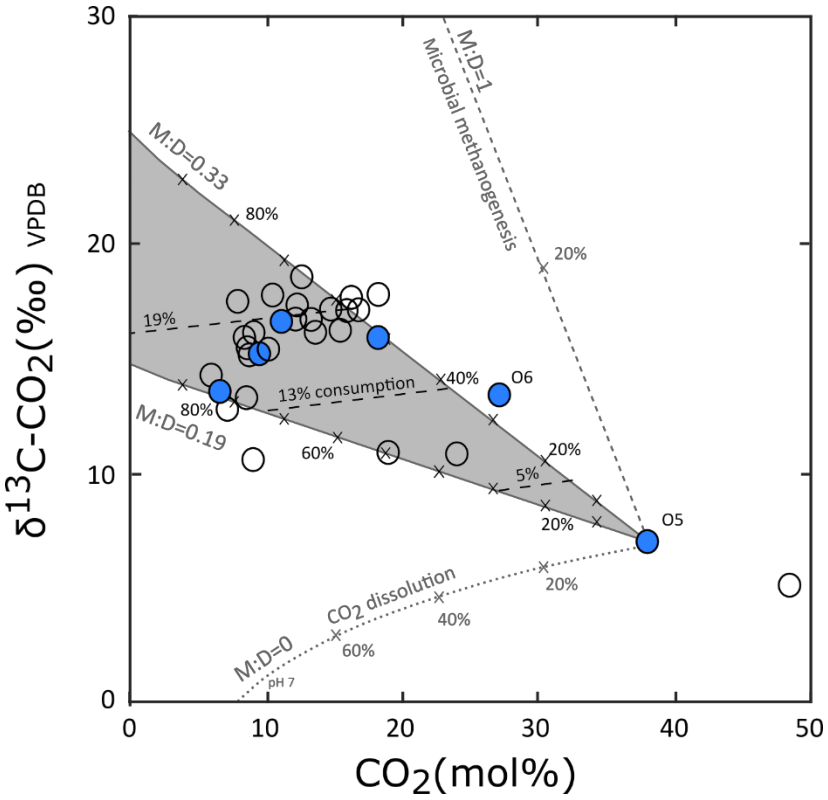
Supplementary Figure S4.3: Comparison of δ^{13}C-CH_4 and δD-CH_4, with typical methane provenances after Whiticar (Whiticar et al., 1986; Whiticar, 1999; Etiope and Lollar, 2013). One standard deviation error bars are within symbol size. In isolation the Olla samples (blue circles- this study, unfilled circles from Shelton et al., (2014)) are consistent with a mainly thermogenic origin, while Nebo-Hemphill (orange triangles (this study), unfilled triangles (Shelton et al., 2014)) appears to be a microbial-thermogenic mix. Clumped isotopologues nevertheless provide clear evidence that the Olla methane is microbial in origin (Figure 4.3).



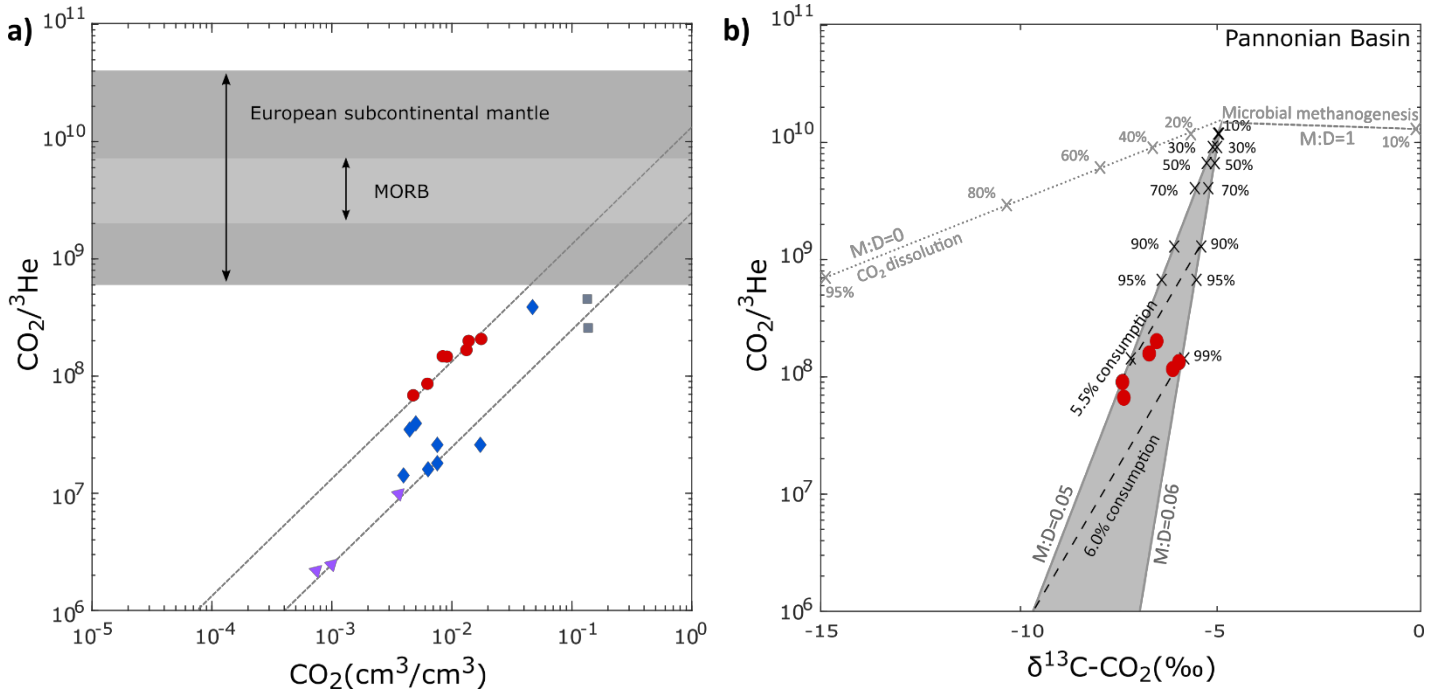
Supplementary Figure S4.4: Plot of δ^{13}C of C_n vs $1/C_n$ variation in natural gases (Chung et al., 1988). One standard deviation error bars are within symbol size. Both the Olla (blue circles) and Nebo-Hemphill (orange triangles) fields show an enrichment in their isotopic signature especially in propane; however, this is most pronounced within the Olla Field.



Supplementary Figure S4.5: Microbial community analysis of most abundant taxa from the SSU rRNA gene sequencing of the V4V5 region with a) archaeal primers and b) bacterial primers. Bar charts represent the most resolved taxa from amplicon sequence variants generated in QIIME 2 (Katoh et al., 2002; Price et al., 2010; Bokulich et al., 2018). Methanogens are shown as bold red text.



Supplementary Figure S4.6: Plotting carbon isotopic composition of the Olla samples as a function of CO_2 concentration allows consideration of data from this study (dark blue circles) with data collected without ^3He analysis (unfilled circles)(Shelton et al., 2014). One standard deviation error bars are within symbol size. Dashed lines show endmember methanogenesis and dissolution fractionation (at pH=7) trajectories. Tick marks represent the total amount of CO_2 trapping within the system, relative to sample O5. The shaded region represents trapping by the combination of both microbial methanogenesis and dissolution. The same combination of dissolution and microbial methanogenesis has been modelled (grey region, cf Figure 4.2, main text). Lines labelled 'consumption' at 5, 13 and 19% show the proportion of original CO_2 that has been removed by net microbial methanogenesis. One sample from Shelton et al., (2014) has a CO_2 concentration greater than our 'most pristine' $CO_2/^3He$ sample (O5). This illustrates that by using sample O5 as our least altered composition we calculate a conservative (minimum) amount of CO_2 consumption, and that initial CO_2 concentrations were likely greater.



Supplementary Figure S4.7: Carbon composition of the Pannonian Basin Samples. Szegholm South (red circles), Szegholm North (purple triangles), Ebes (blue diamonds) and Hajduszoboszlo (grey squares) gas field samples (Sherwood Lollar et al., 1994, 1997) as a function of their CO_2 concentrations and $CO_2/^3He$ (a). Dashed lines represent the projection of CO_2 trapping in the fields. The Szegholm South Field had multiple CO_2 isotope data and this field has been used to investigate the processes controlling this pattern using the carbon isotopic composition as a function of $CO_2/^3He$ (b). Dashed lines show endmember methanogenesis and dissolution fractionation (at pH=7) trajectories. Tick marks represent the total amount of CO_2 trapping within the system. The shaded region represents trapping by the combination of both microbial methanogenesis and dissolution. The upper and lower methanogenesis:dissolution ratios (M:D) are 0.055 and 0.060 respectively, showing dissolution accounts for approximately sixteen times (M:D=0.055) more CO_2 removal than microbial methanogenesis. Lines labelled 'consumption' show the proportion of original CO_2 that has been removed by net microbial methanogenesis.

S4.2. Supplementary tables

Sample	Latitude, Longitude	Producing Zone	CO_2ˇ	CH_4ˇ	$\delta^{13}C$-CO_2	$\delta^{13}C$-CH_4	$\delta^{13}C$-CO_2 – CH_4	CO_2 /^{3}He (x10^8)	±	^{3}He/^{4}He	±	^{4}He (x10^{-5})	±
			mol % (STP)	mol % (STP)	‰ VDPB	‰ VDPB	‰ VDPB					cm^3(STP)/ cm^3	
O1	31.83128, -92.2095	L cent	11	86	16.4	-47.6	64	2.77	0.06	1.78	0.04	23.7	0.2
O2	31.83015, -92.2093	L cent	6.7	89	13.7	-49.3	63	1.92	0.04	1.79	0.04	20.7	0.2
O3	31.82453, -92.2137	2800ft	9.4	88	15.1	-49.3	64.4	2.47	0.06	1.93	0.04	20.9	0.2
O4	31.80899, -92.2297	U cent	18	73	15.8	-48.2	64	6.60	0.15	1.72	0.04	16.0	0.2
O5	31.80119, -92.2224	2800ft	38	57	7.05	-46.7	53.75	17.3	0.4	1.98	0.04	11.8	0.1
O6	31.76926, -92.2133	H2-SD	27	67	13.3	-44.8	58.1	10.6	0.2	1.81	0.04	15.1	0.2
NHH1	31.60037,-92.1668	Wilcox B1	1.9	97	13.9	-46	59.9						
NHH2	31.59793, -92.1468	Wilcox A2	0.28	96	0.33	-49.8	49.5	1.44	0.06	0.38	0.04	5.41	0.04
NHH3	31.58830, -92.1752	T Wilcox	0.77	98	7.1	-61	68.1	1.79	0.05	0.39	0.01	11.8	0.1
NHH4	31.58895, -92.1775	Wilcox C3	1.7	94	9.4	-54.5	63.9	9.97	0.12	0.52	0.01	2.92	0.03
NHH5	31.58907, -92.1666	Wilcox F3a &F3b	1.8	76	3.08	-57	60.08	12.2	0.3	0.58	0.01	2.74	0.03
NHH6	31.58238, -92.1487	Wilcox F2	0.99	84	2.52	-57.5	60.02	2.57	0.6	0.46	0.01	8.93	0.07
NHH7	31.57380, -92.1512	Wilcox H2	0.39	99	-0.93	-59.1	58.17	0.53	0.02	0.50	0.01	15.6	0.2
NHH8	31.56586, -92.1557	Wilcox A1	0.35	97	3.31	-56.2	59.51	0.84	0.03	0.39	0.01	9.64	0.10

Supplementary Table S4.1: Sample location, producing zone, major gas species, carbon isotopes. 1 sigma errors are given. Location is given as latitude and longitude in decimal degrees. The ^{3}He/^{4}He ratio, R, is shown relative to the ^{3}He/^{4}He ratio in air, R_A (*adiabatic corrected, ˇAir corrected)

Sample	Reservoir temp* °C	$\Delta^{13}CH_3D$	±	Apparent $\Delta^{13}CH_3D$ Temperature °C	$\Delta^{12}CH_2D_2$	±	Apparent $\Delta^{12}CH_2D_2$ Temperature °C
O1	39.1	4.89	0.36	56^{+17}_{-15}	12.41	1.29	88^{+15}_{-14}
O2	39.7	4.47^	0.34	74^{+16}_{-14}			
O3	44.4	5.62 ^	0.31	30^{+10}_{-10}	9.13	1.60	132^{+30}_{-23}
O4	39.4	3.93	0.52	100^{+29}_{-25}	12.19	1.39	90^{+17}_{-15}
O5	44.5	5.66	0.39	29^{+14}_{-12}	12.46	1.07	87^{+13}_{-11}
O6	50.7	3.45^	0.26	128^{+17}_{-16}	9.82	1.53	121^{+25}_{-21}
NHH1	51	3.77	0.37	109^{+24}_{-21}	4.27	1.29	252^{+64}_{-44}
NHH2	50	4.38 ^	0.28	78^{+13}_{-12}	3.85	1.81	270^{+118}_{-65}
NHH3	41.9	3.17	0.35	146^{+22}_{-20}	5.03	1.24	224^{+48}_{-36}
NHH4	52.1	3.16	0.54	147^{+32}_{-39}	1.56	1.67	$443^{+n/a}_{-142}$
NHH5	56	3.28	0.40	139^{+34}_{-29}	1.80	1.13	413^{+222}_{-94}
NHH6	55	2.90	0.42	166^{+34}_{-29}	0.01	1.63	$12700^{+n/a}_{-12200}$
NHH7	57.1	3.33	0.57	135^{+44}_{-35}	2.02	1.38	390^{+257}_{-98}
NHH8	49.8	3.64	0.35	116^{+25}_{-20}	5.14	1.10	211^{+41}_{-31}

Supplementary Table S4.2: Reservoir temperatures and sample clumped isotopic compositions and associated apparent temperatures for all samples. 1 sigma errors are given. ^ corrected Δ18 from prototype Ultra.

Sample	^{20}Ne ($x10^{-9}$) $cm^3(STP)/cm^3$	±	^{36}Ar ($x10^{-9}$) $cm^3(STP)/cm^3$	±	^{84}Kr ($x10^{-9}$) $cm^3(STP)/cm^3$	±	^{130}Xe ($x10^{-10}$) $cm^3(STP)/cm^3$	±	$^{20}Ne/^{22}Ne$	±	$^{21}Ne/^{22}Ne$	±	$^{40}Ar/^{36}Ar$	±	$^{86}Kr/^{84}Kr$	±	$^{129}Xe/^{130}Xe$	±
O1	25.8	0.5	84.9	0.8	3.21	0.09	3.46	0.04	10.25	0.03	0.0384	0.0004	1910	17	0.302	0.002	6.59	0.04
O2	26.9	0.5	80.8	0.8	3.66	0.10	3.78	0.05	10.18	0.03	0.0371	0.0003	1797	16	0.302	0.002	6.61	0.04
O3	20.6	0.4	83.3	0.8	1.81	0.05	2.04	0.03	10.42	0.03	0.0405	0.0004	2344	20	0.302	0.002	6.60	0.04
O4	10.5	0.2	66.0	0.6	3.20	0.09	9.04	0.10	10.19	0.03	0.0385	0.0003	1475	13	0.302	0.002	6.57	0.04
O5	10.1	0.2	45.6	0.4	2.07	0.06	2.77	0.03	10.42	0.03	0.0409	0.0004	2484	22	0.302	0.002	6.61	0.04
O6	8.83	0.17	46.0	0.4	2.17	0.05	2.83	0.03	10.64	0.03	0.0459	0.0004	2766	24	0.302	0.002	6.59	0.04
NHH1																		
NHH2	10.3	0.2	44.5	0.4	2.42	0.06	2.12	0.03	9.93	0.03	0.0330	0.0003	435.7	3.8	0.303	0.002	6.51	0.04
NHH3	36.7	0.7	176	2	5.95	0.16	7.39	0.09	9.83	0.03	0.0310	0.0003	369.7	3.2	0.302	0.002	6.52	0.04
NHH4	3.90	0.07	66.0	0.7	4.09	0.11	6.04	0.07	9.76	0.03	0.0342	0.0003	398.6	3.5	0.302	0.002	6.50	0.04
NHH5	3.49	0.07	47.2	0.4	5.23	0.13	10.53	0.11	9.87	0.03	0.0353	0.0003	573.1	5.0	0.304	0.002	6.47	0.04
NHH6	14.9	0.3	79.1	0.7	8.14	0.22	6.15	0.08	9.84	0.03	0.0335	0.0003	494.6	4.3	0.304	0.002	6.50	0.04
NHH7	21.6	0.4	112	1	4.70	0.12	3.99	0.05	10.02	0.03	0.0333	0.0003	603.8	5.3	0.304	0.002	6.47	0.04
NHH8	7.08	0.13	78.6	0.8	2.32	0.06	4.81	0.06	9.77	0.03	0.0308	0.0003	379.4	3.3	0.303	0.002	6.51	0.04
Air									9.81		0.0290		298.56		0.303		6.49	

Supplementary Table S4.3: Noble gas concentrations and ratios for the sampled wells (with 1 sigma errors).

Sample	$\delta^{13}C\text{-}C_2$	$\delta^{13}C\text{-}C_3$	$\delta^{13}C\text{-}nC_4$
	‰$_{VPDB}$	‰ $_{VPDB}$	‰ $_{VPDB}$
O3	-27.3	-17.74	-22.54
O6	-28.14	-20.22	-21.58
NHH2	-24.19	-25.87	-26.00
NHH4	-35.37	-26.52	-27.58
NHH5	-36.96	-28.08	-26.62

Supplementary Table S4.4: Measured carbon isotopic compositions of alkanes

S4.3. Supplementary information

S4.3.1. Geological and production history

The Olla Oil Field is located in La Salle Parish Louisiana, in the Northern Gulf of Mexico and was CO_2 injected between 1983 and 1986 for enhanced oil recovery (CO_2-EOR). The Nebo-Hemphill Oil Field lies 20 km to the southeast of the Olla Field and provides a control field for this study, having had no CO_2 injected (Figure 4.1). Both fields are producing from the Paleocene-Eocene Wilcox Group, which in northern Louisiana comprises of 600-1500m of shallow marine clastic sediments to fluvial deltaic deposits and up to 6m thick coal beds (Tye et al., 1991; Johnston et al., 2000). The Group is bound either side by the Paleocene Midway Group and Eocene Clairborne Group confining units (Johnston et al., 2000). Typically, the Wilcox Group is subdivided into the lower (sandstone with coal beds), middle (sandstone, lignite and clay) and upper (deltaic deposits) intervals, with the 'Big Shale' informal unit separating the middle and upper groups (Echols and Malkin, 1948; Tye et al., 1991). Late cretaceous intrusive igneous bodies in northern Louisiana, west-central Mississippi and south eastern Arkansas are thought to have affected the regional heat flow which may have caused an increase in the thermal maturity of the Wilcox Group during the early Palaeocene (Heydari et al., 1997; Warwick et al., 2008).

CO_2 is present in small concentrations (1.02±0.69 mol%) within the Nebo-Hemphill Field, suggesting there is some natural background CO_2 present in both fields. Between March 1983 and April 1986, the 2800ft sandstone (within the middle Wilcox group) in the Olla Oil Field underwent a pilot project for CO_2 flooding. The CO_2 injected into the field was immiscible and injected in the gas phase (i.e., not supercritical). Gas-oil ratios (GOR) are variable within the field, and do not seem to be associated with proximity to the known gas cap. Higher GORs may instead reflect gas coming out of solution as bottom hole pressure decreases, and not proximity to the known gas cap.

A total of 2.2×10^8 m^3 of CO_2 was injected into the Olla Field and was sourced from the nearby Black Lake Oil Field (produced from the lower cretaceous carbonates of the Petit Formation) in Natchitoches Parish, Louisiana (Figure 4.1). Approximately one third of the injected CO_2 remained within the reservoir after the cessation of the EOR project (Moffet, 1990). It is important to note

here that given the age of this CO_2-EOR project, we were unable to obtain constraints such as the ratio of injected CO_2 to reservoir pore volume that are sometimes cited to quantify the scale of the EOR project and the distribution it achieves within the subsurface. Further, we anticipate that the injected CO_2 is not uniformly distributed within the pore volume of the Olla Field due to different phases of EOR and gas cycling.

In 1984, water flooding also started within the field. In contrast, Nebo-Hemphill has never undergone any type of EOR.

S4.3.2. Molecular geochemistry

Whole oil GC (WOGC) was performed to provide a hydrocarbon fingerprint of each oil, while open column LC (OCLC) was utilised to separate and quantify the saturate, aromatic, resins, and asphaltene fractions of each oil. From these analyses, in general, we see similar fluid compositions between the two fields. The WOGCs show evidence of marine sourced oils with a smooth distribution of n-alkanes, pristine/phytane ratios of approximately 2, and low wax content. Notable differences are likely due to varying levels of biodegradation illustrated by the loss of n-alkanes in some samples and APIs ranging from 21° to 42°. Ultimately, the similarities in the geochemical signatures of these oils provide a basis to use the Nebo-Hemphill Field as a control site for any biogeochemical differences that may arise as a result of the injection of CO_2 at Olla.

Source Facies

Gas chromatography mass spectroscopy (GC/MS) was utilised to analyse the saturate and aromatic fractions to provide the biomarker distributions of each oils. The interpretation of a dominantly marine source is based on the following evidence: (1) a smooth distribution of tricyclic terpanes with C_{23} being the maximum along with extended hopanes (C_{31}-C_{35}) decreasing in order is a classic marine source signature; (2) the high presence of C_{30} hopane compared to C_{29} hopane is indicative of a marine clastic source; (3) higher abundance of C_{28} bisnorhopane compared to oleanane suggesting higher marine input compared to the above source (Wenger et al., 1990); and (4) the observation of C_{26} tricyclic terpane greater than C_{25} tricyclic terpane gives evidence of some terrigeneous input. Consistent with previous interpretations, we consider this source to be a part of

the Wilcox Group oils, more specifically Wilcox Group I as originally described by Sassen et al. (1988) and Sassen (1990).

Thermal Maturity

We adopted standard saturate and aromatic biomarker ratios to develop apparent thermal maturity estimates for each of the oil samples analysed. We discuss these in the context of apparent thermal maturities because we recognise these estimates are based on the bulk weighted average composition of the fluid. The interpretation of the GC/MS analyses of the 12 oils yielded a thermal maturity range of R_o equivalent of 0.9 – 1.25% which we classify as main to late stage oil. The interpretation of this thermal maturity range is based on the following: (1) the presence of higher concentrations of high molecular weight compared to low molecular weight triaromatic steriods, described as % ΔTAS (20-57 %); (2) Isomerization of C_{29} ααα-20S relative to C_{29} ααα-20R steranes (0.45 – 0.48)(Seifurt, 1986); (3) the isomerization of 1,2,5-trimethylnapthalene to 1,3,7-trimethylnapthalene represented as ratio TMNr (0.48 – 0.67) as defined by van Aarssen et al. (1999); (4) ratio C_{23} tricyclic terpane to C_{30} hopane which is calculated as T23/(T23 + H30) (0.10 – 0.37), where the increased presence of C_{23} tricyclic represents higher maturity.

Alteration

The use of WOGC and GC/MS analyses help provide a picture of the alteration history of these oils. We consider the shallow Nebo-Hemphill fluid (NHH3) to be the most biodegraded end member of the samples tested. This interpretation is based on the apparent lack of n-alkanes, an API gravity of 21°, and the presence of demethylated hopanes illustrated. This sample would be classified as severely biodegraded based on the classification of Wenger et al. (2002). The remaining Nebo-Hemphill samples are classified as unbiodegraded to having very-slight biodegradation (Wenger et al., 2002). The Olla Field fluids show evidence of reduced light n-alkanes, display similar n-alkane to isopreniod ratios, and have APIs 33° to 37°, suggesting similar levels of biodegradation between the fluids. Therefore, the Olla fluids would be classified as having very-slight biodegradation (Wenger et al., 2002).

S4.3.3. Identification of injected material

CO_2 concentrations in the injected Olla Field (18±12mol%) are significantly greater than the Nebo-Hemphill Field (1.02±0.69mol%). However, the $\delta^{13}C$ of $CO_2$of the injected material (0.85±0.91‰) is isotopically distinct from the $\delta^{13}C$ of CO_2 now within Olla (13.6±3.2‰) (Figure 4.2b). The injected CO_2 was sourced from the Black Lake Oil Field, which is located close to the Sabine Island Complex. The Sabine Island Complex forms part of the Sabine Uplift basement high and has been suggested to be a likely conduit for mantle derived fluids (Byrne et al., 2020). However, measured $\delta^{13}C$ of CO_2 values at Black Lake (0.85±0.91‰) are elevated relative to mantle CO_2 (-2 to -5‰ (McIntosh et al., 2010; Shelton et al., 2014)), likely reflecting some degree of biological modification when the reservoir was shallower and at temperatures favourable to microbial activity. An alternative interpretation for the elevated $\delta^{13}C$ of CO_2 at Black Lake is that it is a mixture of mantle and crustal derived CO_2, however this would increase the $CO_2/^3He$ above that expected in the mantle, which is not observed in the Olla samples.

As the stable isotopes of carbon are frequently modified by chemical or biological processes, the inert nature of noble gases means they are ideal tracers for injected CO_2 in such scenarios. Because injectate samples were not collected during CO_2-EOR, we do not have access to the noble gas compositions of the material injected into the Olla Field. Nevertheless, it is reasonable that the noble gases at the nearby Nebo-Hemphill Field record pre-injection conditions (given their location and comparable geological histories (supplementary information S4.3.1, S4.3.2), and that these are subsequently modified at the Olla Field through mixing of the injected material during the CO_2 flood.

The $^4He/^{20}Ne$ ratio is between 3,210 and 20,900 in both fields, which is significantly greater than the atmospheric value of 0.32 and thus there is no significant atmospheric contribution to these samples. The air corrected helium isotopic ratio ($^3He/^4He$), reported relative to the atmospheric ratio (R_C/R_A where air=1R_A), in the Olla Field is 1.84±0.10R_A and 0.46±0.08R_A at Nebo-Hemphill (Supplementary Table S4.1). These are both higher than a typical hydrocarbon system where the majority of helium is derived from crustal radiogenic production ($^3He/^4He$ =0.02R_A (Ballentine and

Burnard, 2002)), and higher than other fields within the Gulf of Mexico region (Barry et al., 2018b; Byrne et al., 2018, 2020). The elevated $^{3}He/^{4}He$ ratios are the result of a resolvable mantle contribution. Using a simple two endmember mixing model, with subcontinental lithospheric mantle (SCLM; $^{3}He/^{4}He$ ~6.1 (Day et al., 2015)) and crustal endmembers, we resolve an average 7.8 % mantle ^{3}He contribution at Nebo-Hemphill Oil Field. It is likely that the mantle fluid contribution is coming from the little creek collapse structure, which is situated between the two fields (McCulloh, 2016). At Olla, the average mantle contribution to ^{3}He is 30%, suggesting there is an additional source of mantle fluids to this field which is reasonably explained by the injectate sourced from the Black Lake Field. Ne isotope ratios are elevated at Olla ($^{20}Ne/^{22}Ne$ 10.3±0.2 and $^{21}Ne/^{22}Ne$ 0.0399±0.002) compared to 9.85±0.09 and 0.0335±0.001 at Nebo-Hemphill and 9.8 and 0.029 in air (Supplementary Figure S4.1, Supplementary Table S4.3), again suggest the injected material contains mantle derived fluids.

$^{40}Ar/^{36}Ar$ at Nebo-Hemphill are significantly greater than atmospheric (298.56 (Lee et al., 2006)), with measured ratios of 370±3 to 604±5. The Olla Field has higher $^{40}Ar/^{36}Ar$ (1,476±13 to 2,766±24) than both Nebo-Hemphill and air (Supplementary Table S4.3). Elevated $^{40}Ar/^{36}Ar$ ratios can be a result of both excess of radiogenic ^{40}Ar and mantle derived fluids (Ballentine and Burnard, 2002; Graham, 2002). The difference in the $^{40}Ar/^{36}Ar$ ratios could be due to variable amounts of radiogenic production or fundamental differences in the extent of contact with formation waters between the two fields. However, as all the wells sampled are within the same geological formation (Middle Wilcox Group), the two fields are in relatively close proximity, and they have indistinguishable ^{4}He concentrations, it seems unlikely that this would be the cause. Thus, the difference is likely a result of the injected CO_2, which likely possessed mantle derived $^{40}Ar/^{36}Ar$ excesses, concordant with the observed mantle derived He and Ne isotopes. Finally, while Xe isotope ratios at Nebo-Hemphill are indistinguishable from air, the Olla Field showed excesses in some xenon isotope ratios relative to air. For example, the $^{129}Xe/^{130}Xe$ ratio is 6.59±0.01 compared to an atmospheric value of 6.49 (Supplementary Table S4.3) (Porcelli et al., 2002); this excess in ^{129}Xe relative to ^{130}Xe is consistent with a contribution from mantle fluids with an end member

$^{129}Xe/^{130}Xe$ value of 8.2 (Graham, 2002). The Olla Field therefore shows a clear mantle component that is not present within the Nebo-Hemphill control field.

The detection of injected fluids within the Olla Field using the conservative noble gas tracers differs from the findings of the previous studies that used $\delta^{13}C$ of CO_2 to conclude that injected CO_2 is no longer or never was present in the majority of the sampled wells (e.g., Shelton et al., 2014). The subsurface behaviour of the injected CO_2 within the system can therefore be re-examined using a combination of noble gases, stable isotopes and clumped isotopologues.

S4.3.4. Dissolution within the Olla Oil Field

CO_2 is highly soluble in water under reservoir conditions. The most likely trapping mechanisms for free-phase subsurface CO_2 are dissolution or precipitation as carbonate minerals mediated by dissolution (Gilfillan et al., 2009). A decrease in the $CO_2/^3He$ correlates with increasing ^4He and ^{20}Ne concentrations within the Olla Field (Supplementary Figure S4.2). ^{20}Ne (and often ^4He) are derived from the formation water (Gilfillan et al., 2009), suggesting that CO_2 trapping in the Olla Field is also proportional to the amount of formation water which has been contacted and degassed, consistent with dissolution within the field (Gilfillan et al., 2009). Dissolution (solubility trapping) has previously been found to be a major sink for injected CO_2 (Gilfillan et al., 2009). Furthermore, similar to precipitation, microbial consumption of CO_2 would require the involvement of formation water. Oil-water contact in the reservoir will allow for the dissolution of CO_2 into formation water within the field, a prerequisite for methanogenesis. Solubility trapping imparts a slight pH dependent fractionation towards a light isotopic composition (Clark and Fritz, 1997). However, this fractionation effect is marginal in comparison to the amount of CO_2 that can be trapped and the fractionation that can be imparted by methanogenesis-AOM cycling (Figure 4.2a).

Given the presence of discontinuous coal beds within the Wilcox Group (Warwick et al., 2004, 2008), it is possible that some of the injected CO_2 may have been sorbed onto these coal beds as CO_2 has a much greater affinity to coal than CH_4 (Yee et al., 1993; Busch et al., 2004). The resulting isotopic fractionation imparted by this process remains poorly constrained, with some studies suggesting a >5‰ shift (Prinzhofer and Huc, 1995; Prinzhofer and Pernaton, 1997) while others

suggest negligible effects on the $\delta^{13}C$ of CO_2 (Fuex, 1980; Zhang et al., 1999; Xia and Tang, 2012). Coal sorption would cause fractionation in the opposition direction of the methane isotopic signature. Given the heavier $\delta^{13}C$ of CO_2 and $\delta^{13}C$ of CH_4 isotopic signatures in the injected Olla Field, it is unlikely that CO_2 sorption to coal is a major CO_2 sink in the field, in agreement with finding from Shelton et al. (2014).

S4.3.5. Subsurface behaviour of carbon at Olla

The offset between the $\delta^{13}C$ of CH_4 and $\delta^{13}C$ of CO_2 in the Olla Field are close to those expected under thermally driven isotope exchange equilibrium for the observed temperatures. However, the thermal equilibrium of CO_2 and CH_4 is kinetically limited at the current temperatures (29.2-50.7^oC) in the Olla reservoirs and would not occur on the timescale of injection, without a process to enhance the reaction rate (Giggenbach, 1982). A combination of both microbial methanogenesis and anaerobic oxidation of methane (AOM) active within the field would allow for the system to be approaching equilibrium under the current thermal conditions within the reservoir. The observations detailed below provide evidence for this conclusion and allow for the net microbial methanogenesis to be quantified.

The Olla samples are enriched in both $\delta^{13}C$ of CO_2 and $\delta^{13}C$ of CH_4 compared to Nebo-Hemphill and the injected CO_2 values. The difference in $\delta^{13}C$ of CO_2 and $\delta^{13}C$ of CH_4 varies from 53.7-64.4‰ in the Olla Field and is consistent with the CO_2 and CH_4 approaching isotopic equilibrium at current reservoir temperatures (Figure 4.2b). Carbon isotopes of CO_2 and CH_4 approaching equilibrium in hydrocarbon systems with current reservoir conditions have previously been observed (Thiagarajan et al., 2020a).

The clumped isotopologues of methane ($\Delta^{13}CH_3D$ and $\Delta^{12}CH_2D_2$) can provide independent constraints on its origin within petroleum systems (Stolper et al., 2014, 2018; Douglas et al., 2017; Giunta et al., 2019; Young, 2019). Thermogenic methane is expected to have a composition consistent with the source rock maturation temperature, this is typically at or above 157^oC (Stolper et al., 2014). At Olla we expect methane generation to have occurred at 163±18^oC (based on biomarker maturity estimates following the methods in Sweeney and Burnham, 1990). Microbial

methane is variable in its clumped isotopic compositions with both non-equilibrium (Giunta et al., 2019; Young, 2019) and apparent equilibrium signatures reported in samples obtained from the deep subsurface (Douglas et al., 2017; Young, 2019). Microbial methanogenesis forms methane characterised by low $\Delta^{13}CH_3D$ and extremely low $\Delta^{12}CH_2D_2$ (Giunta et al., 2019; Young, 2019), whereas AOM tends to drive the isotopologue composition of methane towards equilibrium, with equilibrium expected to be reached at a faster rate in $\Delta^{13}CH_3D$ compared to in $\Delta^{12}CH_2D_2$ (Holler et al., 2011; Yoshinaga et al., 2014; Stolper et al., 2015; Ash et al., 2019; Young, 2019; Ono et al., 2021). In the Olla Field, we see $\Delta^{13}CH_3D$ of 3.45-5.62‰ (apparent temperature of 29^{+14}_{-12} to 128^{+17}_{-16}°C) and $\Delta^{12}CH_2D_2$ of 9.13-12.4‰ (apparent temperature of 87^{+13}_{-11}–132^{+30}_{-23}°C) (Figure 4.3, Supplementary Table S4.2), these temperatures preclude a thermogenic origin for the methane and are instead consistent with a microbial contribution. Samples O4 and O6 are in internal clumped isotopologue equilibrium at temperatures lower than expected for the thermogenic methane and appear to be approaching equilibrium with current reservoir conditions. The remaining samples from Olla have already reached apparent equilibrium with the current reservoir conditions in $\Delta^{13}CH_3D$ but have yet to reach apparent equilibrium in $\Delta^{12}CH_2D_2$ likely due to kinetic effects. The clumped isotopologues at Olla are clearly approaching equilibrium at reservoir temperatures, and thus there must be active AOM within the Olla Field. This supports the conclusion that there is active microbial methanogenesis and AOM driving the carbon isotopes to approach equilibrium under current thermal conditions in the Olla Field.

There is microbial degradation of the higher alkane gases (Supplementary Figure S4.4, Supplementary Table S4.4) within the Olla Field. Propane is preferentially consumed during microbial degradation and thus in biodegraded gases propane will see the most pronounced $\delta^{13}C$ enrichment (Head et al., 2003). This $\delta^{13}C$ enrichment is clear within the Olla gases and supports active microbial hydrocarbon degradation within the field.

The presence of methanogenic activity and the idea of a methanogenic ‘hotspot’ in the Olla Field has been previously suggested (McIntosh et al., 2010). The environmental conditions for which methanogenesis can occur are relatively well defined. Within nutrient poor environments such as

oil reservoirs or coal beds, methanogens can survive at temperatures up to 80°C, with the largest growth rates and thus greatest amount of methanogenic activity between 40-50°C (Zinder, 1993; Head et al., 2003; Larter et al., 2005; Doerfert et al., 2009). Methanogenic activity is greatest at near neutral pH and is inhibited at pH <4 and >9 (Zinder, 1993). Formation water salinity can also inhibit methanogenesis above Cl^- concentrations of 1500mM, with greatest growth between 200-600mM (Zinder, 1993; Doerfert et al., 2009; Oren, 2011). The presence of ferric iron and sulfate at concentrations >1mM can also limit methanogenesis (as a result of the dominance of other bacteria) (Rice and Claypool, 1981; Lovley and Klug, 1983; Capone and Kiene, 1988; van Bodegom et al., 2004). Notably, the Olla Field exhibits ideal environmental conditions for methanogenesis, in terms of pH (6.5-7.5), temperature (29.2-50.7°C), salinity (1094-1622mM), sulfate (<0.6mM/l) and iron concentrations (<0.6 mM/l expect for 1 site) (Shelton et al., 2014).

In addition, geochemical and isotopic parameters associated with microbial methanogenesis in organic rich settings are also well established (Rice and Claypool, 1981; Larter et al., 2005; Mcintosh and Martini, 2008; Shelton et al., 2014, 2016). Traditionally carbon isotopes of CH_4 have been used to determine the presence of biogenic methane (typically <-60‰) (Whiticar et al., 1986; Etiope and Lollar, 2013). However, methanogenesis can result in heavy biogenic methane as the residual CO_2 pool gets increasingly elevated, consistent with observations at Olla (Supplementary Figure S4.3). Additionally, where methanogenesis has occurred, formation water alkalinity is > 10meq/kg, acetate concentrations <1mM, Ca/Mg are <1.5 and the δ^{13}C-DIC is greater than +20‰ (Rice and Claypool, 1981; Larter et al., 2005; McIntosh and Martini, 2008). Within the Olla Field alkalinity ranges between 21.4-57.7meq/kg, average Ca/Mg ratios is 0.2 and δ^{13}C-DIC are 14.2-28.7 ‰ (Shelton et al., 2014), again indicating that methanogenesis has occurred within the field.

SSU rRNA gene sequencing analysis of the microbial communities within the Olla Field (samples O1 and O4) indicate that within the archaeal sequences hydrogenotrophic methanogens, methanol/methylotrophic methanogens and ANME assigned sequences are present (Supplementary Figure S4.5). This microbial array would facilitate both microbial methanogenesis and AOM within the field.

During the cycling of carbon between methanogenesis and AOM we would not expect a change in the isotopic composition of hydrogen. It is possible that as a result of microbial activity or the reaction kinetics that extracellular hydrogen is added to the system. This hydrogen could be sourced from the water, free hydrogen from the degradation of the higher hydrocarbon gases or from the oil. As a result we are unable to determine whether the hydrogen isotopes within the system are also approaching equilibrium under current reservoir temperatures.

It is possible that the CO_2 and CH_4 isotopes in the Olla system are reflecting purely the kinetic process of methanogenesis. The difference in the $\delta^{13}C$ of CO_2 and $\delta^{13}C$ of CH_4 at Olla (53.7-64.4‰) is consistent with that expected from microbial methanogenesis (~58‰ (Conrad, 2005)). In such a scenario all the methane at Olla would be microbial in origin, thus requiring any thermogenic methane component originally in the system to be overwhelmed. The high concentration and mixed thermogenic-microbial composition of methane within the Nebo-Hemphill Field (Figure 4.3, Supplementary Information S4.3.6) is inconsistent with such a scenario. In addition, the clumped isotopologues at Olla show a clear need for AOM within the field and metagenomics analysis show active methanotrophs, which is not compatible with a scenario of purely microbial methanogenesis dominating the system. Therefore, future studies investigating the processes effecting CO_2 in potential CCS storage targets will benefit from a complete geological, geochemical and microbiological characterisation of the field study site.

S4.3.6. Subsurface behaviour of carbon in the Nebo-Hemphill Oil Field

The carbon isotopic composition of CO_2 and CH_4 at Nebo-Hemphill are depleted in comparison to the Olla Field (Figure 4.2b). Despite this, the difference in $\delta^{13}C$ of CO_2 and $\delta^{13}C$ of CH_4 at Nebo-Hemphill overlaps with that of Olla (50.8-68.1‰ and 53.7-64.4‰ respectively). The degree of isotopic fractionation at Nebo-Hemphill is consistent with thermal equilibrium at 29.8-85.3^{o}C, in agreement with present day reservoir temperatures (29.7-57.1^{o}C). In addition, $\delta^{13}C$ of CO_2 at Nebo-Hemphill are enriched in comparison with that typically expected for crustal or mantle sourced CO_2 (<2‰) (Clark and Fritz, 1997; Wycherley et al., 1999), consistent with a small amount of microbial methanogenesis within the field. We propose that there is also microbial methanogenesis and AOM

within the Nebo-Hemphill Field, however unlike at Olla this has not been enhanced by any injection to the field and thus is occurring at different rates and to different extents.

Microbiological analysis of NHH3 and NHH6 show that hydrogenotrophic methanogens, methanol/methylotrophic methanogens and ANME assigned sequences are present within Nebo-Hemphill, in agreement with both active methanogenesis and AOM within the field (Supplementary Figure S4.5). Clumped isotopologues of methane within the Nebo-Hemphill Oil Field give apparent temperatures for $\Delta^{13}CH_3D$ of 78^{+14}_{-12}-166^{+34}_{-29}°C and apparent temperatures for $\Delta^{12}CH_2D_2$ which are greater than expected for thermogenic methane in the field (163±18°C, Figure S4.3). Clumped isotopologues suggest that the methane is likely to be dominantly thermogenic with some microbial contributions. Samples NHH1, NHH2 and NHH8 have apparent temperatures below that expected for thermogenic methane and appear to be approaching low temperature equilibrium in $\Delta^{13}CH_3D$, consistent with active methanogenesis and AOM cycling within the field, but likely at different rates and extents to the Olla Field.

S4.3.7. Modelling of the Pannonian Basin

The unequivocal identification and quantification of CO_2 related microbial methanogenesis at Olla has globally significant implications, and warrants the reconsideration of reservoir processes at other sites worldwide. Re-examination of previously published datasets allows the elucidation of the significance of methanogenesis in different reservoir environments, especially in systems that have or had naturally high CO_2 concentrations, such as the Pannonian Basin. A significant proportion of the CO_2 found in natural gas fields within the Pannonian Basin is of mantle origin (Sherwood Lollar et al., 1997). The initial, $CO_2/^3He$ in the Szegholm North, Szegholm South, Ebes and Hajduszoboszlo gas fields was estimated to be 7.9±5.4 $x10^9$**,** consistent with the European subcontinental lithospheric mantle range (0.6-40 $x10^9$) and MORB mantle range ($2±1x10^9$)(Supplementary Figure S4.7)(Ballentine et al., 2001; Kämpf et al., 2007; Holland and Gilfillan, 2013). Since emplacement, significant CO_2 trapping in many fields was identified from lower observed $CO_2/^3He$ (e.g., the Szegholm North and South, Ebes and Hajduszoboszlo gas fields)

and speculation that some of the CO_2 may have been converted into CH_4 (Sherwood Lollar et al., 1997), although no viable mechanism was identified.

Using an average geothermal gradient of 45°C/km (Koncz and Etler, 1994) the temperature within these fields is predicted to be between 40-105°C, (with temperatures being up to 20°C cooler at the time of CO_2 emplacement (Royden et al., 1983)), and thus within the range of microbially-driven methanogenesis. In addition, the presence of thermogenic hydrocarbons would also ensure H_2 availability, similar to the Olla and Nebo-Hemphill fields. We surmise that the Pannonian Basin may be analogous to Olla and that hydrogenotrophic microbial methanogenesis active within the field may provide the missing mechanism for CO_2 removal, which was previously unidentified, and point to this mechanism as an important subsurface process operating on systems naturally enriched in CO_2 as well as anthropogenically CO_2 injected oil and gas fields.

In the absence of supporting clumped isotopologue data, if we assume the system is methanogenesis driven we can nevertheless construct similar methanogenesis-dissolution models using published data from the Szegholm South Field (where multiple CO_2 isotope data is available)(Sherwood Lollar et al., 1994, 1997). By comparing the observed $CO_2/^3He$ ratios against the CO_2 concentration, a clear correlation emerges (Supplementary Figure S4.7). Attributing this to the effect of dissolution (a pre-requisite for microbial methanogenesis), it is possible to extrapolate back to an initial $CO_2/^3He$ end member value of 13.3×10^9, consistent with previous estimates (Kämpf et al.,2007).

Our model assumes mantle-derived CO_2 in the field with a typical isotopic composition of $\delta^{13}C$ of CO_2= -5‰ (Supplementary Figure S4.7b). Taking this as a starting point, 16.4±0.8 times more dissolution than methanogenesis is required in the Szegholm South Field to produce the measured $\delta^{13}C$ of CO_2. As such, proportionally less methanogenesis, relative to the Olla Field, would be expected here as the gas fields are not being constantly perturbed via water injection and therefore nutrient availability is likely much more limited. The presence of biogenic methane (through CO_2 conversion) can also be clearly identified from the measured C_1/C_N in the Szegholm South Field (0.946±0.004) which are greater than what would be expected in a purely thermogenic system (0.909). Using the excess in the C_1/C_N ratios we determine that 41±5% of the CH_4 currently present

in the Szegholm South Field part of the basin is biogenic. Similar C_1/C_N excesses are seen in the other gas fields in the Pannonian Basin (Sherwood Lollar et al., 1994). In addition, other fields such as the Szegholm North, Ebes, Hajduszoboszlo, Kismarja, Répcelak and Mihàly (Pannonian Basin), Subei (China) and JM Brown Bassett (Permian Basin) fields also display geochemical signatures consistent with the occurrence of methanogenesis (Sherwood Lollar et al., 1994, 1997; Sheng et al., 1997; Ballentine et al., 2001; Palcsu et al., 2014). Thus, we conclude that although methanogenesis is not the dominant CO_2 loss mechanism, it may play a substantial role that has not previously been considered in many natural systems.

Acknowledgements

RLT was supported by a Natural Environment Research Council studentship (Grant ref. NE/L002612/1). CJB and PHB acknowledge ExxonMobil funding and Aaron Regberg and Bill Meurer for their support of the project and help with sample collection. CJB was part supported by an Earth4D CIFAR fellowship. PHB was supported by NSF awards 1923915 and 2015789. OW was supported by Natural Sciences and Engineering Research Council of Canada Discovery and Accelerator grants awarded to the Sherwood Lollar research group and would like to acknowledge Barbara Sherwood Lollar's support for the project. ZMS would like to thank Jennifer Biddle and Glenn Christman for their help in generating the microbial data.

Authorship Statement

I hereby give permission to Rebecca L. Tyne to use our joint work as contribution towards her DPhil thesis to be submitted for examination at the University of Oxford.

I confirm that to the best of my knowledge, the author contribution statement below is accurate and Rebecca L. Tyne's contribution towards the work is greater than that of any other co-author.

Chapter author contribution statement:

The project was conceived by RLT, PHB, ML and CJB. RLT performed the noble gas isotopic analysis, managed the project and prepared the first draft of the manuscript. PHB collected the samples. ZS, HX and BS conducted the microbial, clumped isotope and molecular geochemical analysis respectively. Clumped isotope modelling was developed by HX and JME. Integrated noble gas and stable isotope modeling was developed by RLT, PHB, ML, CJB, OW and DJB. All authors contributed to the final manuscript

Chris J. Ballentine

Date: 14/4/21

Darren J. Hillegonds

Date:12th April 2021

Peter H. Barry

Date: 6-4-2021

Michael Formolo

Date: 6-4-2021

Michael Lawson

Date: 06-04-2021

John M. Eiler

Date: April 6, 2021

David J. Byrne

Date: 6/4/21

Hao Xie

Date: 7/4/21

Oliver Warr

Date: 6/4/2021

References

Ash J. L., Egger M., Treude T., Kohl I., Cragg B., Parkes R. J., Slomp C. P., Sherwood Lollar B. and Young E. D. (2019) Exchange catalysis during anaerobic methanotrophy revealed by $\Delta^{12}CH_2D_2$ and $\Delta^{13}CH_3D$ in methane. *Geochemical Perspective Letters* **10**, 26–30.

Bachu S. (2000) Sequestration of CO_2 in geological media: criteria and approach for site selection in response to climate change. *Energy Conversion and Management* **41**, 953–970.

Baines S. J. and Worden R. H. (2004) The long-term fate of CO_2 in the subsurface: natural analogues for CO_2 storage. *Geological Society, London, Special Publications* **233**, 59–85.

Ballentine C. J., O'Nions R. K., Oxburgh E. R., Horvath F. and Deak J. (1991) Rare gas constraints on hydrocarbon accumulation, crustal degassing and groundwater flow in the Pannonian Basin. *Earth and Planetary Science Letters* **105**, 229–246.

Ballentine C. J., Schoell M., Coleman D. and Cain B. A. (2001) 300-Myr-old magmatic CO_2 in natural gas reservoirs of the west Texas Permian basin. *Nature* **409**, 327–331

Ballentine C. J. and Burnard P. G. (2002) Production, Release and Transport of Noble Gases in the Continental Crust. In: *Noble Gases in Geochemistry and Cosmochemistry.(*Eds: D. Porcelli, C.J. Ballentine,, R. Wieler) Reviews in Mineralogy and Geochemistry **47**. Geochemical Society, Mineralogical Society of America, Chapter 12, 481–538.

Ballentine C. J. and Sherwood Lollar B. (2002) Regional groundwater focusing of nitrogen and noble gases into the Hugoton-Panhandle giant gas field, USA. *Geochimica et Cosmochimica Acta* **66**, 2483–2497.

Ballentine C. J., Marty B., Lollar B. S. and Cassidy M. (2005) Neon isotopes constrain convection and volatile origin in the Earth's mantle. *Nature* **433**, 33–38.

Barry P.H., Kulongoski J. T., Tyne R. L., Landon M. K., Gillespie J. M., Stephens M. J., Hillegonds D. J., Byrne D. J. and Ballentine C. J. (2018a) Tracing enhanced oil recovery signatures in casing gases from the Lost Hills oil field using noble gases. *Earth and Planetary Science Letters* **496**, 57–67.

Barry P. H., Lawson M., Meurer W. P., Cheng A. and Ballentine C. J. (2018b) Noble Gases in Deepwater Oils of the U.S. Gulf of Mexico. *Geochemistry, Geophysics, Geosystems* **19**, 4218–4235.

Barry P. H., Lawson M., Meurer W. P., Warr O., Mabry J. C., Byrne D. J. and Ballentine C. J. (2016) Noble gases solubility models of hydrocarbon charge mechanism in the Sleipner Vest gas field. *Geochimica et Cosmochimica Acta* **194**, 291–309.

Boetius A., Ravenschlag K., Schubert C. J., Rickert D., Widdel F., Gieseke A., Amann R., Jørgensen B. B., Witte U. and Pfannkuche O. (2000) A marine microbial consortium apparently mediating anaerobic oxidation of methane. *Nature* **407**, 623–626.

Bokulich N. A., Kaehler B. D., Rideout J. R., Dillon M., Bolyen E., Knight R., Huttley G. A. and Gregory Caporaso J. (2018) Optimizing taxonomic classification of marker-gene amplicon sequences with QIIME 2's q2-feature-classifier plugin. *Microbiome* **6**, 90.

Bolyen E., Rideout, J.R., Dillon, M.R., et al., (2019) Reproducible, interactive, scalable and extensible microbiome data science using QIIME 2. *Nature Biotechnology* **37**, 852–857.

Bottinga Y. (1969) Calculated fractionation factors for carbon and hydrogen isotope exchange in the system calcite-carbon dioxide-graphite-methane-hydrogen-water vapor. *Geochimica et Cosmochimica Acta* **33**, 49–64.

Bui. M.,. Adjiman, C.S., Bardow, A., Anthony, E.J., Boston, A., Brown, S., Fennell, P.S., Fuss, S., Galindo, A., Hackett, L.S., Hallet, J.P., Herzog, H.J., Jackson, G., Kemper, J., Krevor, A., Maitland, G.C., Matuzewski, M., Metcalfe, I.S., Petit, C., Puxty, G., Reimer, J., Reiner, D.M., Rubin, E.S., Scott, S.A., Shah, N., Smit, B., Trusler, J.P.M., Webley, P., Wilcox, J., Mac Dowell, N. (2018) Carbon capture and storage (CCS): the way forward. *Energy & Environmental Science* **11**, 1062–1176.

Burnard P. (2013) *The Noble Gases as Geochemical Tracers*. (Ed. P. Burnard). Advances in Isotope Geochemistry. Springer, Berlin, Heidelberg.

Busch A., Gensterblum Y., Krooss B. M. and Littke R. (2004) Methane and carbon dioxide adsorption–diffusion experiments on coal: upscaling and modelling. *International Journal of Coal Geology* **60**, 151–168.

Byrne D. J., Barry P. H., Lawson M. and Ballentine C. J. (2018) Determining gas expulsion vs retention during hydrocarbon generation in the Eagle Ford Shale using noble gases. *Geochimica et Cosmochimica Acta* **241**, 240–254.

Byrne D. J., Barry P. H., Lawson M. and Ballentine C. J. (2020) The use of noble gas isotopes to constrain subsurface fluid flow and hydrocarbon migration in the East Texas Basin. *Geochimica et Cosmochimica Acta* **268**, 186–208.

Callahan B. J., McMurdie P. J., Rosen M. J., Han A. W., Johnson A. J. A. and Holmes S. P. (2016) DADA2: High-resolution sample inference from Illumina amplicon data. *Nature Methods* **13**, 581–583.

Cao X., Bao H. and Peng Y. (2019) A kinetic model for isotopologue signatures of methane generated by biotic and abiotic CO_2 methanation. *Geochimica et Cosmochimica Acta* **249**, 59–75.

Capone D. G. and Kiene R. P. (1988) Comparison of Microbial Dynamics in Marine and Freshwater Sediments: Contrasts in Anaerobic Carbon Catabolism. *Limnology and Oceanography* **33**, 725–749.

Chung H. M., Gormly J. R. and Squires R. M. (1988) Origin of gaseous hydrocarbons in subsurface environments: Theoretical considerations of carbon isotope distribution. *Chemical Geology* **71**, 97–104.

Clark I. D. and Fritz P. (1997) *Environmental isotopes in hydrogeology*., CRC Press/Lewis Publishers, Boca Raton, FL.

Conrad R. (2005) Quantification of methanogenic pathways using stable carbon isotopic signatures: a review and a proposal. *Organic Geochemistry* **36**, 739–752.

Day J. M. D., Barry P. H., Hilton D. R., Burgess R., Pearson D. G. and Taylor L. A. (2015) The helium flux from the continents and ubiquity of low-$^3He/^4He$ recycled crust and lithosphere. *Geochimica et Cosmochimica Acta* **153**, 116–133.

Doerfert S. N., Reichlen M., Iyer P., Wang M. and Ferry J. G. (2009) Methanolobus zinderi sp. nov., a methylotrophic methanogen isolated from a deep subsurface coal seam. *International Journal of Systematic and Evolutionary Microbiology,* **59**, 1064–1069.

Douglas P. M. J., Stolper D. A., Eiler J. M., et al., (2017) Methane clumped isotopes: Progress and potential for a new isotopic tracer. *Organic Geochemistry* **113**, 262–282.

Echols D. J. and Malkin D. S. (1948) Wilcox (Eocene) Stratigraphy, a Key to Production. *AAPG Bulletin* **32**, 11–33.

Etiope G. and Lollar B. S. (2013) Abiotic Methane on Earth. *Reviews of Geophysics* **51**, 276–299.

Fuex A. N. (1980) Experimental evidence against an appreciable isotopic fractionation of methane during migration. *Physics and Chemistry of the Earth* **12**, 725–732.

Giggenbach W. F. (1982) Carbon-13 exchange between CO_2 and CH_4 under geothermal conditions. *Geochimica et Cosmochimica Acta* **46**, 159–165.

Gannon, R.S., Saraceno, J.F., Kulongoski, J.T., Teunis, J.A., Barry, P.H., Tyne, R.L., Kraus, T.E.C., Hansen, A.M., and Qi, S.L. (2018) Produced water chemistry data for the Lost Hills, Fruitvale, and North and South Belridge study areas, Southern San Joaquin Valley, California: U.S. Geological Survey data release.

Gilfillan S. M. V., Ballentine C. J., Holland G., Blagburn D., Lollar B. S., Stevens S., Schoell M. and Cassidy M. (2008) The noble gas geochemistry of natural CO_2 gas reservoirs from the Colorado Plateau and Rocky Mountain provinces, USA. *Geochimica et Cosmochimica Acta* **72**, 1174–1198.

Gilfillan S. M. V., Lollar B. S., Holland G., Blagburn D., Stevens S., Schoell M., Cassidy M., Ding Z., Zhou Z., Lacrampe-Couloume G. and Ballentine C. J. (2009) Solubility trapping in formation water as dominant CO_2 sink in natural gas fields. *Nature* **458**, 614–618.

Giunta T., Young E. D., Warr O., et al., (2019) Methane sources and sinks in continental sedimentary systems: New insights from paired clumped isotopologues $\Delta^{13}CH_3D$ and $\Delta^{12}CH_2D_2$. *Geochimica et Cosmochimica Acta* **245**, 327–351.

Graham D. W. (2002) Noble Gas Isotope Geochemistry of Mid-Ocean Ridge and Ocean Island Basalts: Characterization of Mantle Source Reservoirs. In: *Noble Gases in Geochemistry and Cosmochemistry.(*Eds: D. Porcelli, C.J. Ballentine,, R. Wieler) Reviews in Mineralogy and Geochemistry **47**. Geochemical Society, Mineralogical Society of America, Chapter 8 247–317.

Gray N. D., Sherry A., Larter S. R., Erdmann M., Leyris J., Liengen T., Beeder J. and Head I. M. (2009) Biogenic methane production in formation waters from a large gas field in the North Sea. *Extremophiles* **13**, 511–519.

Gruen D. S., Wang D. T., Könneke M., Topçuoğlu B. D., Stewart L. C., Goldhammer T., Holden J. F., Hinrichs K.-U. and Ono S. (2018) Experimental investigation on the controls of clumped isotopologue and hydrogen isotope ratios in microbial methane. *Geochimica et Cosmochimica Acta* **237**, 339–356.

Györe D., Stuart F. M., Gilfillan S. M. V. and Waldron S. (2015) Tracing injected CO_2 in the Cranfield enhanced oil recovery field (MS, USA) using He, Ne and Ar isotopes. *International Journal of Greenhouse Gas Control* **42**, 554–561.

Head I. M., Jones D. M. and Larter S. R. (2003) Biological activity in the deep subsurface and the origin of heavy oil. *Nature* **426**, 344–352.

Heydari E., Byerly G. R. and Henry D. J. (1997) *Contact Metamorphism and Over Maturation of Organic Matter Associated with an Igneous Intrusion in the Smackover Formation, Northeastern Louisiana*. Gulf Coast Association of Geological Societies Transactions **47**, 201-213

Holland, G., Gilfillan, S.M.V. (2013). Application of noble gases to the viability of CO_2 storage. In: *The Noble Gases as Geochemical Tracers*. (Ed. P. Burnard). Advances in Isotope Geochemistry. Springer, Berlin, Heidelberg. pp 177-223.

Holler T., Wegener G., Niemann H., Deusner C., Ferdelman T. G., Boetius A., Brunner B. and Widdel F. (2011) Carbon and sulfur back flux during anaerobic microbial oxidation of methane and coupled sulfate reduction. *Proceedings of the National Academy of Sciences* **108**, E1484–E1490.

Johnston J. E. III., Heinrich P. V., Lovelace J. K., McCulloh R. P. and Zimmerman R. K. (2000) Stratigraphic Charts of Louisiana.

Kämpf H., Geissler W. H. and Bäuer K. (2007) Combined Gas-geochemical and Receiver Function Studies of the Vogtland/NW Bohemia Intraplate Mantle Degassing Field, Central Europe. In *Mantle Plumes: A Multidisciplinary Approach* Springer Berlin Heidelberg.

Katoh K., Misawa K., Kuma K. and Miyata T. (2002) MAFFT: a novel method for rapid multiple sequence alignment based on fast Fourier transform. *Nucleic Acids Research* **30**, 3059–3066.

Kennedy B. M., Hiyagon H. and Reynolds J. H. (1990) Crustal neon: a striking uniformity. *Earth and Planetary Science Letters* **98**, 277–286.

Koncz I. and Etler O. (1994) Origin of oil and gas occurrences in the Pliocene sediments of the Pannonian basin, Hungary. *Organic Geochemistry* **21**, 1069–1080.

LaForce T., Ennis-King J., Boreham C. and Paterson L. (2014) Residual CO_2 saturation estimate using noble gas tracers in a single-well field test: The CO_2CRC Otway project. *International Journal of Greenhouse Gas Control* **26**, 9–21.

Larter S. R., Head I. M., Huang H., Bennett B., Jones M., Aplin A. C., Murray A., Erdmann M., Wilhelms A. and Primio R. D. (2005) Biodegradation, gas destruction and methane generation in deep subsurface petroleum reservoirs: an overview. *Geological Society, London, Petroleum Geology Conference series* **6**, 633–639.

Lee J.-Y., Marti K., Severinghaus J. P., Kawamura K., Yoo H.-S., Lee J. B. and Kim J. S. (2006) A redetermination of the isotopic abundances of atmospheric Ar. *Geochimica et Cosmochimica Acta* **70**, 4507–4512.

Leung D. Y. C., Caramanna G. and Maroto-Valer M. M. (2014) An overview of current status of carbon dioxide capture and storage technologies. *Renewable and Sustainable Energy Reviews* **39**, 426–443.

Lovley D. R. and Klug M. J. (1983) Sulfate Reducers Can Outcompete Methanogens at Freshwater Sulfate Concentrations. *Applied and Environmental Microbiology* **45**, 187–192.

Matter, J.M., Stute, M., Snænjörnsdottir, S.Ó., Oelkers, E.H., Gislason, S.R., Aradottir, E.S., Sigfusson, B., Gunnarsson, I., Sigurdardottir, H., Gunnlaugsson, E. Axelsson, G., Alfredsson, H.A., Woff-BOenisch, D., Mesfin, K., Fernandex de la Reguera Taya, D., Hall, J., Dideriksen, K., Broecker, W.S., 2016. Rapid carbon mineralization for permanent disposal of anthropogenic carbon dioxide emissions. Science **352**(6291) 1312-1314.

McCulloh R. P. (2016) Little creek structure, northwestern La Salle Parish, Louisiana. In: *50th Annual GSA South-Central Section Meeting*. 271780.

McDonald D., Price M. N., Goodrich J., Nawrocki E. P., DeSantis T. Z., Probst A., Andersen G. L., Knight R. and Hugenholtz P. (2012) An improved Greengenes taxonomy with explicit ranks for ecological and evolutionary analyses of bacteria and archaea. *ISME Journal* **6**, 610–618.

Mcintosh J. C. and Martini A. M. (2008) Hydrogeochemical Indicators for Microbial Methane in Fractured Organic-Rich Shales: Case Studies of the Antrim, New Albany, and Ohio Shales. In: *Gas Shale in the Rocky Mountains and Beyond*, (Eds: D. Hill, P. Lillis, and J. Curtis) Rocky Mountain Association of Geologists. 162-174.

McIntosh J. C., Warwick P. D., Martini A. M. and Osborn S. G. (2010) Coupled hydrology and biogeochemistry of Paleocene–Eocene coal beds, northern Gulf of Mexico. *Geological Society of America Bulletin* **122**, 1248–1264.

Moffet C. I. (1990) *Post-economic evaluation 2800 foot sand pilot project Olla Field, LaSalle Parish Louisiana*., Hunt Petroleum Corporation, Goodpine, Louisiana.

Ono S., Rhim J. H., Gruen D. S., Taubner H., Kölling M. and Wegener G. (2021) Clumped isotopologue fractionation by microbial cultures performing the anaerobic oxidation of methane. *Geochimica et Cosmochimica Acta* **293**, 70–85.

Oren A. (2011) Thermodynamic limits to microbial life at high salt concentrations. *Environmental Microbiology* **13**, 1908–1923.

Palcsu L., Vető I., Futó I., Vodila G., Papp L. and Major Z. (2014) In-reservoir mixing of mantle-derived CO_2 and metasedimentary CH_4–N_2 fluids – Noble gas and stable isotope study of two multistacked fields (Pannonian Basin System, W-Hungary). *Marine and Petroleum Geology* **54**, 216–227.

Perri P. R. (2003) *Advanced reservoir characterization in the Antelope Shale to establish the viability of CO_2 enhance oil recovery in California's Monterey Formation Siliceous Shales.* Chevron USA Production Company, Bakersfield.

Porcelli D., Ballentine C. J. and Wieler R. (2002) An Overview of Noble Gas Geochemistry and Cosmochemistry. In: *Noble Gases in Geochemistry and Cosmochemistry.(*Eds: D. Porcelli, C.J. Ballentine,, R. Wieler) Reviews in Mineralogy and Geochemistry **47**. Geochemical Society, Mineralogical Society of America, Chapter 1, 1-19.

Price M. N., Dehal P. S. and Arkin A. P. (2010) FastTree 2 – Approximately Maximum-Likelihood Trees for Large Alignments. *PLOS ONE* **5**, e9490.

Prinzhofer A. A. and Huc A. Y. (1995) Genetic and post-genetic molecular and isotopic fractionations in natural gases. *Chemical Geology* **126**, 281–290.

Prinzhofer A. and Pernaton É. (1997) Isotopically light methane in natural gas: bacterial imprint or diffusive fractionation? *Chemical Geology* **142**, 193–200.

Rice D. D. and Claypool G. E. (1981) Generation, Accumulation, and Resource Potential of Biogenic Gas. *AAPG Bulletin* **65**, 5–25.

Royden L., Horváth F., Nagymarosy A. and Stegena L. (1983) Evolution of the Pannonian Basin System: 2. Subsidence and thermal history. *Tectonics* **2**, 91–137.

Sassen R. (1990) Lower Tertiary and Upper Cretaceous Source Rocks in Louisiana and Mississippi: Implications to Gulf of Mexico Crude Oil (1). *AAPG Bulletin* **74**, 857–878.

Sassen R., Tye R. S., Chinn E. W. and Lemoine R. C. (1988) Origin of Crude Oil in the Wilcox Trend of Louisiana and Mississippi: Evidence of Long-Range Migration. **38**.

Sathaye K. J., Larson T. E. and Hesse M. A. (2016) Noble gas fractionation during subsurface gas migration. *Earth and Planetary Science Letters* **450**, 1–9.

Seifurt R. (1986) Use of biological markers in petroleum exploration. *Methods in geochemistry and geophysics* **24**, 261–290.

Shelton J. L., Andrews R. S., Akob D. M., DeVera C. A., Mumford A., McCray J. E. and McIntosh J. C. (2018) Microbial community composition of a hydrocarbon reservoir 40 years after a CO_2 enhanced oil recovery flood. *FEMS Microbiology Ecology* **94**.

Shelton J. L., McIntosh J. C., Warwick P. D. and McCray J. E. (2016a) Impact of formation water geochemistry and crude oil biodegradation on microbial methanogenesis. *Organic Geochemistry* **98**, 105–117.

Shelton J.L., McIntosh, J.C., Hunt, A.G., Beebe, T.L., Parker, A.D., Warwick, P.D., Drake II, R.M., McCray, J.E. (2016b) Determining CO_2 storage potential during miscible CO_2 enhance oil recovery: Noble gas and stable isotope tracers. *International Journal of Greenhouse Gas Control* **51**, 239-253.

Shelton J. L., McIntosh J. C., Warwick P. D. and Yi A. L. Z. (2014) Fate of injected CO_2 in the Wilcox Group, Louisiana, Gulf Coast Basin: Chemical and isotopic tracers of microbial–brine–rock–CO_2 interactions. *Applied Geochemistry* **51**, 155–169.

Sheng X., Nakai S., Wakita H., Yongchang X. and Wang X. (1997) Carbon isotopes of hydrocarbons and carbon dioxide in natural gases in China. *Journal of Asian Earth Sciences* **15**, 89–101.

Sherwood Lollar B., O'Nions R. K. and Ballentine C. J. (1994) Helium and neon isotope systematics in carbon dioxide-rich and hydrocarbon-rich gas reservoirs. *Geochimica et Cosmochimica Acta* **58**, 5279–5290.

Sherwood Lollar B., Ballentine C. J. and Onions R. K. (1997) The fate of mantle-derived carbon in a continental sedimentary basin: Integration of C-He relationships and stable isotope signatures. *Geochimica et Cosmochimica Acta* **61**, 2295–2307.

Stewart R. J. and Haszeldine R. S. (2014) *Carbon Accounting for Carbon Dioxide Enhance Oil Recovery*., Edinburgh.

Stolper D. A., Lawson M., Davis C. L., Ferreira A. A., Neto E. V. S., Ellis G. S., Lewan M. D., Martini A. M., Tang Y., Schoell M., Sessions A. L. and Eiler J. M. (2014) Formation temperatures of thermogenic and biogenic methane. *Science* **344**, 1500–1503.

Stolper D. A., Lawson M., Formolo M. J., Davis C. L., Douglas P. M. J. and Eiler J. M. (2018) The utility of methane clumped isotopes to constrain the origins of methane in natural gas accumulations. *Geological Society, London, Special Publications* **468**, 23–52.

Stolper D. A., Martini A. M., Clog M., Douglas P. M., Shusta S. S., Valentine D. L., Sessions A. L. and Eiler J. M. (2015) Distinguishing and understanding thermogenic and biogenic sources of methane using multiply substituted isotopologues. *Geochimica et Cosmochimica Acta* **161**, 219–247.

Sweeney J. J. and Burnham A. K. (1990) Evaluation of a Simple Model of Vitrinite Reflectance Based on Chemical Kinetics. AAPG *Bulletin* **74**.

Thiagarajan N., Kitchen N., Xie H., Ponton C., Lawson M., Formolo M. and Eiler J. (2020a) Identifying thermogenic and microbial methane in deep water Gulf of Mexico Reservoirs. *Geochimica et Cosmochimica Acta* **275**, 188–208.

Thiagarajan N., Xie H., Ponton C., Kitchen N., Peterson B., Lawson M., Formolo M., Xiao Y. and Eiler J. (2020b) Isotopic evidence for quasi-equilibrium chemistry in thermally mature natural gases. *Proceedings of the National Academy of Science USA* **117**, 3989–3995.

Tye R. S., Moslow T. F., Kimbrell W. C. and Wheeler C. W. (1991) Lithostratigraphy and Production Characteristics of the Wilcox Group (Paleocene-Eocene) in Central Louisiana. *AAPG Bulletin* **75**, 1675–1713.

Tyne R. L., Barry P. H., Hillegonds D. J., Hunt A. G., Kulongoski J. T., Stephens M. J., Byrne D. J. and Ballentine C. J. (2019) A Novel Method for the Extraction, Purification, and Characterization of Noble Gases in Produced Fluids. *Geochemistry, Geophysics, Geosystems* **20**, 5588–5597.

van Aarssen B. G. K., Bastow T. P., Alexander R. and Kagi R. I. (1999) Distributions of methylated naphthalenes in crude oils: indicators of maturity, biodegradation and mixing. *Organic Geochemistry* **30**, 1213–1227.

van Bodegom P. M., Scholten J. C. M. and Stams A. J. M. (2004) Direct inhibition of methanogenesis by ferric iron. *FEMS Microbiology Ecology* **49**, 261–268.

Van Breukelen B. M. (2007) Extending the Rayleigh Equation to Allow Competing Isotope Fractionating Pathways to Improve Quantification of Biodegradation. *Environmental Science and Technology* **41**, 4004–4010.

Wang D. T., Gruen D. S., Sherwood Lollar B., Hinrichs K.-U., et al., (2015) Nonequilibrium clumped isotope signals in microbial methane. *Science* **348**, 428–431.

Warwick P. D., Breland F. C. and Hackley P. C. (2008) Biogenic origin of coalbed gas in the northern Gulf of Mexico Coastal Plain, U.S.A. *International Journal of Coal Geology* **76**, 119–137.

Warwick P. D., Breland F. C. J., Ratchford M. E., Ingram S. L. S. and Pashin J. C. (2004) Coal gas resource potential of Cretaceous and Paleogene coals of the eastern Gulf of Mexico Coastal Plain. In *Southeast Section Meeting* Geological Society of America Northeast/Southest. GSA, Washington DC.

Weiss R. F. (1968) Piggyback sampler for dissolved gas studies on sealed water samples. *Deep Sea Research and Oceanographic Abstracts* **15**, 695–699.

Wenger L. M., Davis C. L. and Isaksen G. H. (2002) Multiple Controls on Petroleum Biodegradation and Impact on Oil Quality. *SPE Reservoir Evaluation & Engineering* **5**, 375–383.

Wenger L. M., Sassen R. and Shurmacher D. S. (1990) Molecular characteristics of Smackover, Tuscaloosa and Wilcox-reservoired oils in the eastern gulf coast. In *GCSSEPM Foundation Ninth Annual Research Conference Proceedings*. 37–57.

Whiticar M. J. (1999) Carbon and hydrogen isotope systematics of bacterial formation and oxidation of methane. *Chemical Geology* **161**, 291–314.

Whiticar M. J., Faber E. and Schoell M. (1986) Biogenic methane formation in marine and freshwater environments: CO_2 reduction vs. acetate fermentation—Isotope evidence. *Geochimica et Cosmochimica Acta* **50**, 693–709.

Wycherley H., Fleet A. and Shaw H. (1999) Some observations on the origins of large volumes of carbon dioxide accumulations in sedimentary basins. *Marine and Petroleum Geology* **16**, 489–494.

Xia X. and Tang Y. (2012) Isotope fractionation of methane during natural gas flow with coupled diffusion and adsorption/desorption. *Geochimica et Cosmochimica Acta* **77**, 489–503.

Yee D., Seidle J. P. and Hanson W. B. (1993) Gas Sorption on Coal and Measurement of Gas Content: In: *Hydrocarbons from Coal* (Eds: B.E. Law, D.D. Rice) AAPG Studies in Geology, Tulsa. Chapter 9, 203–218.

Yoshinaga M. Y., Holler T., Goldhammer T., Wegener G., Pohlman J. W., Brunner B., Kuypers M. M. M., Hinrichs K.-U. and Elvert M. (2014) Carbon isotope equilibration during sulphate-limited anaerobic oxidation of methane. *Nature Geoscience* **7**, 190–194.

Young, E. D., Kohl, I.E., Sherwood Lollar, B., et al., (2017). The relative abundances of resolved $\Delta^{12}CH_2D_2$ and $\Delta^{13}CH_3D$ and mechanisms controlling isotopic bond ordering in abiotic and biotic methane gases. *Geochimica et Cosmochimica Acta* **203**, 235–264

Young E. D. (2019) A Two-Dimensional Perspective on CH_4 Isotope Clumping: Distinguishing Process from Source. In: *Deep Carbon* (Eds. B.N. Orcutt, I. Daniel, and R. Dasgupta). Cambridge University Press. 388–414.

Zevenhoven R., Eloneva S. and Teir S. (2006) Chemical fixation of CO_2 in carbonates: Routes to valuable products and long-term storage. *Catalysis Today* **115**, 73–79.

Zhang T., Wang X. and Chen J. (1999) Chemical composition of gases as a geochemical tracer of natural gas migration. *Acta Sedimentologica Sinica* **17**, 627–632.

Zinder S. H. (1993) Physiological Ecology of Methanogens. In *Methanogenesis: Ecology, Physiology, Biochemistry & Genetics* (Ed. J. G. Ferry). Chapman & Hall Microbiology Series. Springer US, Boston, MA. 128–206.

Chapter 5

Noble gases reveal the role of basin architecture in controlling the chemical evolution of groundwater in the Paradox Basin

R.L. Tyne[1], P.H. Barry[2], A. Cheng[1], D.J. Hillegonds[1], J-H. Kim[3], J.C. McIntosh[3], C.J. Ballentine[1]

[1] Dept. of Earth Sci., University of Oxford, Oxford, UK [2] Dept. of Marine Chem. and Geochem., Woods Hole Oceanographic Institution, Woods Hole, MA, USA [3] Department of Hydrology and Atmospheric Sciences. University of Arizona, Tucson, AZ, USA.

Contents

Abstract 178
5.1 Introduction 179
5.2 Geological context 181
5.3 Methods 183
5.4 Results 184
5.4.1 Helium 184
5.4.2 Neon 192
5.4.3 Argon 192
5.4.4 Krypton and xenon 192
5.5 Discussions 192
5.5.1 Assessing fluid provenance using noble gas isotope ratios 192
5.5.2 Radiogenic noble gases concentrations 195
5.5.3 Fractionation of atmospheric noble gases (ANG) ratios due to fluid interactions 205
5.5.4 Investigating ^{4}He distribution 211
5.6 Conclusions 216
S5.1 Supplementary figures 219
S5.2 Supplementary tables 222
S5.3 Supplementary information 227
Acknowledgments 234
Authorship statement 235
References 236

Abstract

Fluid flow within the subsurface controls the migration, accumulation and storage of groundwater, hydrocarbons, CO_2 and other less abundant gases. However, the inherently complex nature of sedimentary basins means it can be difficult to identify the processes affecting the chemical evolution of the fluids. Noble gases represent powerful tools for understanding this evolution as they are chemically inert and only fractionate by physical processes. Here, we report noble gas isotope and abundance data from 36 wells across the Paradox Basin, on the Colorado Plateau, USA. The Paradox Basin has iconic paleofluid flow features including extensive bleaching and abundant hydrocarbon, ^{4}He and CO_2 accumulations. Samples were collected from 7 stratigraphic units, including within, above and below the Paradox Formation evaporites and from a variety of fluids including groundwater and natural gas. Air-corrected helium isotope ratios vary between 0.046 and 0.127R_A, consistent with radiogenic overprinting of predominantly groundwater-derived noble gases. There is an increased concentration of radiogenic noble gases in formations below the Paradox Formation. Atmosphere-derived noble gas signatures are consistent with groundwater flow and multi-phase interactions both above and below the salt, with higher groundwater flow occurring in the shallower formations. This is in agreement with radiocarbon and ^{81}Kr groundwater residence times (3-900ka above the salt compared to 800Ka below the salt). Models reconstruct observed groundwater helium concentration with the Paradox Formation evaporites forming an effectively impermeable barrier to helium diffusion. However, an additional basement flux is required to accumulate the measured ^{4}He concentrations beneath the salt. Overall, the noble gases allow us to identify dichotomous systems above and below the Paradox Formation, suggesting that the Paradox Formation separates two independent hydrogeological regimes. Furthermore, the models allow for the efficacy of the Paradox Formation to be a seal, even for the most mobile elements such as ^{4}He, to be identified. These findings will have important implications for identifying ^{4}He and H_2 accumulations and developing sustainable hydrocarbon extraction, carbon capture and storage and nuclear waste disposal protocols, as well as implications for crustal fluid dating.

5.1 Introduction

Sedimentary basins are unique and inherently complex hydrogeological systems, due to their stratigraphic, structural and temporal controls. Understanding both the present-day and paleo-fluid flow and the geochemistry of a basin is critical for both temporal and spatial basin reconstructions. In particular, they can inform us about fluid migration, interaction and emplacement, which is essential for identifying potential CO_2 or nuclear waste disposal sites and in hydrocarbon, He and H_2 exploration.

The Paradox Basin, Colorado Plateau, has abundant hydrocarbons, CO_2 and He accumulations within the basin (Figure 1), as well as extensive sandstone bleaching (Barton, et al., 2018). The basin is defined by the extent of a thick evaporite unit which has undergone passive diapirism creating anticlinal structures and affecting the advective and diffusional fluid connectivity within the basin (Hite and Lohman, 1973; Hite and Buckner, 1981; Nuccio and Condon, 1996; Trudgill, 2011; Kim et al., 2021). The complex nature of the fluid flow within the Paradox Basin, makes it an ideal location to investigate the role of basin architecture on the chemical evolution of groundwater and how these could affect fluid migration, accumulation and storage as well as dating. The primary focus of previous paleofluid flow and solute transport studies in the Paradox Basin has been on the rock record, with inferences about the origin, composition, flowpaths and mixing of paleofluids (Shawe, 1968; Morrison and Parry, 1986; Breit and Meunier, 1990; Chan et al., 2000; Beitler et al., 2003, 2005; Parry et al., 2004; Dockrill and Shipton 2010; Loope et al., 2010; Wigley et al., 2012). A recent study has also examined the hydrogeochemical evolution of modern and remnant fluids in the basin to constrain the fluid sources and the geochemical evolution of the paleofluids responsible for the sandstone bleaching and ore mineralisation within the Paradox Basin (Kim et al., 2021). They found brine dissolution on both sides of the Paradox Formation and radiocarbon and ^{81}Kr residence times of ~0.003-0.9Ma, that indicate meteoric flushing through the units both above and below the Paradox Formation (Kim et al., 2020, 2021). However, the role of the basin architecture, in particular the role of the Paradox Formation (a

thick evaporate unit which extends across the basin), in controlling the fluid migration and composition has yet to be investigated.

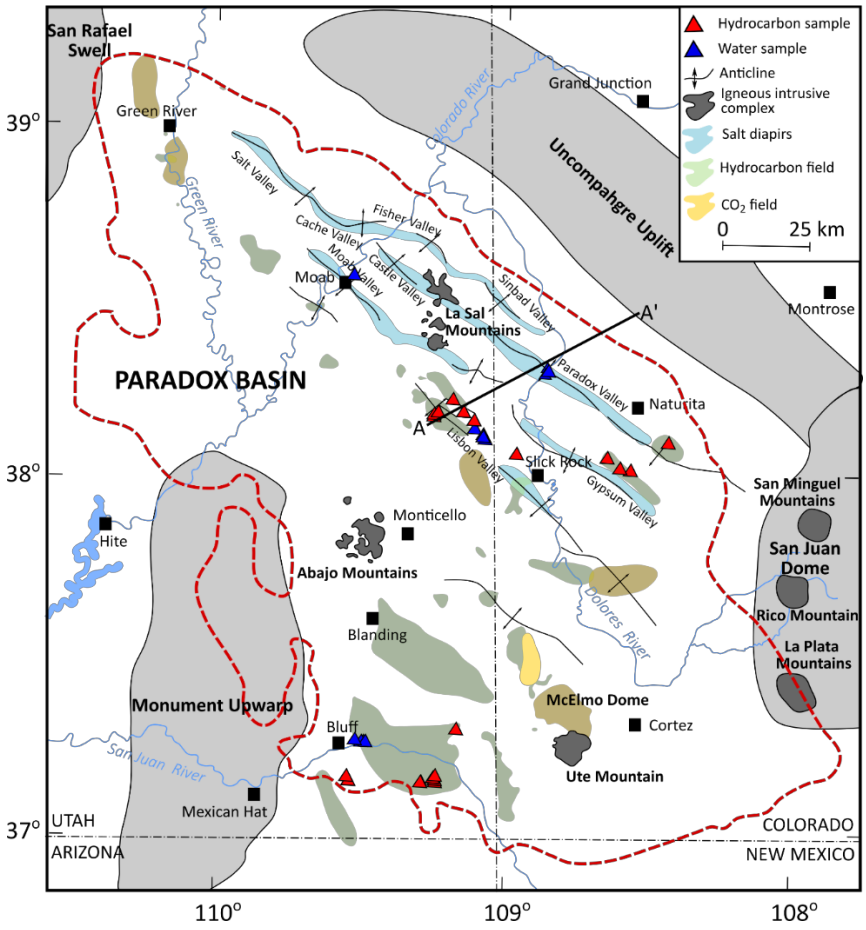


Figure 5.1: Map of the study are showing locations of water and hydrocarbon samples taken across the Paradox Basin. The cross section from A-A' can be found in Figure 5.2. The map has been adapted from Harr (1996), Barton et al. (2018) and Kim et al. (2021).

Noble gases are chemically inert and represent useful tools for investigating the physical processes that occur within sedimentary basins. Terrestrial noble gas reservoirs (atmosphere, crust and mantle) have diagnostic isotopic compositions, meaning fluids from each reservoir can be readily distinguished. Noble gas abundance and isotope characteristics have been extensively used to characterise fluid provenance and migration (e.g., Ballentine et al., 1991; Sherwood Lollar et al., 1994; Ballentine et al., 1996, 2002; Zhou et al., 2005; Gilfillan et al., 2008; Barry et al., 2016, 2017, 2018; Karolytė et al., 2019; Byrne et al., 2020). In addition, the distinct noble gas composition of various fluid sources in sedimentary basins has been used to identify and quantify

the exchange between different subsurface fluid phases (e.g., Zartman et al., 1961; Bosch and Mazor, 1988; Ballentine et al., 2002; Prinzhofer, 2013; Barry et al., 2016, 2017, 2018; Byrne et al., 2018, 2020).

In this study, we present noble gas isotope and abundance data from 16 groundwater and 20 hydrocarbon (12 gas and 8 oil) wells across the Paradox Basin. Samples were taken from throughout the stratigraphic column from below, within and above the Paradox Formation (Figure 5.2). Our aim is both to isotopically characterise the samples across the Basin for their noble gas signatures, and to couple the radiogenic noble gases (indicative of residence times) with atmospheric noble gases to investigate the role of Paradox Formation in controlling the fluid composition, interaction and geochemical variations in the basin. We show that the noble gases within the Paradox Basin are primarily groundwater derived with a radiogenic overprint and there is a marked difference above and below the Paradox Formation. We then develop models to assess phase fractionation and vertical gas migration. An understanding of the nature and extent of connectivity between different fluid reservoirs, especially for mobile elements such as ^{4}He, is critical for both resource development and anthropogenic waste disposal.

5.2 Geological Background

The Paradox Basin is situated in southeastern Utah and southwestern Colorado on the Colorado Plateau (Figure 5.1). It is an approximately 85,000 km^2 eastward deepening flexural basin that developed in response to the Late Palaeozoic Uncompahgre Uplift of the ancestral Rocky Mountains (Hanshaw and Hill, 1969; Nuccio and Condon, 1996; Barbeau, 2003). The sedimentary rocks of the Paradox Basin overlie an early Proterozoic basement, consisting of metamorphic gneiss and schists, which are locally intruded by granite. The extent of the basin is defined by the extent of the Pennsylvanian Paradox Formation. A summary of the geological history is below and more detailed geological histories can be found in Molenaar (1981), Peterson and Turner-Peterson (1987), Turner and Fishman (1991), Nuccio and Condon (1996), Condon (1997), Barbeau (2003), Kluth and DuChene (2009) and Trudgill (2011).

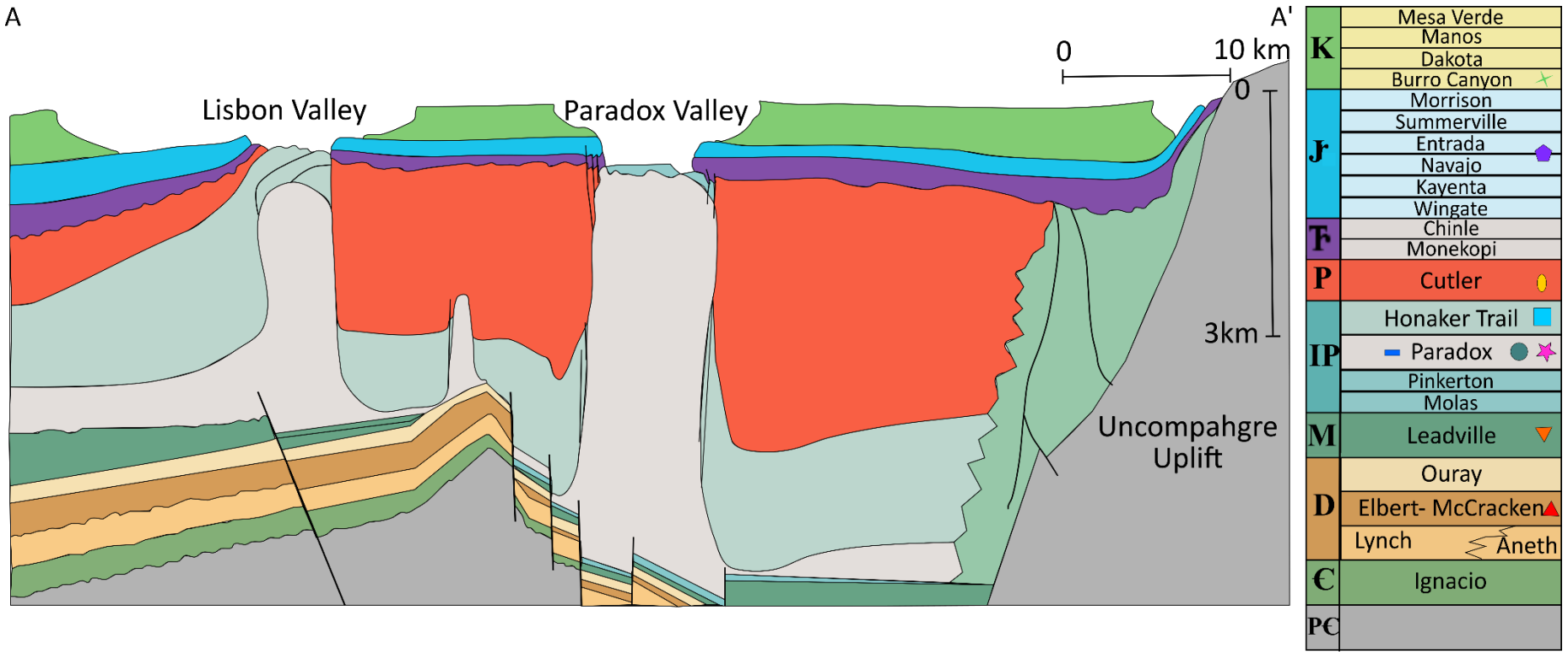


Figure 5.2: Cross section of across part of the Paradox Basin (A-A', see Figure 5.1), showing the variation in formation thickness across a subsection of the basin. Modified from Baars and Stevenson (1982), Baars (1996), King et al (2014) and Kim et al. (2021). A simplified stratigraphic column for the Basin can be found to the right of the cross section (modified from Nuccio and Condon (1996)). Colours used within the cross section correspond to those in the stratigraphic column, and sampled formations are marked with symbols (used hereafter).

In summary, Cambrian to Mississippian deposits are a mixture of sandstone and limestones, although formations are missing due to post Cambrian erosion. Notable extant formations for this study are the hydrocarbon bearing McCracken Sandstone (Devonian) and Leadville Limestone (Mississippian) (Figure 5.2). The Pennsylvanian to Permian period was defined by the collision of the Laurentia and Gondwana supercontinents, which resulted in the large-scale uplift of the Uncompahgre Plateau and subsequent subsidence to the southeast forming a flexural basin (Paradox Basin) (Nuccio and Condon, 1996; Barbeau, 2003). Fluctuations in sea level defined sedimentation during the Pennslyvanian period. This included cyclical desiccation and marine flooding of the basin and the formation of a 2.5km thick evaporite deposit, interbedded with dolomite and black shales (Hite and Lohman, 1973; Hite and Buckner, 1981; Nuccio and Condon, 1996; Trudgill, 2011). The black shales are particularly important as they are believed to be the source facies for many hydrocarbon reservoirs across the basin (e.g., Barton, et al., 2018). Overlying the Paradox Formation is the Honaker Trail Formation, which is composed of cyclically deposited limestone, sandstone and shale (Nuccio and Condon, 1996).

Continued uplift of the Uncompahgre Plateau into the early Permian resulted in the exposure of the Precambrian basement rocks, erosion and subsequent deposition of the Cutler Formation (Cater, 1970; Nuccio and Condon, 1996). Simultaneously, sediment loading from the Honaker Trail and Cutler formations produced a series of northwest-southeast trending salt walls and mini basins through passive diapirism (e.g., Figure 5.2) (Kluth and DuChene, 2009; Trudgill, 2011; Lawton et al., 2015).

Triassic to Cretaceous sedimentation are predominantly sandstone and fluvial deposits. This includes the red Navajo and Entrada formations (which form the Navajo Aquifer) and have subsequently been bleached (Figure 5.2) (e.g., Chan et al., 2000; Beitler et al., 2003, 2005; Parry et al., 2004; Dockrill and Shipton 2010; Loope et al., 2010; Barton et al., 2018; Kim et al., 2021).

During the Tertiary, the Colorado Plateau has undergone three periods of uplift, which are associated with the volcanism in the southeast and centre of the Paradox Basin. The final phase of uplift started 10-6Ma and created the present day geomorphology (Gutiérrez, 2004).

5.3 Methods

A total of 48 samples including 12 duplicates were taken from across 7 stratigraphic units in the Paradox Basin (Figure 5.2, Supplementary Table S5.1). 15 shallow groundwaters were taken from the Paradox Valley, Lisbon Valley and Greater Aneth Field and 1 deep brine from a lithium exploration well. The remaining samples (11 gases, 8 casing gases and 1 produced fluid (condensate, water, gas mixtures)) were taken from hydrocarbon fields across the basin (Figure 5.1).

Water and produced fluid samples were collected in 3/8" refrigeration-grade copper tubes with stainless steel clamps following the methods described in Chapter 2 (Tyne et al., 2019). The Cu tubes were connected to the wellhead sampling point using reinforced PTFE tubing and hose clamps and flushed with water/produced fluids prior to sampling. Casing gases were also collected in Cu tubes using standard sampling methods (Burnard, 2013). A two-stage regulator was attached to the wellhead to step down the pressure to ~1bar. FinCu tubes were flushed with casing gases for 10 minutes while the opposite end of the tubing was submerged in water to prevent atmospheric contamination. Cu tubes were then sealed with stainless steel clamps (Weiss, 1968).

Noble gases were analysed in the Noble Laboratory at the University of Oxford, where there is a dedicated offline fluid extraction system, hydrocarbon extraction system and a purification line interfaced to two noble gas mass spectrometers. Full analytical procedures can be found in the supplementary information (S5.3.1) and are described in detail in Chapter 2 (Tyne et al., 2019).

5.4 Results

All noble gas concentrations, isotope ratios and associated 1σ errors are reported in Tables 5.1 and 5.2. In Chapter 3, we demonstrate that noble gas concentrations in the gas phase of produced fluids and casing gases can essentially be used interchangeably (Tyne et al., 2021). Therefore, for the produced fluid sample (MC 17-21) collected, the concentration in the gas phase has been calculated following the methods in Chapter 2 (Tyne et al., 2019) and from herein treated as a 'gas' phase sample.

Sample Name	Phase	^{4}He ($x10^{-6}$)	±	^{20}Ne ($x10^{-7}$)	±	^{36}Ar ($x10^{-6}$)	±	^{84}Kr ($x10^{-8}$)	±	^{130}Xe ($x10^{-10}$)	±	$^{4}He/^{20}Ne$	±
Water phase ($cm^3(STP)/g_{water}$)													
BOR well 8E	W	1.13	0.03	0.140	0.005	0.289	0.013	1.75	0.10	2.33	0.14	80.7	3.6
BOR well 9E	W	1.14	0.03	0.146	0.006	0.264	0.012	1.64	0.09	2.26	0.13	78.1	3.8
BOR well 3E	W	1.55	0.05	0.191	0.007	0.284	0.013	1.58	0.09	2.03	0.12	81.2	4.1
BOR well 2E	W	1.86	0.06	0.239	0.009	0.348	0.016	1.75	0.10	2.14	0.13	77.8	3.9
PW-4	W	0.0443	0.0014	1.41	0.03	1.09	0.03	4.50	0.12	4.89	0.13	0.314	0.012
PW-4 (dup)	W	0.0449	0.0012	1.52	0.05	1.02	0.04	5.34	0.21	2.78	0.25	0.295	0.013
PW-3	W	0.0742	0.0023	1.82	0.04	1.19	0.03	4.70	0.12	4.89	0.13	0.408	0.015
PW-12	W	0.365	0.004	1.82	0.01	1.21	0.02	4.49	0.12	4.73	0.10	2.01	0.02
PW-8	W			1.91	0.04	1.26	0.03	5.02	0.13	5.27	0.14		
PW-8 (dup)	W	3.95	0.12	1.96	0.08	1.25	0.06	5.93	0.72	5.02	0.44	20.2	1.0
PW-11	W	0.586	0.018	1.78	0.04	1.08	0.03	4.25	0.11	4.43	0.12	3.29	0.13
PW-7	W	0.802	0.025	10.3	0.2	3.28	0.08	5.08	0.13	4.54	0.12	0.779	0.029
STCEC	W	0.899	0.027	2.59	0.1	1.49	0.07	5.32	0.65	5.68	0.49	3.47	0.17
BWC-1	W	0.759	0.023	2.72	0.06	1.52	0.04	3.24	0.08	3.38	0.09	2.79	0.10
BWC-2	W	3.46	0.11	2.50	0.05	1.46	0.04	3.18	0.08	3.35	0.09	13.8	0.5
BWC-3	W	8.26	0.25	2.40	0.09	1.41	0.06	6.15	0.75	5.47	0.48	34.4	1.7
TRTP	W	18.5	0.6	2.24	0.09	1.26	0.06	9.53	1.16	4.83	0.42	82.6	4.3
Cane Creek	W	213	2	0.0835	0.0010	0.0267	0.0005	0.101	0.002	0.118	0.010	25500	400

Table 5.1: Noble gas concentrations with 1σ errors. Measured noble gas concentrations are in $cm^3(STP)/cm^3$ for the gas (G) phase samples and $cm^3(STP)/g_{water}$ for water (W) phase samples.

Sample Name	Phase	^{4}He ($x10^{-6}$)	±	^{20}Ne ($x10^{-7}$)	±	^{36}Ar ($x10^{-6}$)	±	^{84}Kr ($x10^{-8}$)	±	^{130}Xe ($x10^{-10}$)	±	$^{4}He/^{20}Ne$	±
Gas Phase (cm^3(STP)/cm^3)													
AM-75	G	478	16	36.8	1.5	4.86	0.08	6.92	0.13	3.39	0.16	130	7
AM-62	G	1360	40	36.2	1.4	5.50	0.08	7.38	0.14	3.86	0.19	376	18
AM-11-E34	G	705	20	2.87	0.11	0.409	0.007	0.691	0.013	0.559	0.027	2460	120
MM 31-42	G	1280	80	6.11	0.043	1.43	0.10	0.993	0.049	0.963	0.052	16200	1300
MM 31-42 (dup)	G	1270	80										
BI 24-31	G	1300	80	5.43	0.29			0.587	0.029	0.476	0.026	2390	200
BI 24-31 (dup)	G	1660	100										
BH 10-31	G	261	9	27.3	1.1	3.70	0.06	5.39	0.10	2.95	0.14	95.6	5.1
HC 31-31	G	405	13	15.3	0.6	2.68	0.04	4.73	0.09	2.62	0.13	265	13
FF-2-19	G	1530	50	2.97	0.12	0.455	0.007	0.918	0.017	1.05	0.05	5150	270
FF-2-19 (dup)	G	1500	50	3.34	0.12	0.499	0.013	1.03	0.05	0.985	0.018	4500	220
Tohonalda 35-B	G	515	17	0.147	0.003							35000	1400
Tohonalda 1	G	304	10	0.121	0.005	0.0612	0.0014	0.327	0.006	0.608	0.029	25100	1300
Tohonalda 1 (dup)	G	301	10										
Anasazi 1	G	256	8	0.0994	0.0040	0.0620	0.0020	0.338	0.006	0.725	0.035	25800	1300
Sahgzie 1	G	230	8	0.0902	0.0036	0.0616	0.0015	0.321	0.006	0.678	0.033	25500	1300
Sahgzie 1 (dup)	G	244	8										
Monument-8N-2	G	242	8	0.138	0.005	0.0538	0.0014	0.281	0.005	0.572	0.028	17500	900
Monument-8N-2 (dup)	G	239	8										
WM 22-43	G	235	8	0.296	0.012	0.178	0.003	0.746	0.014	1.12	0.05	7940	410
WM 22-43 (dup)	G	238	8			0.273	0.007	0.863	0.044	1.16	0.02		

Table 5.1: continued

Sample Name	Phase	^{4}He (x10^{-6})	±	^{20}Ne (x10^{-7})	±	^{36}Ar (x10^{-6})	±	^{84}Kr (x10^{-8})	±	^{130}Xe (x10^{-10})	±	^{4}He/^{20}Ne	±
Gas Phase (cm^{3}(STP)/cm^{3})													
WM 34-31	G	195	6	0.293	0.012	0.228	0.004	0.637	0.012	0.994	0.048	6660	340
WM 34-31 (dup)	G	197	6	0.347	0.014	0.181	0.003	0.642	0.012	1.01	0.05	5670	290
WM 34-33	G	213	7	0.484	0.019	0.296	0.005	1.24	0.02	1.65	0.08	4410	230
McIntyre 17-21	G	1880	110	0.239	0.015	0.119	0.008	0.477	0.031	0.11	0.01	78800	6800
Lisbon D8-10	G	8970	550			0.120	0.009	0.329	0.016	0.57	0.03		
Lisbon 10-33	G	3600	120	0.211	0.008	0.109	0.002	0.614	0.011	1.35	0.06	171000	9000
Lisbon 10-33 (dup)	G	3540	120	0.209	0.008	0.104	0.003	0.617	0.011	1.34	0.06	170000	9000
Lisbon B8-10	G	9210	560	0.709	0.038	0.212	0.014	0.939	0.046	1.49	0.08	130000	11000
Lisbon B8-10 (dup)	G					0.197	0.005	0.893	0.046	1.32	0.02		

Table 5.1: continued

Sample Name	Phase	$^{3}He/^{4}He$	±	$^{3}He/^{4}He_{c}$	±	$^{21}Ne/^{22}Ne$	±	$^{20}Ne/^{22}Ne$	±	$^{40}Ar/^{36}Ar$	±	$^{38}Ar/^{36}Ar$	±
Water phase													
BOR well 8E	W	0.039	0.001	0.035	0.002	0.02955	0.00026	9.59	0.07	303	2	0.198	0.005
BOR well 9E	W	0.038	0.001	0.034	0.002	0.02946	0.00026	9.56	0.07	304	2	0.199	0.005
BOR well 3E	W	0.039	0.001	0.035	0.002	0.02930	0.00025	9.53	0.07	302	2	0.198	0.005
BOR well 2E	W	0.038	0.001	0.034	0.002	0.02934	0.00026	9.53	0.07	302	2	0.199	0.005
PW-4	W	0.734	0.020			0.02966	0.00001	9.73	0.02	298	2	0.194	0.006
PW-4 (dup)	W	0.790	0.020			0.02873	0.00008	9.80	0.01	299	2	0.190	0.002
PW-3	W	0.614	0.017			0.02966	0.00001	9.82	0.02	299	2	0.195	0.006
PW-12	W	0.164	0.008	0.044	0.001	0.02965	0.00003	9.83	0.02	298	2	0.195	0.006
PW-8	W					0.02967	0.00002	9.77	0.02	299	2	0.195	0.006
PW-8 (dup)	W	0.030	0.001	0.018	0.001	0.02953	0.00006	9.84	0.01	299	1	0.181	0.006
PW-11	W	0.092	0.003	0.016	0.001	0.02968	0.00002	9.74	0.02	299	2	0.194	0.006
PW-7	W	0.347	0.011	0.034	0.002	0.02963	0.00002	9.81	0.02	298	2	0.194	0.006
STCEC	W	0.132	0.003	0.064	0.005	0.02952	0.00010	9.84	0.01	298	1	0.197	0.007
BWC-1	W	0.206	0.008	0.127	0.008	0.02965	0.00002	9.82	0.02	298	2	0.195	0.006
BWC-2	W	0.141	0.004	0.126	0.006	0.02967	0.00002	9.82	0.02	299	2	0.195	0.006
BWC-3	W	0.099	0.002	0.093	0.005	0.02951	0.00008	9.83	0.01	299	1	0.187	0.006
TRTP	W	0.093	0.002	0.090	0.005	0.02959	0.00010	9.85	0.02	300	1	0.181	0.006
Cane Creek	W	0.0046	0.0002	0.0046	0.0001	0.03826	0.00007	9.62	0.02	1110	10	0.224	0.010
Gas Phase													
AM-75	G	0.041	0.003	0.038	0.003	0.03018	0.00005	10.1	0.02	304	2	0.191	0.006
AM-62	G	0.039	0.001	0.039	0.002	0.03032	0.00003	10.1	0.02	328	2	0.191	0.006
AM-11-E34	G	0.031	0.002	0.031	0.002	0.03099	0.00002	10.2	0.02	446	4	0.191	0.008

Table 5.2: Noble gas isotope and elemental ratios and associated 1σ errors. $^{3}He/^{4}He$ ratios are given relative to air ($1.4x10^{-6}$). $^{3}He/^{4}He_{c}$ is corrected for the atmospheric component (following methods in Hilton et al. (1996) and Mackintosh and Ballentine (2012))

Sample Name	Phase	$^{3}He/^{4}He$	±	$^{3}He/^{4}He_{c}$	±	$^{21}Ne/^{22}Ne$	±	$^{20}Ne/^{22}Ne$	±	$^{40}Ar/^{36}Ar$	±	$^{38}Ar/^{36}Ar$	±
Gas Phase													
MM 31-42	G	0.011	0.001	0.011	0.001	0.03378	0.00006	10.1	0.05	819	28	0.189	0.006
MM 31-42(dup)	G	0.013	0.002	0.013	0.002								
BI 24-31	G	0.055	0.002	0.054	0.005	0.03519	0.00031			505	4	0.281	0.001
BI 24-32 (dup)	G	0.058	0.002										
BH 10-31	G	0.025	0.001	0.022	0.001	0.03029	0.00007	10.1	0.02	295	2	0.191	0.006
HC 31-31	G	0.009	0.001	0.008	0.001	0.03029	0.00009	10.2	0.02	308	2	0.191	0.006
FF-2-19	G	0.038	0.002	0.038	0.002	0.03179	0.00002	10.2	0.02	678	6	0.193	0.009
FF-2-19 (dup)	G	0.035	0.001	0.035	0.002	0.03161	0.00005	10.2	0.02	634	4	0.203	0.005
Tohonalda 35-B	G	0.070	0.002	0.070	0.002	0.04127	0.00040	9.66	0.02	841	30	0.200	0.007
Tohonalda 1	G	0.067	0.003	0.067	0.004	0.04046	0.00008	9.68	0.06	888	16	0.221	0.022
Tohonalda 1 (dup)		0.073	0.004										
Anasazi 1	G	0.029	0.002	0.029	0.002			9.69	0.02	708	21	0.122	0.043
Sahgzie 1	G	0.025	0.003	0.025	0.002			9.69	0.02	573	12	0.177	0.024
Sahgzie 1 (dup)	G	0.030	0.003										
Monument-8N-2	G	0.011	0.001	0.011	0.001	0.03494	0.00002	10.0	0.02	525	11	0.139	0.015
Monument-8N-2 (dup)	G	0.012	0.001										
WM 22-43	G	0.024	0.002	0.024	0.002	0.03298	0.00004	9.80	0.03	395	4	0.198	0.011
WM 22-43 (dup)	G	0.029	0.001	0.0290	0.0010	0.03094	0.00005	9.80	0.03	356	3	0.190	0.008
WM 34-31	G	0.021	0.002	0.021	0.002	0.03209	0.00011			372	4	0.188	0.008
WM 34-31 (dup)	G	0.027	0.002	0.027	0.002	0.03200	0.00003	9.79	0.02	376	3	0.187	0.009

Table 5.2: continued

Sample Name	Phase	$^{3}He/^{4}He$	±	$^{3}He/^{4}He_{c}$	±	$^{21}Ne/^{22}Ne$	±	$^{20}Ne/^{22}Ne$	±	$^{40}Ar/^{36}Ar$	±	$^{38}Ar/^{36}Ar$	±
Gas phase													
WM 34-33	G	0.030	0.001	0.0254	0.0020	0.03151	0.00004	9.82	0.03	346	4	0.186	0.010
McIntyre 17-21	G	0.034	0.001	0.034	0.003	0.08454	0.00018	8.80	0.01	3760	30	0.190	0.002
Lisbon D8-10	G	0.046	0.001							4530	150	0.141	0.010
Lisbon 10-33	G	0.042	0.001	0.042	0.003	0.06975	0.00009	8.99	0.03	3510	50	0.182	0.014
Lisbon 10-33 (dup)	G	0.042	0.001	0.042	0.003	0.06930	0.00011	9.01	0.04	3600	80	0.146	0.025
Lisbon B8-10	G	0.041	0.001	0.041	0.004	0.07181	0.00062	8.93	0.06	2620	30	0.171	0.007
Lisbon B8-10 (dup)	G									2710	20		

Table 5.2: continued

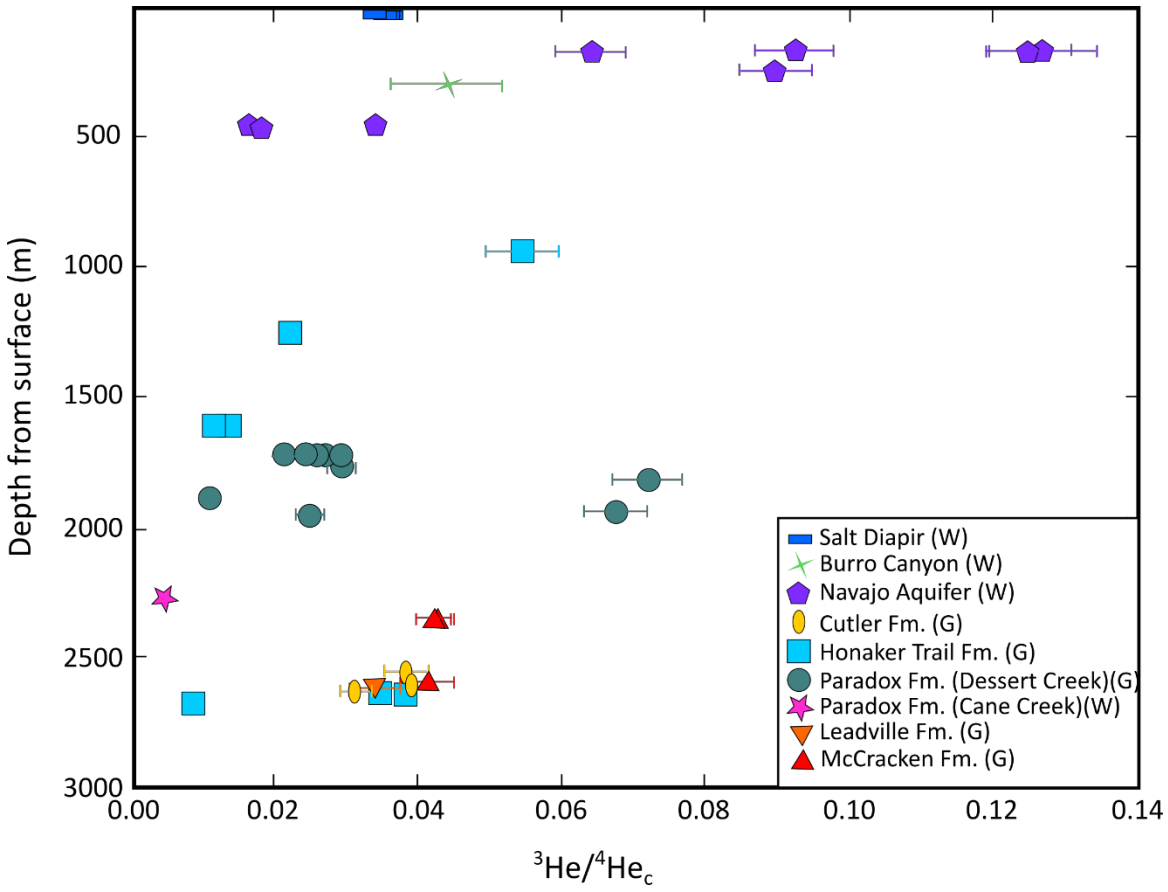


Figure 5.3: Air Corrected $^3He/^4He$ $(R/R_A)_c$ as a function of depth from the surface (m). G (gas) and W (water) represent the sample phase. Samples all have low $^3He/^4He$ relative to sub continental lithospheric mantle ($6.1\pm2.1R_A$, Graham, 2002, Day et al., 2015) and are close to the typical radiogenic production value of $0.02R_A$ (Ballentine and Burnard, 2002).

5.4.1 Helium

Measured helium isotopes ($^3He/^4He$) are between 0.0046 and $0.79R_A$ where R_A is the atmospheric ratio ($R_A=1.4x10^{-6}$). Assuming all ^{20}Ne is atmosphere derived, the $^4He/^{20}Ne$ measured relative to air-saturated water (ASW) value (0.288) can be used to calculate the atmospheric He contribution, which can then be subtracted from the measured $^3He/^4He$ (Hilton, 1996). When the $^4He/^{20}Ne$ is high, the correction is negligible, however it can be significant where $^4He/^{20}Ne$ measured are close to ASW. Measured $^4He/^{20}Ne$ in the samples range from 0.295 to 171000 and increase with depth with the shallowest samples having $^4He/^{20}Ne$ closest to air (Supplementary Figure S5.1). Where measured $^4He/^{20}Ne$ are within error of the air ratio, no correction is possible and we assume that all sample helium is atmosphere-derived (Mackintosh and Ballentine, 2012). Air-corrected helium

isotopes ratios in the Paradox Basin range from 0.0046 to 0.127R_A (Figure 5.3). Low $^3He/^4He$ are consistent with the majority of helium being derived from crustal radiogenic production.

Measured helium (^4He) concentrations are between 0.044 and 213 x10^{-6} $cm^3(STP)/g_{water}$ in the water phase samples and between 195 to 9210 x10^{-6} $cm^3(STP)/cm^3$ in the gas phase samples. In general, an increase in concentration was observed with depth within both the water and gas samples, this relationship is discussed further in section 5.5.2.2.

5.4.2 Neon

Measured ^{20}Ne concentrations range from 0.084 to 10.3 x10^{-7} $cm^3(STP)/g_{water}$ in the water phase samples and from 0.090 to 82.1 x10^{-7} $cm^3(STP)/cm^3$ in the gas phase samples. Most samples have air-like neon isotopes ($^{21}Ne/^{22}Ne$=0.029, $^{20}Ne/^{22}Ne$=9.81 ; Porcelli et al., 2002). Deviations from air are a result of an excess in radiogenically produced ^{21}Ne and ^{22}Ne relative to air or due to mass fractionation effects (Figure 5.4) (Young et al., 2002).

5.4.3 Argon

Argon isotope ratios ($^{40}Ar/^{36}Ar$) range from 295 to 4530. With the exception of samples from the Navajo and Burro Canyon aquifers, we observe an excess radiogenic ^{40}Ar relative to the air value (298.6, Lee et al., 2006). The amount of excess in radiogenic ^{40}Ar relative to ^{36}Ar is correlated with increasing $^{21}Ne/^{22}Ne$ (Figure 5.4b). $^{38}Ar/^{36}Ar$ ratios are between 0.122 and 0.281, there is no correlation between $^{38}Ar/^{36}Ar$ and $^{20}Ne/^{22}Ne$. Argon abundance (^{36}Ar) ranges from 0.027 to 3.28 x10^{-6} $cm^3(STP)/g_{water}$ in the water phase samples and from 0.025 to 5.5 x10^{-6} $cm^3(STP)/cm^3$ in the gas phase samples.

5.4.4 Krypton and Xenon

Krypton (^{84}Kr) concentrations within the gas phase samples range from 0.32 to 7.38 x10^{-8} $cm^3(STP)/cm^3$ and from 0.101 to 9.53 x10^{-8} $cm^3(STP)/g_{water}$ in the water phase. Xenon (^{130}Xe) concentrations are between 0.48 to 386 x10^{-10} $cm^3(STP)/cm^3$ and 0.12 to 5.68 x10^{-10} $cm^3(STP)/g_{water}$ for the gas and water phase samples respectively. Kr and Xe isotope ratios are indistinguishable from air in all samples.

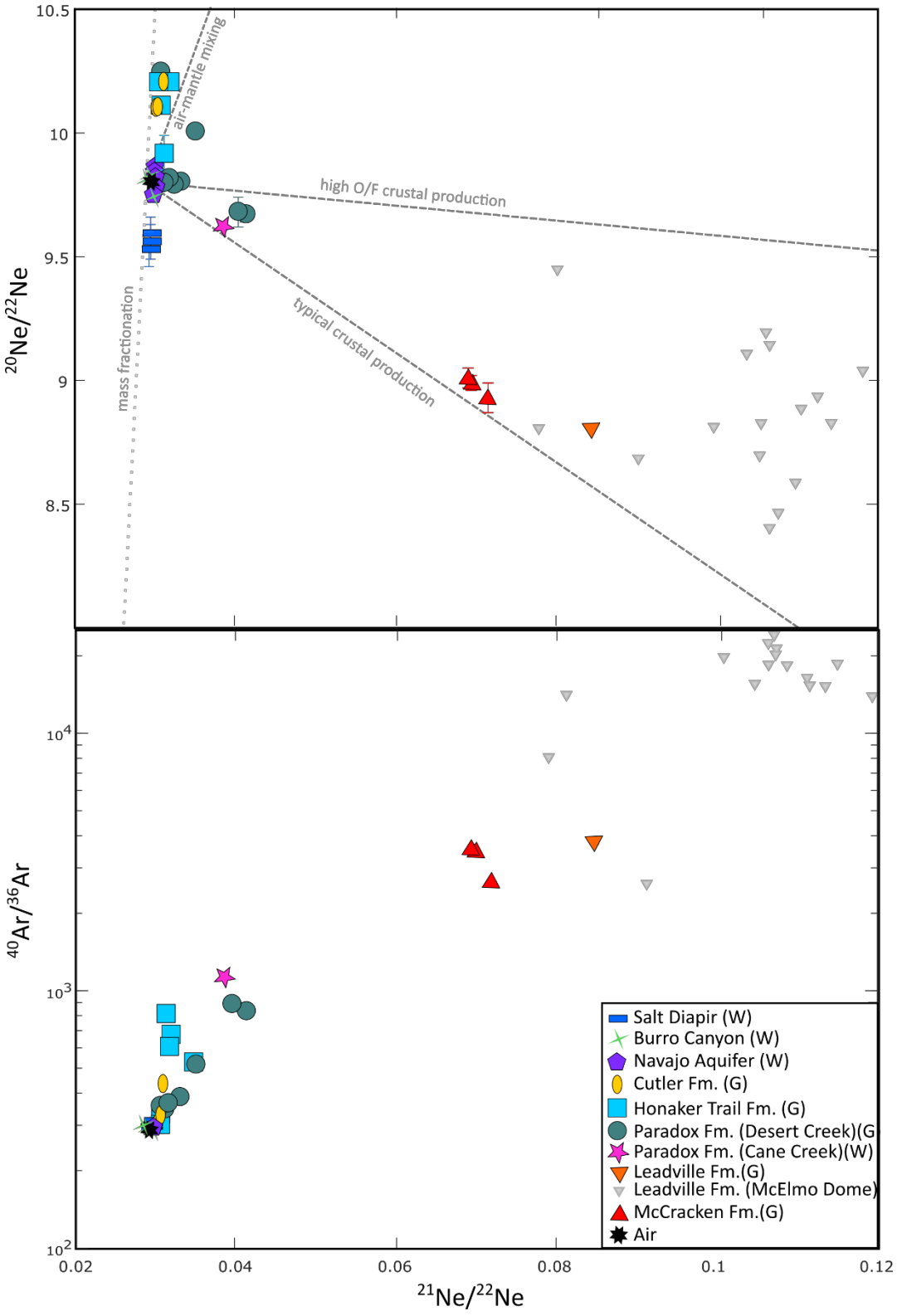


Figure 5.4: $^{21}Ne/^{22}Ne$ vs. a) $^{20}Ne/^{22}Ne$ and b) $^{40}Ar/^{36}Ar$ for all samples. G (gas) and W (water) represent the phase the sample was collected in. The Leadville and McCracken formations beneath the evaporites of the Paradox Formation contain the highest proportion of radiogenic noble gases and are consistent with those measured in McElmo Dome (Gilfillan et al., 2008).

5.5 Discussion

5.5.1 Assessing fluid provenance using noble gas isotope ratios

In order to investigate the distribution of noble gases across the basin, we first need to understand their provenance. The three main terrestrial reservoirs of noble gases (atmosphere, crust, mantle) are isotopically distinct and therefore the contribution from each to a particular sample can be determined. Atmosphere-derived noble gases (ANGs, e.g., ^{20}Ne, ^{36}Ar, ^{84}Kr and ^{130}Xe) enter the subsurface by surface equilibration with groundwater, forming air-saturated water (ASW). ASW has a well-defined elemental composition which is dependent on the temperature, pressure and salinity at recharge and can be traced within the subsurface (Kipfer et al., 2002). Noble gases are also produced within the crust from radiogenic and nucleogenic decay (e.g., ^{4}He, ^{21}Ne, ^{40}Ar) , which are ultimately a function of their parent isotope concentration (U, TH, K, Mg, O, F) and are released into the surrounding fluids by diffusion, recoil and chemical transformation of host minerals (Ballentine and Burnard, 2002).

As helium is not gravitationally bound to Earth, ^{4}He abundance in the atmosphere is extremely low compared to its rate of production within the crust. As such, helium isotopes in ASW are readily overprinted by the release of radiogenic ^{4}He in the subsurface. The air corrected $^{3}He/^{4}He$ $(R/R_A)_C$ is the sum of only two components: the crust and the mantle. The helium isotope ratio associated with typical crustal radiogenic production is $0.02R_A$ (Ballentine and Burnard, 2002) and is $6.1\pm2.1R_A$ for typical sub-continental lithospheric mantle (Graham, 2002; Day et al., 2015). Air corrected $^{3}He/^{4}He$ values fall between 0.0046 and $0.121R_A$ and are consistent with significant radiogenic contributions (Figure 5.3). The slightly higher $^{3}He/^{4}He$ (0.016 to $0.121R_A$) observed in the Navajo Aquifer could either be a result of lower U and Th concentrations in the host rock, or preferential migration of mantle derived fluids through the porous aquifer from the Uncompahgre uplift or nearby igneous intrusions, as was previously observed in East Texas (Byrne et al., 2020). In general, noble gases within the Paradox Basin are groundwater derived with radiogenic overprinting.

Neon ($^{21}Ne/^{22}Ne$, $^{20}Ne/^{22}Ne$) and argon ($^{40}Ar/^{36}Ar$) isotopes are consistent with an atmospheric-radiogenic system (Figure 5.4a). In the formations overlying the Paradox Formation, neon isotope ratios are air-like ($^{21}Ne/^{22}Ne$=0.029, $^{20}Ne/^{22}Ne$=9.81, Porcelli et al., 2002) and deviations from the atmospheric value, in $^{20}Ne/^{22}Ne$, are consistent with small mass fractionation effects. However, significant deviations from the atmospheric Ne isotopic compositions are observed within and beneath the Paradox Formation, consistent with crustal production (Figure 5.2). Within the Desert Creek Member of the Paradox Formation neon isotopes are consistent with radiogenic production within a high O/F environment (Lippmann-Pipke et al., 2011; Kendrick et al., 2011). Whereas samples from the Cane Creek Member of the Paradox Formation, Leadville Formation and McCracken Formation are consistent with typical crustal O/F production (Kennedy et al., 1990). The Leadville and McCracken formations beneath the Paradox Formation have the most significant crustal Ne contributions and are consistent with the isotopic ratios previously measured in the Leadville Formation at McElmo Dome in the southeast of the basin (Figure 5.1 and 5.2)(Gilfillan et al., 2008).

Samples from the shallow Burro Canyon and Navajo aquifers have air-like $^{40}Ar/^{36}Ar$ (298 to 300, where air=298.6 in air, Lee et al., 2006). The remaining samples have measurable radiogenic ^{40}Ar ($^{40}Ar^{*}$) excesses with elevated $^{40}Ar/^{36}Ar$ signatures between 302 and 4530. The $^{40}Ar/^{36}Ar$ generally increase with increasing stratigraphic age and are correlated to the ^{21}Ne excesses (Figure 5.4, Table 5.2). Similar to the neon isotopes, the most significant $^{40}Ar/^{36}Ar$ excesses are found beneath the Paradox Formation in the Leadville and McCracken formations.

Both the Ne and Ar isotopes clearly demonstrate a higher radiogenic isotopic contribution beneath the Paradox Formation compared to samples collected within and above it. We hypothesise from the noble gas isotope ratios that the evaporite Paradox Formation is acting as a near complete barrier to vertical fluid migration within the basin, resulting in the accumulation of radiogenic noble gas beneath the Paradox Formation and the evolution of distinct fluid compositions on either side of the Paradox Formation. The lack of connectivity between the Paradox Formation evaporite and adjacent stratigraphic units demonstrates the effectiveness of the seal, could impact assumptions

used in ^{4}He dating and has important implications for CO_2 storage, resources prospecting and groundwater pollution.

5.5.2 Radiogenic noble gases concentrations

5.5.2.1. Calculating radiogenic noble gas concentrations in groundwater

In order to compare radiogenic noble gas concentrations across the basin, hydrocarbon phase concentrations are first converted into their equivalent in groundwater assuming equilibrium partitioning. Hydrocarbons are assumed to be initially devoid of all noble gases and to have inherited their unique ANG signature from solubility exchange with groundwater. The concentration of ANGs in the groundwater can be calculated based on assumed recharge conditions and are $2.57x10^{-7}$ cm^3/g_{water} and $1.65x10^{-6}$ cm^3/g_{water} for ^{20}Ne and ^{36}Ar respectively (10°C, 0 M, 2000m, 10% Ne excess (Gilfillan et al., 2008)).

On interaction with a gas or oil phase, the least soluble noble gases will preferential partition into the gas resulting in relatively higher proportion of the less soluble noble gases in the gas/oil phase and a higher proportion of the more soluble noble gases in the water phase. The extent of this partitioning is moderated by volumes of water to oil/gas. Where species have the same solubility, there is not expected to be any fractionation in the noble gas ratio between the water and gas/oil phases and the noble gas ratio in the gas/oil phase can be predicted from that originally the water. Using the solubility corrected noble gas ratios and concentrations of ANG (^{20}Ne, ^{36}Ar) in ASW, the concentration of radiogenic noble gases in the groundwater can then be calculated for the hydrocarbon samples (Zhou and Ballentine, 2005; Cheng et al., 2021).

^{4}He and ^{20}Ne have similar solubilities in groundwater (Smith and Kennedy, 1983; Fernández-Prini et al., 2003). In previous work the small solubility difference between them has been neglected and therefore, any fractionation was assumed to be negligible. As a result, the $^{4}He/^{20}Ne$ was assumed be the same in the different phases (Zhou and Ballentine, 2005; Cheng et al., 2021). Here, we take into account the small differences in solubility between ^{4}He and ^{20}Ne using their solubility coefficients for both gas-water partitioning (Eq. 5.1) and water-oil partitioning (Eq. 5.2) (Ballentine et al., 2002).

$$\left(\frac{^4He}{^{20}Ne}\right)_{gw} = \left(\frac{^4He}{^{20}Ne}\right)_m \frac{V_g/V_w + 1/K_w^{He}}{V_g/V_w + 1/K_w^{Ne}} \quad \text{(Eq. 5.1)}$$

$$\left(\frac{^4He}{^{20}Ne}\right)_{gw} = \left(\frac{^4He}{^{20}Ne}\right)_m \frac{\frac{V_o}{V_w}+\frac{K_o^{He}}{K_w^{He}}}{\frac{V_o}{V_w}+\frac{K_o^{Ne}}{K_w^{Ne}}} \quad \text{(Eq. 5.2)}$$

where $\left(\frac{^4He}{^{20}Ne}\right)_{gw}$ is the $^4He/^{20}Ne$ ratio in the groundwater. V_o , V_g and V_w are the volumes of oil, gas and groundwater (estimated from the production data) and K^i_o and K^i_w are the solubilities of noble gas *i* in oil and water respectively under reservoir conditions (Supplementary Table S5.2). Notably, changes in reservoir conditions do not have a significant effect on the $^4He/^{20}Ne$. The $^4He/^{36}Ar$ in water phase can be predicted analogously to $^4He/^{20}Ne$ using the measured ratio in the hydrocarbon phase (Eq. 5.1 and 5.2; Ballentine et al., 2002; Zhou and Ballentine, 2006).

The measured $^4He/^{20}Ne$ (neglecting solubility partitioning) and solubility corrected $^4He/^{20}Ne$ and $^4He/^{36}Ar$ for the water phase can be combined with the ^{20}Ne or ^{36}Ar concentration in ASW, to calculate the expected ^4He concentration in the groundwater prior to hydrocarbon interaction ($[^4He]_{gw}$)(Eq. 5.3, Table 5.3; Supplementary Table S5.3).

$$[\,^4He]_{gw} = [i]_{asw} \times \left(\frac{^4He}{i}\right) \quad \text{(Eq. 5.3)}$$

where *i* is either ^{20}Ne or ^{36}Ar and the $\left(\frac{^4He}{i}\right)$ is either the measured or solubility corrected ratio.

In Figure 5.5, we show the agreement between the calculated ^4He concentrations in groundwater for the gas phase samples using the different methods outlined above. We observe good agreement in the calculated groundwater concentrations using the different correction approaches within and below the Paradox Formation. Variation in the ^4He concentrations in groundwater calculated using the $^4He/^{20}Ne$ and $^4He/^{36}Ar$ within the Cutler and Honaker Trail formations is likely due to open system solubility fractionation (resulting from groundwater flow) beyond that expected for closed system equilibrium in equations 5.1 and 5.2 (section 5.5.3). Given the smaller difference in the solubility between ^4He and ^{20}Ne, compared to ^4He and ^{36}Ar, only the ^4He concentration calculated from the solubility corrected $^4He/^{20}Ne$, will be considered in the remainder of this study.

Sample Name	$^{4}He_{(gw)}$ ($x10^{-6}$)	±	$^{21}Ne^{*}_{(gw)}$ ($x10^{-12}$)	±	$^{40}Ar^{*}_{(gw)}$ ($x10^{-6}$)	±	^{4}He age (in-situ) (Ma)	±	$^{4}He_{(gw)ppc}$ ($x10^{-6}$)	±	^{4}He age$_{ppc}$ (in-situ) (Ma)	±
Water phase (cm^3(STP)/g_{water})												
BOR well 8E	1.13	0.03	1.71	0.07	7.36	0.35	0.108	0.054	11.6	0.6	0.55	0.28
BOR well 9E	1.14	0.03	1.80	0.07	9.27	0.44	0.110	0.055	11.3	0.5	0.54	0.27
BOR well 3E	1.55	0.05	2.17	0.09	6.28	0.30	0.149	0.075	11.8	0.6	0.56	0.28
BOR well 2E	1.86	0.06	1.71	0.07	5.38	0.25	0.179	0.089	11.3	0.5	0.54	0.27
PW-4	0.044	0.001					0.0372	0.0074				
PW-4 (dup)	0.045	0.001					0.0377	0.0075				
PW-3	0.074	0.002					0.0623	0.0125				
PW-12	0.365	0.004					0.307	0.006				
PW-8												
PW-8 (dup)	3.95	0.12					4.59	0.92				
PW-11	0.586	0.018					0.682	0.136				
PW-7	0.802	0.025					0.933	0.187				
STCEC	0.899	0.027					0.0515	0.0103				
BWC-1	0.759	0.023					0.0435	0.0087				
BWC-2	3.46	0.11					0.198	0.040				
BWC-3	8.26	0.25					0.473	0.092				
TRTP	18.5	0.6					1.06	0.21				
Cane Creek	213	2	8.48	0.10	859	58	10.2	5.1	6590	100	310	160
Gas Phase (cm^3(STP)/g_{water})												
AM-75	33.5	4	3.85	0.02	8.64	0.15	5.22	1.04	33.8	3.8	5.3	1.1
AM-62	96.5	10.8	13.3	0.5	48.1	0.8	15.0	3.01	97.5	1.1	15	3

Table 5.3: Noble gas concentrations in cm^3(STP)/g_{water} within groundwater 1σ errors. Concentrations in groundwater for the gas phase samples were calculating using the solubility corrected $^{4}He/^{20}Ne$ (see section 5.5.2.1 for details). $[^{4}He]_{(gw)ppc}$-is the ^{4}He concentration in groundwater after correction for phase partitioning (cf section 5.5.3).

Sample Name	$^{4}He_{(gw)}$ ($x10^{-6}$)	±	$^{21}Ne^{*}_{(gw)}$ ($x10^{-12}$)	±	$^{40}Ar^{*}_{(gw)}$ ($x10^{-6}$)	±	^{4}He age (in-situ) (Ma)	±	$^{4}He_{(gw)ppc}$ ($x10^{-6}$)	±	$^{4}He\ age_{ppc}$ (in-situ) (Ma)	±
Gas Phase (cm^3(STP)/g_{water})												
AM-11-E34	633	71	17.5	0.7	24	4	99	20	640	72	100	20
MM 31-42	4140	540	98.6	5.5	859	58	213	43	4170	520	220	40
BI 24-31	610	80	220	12			99	20				
BH 10-31	24.4	2.8	8.81	0.35			1.7	0.25	24.7	2.8	1.3	0.3
HC 31-31	67.7	7.6	3.43	0.14	15.5	0.3	3.5	0.7	68.4	7.7	3.5	0.7
FF-2-19	1310	150	40.7	1.6	627	11	677	13.5	1330	150	68	14
FF-2-19 (dup)	1150	130	37.6	1.4	554	19	593	11.9	1160	130	60	12
Tohonalda 35-B	12000	1800	6.54	0.13			426	213				
Tohonalda 1	8590	1290	177	7	973	23	305	152				
Anasazi 1	8800	1320			676	23	312	156				
Sahgzie 1	8710	1310			454	12	309	154				
Monument-8N-2	6000	900			374	10	213	106				
WM 22-43	2720	410	58.8	2.4	159	3	96	48				
WM 34-31					122	2						
WM 34-31 (dup)	1940	290	44.4	1.8	129	2	68.8	34.4				
WM 34-33	1510	230	36.2	1.5	78.7	1.5	53.5	26.8				
McIntyre 17-21	20300	2700	1710	110	5720	370	1750	350	20300	2700	1750	350
Lisbon D8-10					6980	470						
Lisbon 10-33	44000	5000	1230	50	5300	110	3790	760	44100	5000	3800	800
Lisbon 10-33 (dup)	43700	4900	1220	50	5450	150	3760	750	43800	4900	3800	800
Lisbon B8-10	33400	4300	1310	70	3840	230	2880	580	33600	4340	2900	600

Table 5.3: continued

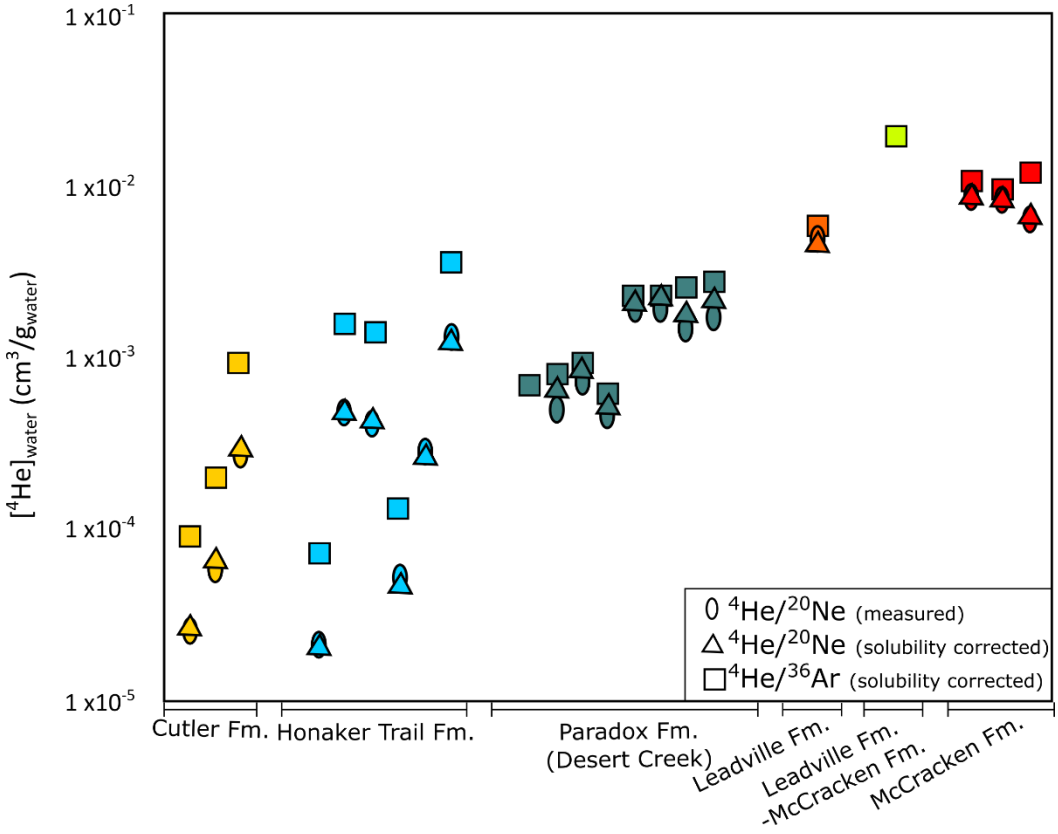


Figure 5.5: Comparison of ^{4}He concentrations in groundwater calculated for the hydrocarbon samples. $[^{4}He]_{gw}$ is calculated using initial ANG concentration in groundwater and the measured $^{4}He/^{20}Ne$ (ovals), the solubility corrected $^{4}He/^{20}Ne$ (triangles) and the solubility corrected $^{4}He/^{36}Ar$ (squares). The Paradox Formation Desert Creek samples are from oil fields and have been solubility corrected for oil-water partitioning. The remaining samples are from gas fields and have been corrected for gas-water partitioning. 1 sigma errors are within symbol size.

Prior to groundwater interaction, hydrocarbon phases contain insignificant amounts of ^{21}Ne and ^{40}Ar (Byrne et al., 2018). As there is negligible isotopic fractionation associated with the solubility partitioning of noble gases, ^{40}Ar and ^{21}Ne concentrations in groundwater can also be calculated for the gas phase samples using the measured $^{40}Ar/^{36}Ar$ and $^{21}Ne/^{20}Ne$ and predicted ^{36}Ar and ^{20}Ne ASW concentrations (Ballentine et al., 2002). With the exception of McElmo Dome where mantle CO_2 is present (Gilfillan et al., 2008), we assume the Paradox Basin is a two component system consisting of ANG and radiogenic noble gases (Section 5.5.1). This allows for the radiogenic ^{40}Ar ($^{40}Ar^{*}$) and ^{21}Ne ($^{21}Ne^{*}$) concentrations to be calculated using the following equations (Table 5.3)(Ballentine et al., 2002):

$$[^{21}Ne^{*}] = [^{21}Ne] \times [1 - \frac{(^{21}Ne/^{20}Ne)_{air}}{(^{21}Ne/^{20}Ne)_{m}}]$$ (Eq. 5.4)

$$[^{40}Ar^{*}] = [^{40}Ar] \times [1 - \frac{(^{40}Ar/^{36}Ar)_{air}}{(^{40}Ar/^{36}Ar)_{m}}]$$ (Eq. 5.5)

where the subscripts *air* and *m* denote the isotope ratios in air and the measured sample respectively

5.5.2.2. Comparison of radiogenic noble gas concentrations

The measured ^{4}He, ^{21}Ne* and ^{40}Ar* concentrations in the groundwater samples and the calculated concentrations in groundwater from the gas phase samples can be compared across the basin (Figure 5.6). We calculate the expected in-situ production rates for ^{4}He, ^{21}Ne* and ^{40}Ar* using average crustal U (2.8ppm), Th (10.7ppm), K (28,200ppm), O (48wt%) and Mg (2wt%) concentrations following the methods of Ballentine & Burnard (2002). Predicted ^{4}He/^{40}Ar* and ^{21}Ne*/^{40}Ar* production ratios are 6.01 and 2.75x10^{-7}, respectively. Measured concentrations of ^{4}He, ^{21}Ne* and ^{40}Ar* are strongly correlated, and in close agreement with typical production ratios (black line, Figure 5.6). The sample taken from the Cane Creek Member of the Paradox Formation, shows a significant excess ^{40}Ar* compared to both ^{4}He and ^{21}Ne*, due to the high potassium concentrations within the Paradox Formation (e.g., Tripp, 2010; Barton, et al., 2018).

^{4}He concentrations in the groundwater vary by 6 orders of magnitude from 4.40 x10^{-8} to 4.40 x10^{-2} cm^{3}/g$_{water}$. ^{4}He concentrations are lowest in the shallowest formations, however, there is no clear trend with depth below ~1000m (Figure 5.7a). Salt tectonics and basin formation processes have resulted in significant differences in formation thickness across the basin (i.e., Figure 5.2) and therefore, it is easier to compare trends with depth by investigating the concentration vs. stratigraphic age (Figure 5.7b). We observe a clear increase in ^{4}He concentrations with increasing stratigraphic age, with the lowest concentrations in the Burro Canyon Aquifer and the highest concentrations in the oldest McCracken Formation, which could indicate that in-situ production is dominant over the external ^{4}He flux. Although part of the Paradox Formation, the Salt Diapir represents very shallow brine samples (14m), adjacent to the Dolores River that have high sulfide concentrations with H_2S gas actively forming from them (Amec Foster Wheeler, 2017) and thus lower concentrations compared to the rest of the Paradox Formation are expected.

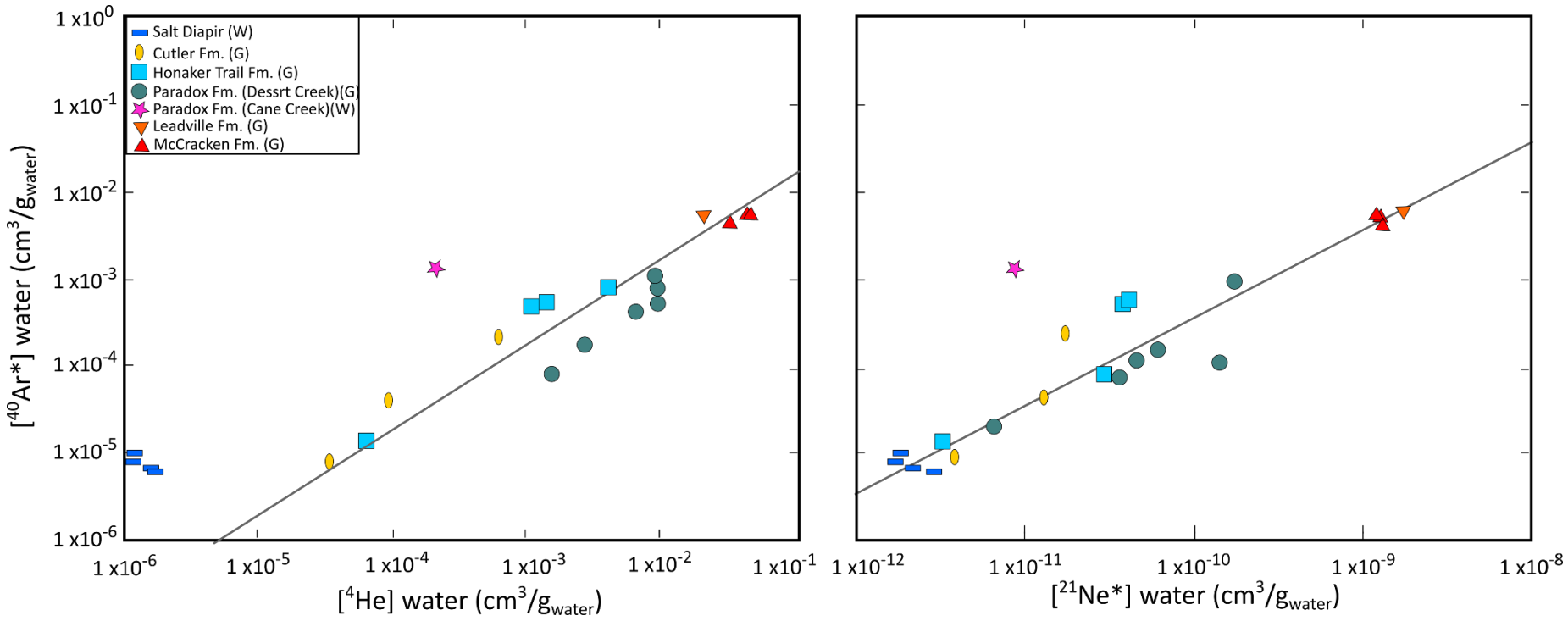


Figure 5.6: Radiogenic isotope abundances in the samples. G (gas) and W (water) represents the sample phase collected. 1 sigma errors are within symbol size. Black lines indicate typical crustal production ratios (see text for details). The majority of samples lie close to typical crustal production. Excess $^{40}Ar^*$ above typical crustal production (relative to ^{4}He and ^{21}Ne) in the Cane Creek Member of the Paradox formation due to elevated K concentrations.

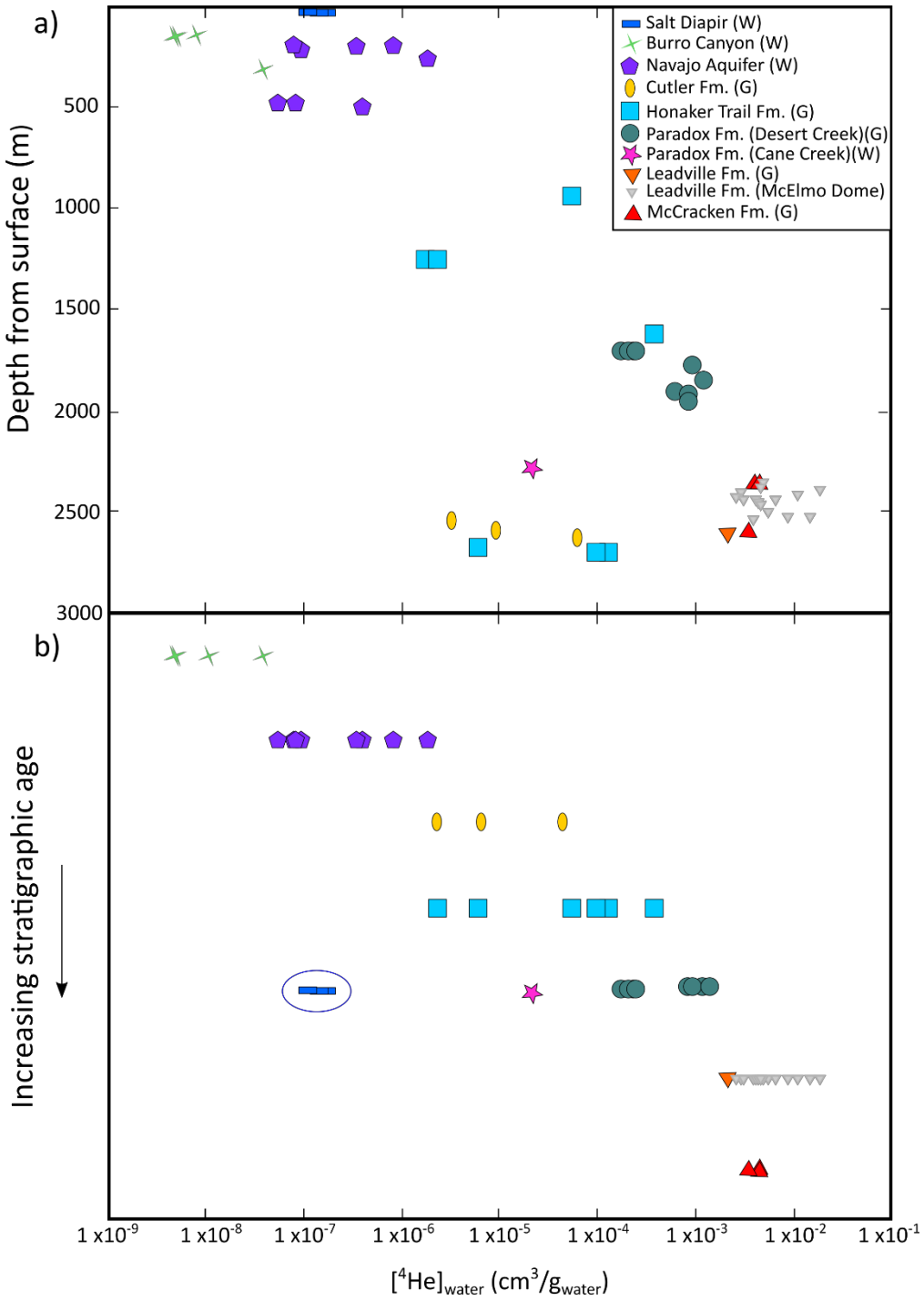


Figure 5.7: ^{4}He concentration in the water phase vs. a) depth and b) stratigraphic age. G (gas) and W (water) represents the phase the sample phase was collected in. 1 sigma errors are within symbol size. Samples show an increasing ^{4}He concentration with depth/stratigraphic age. McElmo dome samples are from Gilfillan et al. (2008). Salt Diaper samples (encircled on b) have lower concentrations than the rest of the Paradox Formation, likely due to their shallow origin, gas exsolution and adjacent location next to the Dolores River.

A similar trend is also observed in both $^{40}Ar^*$ and $^{21}Ne^*$, with the highest concentrations in the Leadville and McCracken formations below the Paradox Formation (Supplementary Figure S5.2) this is consistent with the $^{21}Ne/^{22}Ne$ and $^{40}Ar/^{36}Ar$ ratios. An increase in radiogenic noble gas concentrations with increasing stratigraphic age/depth is consistent with an increased accumulation time.

We can predict the ^4He residence time for the groundwater from in-situ production using the groundwater ^4He concentration, density (assumed to be 2.6g/cm^3 throughout), porosity and assuming a 100% release efficiency from the source mineral (Table 5.3)(Torgersen, 1980; Zhou and Ballentine, 2006). Samples from the Dessert Creek Member of the Paradox Formation, which have not undergone waterflooding for enhanced oil recovery (EOR), have ^4He residences times similar to their formation ages, however both the Cane Creek Member and Salt Diapir samples have lower residence times likely as a result of noble gas partitioning following a change in physical conditions. In the formations overlying the Paradox Formation, ^4He concentrations are lower than predicted for closed system in-situ production, likely due to the circulation of younger groundwaters. Beneath the Paradox Formation, ^4He concentrations are higher than can be explained by in-situ production alone. ^4He concentrations greater than predicted by in-situ production have been observed in many sedimentary basins and are thought to be a result of a ^4He flux from the basement (Section 5.5.4.3; e.g. Torgersen and Clarke, 1985; Torgersen, 1989; Zhou et al., 2005).

The dichotomy in radiogenic ^4He, $^{21}Ne^*$ and $^{40}Ar^*$ concentrations above and below the Paradox Formation is consistent with the significant differences observed in the isotopic ratios and indicate that the Paradox Formation is playing a key role in controlling the fluid composition within the basin, and that the noble gases can be used to investigate the effectiveness of the Paradox Formation as a 'seal'. To investigate the role of the Paradox Formation in controlling the ^4He distribution within the basin (Section 5.4), we first need to be able to identify and quantify the fluid interactions that have occurred (Section 5.3).

5.5.3. Fractionation of atmospheric noble gas (ANG) ratios due to fluid interactions

Due to the differences in relative solubility between the noble gases, fractionation in the ANG ratios ($^{20}Ne/^{36}Ar$, $^{84}Kr/^{36}Ar$ and $^{130}Xe/^{36}Ar$) can be useful in investigating phase interactions (Bosch and Mazor, 1988; Ballentine et al., 1991, 2002; Gilfillan et al., 2008). Measured $^{20}Ne/^{36}Ar$ are between 0.049-0.756 (Table 5.4). The highest $^{20}Ne/^{36}Ar$ are in Cutler and Honker Trail formation gas samples (0.55-0.756), whilst the lowest $^{20}Ne/^{36}Ar$ are in the Salt Diapir groundwater samples (0.049-0.069)(Figure 5.8). $^{84}Kr/^{36}Ar$ and $^{130}Xe/^{36}Ar$ range from 0.0134 to 0.0756 and 0.698 to 12.8 $x10^{-4}$ respectively (compared to ASW values of 0.04 and 4.9 $x10^{-4}$) and are anti-correlated with $^{20}Ne/^{36}Ar$.

Groundwaters from the Burro Canyon Aquifer, have ANG ratios within error of ASW (Table 5.4), suggesting no fluid interaction/phase fractionation has occurred. Within the Navajo Aquifer, $^{20}Ne/^{36}Ar$ are ASW-like, however significant fractionation is observed in the heavy ANGs. Kr to Xe ratios in the Navajo Aquifer are similar to those expected from sorption to organic rich sediments (e.g., Podosek et al., 1980, 1981; Staudacher and Allègre, 1988; Marrocchi et al., 2005) and likely a result of sorption to tar sands and bitumen veins found throughout the aquifer (Chan et al., 2000). Similarly, we see $^{20}Ne/^{36}Ar$ within oil-water equilibrium limits in the Desert Creek Member hydrocarbon samples that were not subjected to EOR, yet $^{84}Kr/^{36}Ar$ and $^{130}Xe/^{36}Ar$ are variable. This is a common observation within hydrocarbon reservoirs (e.g., Chapter 3; Torgersen and Kennedy, 1999; Zhou et al., 2005; Barry et al., 2018; Tyne, et al., 2021) and therefore, we assume the system represents a closed system phase equilibrium between oil and water (Chapter 3; Barry et al., 2018, Tyne et al., 2021). In the Desert Creek Member (WM field) samples that have undergone EOR, elevated $^{20}Ne/^{36}Ar$ are observed, as a result of air incorporation during enhanced oil recovery (Chapter 3; Barry et al., 2018; Tyne et al., 2021).

When groundwater contacts a gas phase, noble gases will partition into the gas phase (exsolution).As Ne is less soluble in water than Ar, a decrease in $^{20}Ne/^{36}Ar$ in the residual groundwater phase occurs together with a proportional increase in the gas phase (Section 5.3.1, Barry et al., 2016). When the gas phase interacts with groundwater that has been stripped of noble

gases, the noble gases will re-dissolve into the water phase (partial redissolution). Partial redissolution causes an increase in the $^{20}Ne/^{36}Ar$ of the gas phase (as ^{36}Ar is more soluble in water) and the initial $^{20}Ne/^{36}Ar$ in the water phase will be low. As more noble gases redissolve the $^{20}Ne/^{36}Ar$ in the gas and water phase will progressively increase to either equilibrium (under closed system conditions) or to higher values (in an open system). Partial redissolution has previously been observed at McElmo Dome (Gilfillan et al., 2008).

5.5.3.1 Exsolution

Noble gas solubility in groundwater is dependent on the reservoir conditions (e.g., temperature, pressure, salinity) and generally increases with mass (Ne<Ar<Kr<Xe, Crovetto et al., 1982; Fernández-Prini et al., 2003). On interaction with a gas phase, the lighter noble gases will preferentially partition from groundwater into the gas phase, resulting in a lower $^{20}Ne/^{36}Ar$, higher $^{84}Kr/^{36}Ar$ and higher $^{130}Xe/^{36}Ar$ in the residual groundwater (Figure 5.8a,b). The magnitude of fraction is controlled by the gas/water volume ratio where, in the limit as $Vg/Vl \rightarrow 0$, $F \rightarrow K_i/K_j$ but as $Vg/Vl \rightarrow O$, $F \rightarrow 1$. In groundwaters collected from the Salt Diapir, $^{20}Ne/^{36}Ar$ values are between 0.049 and 0.069 (lower than ASW values) and $^{84}Kr/^{36}Ar$ values are elevated compared to ASW (0.0504-0.0621). These values are consistent with exsolution from the groundwater into a gas phase. Noble gas exsolution is most likely occurring alongside H_2S volatilisation and degassing from the Salt Diapir brines. High H_2S concentrations have been measured in the air above the brine surface (Amec Foster Wheeler, 2017) and therefore we assume open system behaviour. The exsolution of the noble gases is then modelled (following Rayleigh fractionation) and the proportion of gas loss in the Salt Diapir is calculated to be between 30 and 44 % using $^{20}Ne/^{36}Ar$ vs $^{84}Kr/^{36}Ar$ and 18-50% using $^{84}Kr/^{36}Ar$ vs $^{130}Xe/^{36}Ar$ (Figure 5.8a,b, Table 5.4). The groundwater ^{4}He concentration can then be corrected for this gas loss using the measured $^{4}He/^{20}Ne$ and ^{20}Ne expected in ASW (Eq. 5.3).

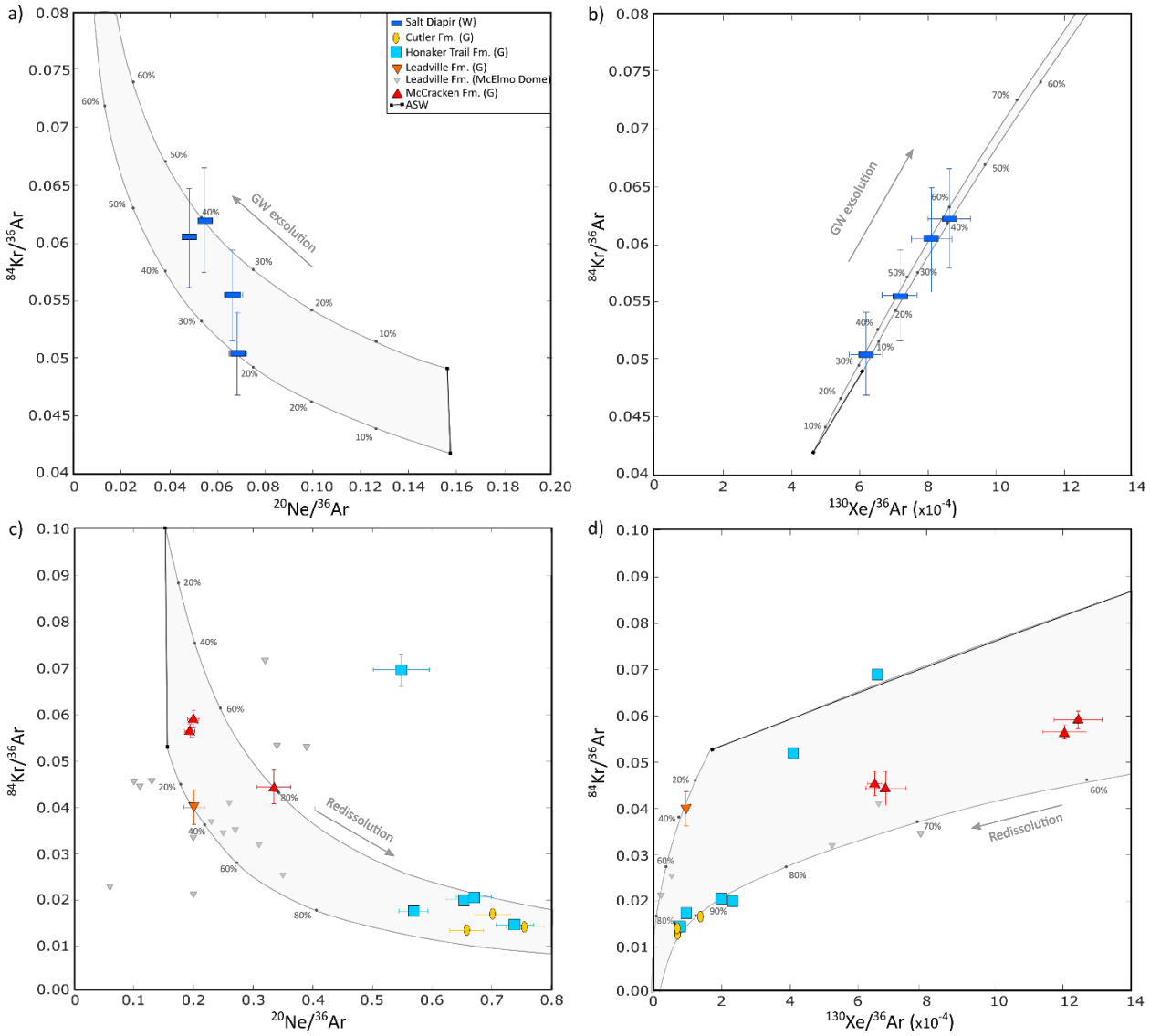


Figure 5.8: Phase (water and gas) fractionation models of exsolution (water to gas; a & b) and partial redissolution (water to gas to water; b and c) for the atmospheric noble gas ratio in the Paradox Basin samples. a) & c) $^{20}Ne/^{36}Ar$ vs. $^{84}Kr/^{36}Ar$. b) & d) $^{130}Xe/^{36}Ar$ vs. $^{84}Kr/^{36}Ar$. a) & b) show groundwater samples alongside the modelled composition of groundwater with exsolution into the gas phase (shaded region). Tick marks represent the percentage of gas exsolved. c) & d) show gas phase samples with the modelled compositions of the gas phase with partial redissolution (shaded region). Tick marks represent the percentage of gas re-dissolved. Partial redissolution is observed in the McCracken, Leadville, Honaker Trail and Cutler formations, with the greatest proportions occurring in the Honaker Trail and Cutler formations. McElmo Dome samples taken from Gilfillan et al 2008. ASW, in all panels, is modelled for variable Kr and Xe excesses (thick black line).

Sample Name	$^{20}Ne/^{36}Ar$	±	$^{84}Kr/^{36}Ar$ ($x10^{-2}$)	±	$^{130}Xe/^{36}Ar$ ($x10^{-4}$)	±	Process occurring	Fraction exsolved/ redissolved*		Excess Kr	Excess Xe
								(Ne-Ar-Kr)	(Xe-Ar-Kr)		
ASW	0.156		3.84		3.90						
Water phase											
BOR well 8E	0.0486	0.0029	6.04	0.44	8.06	0.61	Exsolution	0.44	0.42	1.18	1.30
BOR well 9E	0.0552	0.0033	6.21	0.45	8.55	0.64	Exsolution	0.40	0.41	1.23	1.40
BOR well 3E	0.0671	0.0040	5.55	0.40	7.16	0.54	Exsolution	0.34	0.35	1.15	1.24
BOR well 2E	0.0687	0.0041	5.04	0.36	6.17	0.46	Exsolution	0.33	0.35	1.05	1.07
PW-4	0.129	0.004	4.12	0.15	4.47	0.16					
PW-4 (dup)	0.149	0.008	5.24	0.29	2.73	0.26					
PW-3	0.153	0.005	3.95	0.14	4.10	0.15					
PW-12	0.150	0.002	3.70	0.11	3.89	0.10					
PW-8	0.152	0.005	3.27	0.12							
PW-8 (dup)	0.157	0.009	4.75	0.62	4.03	0.40					
PW-11	0.165	0.005	3.94	0.14	4.11	0.15					
PW-7	0.313	0.009	1.55	0.05	1.38	0.05					
STCEC	0.173	0.010	3.57	0.46	3.81	0.37					
BWC-1	0.179	0.006	2.13	0.08	2.22	0.08					
BWC-2	0.171	0.005	2.18	0.08	2.29	0.08					
BWC-3	0.171	0.010	4.36	0.57	3.88	0.38					
TRTP	0.178	0.011	7.56	0.98	3.83	0.38					
Cane Creek	0.313	0.007	3.80	0.09	4.44	0.39					
Gas Phase											
AM-75	0.756	0.032	1.42	0.03	0.698	0.035	Partial redissolution	0.95	0.97	2.1	8.0
AM-62	0.658	0.028	1.34	0.03	0.702	0.036	Partial redissolution	0.95	0.96	1.6	5.0

Table 5.4: Atmosphere-derived noble gas ratios. *to groundwater for gas phase samples and to gas phase for groundwater samples

Sample Name	$^{20}Ne/^{36}Ar$	±	$^{84}Kr/^{36}Ar$ ($x10^{-2}$)	±	$^{130}Xe/^{36}Ar$ ($x10^{-4}$)	±	Process occurring	Fraction exsolved/ redissolved* (Ne-Ar-Kr)	(Xe-Ar-Kr)	Excess Kr	Excess Xe
Gas Phase											
AM-11-E34	0.701	0.030	1.69	0.04	1.37	0.07	Partial redissolution	0.96	0.96	1.9	6.0
MM 31-42	0.427	0.030	0.694	0.059	0.673	0.60	Partial redissolution	0.81	0.84	7.5	50
BH 10-31	0.739	0.032	1.46	0.04	0.798	0.04	Partial redissolution	0.92	0.92	2.2	15
HC 31-31	0.569	0.024	1.76	0.04	0.978	0.05	Partial redissolution	0.93	0.93	1.7	4.5
FF-2-19	0.652	0.028	2.02	0.05	2.30	0.12	Partial redissolution	0.95	0.95	2.3	14
FF-2-19 (dup)	0.670	0.030	2.06	0.12	1.98	0.06	Partial redissolution	0.95	0.95	2.3	14
Tohonalda 1	0.198	0.009	5.35	0.16	9.95	0.53					
Anasazi 1	0.160	0.008	5.46	0.21	11.7	0.7					
Sahgzie 1	0.146	0.007	5.20	0.16	11.0	0.6					
Monument-8N-2 (dup)	0.257	0.012	5.21	0.16	10.6	0.6					
WM 22-43	0.166	0.007	4.19	0.11	6.29	0.32					
WM 22-43 (dup)			3.16	0.18	4.25	0.13					
WM 34-31	0.139	0.006	2.80	0.07	4.36	0.22					
WM 34-31 (dup)	0.191	0.008	3.54	0.09	5.55	0.28					
WM 34-33	0.163	0.007	4.20	0.11	5.56	0.29					
McIntyre 17-21	0.201	0.018	4.00	0.37	0.947	0.115	Partial redissolution	0.40	0.41	1.32	0.4
Lisbon D8-10			2.75	0.02	4.75	0.43					
Lisbon 10-33	0.194	0.009	5.65	0.15	12.4	0.6	Partial redissolution	0.37	0.38	1.85	5.0
Lisbon 10-33 (dup)	0.200	0.009	5.91	0.19	12.8	0.7	Partial redissolution	0.39	0.37	1.85	5.0
Lisbon B8-10	0.335	0.028	4.44	0.36	7.03	0.59	Partial redissolution	0.78	0.78	2.60	10
Lisbon B8-10 (dup)			4.54	0.26	6.70	0.20					

Table 5.4: continued

5.5.3.2. Partial redissolution

Partial redissolution is a two-stage process. During the first stage, noble gases in groundwater are completely degassed into a gas phase. In the second stage, the noble gases in the gas phase redissolve into stripped groundwater as a result of groundwater flow or a change in the physical conditions (e.g., increase in pressure), following Rayleigh fractionation. Both the exsolution and the subsequent redissolution of the noble gases are solubility dependent and therefore depend on the temperature and salinity of the field (Supplementary Table S5.2). The initial Kr and Xe excesses predicted for each sample are given in Table 5.4.

It is important to understand the extent of partial redissolution as it could have an effect on the $^{4}He/^{20}Ne$ ratio and therefore the calculated ^{4}He concentration in groundwater for the gas phase samples. By calculating the change in $^{4}He/^{36}Ar$ and $^{20}Ne/^{36}Ar$ with redissolution, we can predict the resulting change in $^{4}He/^{20}Ne$. We find that with 100% redissolution there is a 9.7% increase in the $^{4}He/^{20}Ne$. Below 95% redissolution, the effect of partial redissolution on the $^{4}He/^{20}Ne$ is within error of our samples (<3%). Nevertheless, by quantifying the extent of partial redissolution, we can iteratively correct the $^{4}He/^{20}Ne$ used for calculating ^{4}He concentrations in groundwater ($^{4}He_{corr}$)(Tables 5.3 and 5.4).

Elevated $^{20}Ne/^{36}Ar$ in the gas samples, in excess of that which can be explained by simple gas-water equilibrium, is observed both above (0.55-0.76, Cutler and Honaker Trail formations) and below (0.19-0.34, Leadville and McCracken formations) the Paradox Formation, consistent with partial redissolution (Figure 5.8, Supplementary Information S5.3.3). For partial redissolution to have occurred either noble gas-stripped groundwater flow (possibly caused regionally by exsolution) or a change in physical conditions is required. However, a coherent change in physical condition across the sampled area is unlikely and therefore we discount this as a viable fieldscale mechanism. Groundwater flow through these units is in agreement with the relatively young ^{81}Kr residence times and with the major ion chemistry of the brines which suggest there has been dissolution of the Paradox Formation as a result of the influx of meteoric water (Kim et al., 2020, 2021). The influx of meteoric water and flushing of these formations was likely initiated by the denudation to the

Colorado Plateau ~6Ma (Murray et al., 2016; Murray et al., 2019), which created higher topographic gradients and brought the salt anticlines closer to the surface in contact with meteoric water circulation (Kim, et al 2021). In the Cutler and Honaker Trail formations (above the Paradox Formation), the proportion of noble gases that have been partially redissolved is between 87 and 96% (Table 5.4) and is significantly greater than the proportion redissolved in the Leadville and McCracken formations (37-78%, Figure 5.8). This suggests that either the gas phases in the Cutler and Honaker Trail formations have contacted a greater volume of groundwater than in the Leadville and McCracken formations or the circulated groundwater is less stripped (degassed) in the Leadville and McCracken formation than above the Paradox Formation. We also observe higher ^{36}Ar concentrations in the Cutler and Honaker Trail formations consistent with more groundwater flow through these units. The disconnect between the hydrogeological systems suggests groundwater circulation is more active above the Paradox Formation and that the Paradox Formation is a barrier between the two hydrogeological regimes, in agreement with the radiogenic isotope ratios (Section 5.5.1). This finding highlights the utility of stable noble gases isotopes in tracing and identifying the differences in hydrogeological regimes either side of the Paradox Formation.

5.5.4 Investigating ^{4}He distribution

^{4}He is the most sensitive noble gas to diffusion due to its high diffusivity in water and is therefore an ideal tracer for investigating diffusional gas transport within a basin (Jähne et al., 1987). To determine the role of the Paradox Formation in controlling fluid connectivity and compositions in the basin, we can compare the initial ^{4}He distribution in groundwater (i.e., prior to any phase interactions), with that of a time-dependent vertical 1D ^{4}He diffusion model (Cheng 2020, Cheng et al., 2021).

5.5.4.1 Vertical 1D ^{4}He diffusion reference model

There are two sources of ^{4}He within sedimentary units, one from in-situ radiogenic production and one from an external flux (Supplementary Figure S5.3a). We also consider two mechanisms of ^{4}He loss to a unit: flushing with ASW and diffusion to adjacent formations. We use the simplest scenario, of only in-situ production and vertical diffusion, to create a reference model that predicts

the ^{4}He concentrations expected in the groundwater (Supplementary Information S5.3.4.1)(Cheng 2020, Cheng et al., 2021). Given the variable thicknesses of the sedimentary units across the basin, discrete models are presented for the different sampling areas. The parameters used in constructing these models (e.g., [U], [Th], porosity, age) are given in Supplementary Table S5.4. We assume the effective porosity in the Paradox Formation is approaching zero (0.00001%)(Beauheim and Roberts, 2002). Notably, U and Th concentrations within an evaporite layer are poorly constrained (Supplementary Information S5.3.2).

The ^{4}He concentration in groundwater, from in-situ production and diffusion only, can then be predicted for the whole sedimentary column using this reference model (e.g., grey dashed line Figure 5.9a,b). The models show that once the Paradox Formation has reached a thickness of ~50m thickness, ^{4}He concentrations become constant and are dominated by in-situ production and that ^{4}He diffusion from the formation below is impeded (Figure 5.9, Supplementary Figure S5.3b).

Within the Desert Creek Member of the Paradox Formation samples can be split into two subgroups; those with lower ^{4}He concentrations due to EOR in the WM Oil Field ($2.06\pm0.61 \times 10^{-3}$ cm^3/g_{water}) and those which have not been subject to EOR ($8.82\pm2.13 \times 10^{-3}$ cm^3/g_{water}; Figure 5.9a). By comparing the ^{4}He concentrations in the samples which have not been subjected to EOR, to the reference model we see that the ^{4}He concentration is remarkably constant over the range of depths sampled and is consistent with that predicted for solely in-situ production. This agrees with the model and demonstrates that the Paradox Formation is a barrier to ^{4}He diffusion and fluid communication and acting as an effective seal, consistent with the observed noble gas elemental ratios and radiogenic noble gas concentrations. Although this result is not necessarily surprising, as salt is known to be an effective trap for hydrocarbon migration (e.g., Read, 1959; Wescott and Hood, 1994), the verification that >~50m of salt can act as a barrier to mobile elements such as ^{4}He, could have implications for ^{4}He and H_2 prospecting as well as carbon capture and storage and nuclear waste disposal.

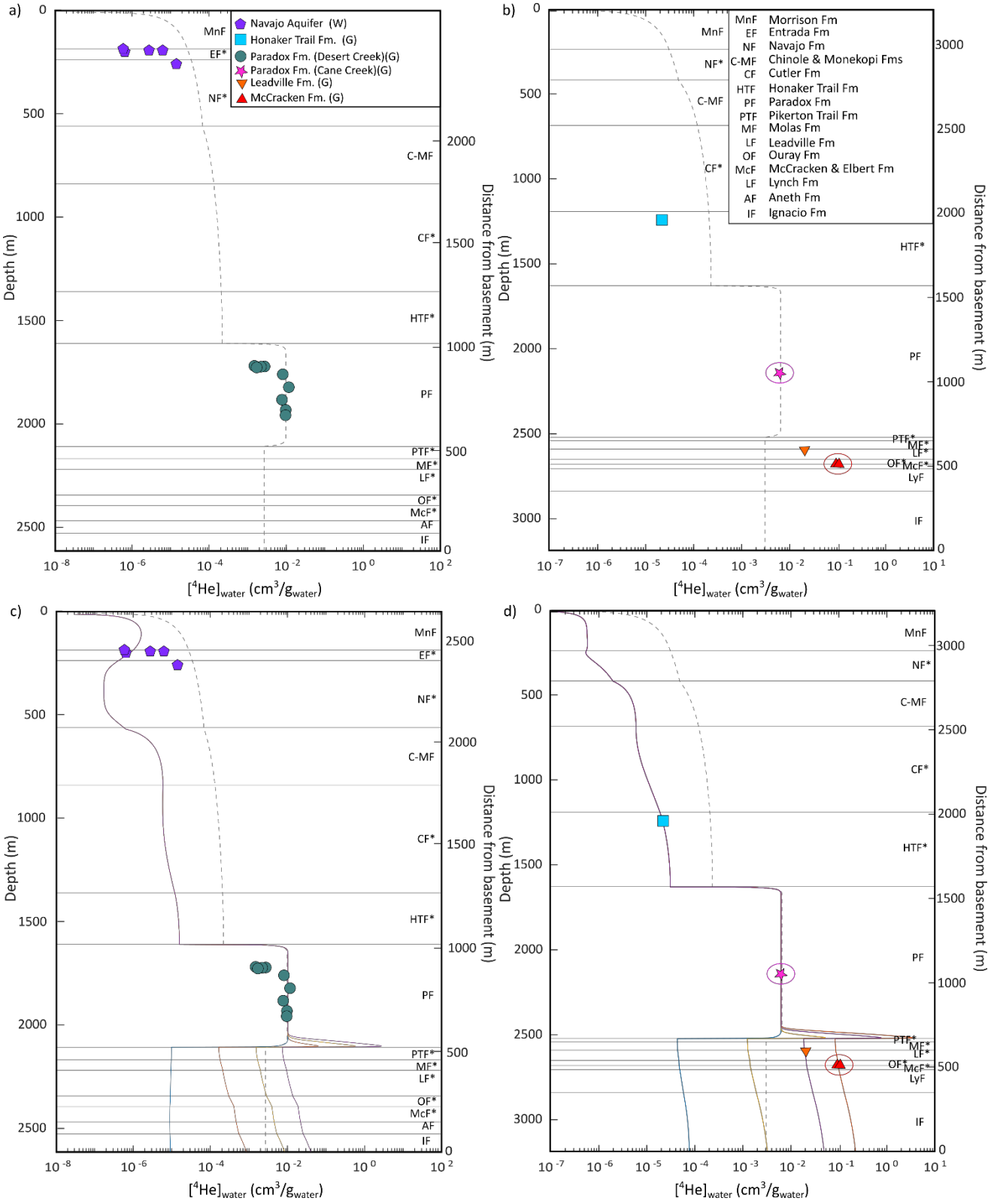


Figure 5.9: Vertical 1D diffusion model ^{4}He profiles compared with water concentrations inferred for the samples for a) Greater Aneth Oil Field, b) Lisbon Southeast Gas Field, as a function of depth and distance

Figure 5.9 caption continued: from the Precambrian basement. 1 sigma errors are within symbol size. a) and b) represent the 'reference' model for ^{4}He concentrations in groundwater i.e., in-situ helium production,

zero basement flux, no horizontal flow (grey dashed line). McCracken and Paradox (Cane Creek) formations (encircled on b,d) have been transposed from their own discrete models to the appropriate depth and concentration onto profile b/d. ^{4}He diffusion is limited to the bottom ~50m of the Paradox Formation and the Paradox Formation samples can be explained solely by in-situ production. Concentrations lower than predicted by the reference model suggest lateral flushing through these units, where ^{4}He concentrations greater than predicted require a ^{4}He basement flux. c) and d) represent the modelled ^{4}He concentration profiles or groundwater with lateral flow (flushed units marked with *) for different basement fluxes. Modelled basement fluxes (in mol/m^{2}/yr) are as follows: blue=0; yellow=1.5 x10^{-6} (crustal average, Torgersen and Clarke, 1985); purple=23 x10^{-6} (required to fit the Leadville Formation sample in the Lisbon Southeast Field) and; orange=105 x10^{-6} (required to fit McCracken samples within the Lisbon Field). The convergence of modelled flux lines in the Paradox Formation is a result of no diffusion within the formation and demonstrates that the Paradox Formation is effective at preventing vertical communication to the shallower formations.

^{4}He concentrations in the samples both above and below the Paradox Formation are not consistent with the reference model (Figure 5.9.a,b). Deviations from the reference models can provide insights into the rates, timings and additional processes (e.g., groundwater circulation, basement flux) occurring within the basin, and allow us to investigate cross formational gas migration. Above the Paradox Formation, ^{4}He concentrations are lower than predicted by the reference model, consistent with lateral flow through these units. Below the Paradox Formation, ^{4}He concentrations are higher than predicted by the reference model, indicating that there is a ^{4}He flux from the basement.

5.5.4.2 Identification of lateral flow

Sample taken from above the Paradox Formation (Burro Canyon and Navajo aquifers and the Cutler and Honaker Trail formations) have ^{4}He concentrations lower than predicted by our reference model (grey dashed line; Figure 5.9). One mechanism that can lower the ^{4}He concentrations is lateral (advective) flow of meteoric water into a unit. This lateral 'flushing' through of a stratigraphic unit decreases the ^{4}He concentrations, effectively 'resetting' them to ASW concentrations for the duration of flushing (Supplementary Information S5.3.4.2), once lateral flow ceases, ^{4}He accumulation and accumulation is restarted. Flushing of meteoric water has been added

to the ^{4}He diffusional model from 6Ma to 0.005Ma in the Burro Canyon formation and to 0.025Ma in the Navajo Aquifer (average groundwater residence time from Noyes, 2019), as well as from 6-0.9Ma in the Cutler and Honker Trail formations (^{81}Kr residence time, Kim et al., 2020) (Figure 5.9c,d). Lateral flow through these units is in agreement with the fractionation observed in ANG ratios (Section 5.5.3), major ion composition of the brines (Kim et al., 2021) and radiocarbon and ^{81}Kr groundwater residence times in the basin (3ka- 0.9Ma (Noyes, 2019; Kim et al., 2020)). The addition of lateral flushing to the vertical 1D ^{4}He diffusion model accounts for the lower ^{4}He concentrations observed within the samples overlying the Paradox Formation (Figure 5.9c,d). Some samples have higher concentrations than predicted by the model, this deviation could result from the variation in groundwater residence time (e.g., 3,256-10,789 years in the Burro Canyon Aquifer, Noyes, 2019) meaning ^{4}He concentrations in the model are underestimated, from upwelling of deeper fluid through faults or from differences in U and Th concentrations.

Despite having ^{4}He concentrations greater than can be explained by in-situ production (Figure 5.9b), the fractionation in the ANG ratios, ^{81}Kr residence time of ~0.8Ma and the major ion composition of the brines suggest there has been some meteoric water influx beneath the Paradox Formation (Kim et al., 2020,2021). With this in mind, we also model lateral flow from 6 – 0.8Ma in the Pinkerton, Molas, Leadville, Ouray and McCracken formations beneath the salt.

5.5.4.3 Determining the basement helium flux

Regardless of whether there is lateral flushing below the Paradox Formation, ^{4}He concentrations in the Leadville and McCracken formations beneath the Paradox Formation are higher than can be explained solely by in-situ production and a basement flux of ^{4}He is required (Grey dashed and blue lines Figure 5.9b,d). A volatile flux from the Precambrian basement is in agreement with previous observations of radiogenic Sr in the brines below the Paradox Formation (Crossey et al., 2006; Kim et al., 2021). Assuming lateral flow through these units from 6-0.8Ma (^{81}Kr residence time) and complete resetting of ^{4}He to ASW concentrations during this period, we find a constant basement flux of between 23– 105 x10^{-6} mol ^{4}He/m^{2}/yr (purple and orange lines respectively, Figure 5.9d) is required to fit the model to the measured ^{4}He concentrations in these units. This is significantly

greater than the average basement flux (1.47 x 10^{-6} mol $^{4}He/m^{2}/yr$, yellow line Figure 5.9d Torgersen and Clarke, 1985).

Elevated ^{4}He fluxes similar to that predicted by the model are observed in volcanic areas and areas under tectonic strain (Torgersen, 2010). However, the intrusion of the proximal La Sal mountains occurred approximately 20-31 Ma (Nelson et al., 1992; Rønnevik et al., 2017), and the associated heat pulse is thought to be short-lived (Supplementary Information S5.3.4.3)(Getz, 2020). Inverse mixing models beneath the Paradox Formation suggest that the formation waters are a mix of paleo-evaporated seawater and meteoric water (Kim et al., 2021). Incomplete flushing of the units below the Paradox Formation, will result in a proportion of old groundwater with accumulated ^{4}He to remain trapped in the pore spaces. Mixing between the ^{4}He depleted waters introduced during flushing and the trapped water (enriched in ^{4}He) can result in a higher ^{4}He concentration than predicted in our models. As such, the portion of old groundwater remaining throughout lateral flushing will control the ^{4}He concentration in the water and the size of the basement flux needed to accumulate sufficient He to match the measured concentrations. A larger portioning of trapped ^{4}He will result in a smaller required basement flux. In addition, if flushing of these units ended prior to 0.8Ma, a lower basement flux would be to fit the model. It is important to note here that none of these scenarios are mutually exclusive and a combination of them is possible.

5.6 Implications and Conclusions

We present noble gas isotope and abundance data from 36 different samples collected in the Paradox Basin. These samples range across 7 stratigraphic units (Cretaceous-Devonian) and include a thick evaporite unit (Paradox Formation). By sampling fluids across a range of stratigraphic units we are able to investigate the role of basin architecture has had on the chemical evolution of groundwater.

Low $^{3}He/^{4}He$ measured across all units is consistent with the noble gases in the system being predominantly groundwater-derived, with a radiogenic overprint. Radiogenic noble gas concentrations (^{4}He, $^{21}Ne^{*}$ and $^{40}Ar^{*}$) and isotope ratios ($^{40}Ar/^{36}Ar$ and $^{21}Ne/^{22}Ne$) increase with

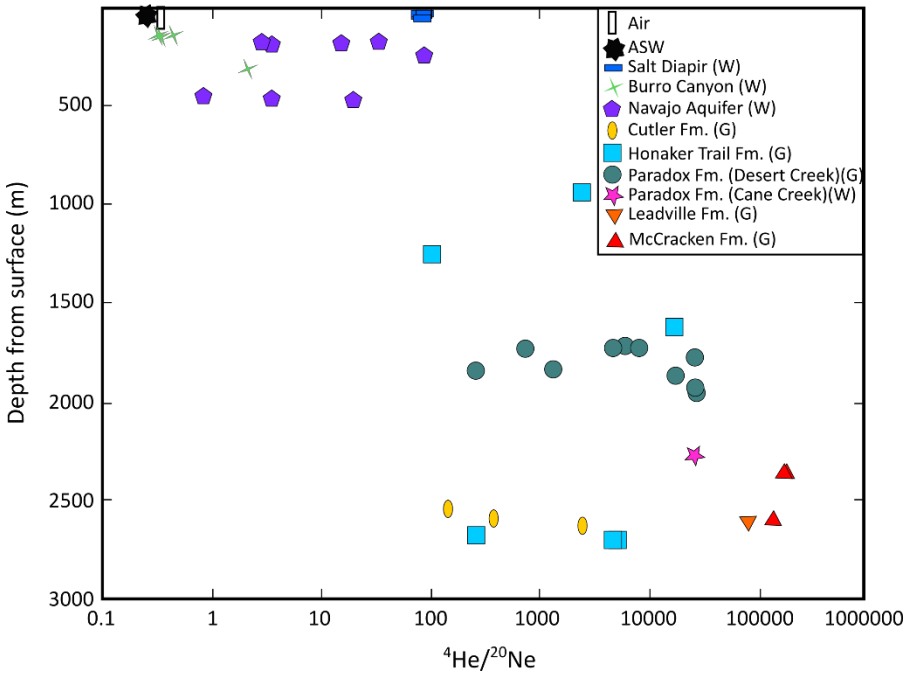
depth consistent with increased accumulation at crustal production ratios with time, however there is a significant difference either side of the Paradox Formation, likely as a result of Paradox Formation acting a barrier to fluid migration.

We show that deviations from air-saturated water in atmosphere-derived noble gas ratio ($^{20}Ne/^{36}Ar$, $^{84}Kr/^{36}Ar$ and $^{130}Xe/^{36}Ar$) are a result of phase partitioning during fluid interactions, and see evidence of groundwater migration both below and above the Paradox Formation, in agreement with the major ion composition of the brines and ^{81}Kr ages (Kim et al., 2020, 2021). Furthermore, we observe greater phase partitioning from partial redissolution in the gas samples taken above the Paradox formation (90-96%) than below (37-87%), suggesting different fluid flow regimes on either side of the Paradox Formation.

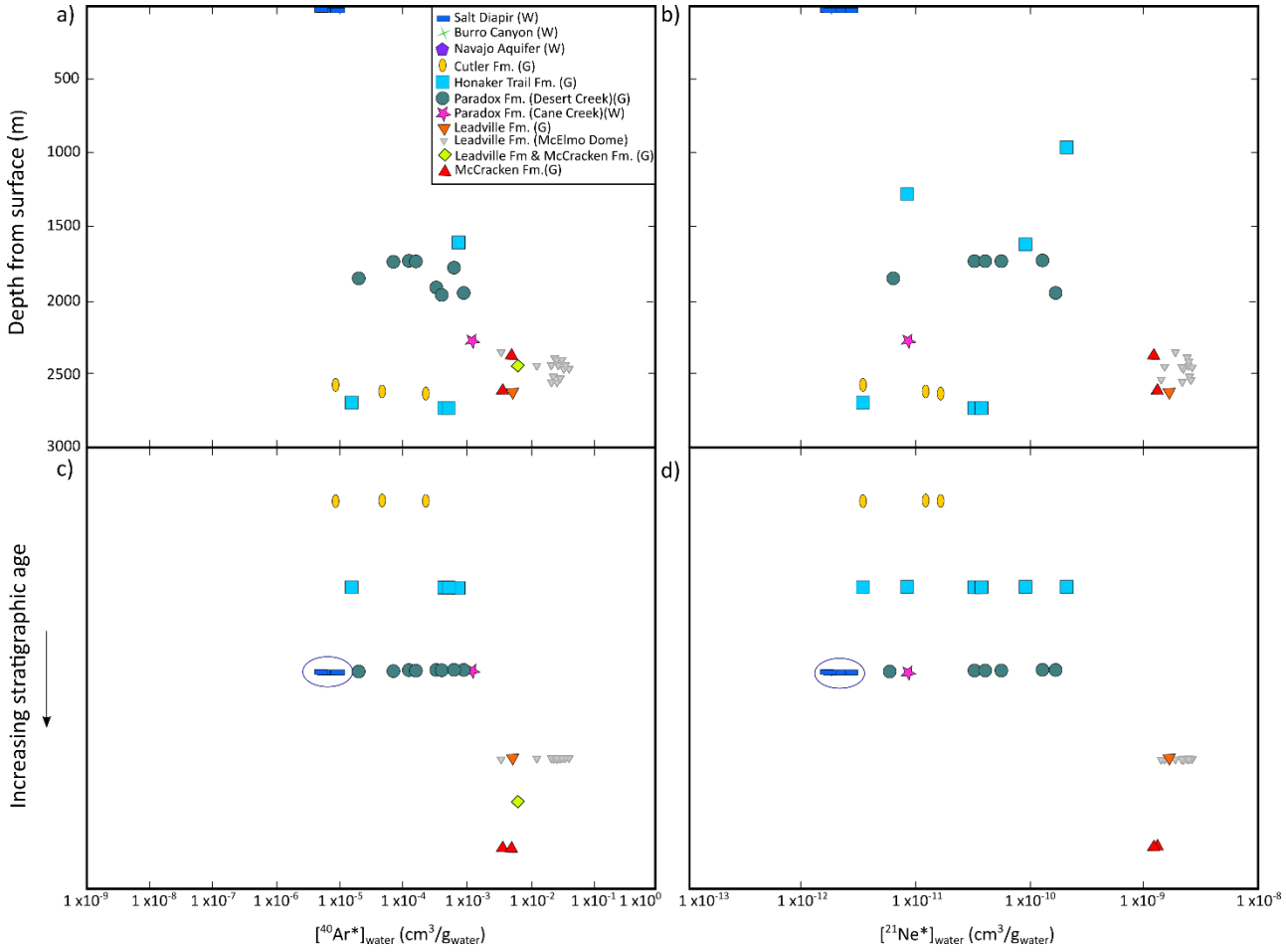
Considering both in-situ radiogenic production and external helium basement fluxes, we develop vertical 1D ^{4}He diffusion models. We find that the Paradox Formation is impermeable to ^{4}He diffusion, allowing for the accumulation of ^{4}He and radiogenic noble gases below. Deviations from the theoretically calculated ^{4}He diffusion reference model can largely be accounted for by meteoric water recharge likely associated with the denudation and uplift of the Colorado Plateau. High helium concentrations observed beneath the Paradox Formation are likely a result of a ^{4}He basement flux combined with only partial flushing of the units. Typically, the determination of groundwater residence time assumes a simple system of in-situ production and a potential diffusive external flux from below usually based on an average crustal porosity (Torgersen and Clarke, 1985; Zhou and Ballentine, 2006). Through the development of the ^{4}He diffusional models, we show that the magnitude of the basement flux and lithology type can control the diffusive helium flux. For example, below the Paradox Formation, where there is a high basement flux and ^{4}He diffusion into shallow formations is prohibited, the ^{4}He residence time could be overestimated. Whereas above the Paradox Formation, fluid circulation and lack of diffusion form the deepest formations could lead to an underestimation of ^{4}He residence times. Therefore, an understanding and a consideration of the basin architecture and history is critical to accurately determine ^{4}He groundwater residence times.

We show that through understanding the stable noble gas isotopes and abundances, we are able to identify the dichotomous hydrogeological regimes and quantify the efficacy of the reservoir seal (i.e., Paradox Formation evaporites). This is critical in understanding subterranean modern and paleo-fluid flow within sedimentary basins, such as in the Paradox Basin. Stratigraphy ultimately controls the connectivity and hydrogeology of various sedimentary reservoirs and understanding the nature and extent of communication between different fluid reservoirs will be critical for resource prospecting and waste storage within the subsurface.

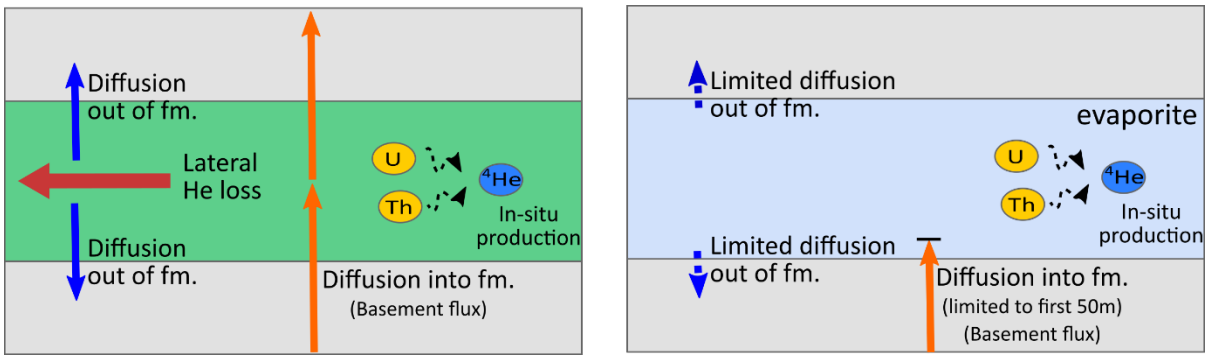
Supplementary figures



Supplementary Figure S5.1: $^{4}He/^{20}Ne$ vs depth across the Paradox Basin. 1σ errors are within symbol size. G (gas) and W (water) represent the sample phase. $^{4}He/^{20}Ne$ generally decreases towards the surface consistent with greater atmospheric contribution.



Supplementary Figure S5.2: Relationship between $^{40}Ar^*$ (a) and $^{21}Ne^*$ (b) with depth. Basin structure means relationships with depth are hard to identify and thus concentration vs. increasing stratigraphic age are also shown (c and d). G (gas) and W (water) represent the sample phase. 1σ errors are within symbol size. a) and c) Samples show increasing $^{40}Ar^*$ accumulation with increasing depth/stratigraphic age with the highest concentrations in the formations beneath the salt. b) and d) $^{21}Ne^*$ concentrations within and above the salt are fairly consistent, however a significant increase in $^{21}Ne^*$ is observed below the Paradox Formation. Salt Diaper samples (encircled on Figure 5.7b) have lower concentrations than the rest of the Paradox Formation, likely due to their shallow origin, H_2S exsolution and location adjacent to the Dolores River.



Supplementary Figure S5.3: Conceptual models for ^{4}He accumulation and loss within a geological formation for the vertical 1D ^{4}He diffusion models (a) and specifically within an evaporite formation (b). ^{4}He diffusion models (Figure 5.9) suggest diffusion into an evaporite formation is limited to the first 50m and there is only limited diffusion out of an evaporite in comparison to other formations.

S5.2 Supplementary tables

Sample Name	Latitude	Longitude	Type	Period	Formation	Depth (m)	Field	Well type
Groundwater samples								
BOR well 2E	38.3263	-108.86042	GW	Pennsylvanian	Salt Diapir, Paradox	14	Paradox Valley	Brine pumping well
BOR well 3E	38.32697	-108.85925	GW	Pennsylvanian	Salt Diapir Paradox	14	Paradox Valley	Brine pumping well
BOR well 8E	38.34356	-108.85565	GW	Pennsylvanian	Salt Diapir Paradox	14	Paradox Valley	Brine pumping well
BOR well 9E	38.34318	-108.8567	GW	Pennsylvanian	Salt Diapir Paradox	14	Paradox Valley	Brine pumping well
PW-4	38.15272	-109.14219	GW	Cretaceous	Burro Canyon Aquifer	145	Lisbon Valley	Groundwater monitoring
PW-3	38.14729	-109.13584	GW	Cretaceous	Burro Canyon Aquifer	130	Lisbon Valley	Groundwater monitoring
PW-12	38.1246	-109.12093	GW	Cretaceous	Burro Canyon Aquifer	305	Lisbon Valley	Groundwater monitoring
PW-8	38.14783	-109.13448	GW	Jurassic	Navajo Aquifer	472	Lisbon Valley	Groundwater monitoring
PW-11	38.12621	-109.10073	GW	Jurassic	Navajo Aquifer	457	Lisbon Valley	Groundwater monitoring
PW-7	38.12497	-109.11137	GW	Jurassic	Navajo Aquifer	457	Lisbon Valley	Groundwater monitoring (screened into Morison Fm.)
STCEC	37.28583	-109.515	GW	Jurassic	Navajo Aquifer	183	Bluff	Drinking water
BWC-1	37.28583	-109.5425	GW	Jurassic	Navajo Aquifer	177	Bluff	Drinking water
BWC-2	37.28472	-109.5389	GW	Jurassic	Navajo Aquifer	177	Bluff	Drinking water
BWC-3	37.28472	-109.5342	GW	Jurassic	Navajo Aquifer	177	Bluff	Drinking water
TRTP	37.28722	-109.5478	GW	Jurassic	Navajo Aquifer	251	Bluff	Groundwater monitoring
Cane Creek	38.58033	-109.73555	GW	Pennsylvanian	Cane Creek Mbr, Paradox	2270	NW of Moab	Lithium exploratory (active)

Supplementary Table S5.1: Sample location, formation and type. GW= groundwater. CG= casing gas, PF= produced fluid

Sample Name	Latitude	Longitude	Type	Period	Formation	Depth (m)	Field	Well type
Hydrocarbon samples								
AM-75	38.03914	-108.63336	CG	Permian	Cutler	2558	Andys Mesa	Gas (plugged)
AM-62	38.03054	-108.2685	CG	Permian	Cutler	2607	Andys Mesa	Gas (plugged)
AM-11-E34	38.03054	-108.2685	CG	Permian	Cutler-Honaker Trail	2632	Andys Mesa	Gas (plugged)
MM 31-42	38.23187	-109.2099	CG	Pennsylvanian	Honaker Trail	1613	Middle Mesa	Gas + Condensate (active)
BI 24-31	38.16899	-109.134	CG	Pennsylvanian	Honaker Trail	947	Big Indian South	Gas + Condensate (active)
BH 10-31	38.19219	-109.17191	CG	Pennsylvanian	Honaker Trail	1247	Big Indian South	Gas + Condensate (active)
HC 31-31	38.1081	-108.46143	CG	Pennsylvanian	Honaker Trail	2682	Hamilton Creek	Gas (active)
FF-2-19	38.06586	-108.67162	CG	Pennsylvanian	Honaker Trail	2632	Double Eagle	Gas (plugged)
Tohonalda 35-B	37.18559	-109.57544	CG	Pennsylvanian	Desert Creek Mbr, Paradox	1830	Greater Aneth Field	Oil (active)
Tohonalda 1	37.17495	-109.57433	CG	Pennsylvanian	Desert Creek Mbr, Paradox	1932	Greater Aneth Field	Oil (active)
Anasazi 1	37.16669	-109.31075	CG	Pennsylvanian	Desert Creek Mbr, Paradox	1762	Greater Aneth Field	Oil (active)
Sahgzie 1	37.16963	-109.30639	CG	Pennsylvanian	Desert Creek Mbr, Paradox	1954	Greater Aneth Field	Oil (active)
Monument-8N-2	37.31628	-109.19794	CG	Pennsylvanian	Desert Creek Mbr, Paradox	1895	Greater Aneth Field	Oil (active)

Supplementary Table S5.1: continued.

Sample Name	Latitude	Longitude	Type	Period	Formation	Depth (m)	Field	Well type
Hydrocarbon samples								
WM 22-43	37.19517	-109.27129	CG	Pennsylvanian	Desert Creek Mbr, Paradox	1722	Greater Aneth Field	Oil (active, waterflooded)
WM 34-31	37.18485	-109.26808	CG	Pennsylvanian	Desert Creek Mbr, Paradox	1722	Greater Aneth Field	Oil (active, waterflooded)
WM 34-33	37.17855	-109.26788	CG	Pennsylvanian	Desert Creek Mbr, Paradox	1722	Greater Aneth Field	Oil (active, waterflooded)
McIntyre 17-21	38.07719	-108.99125	PF	Mississippian	Leadville	2615	Lisbon Southeast	Gas with condensate (active)
Lisbon D8-10	38.19017	-109.26868	CG	Mississippian-Devonian	Leadville McCracken	2438	Lisbon	Gas (active)
Lisbon 10-33	38.1915	-109.27369	CG	Devonian	McCracken	2364	Lisbon	Gas with condensate (active)
Lisbon B8-10	38.19008	-109.27585	CG	Devonian	McCracken	2595	Lisbon	Gas with condensate (active)

Supplementary Table S5.1: continued.

Reservoir (Field)	Temperature ºC	Salinity M	WOR	GWR
Cane Creek	60	6.07		
Andys Mesa	70	2.16		13300
Middle Mesa	40	1.97		2550
Big Indian South	30	1.97		10800
Hamilton Creek	70	1.97		21200
Double Eagle	70	1.97		21200
Greater Aneth Field	50	1.84	7.81	
Lisbon Southeast	65	2.30		14500
Lisbon	65	2.30		18100

Supplementary Table S5.2: Reservoir conditions for the different hydrocarbon and deep brine fields sampled. Salinity data is from Kim et al. (2021). Temperature, water to oil ratio and gas to water ratios are calculated using the integrated average of all the wells from the production data (DNR, 2020; COGIS, 2020).

Sample	$[^4He]_{gw}$ x10^{-6} (cm^3(STP)/g_{water})					
	$^4He/^{20}Ne$ (measured)	±	$^4He/^{20}Ne$ (SC)	±	$^4He/^{36}Ar$ (SC)	±
Gas Fields						
AM-75	130	7	130	7	98.4	3.6
AM-62	375	19	375	19	246	9
AM-11-E34	2460	126	2460	126	1720	63
MM 31-42	16200	1200	16100	1200	8950	780
BI 24-31	2390	170	2370	170	11600	900
BH 10-31	95.6	4.9	94.9	2.8	70.7	2.6
HC 31-31	265	14	263	14	151	5
FF-2-19	5140	260	5100	260	3350	120
FF-2-19 (dup)	4500	220	4470	220	3020	130
McIntyre 17-21	78800	6800	78800	6800	15800	1400
Lisbon D8-10					74900	6400
Lisbon 10-33	171000	9000	171000	9000	33200	1200
Lisbon 10-33 (dup)	170000	9000	170000	9000	34000	1400
Lisbon B8-10	130000	9000	130000	9000	43500	3500
Oil Fields						
Tohonalda 35-B	35100	1300	46700	1800		
Tohonalda 1	25100	1300	33400	1700	6670	260
Anasazi 1	25700	1300	34200	1800	5540	260
Sahgzie 1	25400	1300	33800	1700	5000	200
Monument-8N-2	17500	900	23300	1200	6040	250
WM 22-43	1270	60	1690	80	1170	65
WM 34-31	6640	340	8830	450	1150	40
WM 34-31 (dup)	5670	290	7540	390	1460	50
WM 34-33	4410	230	5860	300	967	36

Supplementary Table 5.3: Collected ^4He concentrations in the groundwater prior to hydrocarbon interaction using the three different methods described in the text (section 5.5.2.1). SC= solubility corrected

Formation	Age Ma	Total porosity	Effective porosity	[U] ppm	[Th] ppm
Ignacio	517	0.10	0.10	2.8	10.7
Lynch	507	0.10	0.10	2.8	10.7
Aneth	416	0.15	0.15	2.8	10.7
McCracken-Elbert	382	0.20	0.20	2.8	10.7
Ouray	372	0.05	0.05	2.8	10.7
Leadville	359	0.10	0.10	2.8	10.7
Molas	318	0.05	0.05	2.8	10.7
Pikerton Trail	316	0.05	0.05	2.8	10.7
Paradox (evaporite)	313	0.01	0.00001	0.35	1.35
Paradox (evaporite + shales+ carbonates)	313	0.01	0.00001	0.44	1.02
Honaker Trail	311	0.10	0.10	4.1	15.7
Cutler	299	0.10	0.10	1.64	3.93
Chinole-Monekopi	251	0.1	0.1	2.45	10.6
Navajo	197	0.30	0.30	2.8	10.7
Entrada	180	0.30	0.30	7.53	2.42
Morrison	155	0.05	0.05	22	4.06
Burro Canyon	146	0.13	0.13	0.57	1.60
Dakota	105	0.13	0.13	0.57	1.60
Mancos Shale	99	0.20	0.20	0.57	1.60

Supplementary Table S5.4: Parameters for in-situ ^{4}He production and vertical 1D ^{4}He diffusion models

S5.3. Supplementary information

S5.3.1. Sample analysis

Casing gas samples are connected to an ultra-high vacuum hydrocarbon extraction and purification line and expanded to a calibrated volume where the pressure is recorded on a baratron capacitance manometer. By recording the pressure and volume, the total number of moles in a sample and thus noble gas abundances can be determined. The samples are then expanded onto a Ti-sponge held at 950ºC, then cooled to room temperature to remove the reactive gases. The sample is then further purified by exposure to a SAES GP-50 getter at 250°C and a SAES NP-10 getter at room temperature. The gas pressure is monitored to ensure the sample has successfully been purified. A small aliquot of gas is transferred into a Hidden Analytical HAL-200 quadrupole mass spectrometer and is analysed to estimate purified noble gas concentrations prior to inlet to the automated preparatory system. On inlet to the automated system, the noble gases are sequentially trapped onto a stainless-steel trap held at ~15K (trapping Ar, Kr and Xe) and an activated charcoal trap held at ~10K (trapping He and Ne). He is then released by the gradual heating of the 10K trap to 34K, expanded and inlet into a Helix SFT Mass Spectrometer. The remaining He is removed and the trap heated to 90K in order to release Ne, which is inlet into a Thermo ARGUS VI. Once the Ne has been analysed, the preparatory system is pumped before the stainless-steel trap is heated to 200K and a small sub-aliquot of gas is taken and inlet into the Argus for Ar analysis. Kr and Xe are isolated from any remaining Ar in the preparatory system by three heating and cooling cycles (between 70K and 52K), before being inlet simultaneously into the Argus VI for analysis. The samples are analysed for both noble gas concentration and isotopes. Upon gas inlet to the mass spectrometers, they are measured by a combination of multi-collection and peak jumping.

Groundwater and produced fluids samples were initially connected to an offline extraction system. Samples are attached and inlet to an ultra-high vacuum line and the noble gases were cryogenically drawn across two capillaries to a stainless-steel trap at -196ºC. This method allows for the quantitative isolation of the noble gases while effectively removing all water, oil and less volatile hydrocarbons if present (Chapter 2; Tyne et al., 2019). Once extracted, the isolated gases are

transferred to the hydrocarbon extraction and purification system. Gases are initially expanded and quantitatively transferred across a capillary onto a Ti-sponge getter held at 950°C for 30 minutes. The remaining procedure and analytical protocols are the same as for a gas sample after its expansion to the hot Ti-sponge for clean-up (Chapter 2; Tyne et al., 2019). The quantitative transfer of all noble gases allows for noble gas abundances to be determined (Chapter 2; Tyne et al., 2019). Concentrations of noble gas within each phase of the produced fluid needs to be calculated following the methods in Chapter 2 (Tyne et al., 2019).

Automated internal air standards were run each night to monitor and account for any changes in machine sensitivity between analyses. Preparatory system blanks were run daily on the automated preparatory system in the same way as the internal air standard to ensure there is no significant contribution from residual or background gases. Additionally, procedural blanks, air and air-saturated water standards were run biweekly using the same procedures as for samples. A maximum blank contribution to samples of less than 3% is required for the key indicator isotopes (^{4}He, ^{20}Ne, ^{36}Ar, ^{40}Ar, ^{82}Kr, ^{84}Kr, ^{86}Kr, ^{130}Xe, ^{132}Xe, ^{136}Xe). ^{20}Ne signals were corrected for $^{40}Ar^{++}$ interference following Niedermann et al., 1993. $^{44}CO_2^{++}$ is also monitored during neon analysis, but levels are found to be insignificant compared to ^{22}Ne signals (<1%) in all cases.

S5.3.2. U and Th concentrations in the Paradox Formation

The concentration of U and Th within evaporate deposits is poorly constrained. The groundwater sample from the Cane Creek Member of the Paradox Formation is from a lithium exploration well. Li can help facilitate ^{3}He production within the crust and thus a higher ^{3}He /^{4}He is expected where Li concentrations are high. Measured Li concentrations in the cane creek brine were 110ppm (Kim et al., 2021), however, the measured helium isotopic ratio ($0.0045R_A$) is extremely radiogenic, which suggests that U and Th concentrations within the Paradox formation are very low. Using a 0.00001% porosity for the Paradox Formation (Beauheim and Roberts, 2002), we calculate U and Th concentrations to be 0.35 and 1.35 ppm respectively. We assume slightly higher U and Th concentrations (0.437 and 1.016 ppm respectively) in the Desert Creek Member as the samples are hydrocarbons likely from the carbonate and shale interbeds.

S5.3.3. Atmospheric Noble Gas (ANG) Fractionation

Fractionated $^{20}Ne/^{36}Ar$ (and $^{84}Kr/^{36}Ar$ and $^{130}Xe/^{36}Ar$) beyond the limit imposed by simple gas-water phase equilibrium have previously been observed in many different systems, including in natural CO_2 gas reservoirs on the Colorado Plateau and Rocky Mountain Provinces ($^{20}Ne/^{36}Ar$ between 0.061-3.076, Gilfillan et al., 2008), in the Indus Basin ($^{20}Ne/^{36}Ar$ up to 1.4, Battani et al., 2000) and in the Macuspana Basin ($^{20}Ne/^{36}Ar$ up to 4.9, Prinzhofer et al., 2000). Multiple mechanisms have been proposed that could result in this fractionation including oil interaction, non-equilibrium diffusion, multiple stages of exsolution and dissolution and partial redissolution (discussed below).

When groundwater comes into contact with an oil, the heavy noble gases will preferentially partition into the oil phase, resulting in an increase in the $^{20}Ne/^{36}Ar$ of groundwater (Bosch and Mazor, 1988). Oil involvement is thought to have been the cause of the elevated $^{20}Ne/^{36}Ar$ in the Indus Basin (Battani et al., 2000). In such a scenario, you would expect to see an increase in $^{20}Ne/^{36}Ar$ with decreasing ^{36}Ar concentrations, however no such relationship is observed within the Paradox Basin data.

Mass dependent fractionation of both elemental and isotopic compositions of Ne and Ar can occur when there is incomplete emptying and partial refilling of lithic grains and half spaces (similar to Pinti et al., 1999). This non-equilibrium diffusion would cause mass dependent fractionation in both $^{20}Ne/^{22}Ne$ and $^{38}Ar/^{36}Ar$, however within the Paradox samples there is no relationship between $^{20}Ne/^{22}Ne$ and $^{38}Ar/^{36}Ar$. In addition, where mass dependent fractionation in both $^{20}Ne/^{22}Ne$ and $^{38}Ar/^{36}Ar$ has been observed, the fractionation appears to be solubility controlled (Zhou et al., 2005) and thus we discount this fractionation mechanism for these reservoirs.

Multiple stages of complete exsolution solution, followed by complete dissolution in areas of changing gas-to-water ratios could increase the solubility fractionation limit (Zartman et al., 1961). Exsolution will result in an increase in $^{20}Ne/^{36}Ar$ ratio, if this gas is then redissolved into a larger volume of water (by a change in physical conditions) there will be a local increase to both the groundwater noble gas concentrations and the $^{20}Ne/^{36}Ar$ in the water. Subsequent gas phase formed will have a more elevated $^{20}Ne/^{36}Ar$ ratio. This mechanism requires fluctuating physical conditions

as well as a small gas-to-water ratio, and thus is unlikely to have caused the observed fractionation on the basin scale.

Partial redissolution involves the complete degassing of groundwater and subsequent partial-equilibration back into noble gas stripped groundwater and results in the fractionation of noble gases that is solubility driven. Partial redissolution has previously been observed at McElmo Dome and across the Colorado Plateau (Gilfillan et al., 2008) and can account for the fractionation observed within the Paradox Basin (Figure 5.7c,d; Section 5.3.2).

The brine sample collected from the Cane Creek Member of the Paradox Formation has similar $^{84}Kr/^{36}Ar$ and $^{130}Xe/^{36}Ar$ values to ASW, however the $^{20}Ne/^{36}Ar$ is elevated (0.31). As only one sample was collected from this formation, no robust model can be developed, however it seems likely that there has been interaction between the brine and another phase and therefore, the initial ^{4}He concentration in the brine prior can be calculated using equation 5.3 and is 1 order of magnitude greater than measured (3.69 x10^{-3} cm^3/g_{water} compared to 2.13 x10^{-4} cm^3/g_{water}).

S5.3.4. Vertical 1D ^{4}He diffusion model

S5.3.4.1. Vertical 1D helium diffusion reference models

Vertical 1D ^{4}He diffusion models were constructed following methods described in Cheng, 2020 and Cheng et al., 2021. In the model we assume that each formation is deposited at the beginning of the formation age and has a ^{4}He concentration of ASW (3.04 x10^{-8} cm^3/cm^3). Once deposited, in-situ production (calculated using Eq. S5.1; Torgersen, 1980) and a flux from depth is initiated. Scenarios were modelled both with and without a ^{4}He basement flux.

$$[{}^{4}He]_{in-situ} = \frac{\rho J({}^{4}He)\Lambda}{\varphi} t \quad \text{(Eq. S5.1)}$$

Where ρ is the rock density (g/cm^3), t is the groundwater residence time and φ is the porosity. Λ is a parameter defining the efficiency of transfer from mineral to groundwater, this is thought to be ~1 over geological time (Ballentine and Burnard, 2002). $J(^{4}He)$ is the in-situ production of ^{4}He (cm^3(STP)/g) and is a function of the U and Th concentrations (ppm) of the rock (Craig and Lupton, 1976):

$$J(^4He) = 0.2355 \times 10^{-12}[U](1 + 0.123\left(\frac{[Th]}{[U]} - 4\right)) \text{ (Eq. S5.2)}$$

The surface was assumed to be equilibrated with air and thus have an ASW composition allowing for diffusive loss of ^{4}He at the surface. Assuming the maximum diffusive flux (J_d) for ^{4}He can be described as in Eq. S5.3, where diffusion through the unit is a function of time and distance (Eq. S5.4; Cheng, 2020).

$$J_d = -D_e \frac{\partial C}{\partial Z} \text{ (Eq. S5.3)}$$

$$\varphi \frac{\partial C}{\partial t} + q \frac{\partial C}{\partial Z} = De \frac{\partial^2 C}{\partial Z^2} + \varphi p \text{ (Eq. S5.4)}$$

where C is the concentration, Z is distance, t is time, φ is rock porosity and p is the production rate per volume (in-situ production). D_e is the effective diffusion coefficient. q is average linear porosity, which is 0, as it is assumed there is no advection. The D_e of ^{4}He in pure water ($D_{e\,He}^{H_20}$) is a function of temperature (T, in K) (Eq. S5.5; Ohsumi and Horibe, 1984). A thermal gradient of 30K/km is assumed within the Paradox Basin and the temperature throughout the units that is updated on deposition of younger formation.

$$D_{e\,He}^{H_20} = 0.02309e^{\frac{-1706}{T}} \text{ (Eq. S5.5)}$$

Diffusion within a porous media, as opposed to pure water, will be retarded by both physical and chemical constraints (e.g., grain surface, pore geometry and connectivity). This retardation can be described using a power law model derived by Boving and Grathwohl, 2001:

$$D_e = \varphi^{2.2} D_{e\,He}^{H_20} \text{ (Eq. S5.6)}$$

Within a tight formation D_e is thought to be larger than described in Eq. S5.6 (Peng et al., 2012). Therefore, within the Paradox Formation, an effective porosity is used instead of the rock porosity (Shackelford and Moore, 2013).

^{4}He concentrations within the pore spaces of a unit are calculated iteratively with time. A basement flux is added into the deepest formation (in the reference model this is set to 0), the flux into

subsequently deposited formations is a function of the ^{4}He concentration in the pore waters directly below. Additionally, the deposition of younger formations at the surface will cause the compaction of underlying formations and a decrease in their porosity, which will increase with time. This decrease in porosity is modelled as a series of steps that occur on the deposition of younger formations. It is assumed that pore water will be laterally displaced and thus it will not affect the dissolved ^{4}He concentrations in the pore spaces. We assume the porosity in the Paradox Formation is not reduced through time due to the nature of a salt layer.

S5.3.4.2. Modelling of lateral flushing

In the model, during lateral flushing there is no build up or diffusion of He within the layer affected, however, helium loss from the adjacent units can occur. Once 'flushing' has terminated, ^{4}He concentrations in the unit are that in ASW and the groundwater can start accumulating ^{4}He again. We assume that lateral active flow was initiated ~6Ma during the last stage of the denudation to the Colorado plateau which created higher topographic gradients and could have initiated groundwater circulation (Gutiérrez, 2004; Kim et al., 2021). The Burro Canyon and Navajo aquifers are shallow groundwater aquifers that are being actively recharged (Noyes, 2019; Kim et al., 2021). Radiocarbon groundwater residence times from the Navajo Aquifer are between 19,013 and 36,487 years and 3,256-10,789 years for in the Burro Canyon Aquifer (Noyes, 2019)). Flushing was modelled to end at the average residence time (~5ka and ~25ka respectively). We assume that flushing ceased in the Cutler and Honaker Trail formations at the measured ^{81}Kr residence time ~0.9Ma and ~0.8Ma for the formations below the Paradox Formation (Kim et al., 2020).

S5.3.4.3. Elevated ^{4}He concentrations below the Paradox Formation

Assuming there is complete lateral flushing below the Paradox Formation from 6Ma-0.8Ma, a basement flux of 23-105 $x10^{-6}$ mol $^{4}He/m^{2}/yr$ is required. This is significantly higher than the crustal average and similar to that in some volcanic settings (Torgersen and Clarke 1985; Torgersen, 2010). The emplacement of an igneous intrusion can invoke an increase in regional heat flow and can result in a greater volatile flux from the basement (Ballentine and Burnard, 2002; Mörner and Etiope, 2002). The samples taken from the Lisbon Field, have the highest required basement fluxes

(105 x10^{-6} mol $^{4}He/m^2/yr$)and are only 15km from the La Sal Mountains, the sample from the Lisbon Southeast field is ~40km from the La Sal mountains has the lower flux (23 x10^{-6} mol $^{4}He/m^2/yr$). Average Cenozoic heat flows in the sampled areas (~60-80 mW/m^2) are greater than the regional baseflow (40-50 mW/m^2 (Blackwell and Richards, 2004; Craddock et al., 2017). However, the heat flow is higher in the Lisbon Southeast Field where the predicted ^{4}He basement fluxes is lower (Blackwell and Richards, 2004; Craddock et al., 2017). In addition, the intrusion of the La Sal Mountains occurred approximately 20-31 Ma (Nelson et al., 1992; Rønnevik et al., 2017). Given that we envisage groundwater to be 0.8Ma (based on ^{81}Kr; Kim et al., 2020) it is unlikely that any associated ^{4}He pulse from this volcanism, on the magnitude of that predicted, would be observed in the present day system (Getz, 2020).

Alternatively, recent studies have suggested that the crustal production of ^{81}Kr could be higher in certain environments than previously considered (Purtschert et al., 2021). If this is the case within the Leadville and McCracken formations, it is possible that the ^{81}Kr residence time has been underestimated, and thus the flux overestimated.

It is also important to note here, that the model and subsequent flux estimates assume that the reservoir has been completely flushed through. Inverse mixing models of the formation waters beneath the Paradox Formation suggest that is a mix of paleoevaporated seawater and meteoric water (Kim et al., 2021). As the system was only partially flushed, some older water containing high ^{4}He concentrations could remain trapped in pore spaces and the younger ^{4}He poor water and older ^{4}He rich waters could have mixed. The proportion of old water that remains throughout lateral flushing will control the ^{4}He concentration in the water and the size of the basement flux needed to accumulate sufficient ^{4}He to match the measured concentrations. A larger portioning of trapped ^{4}He will result in a smaller required basement flux. It is noteworthy to mention, that none of these mechanisms are mutually exclusive.

Acknowledgements

This work was supported by a Natural Environment Research Council studentship to R.L.Tyne (Grant ref. NE/L002612/1) and the W.M. Keck Foundation. The authors would like to acknowledge the U.S. Bureau of Reclamation, Paradox Resources, Navajo Petroleum, US Oil and Gas INC, Anson Resources, Lantz Indergard (Lisbon Valley Mining Co.), Ambria Dell'Oro and Mohammad Marza for help with sampling. We also thank David J. Byrne and Rūta Karolytė for their helpful comments on an earlier version of the manuscript.

Authorship Statement

I hereby give permission to Rebecca L Tyne to use our joint work as contribution towards her DPhil thesis to be submitted for examination at the University of Oxford.

I confirm that to the best of my knowledge, the author contribution statement below is accurate and Rebecca L Tyne's contribution towards the work is greater than that of any other co-author.

Chapter author contribution statement:

The project was conceived by RLT, PHB, JCM and CJB. RLT managed the project and prepared the first draft of the manuscript. Noble gas analysis was performed by RLT with the support of DJH. RLT, JHK and JCM collected the samples. Noble gas modelling was developed by RLT, PHB, AC and CJB. All authors commented on an earlier version of the manuscript.

Chris J. Ballentine



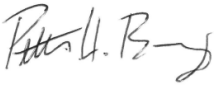
Date: 13/04/21

Jennifer C. McIntosh



Date: 16 April 21

Peter H. Barry



Date: 6/04/21

Ji-Hyun Kim

Date

Anran Cheng



Date 16/4/2021

Darren J. Hillegonds



References

Amec Foster Wheeler Environment & Infrastructure a division of Amec Foster Wheeler Americas Limited (2017) *Paradox Valley unit salinity control investigations study 1- hydrogen sulfide management.* Final Report. Project Number: 1655500023.0001.0004

Baars D. L. and Stevenson G. M. (1982) Subtle Stratigraphic Traps in Paleozoic Rocks of Paradox Basin. In: *The Deliberate search for the subtle trap*. AAPG Special Volume. (Ed. Halbouty, M.T.) 131–158.

Baars D. L. (1996) Pre-Pennsylvanian Paleotectonics—Key to Basin Evolution and Petroleum Occurrences in Paradox Basin, Utah and Colorado. *AAPG Bulletin* **50**.

Ballentine C. J., Burgess R. and Marty B. (2002) Tracing fluid origin, transport and interaction in the crust. In: *Noble Gases in Geochemistry and Cosmochemistry.*(Eds: D. Porcelli, C.J. Ballentine,, R. Wieler) Reviews in Mineralogy and Geochemistry **47**. Geochemical Society, Mineralogical Society of America, Chapter 13, 539–614.

Ballentine C. J. and Burnard P. G. (2002) Production, Release and Transport of Noble Gases in the Continental Crust. In: *Noble Gases in Geochemistry and Cosmochemistry.*(Eds: D. Porcelli, C.J. Ballentine,, R. Wieler) Reviews in Mineralogy and Geochemistry **47**. Geochemical Society, Mineralogical Society of America, Chapter 12, 481–538.

Ballentine C. J., O'Nions R. K. and Coleman M. L. (1996) A Magnus opus: Helium, neon, and argon isotopes in a North Sea oilfield. *Geochimica et Cosmochimica Acta* **60**, 831–849.

Ballentine C. J., O'Nions R. K., Oxburgh E. R., Horvath F. and Deak J. (1991) Rare gas constraints on hydrocarbon accumulation, crustal degassing and groundwater flow in the Pannonian Basin. *Earth and Planetary Science Letters* **105**, 229–246.

Barbeau D. L. (2003) A flexural model for the Paradox Basin: implications for the tectonics of the Ancestral Rocky Mountains: A flexural model for the Paradox Basin. *Basin Research* **15**, 97–115.

Barry P.H., Kulongoski J. T., Tyne R. L., Landon M. K., Gillespie J. M., Stephens M. J., Hillegonds D. J., Byrne D. J. and Ballentine C. J. (2018) Tracing enhanced oil recovery signatures in casing gases from the Lost Hills oil field using noble gases. *Earth and Planetary Science Letters* **496**, 57–67.

Barry P. H., Lawson M., Meurer W. P., Cheng A. and Ballentine C. J. (2018) Noble Gases in Deepwater Oils of the U.S. Gulf of Mexico. *Geochemistry, Geophysics, Geosystems* **19**, 4218–4235.

Barry P. H., Lawson M., Meurer W. P., Danabalan D., Byrne D. J., Mabry J. C. and Ballentine C. J. (2017) Determining fluid migration and isolation times in multiphase crustal domains using noble gases. *Geology* **45**, 775–778.

Barry P. H., Lawson M., Meurer W. P., Warr O., Mabry J. C., Byrne D. J. and Ballentine C. J. (2016) Noble gases solubility models of hydrocarbon charge mechanism in the Sleipner Vest gas field. *Geochimica et Cosmochimica Acta* **194**, 291–309.

Barton M. D., Barton I. F. and Thorson J. P. (2018) Paleofluid Flow in the Paradox Basin: Introduction. In: *Guidebook series* SEG. SEG. pp 12.

Battani A., Sarda P. and Prinzhofer A. (2000) Basin scale natural gas source, migration and trapping traced by noble gases and major elements: the Pakistan Indus basin. *Earth and Planetary Science Letters* **181**, 229–249.

Beitler, B., Chan, M.A., Parry, W.T. (2003) Bleaching of Jurassic Navajo Sandstone on Colorado Plateau Laramide highs: Evidence of exhumed hydrocarbon supergiants? *Geology* **31**(12) 1041-1044

Beitler, B., Parry, W.T., Chan, M.A., (2005) Fingerprints of Fluid Flow: Chemical Diagenetic History of the Jurassic Navajo Sandstone, Southern Utah, U.S.A. *Journal of Sedimentary Research* **75**(4) 547-561

Blackwell D. D. and Richards M. (2004) Geothermal map of North America. Geological Society of America.

Bosch A. and Mazor E. (1988) Natural gas association with water and oil as depicted by atmospheric noble gases: case studies from the southeastern Mediterranean Coastal Plain. *Earth and Planetary Science Letters* **87**, 338–346.

Boving T. B. and Grathwohl P. (2001) Tracer diffusion coefficients in sedimentary rocks: correlation to porosity and hydraulic conductivity. *Journal of Contaminant Hydrology* **53**, 85–100.

Breit G. N. and Meunier J.-D. (1990) Fluid inclusion, $\delta^{18}O$, and $^{87}Sr/^{86}Sr$ evidence for the origin of fault-controlled copper mineralization, Lisbon Valley, Utah, and Slick Rock District, Colorado. *Economic Geology* **85**, 884–891.

Byrne D. J., Barry P. H., Lawson M. and Ballentine C. J. (2018) Determining gas expulsion vs retention during hydrocarbon generation in the Eagle Ford Shale using noble gases. *Geochimica et Cosmochimica Acta* **241**, 240–254.

Byrne D. J., Barry P. H., Lawson M. and Ballentine C. J. (2020) The use of noble gas isotopes to constrain subsurface fluid flow and hydrocarbon migration in the East Texas Basin. *Geochimica et Cosmochimica Acta* **268**, 186–208.

Cater F. W. (1970) Geology of the Salt Anticline Region in Southwestern Colorado. US *Geological survey professional paper* 637, Washington DC.

Chan M. A., Parry W. T. and Bowman J. R. (2000) Diagenetic Hematite and Manganese Oxides and Fault-Related Fluid Flow in Jurassic Sandstones, Southeastern Utah. *AAPG Bulletin* **84**, 1281–1310.

Cheng, (2020). Noble Gas Sources, Transport and Groundwater Interaction in Sedimentary Basins. DPhil Thesis. University of Oxford.

Cheng A., Sherwood Lollar B., Warr O., Ferguson G., Idiz E., Mundle S.O.C., Barry P. H., Byrne D., Mabry J. and Ballentine C. J. (2021) Determining the role of diffusion and basement flux in controlling ^{4}He distribution in sedimentary basin fluids. *Earth and Planetary Science Letters.* **In review**

COGIS (2020). Production Data. Colorado oil and gas conservation commission. Department of Natural Resources. Available at: https://cogcc.state.co.us/data.html#/cogis. [Accessed November 2020]

Condon S. M. (1997) *Geology of the Pennsylvanian and Permian Cutler Group and Permian Kaibab Limestone in the Paradox Basin, southeastern Utah and southwestern Colorado*., Available at: http://pubs.er.usgs.gov/publication/b00P [Accessed November 10, 2020].

Craddock W. H., Blondes M. S., DeVera C. A. and Hunt A. G. (2017) Mantle and crustal gases of the Colorado Plateau: Geochemistry, sources, and migration pathways. *Geochimica et Cosmochimica Acta* **213**, 346–374.

Craig H. and Lupton J. E. (1976) Primordial neon, helium, and hydrogen in oceanic basalts. *Earth and Planetary Science Letters* **31**, 369–385.

Crossey L. J., Fischer T. P., Patchett P. J., Karlstrom K. E., Hilton D. R., Newell D. L., Huntoon P., Reynolds A. C. and de Leeuw G. A. M. (2006) Dissected hydrologic system at the Grand Canyon: Interaction between deeply derived fluids and plateau aquifer waters in modern springs and travertine. *Geology* **34**, 25–28.

Crovetto R., Fernández-Prini R. and Japas M. L. (1982) Solubilities of inert gases and methane in H_2O and in D_2O in the temperature range of 300 to 600 K. *Journal of Chemical Physics* **76**, 1077–1086.

Day, J.M., Barry, P.H., Hilton, D.R., Burgess, R., Pearson, D.G. and Taylor, L.A. (2015). The helium flux from the continents and ubiquity of low-$^{3}He/^{4}He$ recycled crust and lithosphere. *Geochimica et Cosmochimica Acta*, **153**, 116-133.

Dockrill, B., Shipton, Z.K. (2010) Structural controls on leakage from a natural CO_2 geologic storage site: Central Utah, U.S.A. *Journal of Structural Geology* **32**(11) 1768-1782.

DNR (2020). Production Data. Utah Division of oil, gas and mining. Department of Natural Resources. Available at: https://oilgas.ogm.utah.gov/oilgasweb/live-data-search/lds-prod/prod-lu.xhtml . [Accessed November 2020]

Ekren E. B. and Houser F. N. (1965) *Geology and Petrology of the Ute Mountains Area Colorado*., US Geological Survery Professional Paper 481Washington DC.

Fernández-Prini R., Alvarez J. L. and Harvey A. H. (2003) Henry's Constants and Vapor–Liquid Distribution Constants for Gaseous Solutes in H_2O and D_2O at High Temperatures. *Journal of Physical and Chemical Reference Data* **32**, 903–916.

Getz C. M. (2020) Igneous-related hydrothermal systems in a saline basinal setting: La Sal Mountains, Paradox Basin, Utah. Masters Thesis, University of Arizona.

Gilfillan S. M. V., Ballentine C. J., Holland G., Blagburn D., Lollar B. S., Stevens S., Schoell M. and Cassidy M. (2008) The noble gas geochemistry of natural CO_2 gas reservoirs from the Colorado Plateau and Rocky Mountain provinces, USA. *Geochimica et Cosmochimica Acta* **72**, 1174–1198.

Graham D. W. (2002) Noble Gas Isotope Geochemistry of Mid-Ocean Ridge and Ocean Island Basalts: Characterization of Mantle Source Reservoirs. In: *Noble Gases in Geochemistry and Cosmochemistry*.(Eds: D. Porcelli, C.J. Ballentine,, R. Wieler) Reviews in Mineralogy and Geochemistry **47**. Geochemical Society, Mineralogical Society of America, Chapter 8, 247–317.

Gutiérrez F. (2004) Origin of the salt valleys in the Canyonlands section of the Colorado Plateau: Evaporite-dissolution collapse versus tectonic subsidence. *Geomorphology* **57**, 423–435.

Hanshaw B. B. and Hill G. A. (1969) Geochemistry and hydrodynamics of the Paradox Basin region, Utah, Colorado and New Mexico. *Chemical Geology* **4**, 263–294.

Harr C. L. (1996) Paradox Oil and Gas Potential of the Ute Mountain Ute Indian Reservation: Phase II Geology/Seismic Study. *Geology and Resources of the Paradox Basin*, Utah Geological Association, 13–28.

Hilton, D.R. (1996) The helium and carbon isotope systematics of a continental geothermal system: results from monitoring studies at Long Valley caldera (California, USA). *Chemical Geology,* **127**

Hite R. J. and Buckner D. H. (1981) Stratigraphic Correlations, Facies Concepts, and Cyclicity in Pennsylvanian Rocks of the Paradox Basin. In: *Geology of the Paradox Basin.* Rocky Mountain Association of Geologists 1981 Field Conference

Hite R. J. and Lohman S. W. (1973) *Geologic appraisal of Paradox basin salt deposits for water emplacement*. U.S. Geological Survey Open File Report 73-114, Denver, CO.

Jähne B., Heinz G. and Dietrich W. (1987) Measurement of the diffusion coefficients of sparingly soluble gases in water. *Journal of Geophysical Research: Oceans* **92**, 10767–10776.

Karolytė R., Johnson G., Györe D., Serno S., Flude S., Stuart F. M., Chivas A. R., Boyce A. and Gilfillan S. M. V. (2019) Tracing the migration of mantle CO_2 in gas fields and mineral water springs in south-east Australia using noble gas and stable isotopes. *Geochimica et Cosmochimica Acta* **259**, 109–128.

Kendrick M. A., Honda M., Walshe J. and Petersen K. (2011) Fluid sources and the role of abiogenic-CH_4 in Archean gold mineralization: Constraints from noble gases and halogens. *Precambrian Research* **189**, 313–327.

Kennedy B. M., Hiyagon H. and Reynolds J. H. (1990) Crustal neon: a striking uniformity. *Earth and Planetary Science Letters* **98**, 277–286.

Kim J.-H., Bailey L., Noyes C., Tyne R. L., Ballentine C. J., Person M., Ma L., Barton M. D., Barton I. F., Reiners P., Ferguson G. and McIntosh J. C. (2021) Hydrogeochemical evolution of formation waters responsible for sandstone bleaching and ore mineralization in the Paradox Basin. *GSA Bulletin* **In review**.

Kim J.-H., Noyes C., Dell'Oro A., Tyne R. L., Ferguson G., Person M. A., Ma L., Lu Z.-T., Jiang W., Yang G.-M., Ballentine C. J., Reiners P. and McIntosh J. C. (2020) The hydrogeochemical evolution of basinal fluids in the Paradox Basin: implications for sources, flowpaths, and residence time. In *Goldschmidt Abstracts* Goldschmidt. Online.

King V. M., Block L. V., Yeck W. L., Wood C. K. and Derouin S. A. (2014) Geological structure of the Paradox Valley Region, Colorado, and relationship to seismicity induced by deep well injection. *Journal of Geophysical Research Solid Earth* **119**, 4955–4978.

Kipfer R., Aeschbach-Hertig W., Peeters F. and Stute M. (2002) Noble gases in Lakes and Groundwaters. In: *Noble Gases in Geochemistry and Cosmochemistry*.(Eds: D. Porcelli, C.J. Ballentine,, R. Wieler) Reviews in Mineralogy and Geochemistry **47**. Geochemical Society, Mineralogical Society of America, Chapter 14, 615–700.

Kluth C. F. and DuChene H. R. (2009) Late Pennsylvanian and Early Permian Structural Geology and Tectonic History of the Paradox Basin and Uncompahgre Uplift, Colorado and Utah. T*he Paradox Basin Revisited – New Developments in Petroleum Systems and Basin Analysis*, Rocky Mountain Association of Geologists, 178–197.

Lawton T. F., Buller C. D. and Parr T. R. (2015) Provenance of a Permian erg on the western margin of Pangea: Depositional system of the Kungurian (late Leonardian) Castle Valley and White Rim sandstones and subjacent Cutler Group, Paradox Basin, Utah, USA. *Geosphere* **11**, 1475–1506.

Lee J.-Y., Marti K., Severinghaus J. P., Kawamura K., Yoo H.-S., Lee J. B. and Kim J. S. (2006) A redetermination of the isotopic abundances of atmospheric Ar. *Geochimica et Cosmochimica Acta* **70**, 4507–4512.

Lippmann-Pipke J., Sherwood Lollar B., Niedermann S., Stroncik N. A., Naumann R., van Heerden E. and Onstott T. C. (2011) Neon identifies two billion year old fluid component in Kaapvaal Craton. *Chemical Geology* **283**, 287–296.

Loope D. B., Kettler R. M. and Weber K. A. (2010) Follow the water: Connecting a CO_2 reservoir and bleached sandstone to iron-rich concretions in the Navajo Sandstone of south-central Utah, USA. *Geology* **38**, 999–1002.

Mackintosh, S., Ballentine, C.J. (2012) Using $^{3}He/^{4}He$ isotope ratios to identify the source of deep reservoir contributions to shallow fluids and soil gas. *Chemical Geology* **304-305**, 142-150

Marrocchi Y., Razafitianamaharavo A., Michot L. J. and Marty B. (2005) Low-pressure adsorption of Ar, Kr, and Xe on carbonaceous materials (kerogen and carbon blacks), ferrihydrite, and montmorillonite: Implications for the trapping of noble gases onto meteoritic matter. *Geochimica et Cosmochimica Acta* **69**, 2419–2430.

Molenaar C. M. (1981) Mesozoic Stratigraphy of the Paradox Basin - An Overview. In: *Geology of the Paradox Basin.* Rocky Mountain Association of Geologists 1981 Field Conference

Mörner N.-A. and Etiope G. (2002) Carbon degassing from the lithosphere. *Global and Planetary Change* **33**, 185–203.

Morrison S. J. and Parry W. T. (1986) Formation of carbonate-sulfate veins associated with copper ore deposits from saline basin brines, Lisbon Valley, Utah; fluid inclusion and isotopic evidence. *Economic Geology* **81**, 1853–1866.

Nelson S. T., Davidson J. P. and Sullivan K. R. (1992) New age determinations of central Colorado Plateau laccoliths, Utah: Recognizing disturbed K-Ar systematics and re-evaluating tectonomagmatic relationships. *GSA Bulletin* **104**, 1547–1560.

Noyes C. (2019) Geochemical and Isotopic Assessment of Regional Groundwater Flow and Aquifer Connectivity in the Lisbon Valley. Masters Thesis, University of Arizona.

Nuccio V. F. and Condon S. M. (1996) Burial and Thermal History of the Paradox Basin, Utah and Colorado, and Petroleum Potential of the Middle Pennsylvanian Paradox Formation. *Evolution of Sedimentary Basins- Paradox Basin*. USGS Bulletin 2000-O.

Ohsumi T. and Horibe Y. (1984) Diffusivity of He and Ar in deep-sea sediments. *Earth and Planetary Science Letters* **70**, 61–68.

Parry, W.T., Chan, M.A., Beitler, B. (2004) Chemical bleaching indicates episodes of fluid flow in deformation bands in sandstone. *AAPG Bulletin* **88**(2) 175-191

Peng S., Hu Q. and Hamamoto S. (2012) Diffusivity of rocks: Gas diffusion measurements and correlation to porosity and pore size distribution. *Water Resources Research* **48**.

Peterson R. and Turner-Peterson C. E. (1987) The Morrison Formation of the Colorado Plateau. In: *Recent advances in sedimentology, stratigraphy, and paleotectonics* 4. North American Paleontological Conference. Hunteria. 1–18.

Pinti D. L., Wada N. and Matsuda J.I. (1999) Neon excess in pumice: volcanological implications. *Journal of Volcanology and Geothermal Research* **88**, 279–289.

Podosek F. A., Bernatowicz T. J. and Kramer F. E. (1981) Adsorption of xenon and krypton on shales. *Geochimica et Cosmochimica Acta* **45**, 2401–2415.

Podosek F. A., Honda M. and Ozima M. (1980) Sedimentary noble gases. *Geochimica et Cosmochimica Acta* **44**, 1875–1884.

Porcelli D., Ballentine C. J. and Wieler R. (2002) An Overview of Noble Gas Geochemistry and Cosmochemistry.In: *Noble Gases in Geochemistry and Cosmochemistry.*(Eds: D. Porcelli,

C.J. Ballentine,, R. Wieler) Reviews in Mineralogy and Geochemistry **47**. Geochemical Society, Mineralogical Society of America, Chapter 1, 1-19

Prinzhofer, A. (2013). Noble gases in oil and gas accumulations. In: *The Noble Gases as Geochemical Tracers*. (Ed. P. Burnard). Advances in Isotope Geochemistry. Springer, Berlin, Heidelberg. 225–247

Prinzhofer A., Vega M. A. G., Battani A. and Escudero M. (2000) Gas geochemistry of the Macuspana Basin (Mexico): thermogenic accumulations in sediments impregnated by bacterial gas. *Marine and Petroleum Geology* **17**, 1029–1040.

Purtschert R., Yokochi R., Jiang W., Lu Z.-T., Mueller P., Zappala J., Van Heerden E., Cason E., Lau M., Kieft T. L., Gerber C., Brennwald M. S. and Onstott T. C. (2021) Underground production of ^{81}Kr detected in subsurface fluids. *Geochimica et Cosmochimica Acta* **295**, 65–79.

Read J. L. (1959) Geologic Case History of Slocum Dome, Anderson County, Texas. *AAPG Bulletin* **43**, 958–973.

Rønnevik C., Ksienzyk A. K., Fossen H. and Jacobs J. (2017) Thermal evolution and exhumation history of the Uncompahgre Plateau (northeastern Colorado Plateau), based on apatite fission track and (U-Th)-He thermochronology and zircon U-Pb dating. *Geosphere* **13**, 518–537.

Shawe D. R. (1968) Petrography of sedimentary rocks in the Slick Rock district, San Miguel and Dolores Counties, Colorado. US Geological Survey *Professional Paper* 576-B Washington DC.

Shackelford C. D. and Moore S. M. (2013) Fickian diffusion of radionuclides for engineered containment barriers: Diffusion coefficients, porosities, and complicating issues. *Engineering Geology* **152**, 133–147.

Sherwood Lollar B., O'Nions R. K. and Ballentine C. J. (1994) Helium and neon isotope systematics in carbon dioxide-rich and hydrocarbon-rich gas reservoirs. *Geochimica et Cosmochimica Acta* **58**, 5279–5290.

Smith S. P. and Kennedy B. M. (1983) The solubility of noble gases in water and in NaCl brine. *Geochimica et Cosmochimica Acta* **47**, 503–515.

Staudacher T. and Allègre C. J. (1988) Recycling of oceanic crust and sediments: the noble gas subduction barrier. *Earth and Planetary Science Letters* **89**, 173–183.

Torgersen T. (2010) Continental degassing flux of ^{4}He and its variability. *Geochemistry, Geophysics, Geosystems* **11**.

Torgersen T. (1980) Controls on pore-fluid concentration of ^{4}He and ^{222}Rn and the calculation of ^{4}He/^{222}Rn ages. *Journal of Geochemical Exploration* **13**, 57–75.

Torgersen T. (1989) Terrestrial helium degassing fluxes and the atmospheric helium budget: Implications with respect to the degassing processes of continental crust. *Chemical Geology: Isotope Geoscience section* **79**, 1–14.

Torgersen T. and Clarke W. B. (1985) Helium accumulation in groundwater, I: An evaluation of sources and the continental flux of crustal ^{4}He in the Great Artesian Basin, Australia. *Geochimica et Cosmochimica Acta* **49**, 1211–1218.

Torgersen T. and Kennedy B. M. (1999) Air-Xe enrichments in Elk Hills oil field gases: role of water in migration and storage. *Earth and Planetary Science Letters* **167**, 239–253.

Tripp B. (2010) Utah Potash: Resources, Production, and Exploration – Utah Geological Survey. Available at: https://geology.utah.gov/map-pub/survey-notes/utah-potash-resources-production-and-exploration/ [Accessed March 2021].

Trudgill B. D. (2011) Evolution of salt structures in the northern Paradox Basin: controls on evaporite deposition, salt wall growth and supra-salt stratigraphic architecture. *Basin Research* **23**, 208–238.

Turner C. E. and Fishman N. S. (1991) Jurassic Lake T'oo'dichi': A large alkaline, saline lake, Morrison Formation, eastern Colorado Plateau. *GSA Bulletin* **103**, 538–558.

Tyne R. L., Barry P. H., Hillegonds D. J., Hunt A. G., Kulongoski J. T., Stephens M. J., Byrne D. J. and Ballentine C. J. (2019) A Novel Method for the Extraction, Purification, and Characterization of Noble Gases in Produced Fluids. *Geochemistry, Geophysics, Geosystems* **20**, 5588–5597.

Tyne R. L., Barry P. H., Karolytė R., Byrne D. J., Kulongoski J. T., Hillegonds D. J. and Ballentine C. J. (2021) Investigating the effect of enhanced oil recovery on the noble gas signature of casing gases and produced waters from selected California oil fields. **In review.**

Wescott W. A. and Hood W. C. (1994) Hydrocarbon Generation and Migration Routes in the East Texas Basin1. *AAPG Bulletin* **78**, 287–306.

Wigley M., Kampman N., Dubacq B. and Bickle M. (2012) Fluid-mineral reactions and trace metal mobilization in an exhumed natural CO_2 reservoir, Green River, Utah. *Geology* **40**, 555–558.

Young, E.D., Galy, A., Nagahara, H. (2002) Kinetic and equilibrium mass-dependent isotope fractionation laws in nature and their geochemical and cosmochemical significance *Geochimica et Cosmochimica Acta* **66**(6) 1095-1104.

Zartman R. E., Wasserburg G. J. and Reynolds J. H. (1961) Helium, argon, and carbon in some natural gases. *Journal of Geophysical Research (1896-1977)* **66**, 277–306.

Zhou Z. and Ballentine C. J. (2006) ^{4}He dating of groundwater associated with hydrocarbon reservoirs. *Chemical Geology* **226**, 309–327.

Zhou Z., Ballentine C. J., Kipfer R., Schoell M. and Thibodeaux S. (2005) Noble gas tracing of groundwater/coalbed methane interaction in the San Juan Basin, USA. *Geochimica et Cosmochimica Acta* **69**, 5413–5428.

Chapter 6

Conclusions

Contents

6.1 Summary and impact 244
6.2 Outlook and future work 247
References 251

6.1. Summary and impact

Understanding the processes that control the behaviour of subsurface fluids is critical to many environmental issues. Noble gas, stable and clumped isotopes in crustal fluids have previously been used for investigating fluid provenance, migration and/or residence times (e.g., Bernard et al., 1976; Torgersen and Clarke, 1985; Whiticar et al., 1986; Bosch and Mazor, 1988; Zaikowski and Spangler, 1990; Ballentine et al., 1996; Wycherley et al., 1999; Zhou and Ballentine, 2006; Ballentine and Holland, 2008; Douglas et al., 2017; Stolper et al., 2018; Young, 2019). We adapt, develop and combine these approaches to further explore their utility in investigating different processes in complex crustal fluid systems with a specific focus on groundwater contamination and CO_2 storage. To do this, we exploit a number of case studies using different sample types to assess the processes controlling subsurface fluid behaviour. As part of this approach, we develop a method to analyse noble gases in a new sample medium (multi-phase fluids) and validate assumptions previously used in reservoir reconstructions from casing gases. In addition, this approach allows us to identify and investigate previously unrecognised processes.

In Chapter 2, we detail the development of a novel noble gas extraction system that is interfaced with a gas purification system and two mass spectrometers (Argus IV and Helix SFT). The ability to analyse multi-phase fluids is crucial, as it is not always practical or possible to collect single phase samples. However, multi-phase fluids are not amenable to standard high-vacuum noble gas purification procedures (e.g., Beyerle et al., 2000; Hunt, 2015; Barry et al., 2016). Therefore, we developed an offline noble gas extraction system which allows for the measurement of the noble gas abundance and isotopic composition in these multi-phase fluids. We find the reproducibility of air-saturated water samples through the newly developed system is within 2.9% for ^{4}He, 3.8% for ^{20}Ne, 4.5% for ^{36}Ar, 5.3% for ^{84}Kr and 5.7% for ^{132}Xe. We then test the system for produced fluid (oil-water-gas mixtures) samples, which represents the first time multi-phase oil-field fluids have been directly analysed for their noble gas composition. We calculate the concentration of noble gases in each phase and show that the concentration in the gas phase is orders of magnitude greater than in the oil and water phases.

We analyse casing gases and produced fluids from the same wells from two oil fields in California in order to compare noble gas concentrations in these distinct sample types for the first time (Chapter 3). Concentrations of noble gases were on average 3.0±1.8 times greater in the casing gases than the gas phase in the produced fluids, verifying previous methods of phase and reservoir reconstructions that rely on casing gas compositions. We hypothesise that variability between sample types is a result of differences in production practices, both between wells and between casing cases and produced fluids, which highlights the need to take these into account during subsurface analysis. This validation allows, for the first time, a direct comparison of the noble gas compositions in different fields, where only singular sample types are available, regardless of sample type.

Once the reservoir has been fully characterised, reservoir evolution can be modelled. Understanding endmembers is the critical first step when identifying the presence and source of fugitive gases within shallow aquifers. We compile an original dataset consisting of noble gas isotopes and abundance data from both casing gases and produced fluids in 4 different oil fields (Chapter 3). This allows us to directly assess the effects of enhanced oil recovery on the noble gas composition of a reservoir which is crucial for characterising the evolution of a reservoir throughout production. We make the novel observation that atmospheric-noble gas composition is strongly correlated to the injected volume within 500m of the sampled wells. This is most clearly supported by $^{20}Ne/^{36}Ar$ data (r^2= 0.88-0.98, *p*-value= 0.0030-0.0195), although the increase in $^{20}Ne/^{36}Ar$ per unit volume of injected material is field dependent. We employ a mixing model, to examine and quantify the reservoir evolution with enhanced oil recovery and ascertain that the injectate composition and relative volumes of oil and injectate involved are key in controlling the reservoir composition. This is important, as it allows us to predict the initial baseline noble gas composition of a reservoir and predict how it may evolve during hydrocarbon production.

In Chapter 4, we focus on the behaviour of CO_2 in CO_2 storage analogues, which is critical for understanding a reservoir's long-term storage potential. Depleted oil and gas fields have the second largest storage potential for CO_2, after deep saline aquifers (Stewart and Haszeldine, 2014; Leung

et al., 2014) and numerous hydrocarbon reservoirs have previously undergone CO_2 injection to enhance oil production. In this contribution, we use a novel multi-interdisciplinary approach, including noble gas, stable and clumped isotopes, and microbial analysis, to determine the subsurface behaviour of CO_2 in a CO_2 injected oil field (Olla) in Louisiana, USA. By integrating the information from these techniques, we identify microbial cycling of carbon between CO_2 and CH_4 within the field and demonstrate net CH_4 production. Our findings suggest that conservatively between 13-19% of the emplaced CO_2 has been consumed via microbial methanogenesis in the 29 years since injection. We are therefore able to calculate the minimum rate of methanogenesis (73-109 mmol CH_4/m^3(STP)/yr), which is the first time an *in-situ* rate determination has been possible for microbial methanogenesis. We suggest, based on evidence from other CO_2 injected hydrocarbon fields and in natural CO_2 fields, that microbial methanogenesis of CO_2 in such environments is a globally significant phenomenon. CH_4 is less soluble, less compressible and less reactive and a stronger greenhouse gas than CO_2. Therefore a reservoir's potential for CO_2-driven microbial methanogenesis needs to be carefully factored into future storage site selection and models to ensure low-risk long-term storage.

Critical to understanding crustal fluid behaviour is understanding the basin and reservoir architecture and how this impacts the fluid composition and connectivity within the subsurface (Chapter 5). The Paradox Basin is a flexural basin on the Colorado Plateau that is defined by the extent of the Paradox Formation (thick evaporate unit). We measure the full suite of noble gas isotopes from 7 different stratigraphic units including the Paradox Formation. Helium and neon isotope systematics are consistent with radiogenic overprinting of the groundwater derived noble gases. We observe an increase in radiogenic noble gases with stratigraphic age, and a significant difference either side of the Paradox Formation, which is most evident in the $^{40}Ar/^{36}Ar$ and $^{21}Ne/^{22}Ne$ ratios. Atmospheric noble gases both above and below the Paradox Formation show clear evidence of fractionation beyond simple water-gas solubility equilibrium limits. We show that this fractionation is consistent with exsolution and partial redissolution and identify fluid flow beneath the Paradox Formation in agreement with the major ion composition of brines (which suggest there

has been some dissolution of the Paradox Formation as a result of meteoric water flushing) and the relatively young ^{81}Kr residence times (0.8Ma) (Kim et al., 2020, 2021). Using models adapted from those of Gilfillan et al. (2008), we calculate a greater proportion of redissolution above the Paradox Formation than below, consistent with different fluid flow regimes either side of the Paradox Formation. Finally, vertical 1D ^{4}He diffusion models were built in order to provide insights into cross formational migration and the additional processes occurring within the Basin (Cheng, 2020; Cheng et al., 2021). We demonstrate that the Paradox Formation is acting as an impermeable barrier to fluid migration and communication within the basin, allowing for the evolution of two distinct noble gas compositions and hydrological regimes either side of the Paradox Formation. We verify that the stratigraphy ultimately controls the nature and extent of communication between different subsurface fluid reservoirs, and demonstrate the great potential that noble gases have in understanding this. These findings will be important not only for CO_2 storage and groundwater security but also for identifying ^{4}He and H_2 accumulations, developing sustainable hydrocarbon extraction and nuclear waste disposal protocols as well as for using ^{4}He to date crustal fluids.

6.2. Outlook and Future work

This work identified and investigated subsurface fluid processes and clearly demonstrated the utility of a multi-isotope approach. We build on data and methods in subsurface systems and extended their use in complex multi-phase crustal systems to address uncertainties surrounding groundwater contamination and CO_2 storage. We developed a new method that allows for the noble gas analysis of multi-phase fluids. In addition, we conducted case studies that demonstrate how a system responds to anthropogenic perturbations and investigated the migration of fluids within the subsurface. Results from this study and others (e.g., Gilfillan et al., 2009; Darrah et al., 2014; Barry et al., 2018; McIntosh et al., 2019; Whyte et al., 2021) will help reduce the uncertainties surrounding issues of environmental concern within the subsurface. However, more studies are needed to further explore their application, especially with the inclusion and integration of less widely used tracers, such as the clumped isotopes. Only by combining multiple studies can systematic patterns and processes be identified, this would then allow for these tracers to become more predictive. Several

potential avenues of future research are outlined below, grouped by method, tracer utility and application.

Methods- As part of this study, we developed an extraction system that allowed for the noble gas analysis of multi-phase fluid. However, in comparison to single phase samples, reproducibility is lower and uncertainties are higher. This method could be improved by developing a consistent ASW standard and by developing additional multi-phase standards (similar to sample type) to run alongside the ASW standards.

Utility of tracers- We demonstrated that noble gases in produced fluid and casing gases can be effectively used interchangeably, however some variability between sample types does exist. A larger data set of multi-phase and single-phase samples from the same wells will allow for any systematic offset and correction to be determined. Furthermore, an understanding of the subsurface composition and processes requires several assumptions regarding partitioning. Whilst there are a few studies that investigate the solubility of noble gases in different phases (gas-water, gas-brine, gas-oil), they are limited by their scope and their analytical capabilities (Smith and Kennedy, 1983; Kharaka and Specht, 1988; Fernández-Prini et al., 2003). Therefore, renewed efforts to constrain these parameters (such as that done for CO_2-water systems (Warr et al., 2015)) would expand the scope and increase precision of studies giving a much greater confidence in the assumptions and extrapolations used in this type of study (Byrne et al., 2018a).

Variable air-like Kr and Xe excesses above those predicted using the solubility coefficients is a common observation in many systems globally and is observed in all the case studies within this thesis (e.g., Torgersen and Kennedy, 1999; Zhou et al., 2005; Barry et al., 2018; Byrne et al., 2018b). Torgersen et al., (2004) previously attempted to investigate the cause of excess Kr and Xe, however given the advancement in analytical techniques which has allowed for many studies to now include Kr and Xe data, it is timely to reinvestigate these variable excesses.

Clumped isotopes are nascent tracers and Chapter 4 represents the first application of methane clumped isotopes to a carbon capture and storage scenario. As with any emerging field, more case studies and data are required in order to display their full utility.

In Chapter 5, we demonstrated how basin architecture controls fluid migration and connectivity, using vertical 1D ^{4}He diffusion models. These models required many assumptions about porosity and U and Th concentrations within the different formations. Many uncertainties still exist for these parameters especially low porosity units, such as those within evaporites and crystalline formations (Bethke, 1985; Sherwood Lollar et al., 2014). Further work is needed to constrain many of these parameters. Moreover, to fully understand fluid migration in these models, vertical advection and horizontal migration must also be considered.

Bayesian modelling represents a potentially powerful technique that has yet to be widely applied to crustal fluid geochemistry, as it allows for the inclusion of all types of uncertainty when interpreting a particular system. This includes analytical uncertainties and uncertainties associated with model assumptions. In addition, such an approach allows for prior system knowledge to be considered in the model. For example, Bayesian modelling using comparable datasets may allow for a better understanding of fluids within geological systems, as it allows for a rigorous comparison of competing alternative hypotheses and reasonable bounds can be inferred from our knowledge of reservoir geology (e.g., Karolytė et al., 2020).

Application of tracers- We investigated the composition and evolution of endmembers relating to hydrocarbon contamination of groundwater, and developed new methods that allow for the analysis of oil-field fluids including produced fluids, injectate and produced water disposal ponds (Chapters 2 and 3; McMahon et al., 2019). The logical next step is to use these endmembers to develop mixing models with shallow aquifers (e.g., Karolytė, et al., 2019) and combine these with other geochemical data. This would allow for the identification of contaminant sources. Where endmembers can be identified, these types of models could be reproduced in other environments, such as surrounding CO_2 storage sites.

In Chapter 4, we identified a previously unrecognised process of microbial conversion of injected CO_2 into methane within potential CO_2 storage sites. This discovery raises many questions and avenues of future research, particularly at the interplay between biological and geochemical

processes within the reservoirs, the rates at which this process can occur and how such processes can affect a systems storage potential.

Overall, this study demonstrated the potential of a multi-isotope tracer approach in understanding the processes occurring in complex crustal fluid systems, in particular those associated with CO_2 storage and groundwater contamination. In addition, we have developed a method which has enabled analysis of a new sample type for high precision analysis for all noble gas isotopes. We demonstrate that by integrating multiple noble gases, stable and clumped isotopes, subsurface processes can be identified with higher certainty. We expect multi-isotope gas tracing to be an important tool in identifying and understanding subsurface processes related to environmental issues, exploration of H_2 and ^4He, sustainable hydrocarbon production and the development of nuclear waste disposal protocols. We hope that this study assists in this effort.

References

Ballentine C. J. and Holland G. (2008) What CO_2 well gases tell us about the origin of noble gases in the mantle and their relationship to the atmosphere. *Philosophical Transactions of the Royal Society A: Mathematical, Physical and Engineering Sciences* **366**, 4183–4203.

Ballentine C. J., O'Nions R. K. and Coleman M. L. (1996) A Magnus opus: Helium, neon, and argon isotopes in a North Sea oilfield. *Geochimica et Cosmochimica Acta* **60**, 831–849.

Barry P. H., Kulongoski J. T., Tyne R. L., Landon M. K., Gillespie J. M., Stephens M. J., Hillegonds D. J., Byrne D. J. and Ballentine C. J. (2018) Tracing enhanced oil recovery signatures in casing gases from the Lost Hills oil field using noble gases. *Earth and Planetary Science Letters* **496**, 57–67.

Barry P. H., Lawson M., Meurer W. P., Warr O., Mabry J. C., Byrne D. J. and Ballentine C. J. (2016) Noble gases solubility models of hydrocarbon charge mechanism in the Sleipner Vest gas field. *Geochimica et Cosmochimica Acta* **194**, 291–309.

Bernard B. B., Brooks J. M. and Sackett W. M. (1976) Natural gas seepage in the Gulf of Mexico. *Earth and Planetary Science Letters* **31**, 48–54.

Bethke C. M. (1985) A numerical model of compaction-driven groundwater flow and heat transfer and its application to the paleohydrology of intracratonic sedimentary basins. *Journal of Geophysical Research: Solid Earth* **90**, 6817–6828.

Beyerle U., Aeschbach-Hertig W., Imboden D. M., Baur H., Graf T. and Kipfer R. (2000) A Mass Spectrometric System for the Analysis of Noble Gases and Tritium from Water Samples. *Environmental Science & Technology* **34**, 2042–2050.

Bosch A. and Mazor E. (1988) Natural gas association with water and oil as depicted by atmospheric noble gases: case studies from the southeastern Mediterranean Coastal Plain. *Earth and Planetary Science Letters* **87**, 338–346.

Byrne D.J., Barry P. H., Lawson M. and Ballentine C. J. (2018a) Noble gases in conventional and unconventional petroleum systems. *Geological Society, London, Special Publications* **468**, 127–149.

Byrne D.J., Barry P. H., Lawson M. and Ballentine C. J. (2018b) Determining gas expulsion vs retention during hydrocarbon generation in the Eagle Ford Shale using noble gases. *Geochimica et Cosmochimica Acta* **241**, 240–254.

Cheng, (2020). Noble Gas Sources, Transport and Groundwater Interaction in Sedimentary Basins. DPhil Thesis. University of Oxford.

Cheng A., Sherwood Lollar B., Warr O., Ferguson G., Idiz E., Mundle S.O.C., Barry P. H., Byrne D., Mabry J. and Ballentine C. J. (2021) Determining the role of diffusion and basement flux in controlling ^{4}He distribution in sedimentary basin fluids. *Earth and Planetary Science Letters.* **In review**

Darrah T. H., Vengosh A., Jackson R. B., Warner N. R. and Poreda R. J. (2014) Noble gases identify the mechanisms of fugitive gas contamination in drinking-water wells overlying the Marcellus and Barnett Shales. *Proceedings of the National Academy of Sciences* **111**, 14076–14081.

Douglas P. M. J., Stolper D. A., Eiler J. M., Sessions A. L., Lawson M., Shuai Y., Bishop A., Podlaha O. G., Ferreira A. A., Santos Neto E. V., Niemann M., Steen A. S., Huang L., Chimiak L., Valentine D. L., Fiebig J., Luhmann A. J., Seyfried W. E., Etiope G., Schoell M., Inskeep W. P., Moran J. J. and Kitchen N. (2017) Methane clumped isotopes: Progress and potential for a new isotopic tracer. *Organic Geochemistry* **113**, 262–282.

Fernández-Prini R., Alvarez J. L. and Harvey A. H. (2003) Henry's Constants and Vapor–Liquid Distribution Constants for Gaseous Solutes in H_2O and D_2O at High Temperatures. *Journal of Physical and Chemical Reference Data* **32**, 903–916.

Gilfillan S. M. V., Lollar B. S., Holland G., Blagburn D., Stevens S., Schoell M., Cassidy M., Ding Z., Zhou Z., Lacrampe-Couloume G. and Ballentine C. J. (2009) Solubility trapping in formation water as dominant CO_2 sink in natural gas fields. *Nature* **458**, 614–618.

Stewart, R. J. & Haszeldine, R. S. (2014) Carbon Accounting for Carbon Dioxide Enhance Oil Recovery. Scottish Carbon and Capture and Storage Edinburgh

Hunt, A.G. (2015). Noble Gas Laboratory's standard operating procedures for the measurement of dissolved gas in water samples: *U.S. Geological Survey Techniques and Methods* 5- A11. U.S. Geological Survey, Reston, Virginia

Karolytė, R., Barry, P.H., Kulongoski, J.T., Tyne, R.L., Ballentine, C.J., (2019) *Using noble gases to trace the migration of hydrocarbons into shallow aquifers: separating signal from noise with inverse modelling techniques*. AGU Fall Meeting, December 8-13, 2019, San Francisco, USA.

Karolytė, R., Johnson, G., Yielding, G., Gilfillan, S.M.V. (2020) Reply to Discussion on 'Fault seal modelling–the influence of fluid properties on fault sealing capacity in hydrocarbon and CO_2 systems', Petroleum Geoscience, 2020.*Petroleum Geosciences* **26**, 610-612.

Kharaka Y. K. and Specht D. J. (1988) The solubility of noble gases in crude oil at 25–100°C. *Applied Geochemistry* **3**, 137–144.

Leung, D. Y. C., Caramanna, G. & Maroto-Valer, M. M. (2014).An overview of current status of carbon dioxide capture and storage technologies. *Renewable and Sustainable Energy Reviews* **39**, 426–443.

McIntosh J. C., Hendry M. J., Ballentine C. J., Haszeldine R. S., Mayer B., Etiope G., Elsner M., Darrah T. H., Prinzhofer A., Osborn S. G., Stalker L., Kuloyo O., Lu Z.-T., Martini A. M. and Sherwood Lollar B. (2019) A Critical Review of State-of-the-Art and Emerging Approaches to Identify Fracking-Derived Gases and Associated Contaminant in Aquifers. *Environmental Science & Technology* **53**, 1063–1077.

McMahon P. B., Vengosh A., Davis T. A., Landon M. K., Tyne R. L., Wright M. T., Kulongoski J. T., Hunt A. G., Barry P. H., Kondash A. J., Wang Z. and Ballentine C. J. (2019) Occurrence and Sources of Radium in Groundwater Associated with Oil Fields in the Southern San Joaquin Valley, California. *Environmental Science & Technology* **53**, 9398–9406.

Sherwood Lollar B. S., Onstott T. C., Lacrampe-Couloume G. and Ballentine C. J. (2014) The contribution of the Precambrian continental lithosphere to global H_2 production. *Nature* **516**, 379–382.

Smith S. P. and Kennedy B. M. (1983) The solubility of noble gases in water and in NaCl brine. *Geochimica et Cosmochimica Acta* **47**, 503–515.

Stolper D. A., Lawson M., Formolo M. J., Davis C. L., Douglas P. M. J. and Eiler J. M. (2018) The utility of methane clumped isotopes to constrain the origins of methane in natural gas accumulations. *Geological Society, London, Special Publications* **468**, 23–52.

Torgersen T. and Clarke W. B. (1985) Helium accumulation in groundwater, I: An evaluation of sources and the continental flux of crustal ^{4}He in the Great Artesian Basin, Australia. *Geochimica et Cosmochimica Acta* **49**, 1211–1218.

Torgersen T. and Kennedy B. M. (1999) Air-Xe enrichments in Elk Hills oil field gases: role of water in migration and storage. *Earth and Planetary Science Letters* **167**, 239–253.

Torgersen T., Kennedy B. M. and van Soest M. C. (2004) Diffusive separation of noble gases and noble gas abundance patterns in sedimentary rocks. *Earth and Planetary Science Letters* **226**, 477–489.

Warr O., Rochelle C. A., Masters A. and Ballentine C. J. (2015) Determining noble gas partitioning within a CO_2–H_2O system at elevated temperatures and pressures. *Geochimica et Cosmochimica Acta* **159**, 112–125.

Whiticar M. J., Faber E. and Schoell M. (1986) Biogenic methane formation in marine and freshwater environments: CO_2 reduction vs. acetate fermentation—Isotope evidence. *Geochimica et Cosmochimica Acta* **50**, 693–709.

Whyte C. J., Vengosh A., Warner N. R., Jackson R. B., Muehlenbachs K., Schwartz F. W. and Darrah T. H. (2021) Geochemical evidence for fugitive gas contamination and associated water quality changes in drinking-water wells from Parker County, Texas. *Science of The Total Environment*, **780**, 146555.

Wycherley H., Fleet A. and Shaw H. (1999) Some observations on the origins of large volumes of carbon dioxide accumulations in sedimentary basins. *Marine and Petroleum Geology* **16**, 489–494.

Young E. D. (2019) A Two-Dimensional Perspective on CH_4 Isotope Clumping: Distinguishing Process from Source. In: *Deep Carbon* (Eds. B. N. Orcutt, I. Daniel, and R. Dasgupta). Cambridge University Press. pp. 388–414.

Zaikowski A. and Spangler R. R. (1990) Noble gas and methane partitioning from ground water: An aid to natural gas exploration and reservoir evaluation. *Geology* **18**, 72.

Zhou Z. and Ballentine C. J. (2006) ^{4}He dating of groundwater associated with hydrocarbon reservoirs. *Chemical Geology* **226**, 309–327.

Zhou Z., Ballentine C. J., Kipfer R., Schoell M. and Thibodeaux S. (2005) Noble gas tracing of groundwater/coalbed methane interaction in the San Juan Basin, USA. *Geochimica et Cosmochimica Acta* **69**, 5413–5428.